Title

Implications of California vertical array data for the analysis of site response with 1D geotechnical modeling

Authors

Afshari, Kioumars
Stewart, Jonathan

Publication Date

2017-10-31

Peer reviewed

Implications of California Vertical Array Data for the Analysis of Site Response with 1D Geotechnical Modeling

Kioumars Afshari and Jonathan P. Stewart
Department of Civil and Environmental Engineering
University of California, Los Angeles

A report on research conducted under grant no. 1014-961 from California Strong Motion Instrumentation Program, California Geological Survey

Civil & Environmental Engineering Department
University of California, Los Angeles
October 2017
(Revised August 2018)

CONTENTS

LIST OF FIGURES

LIST OF FIGURES

ACKNOWLEDGMENTS

This research was supported by the California Strong Motion Instrumentation Program (CSMIP) of the California Geological Survey (CGS) (Agreement no. 1014-961). Partial support was also provided by the UCLA Civil & Environmental Engineering Department. This support is gratefully acknowledged.

We are appreciative of Tadahiro Kishida of the Khalifa University of Science Technology and Research (formerly with the Pacific Earthquake Engineering Research Center, PEER) and Yousef Bozorgnia of UCLA (also formerly with PEER) for providing access to data processing codes and their efforts in developing data resources used in this study. We also thank Hamid Haddadi of CSMIP for providing weak motion records from the Center for Engineering Strong Motion Data FTP folders, Javier Vargas Ortiz, Bahareh Heidarzadeh, and Jamison Steidl for providing geotechnical logs for vertical arrays sites considered in this project, and Eric Thompson and Adrian Rodriguez-Marek for providing data and valuable insight on their previous studies involving vertical arrays.

EXECUTIVE SUMMARY

Along with source and path effects, site response is an essential component of ground motion prediction. Widely used ground motion models (GMMs), also known as ground motion prediction equations, provide an ergodic representation of each component in the sense that observations from global databases during the observation period (generally the last few decades) are taken to apply for a particular site and tectonic setting of interest, following conditioning on relevant parameters (magnitude, distance, time-averaged shear wave velocity in the upper 30 m, V_{S30}). Such models inherently average across effects that may exhibit location-to-location variability, increasing model dispersion. The use of non-ergodic site response has gained increasing attention in recent years as a means by which to increase model accuracy and reduce model dispersion, both of which affect the outcomes of seismic hazard analysis.

The analysis of non-ergodic site response can, in general, be undertaken through analysis of recordings at the site of interest, or (in the absence of such data) through the use of geotechnical simulations. The most common simulation approach, known as ground response analyses, simplifies the actual site response problem by assuming horizontal soil layers and vertically propagating waves. The objective of this research was to compile and analyze data from vertical arrays in California for the purpose of evaluating ground response analysis as a method of predicting non-ergodic site response and to estimate epistemic uncertainties associated with its application. More specifically, we investigated three questions: (1) how effective is ground response analysis at predicting observed small strain, essentially visco-elastic, site response as observed at California vertical arrays?; (2) which models for small strain damping are most effective for use in ground response analyses?; and (3) recognizing the imperfect ability of ground response analysis to capture observed site response effects, how should epistemic uncertainty in site response be represented when it is estimated using ground response analysis procedures?

We consider a database of 21 California vertical arrays operated by the California Strong Motion Instrumentation Program (CSMIP) and the University of California Santa Barbara. Each of the considered arrays has ≥ four surface and downhole ground motion recordings, and cumulatively our database contains 287 ground motion pairs from 207 earthquakes. Uncorrected (version 1) acceleration time series were processed using standard procedures developed for the

Next Generation Attenuation projects. Although this database is considerably smaller than the KiK-net database that has been widely used in prior research, it has two notable benefits: (1) it represents site response for a distinct region (California) with a different geologic history and (2) the available velocity profile data is of higher resolution and quality, and is mostly accompanied by geotechnical logs with detailed information on soil conditions.

The processed data were plotted as surface-to-downhole transfer functions and ratios of 5% damped pseudo acceleration response spectra, each of which represents in different ways the frequency-dependent site response for essentially visco-elastic conditions over the depth range of the arrays. The site response is considered visco-elastic because relatively weak ground motions were selected for analysis. Ground response analyses were performed using the measured shear wave velocities, various damping models, and the recorded base motion as input. We find a higher percentage of California sites, as compared to KiK-net sites from Japan, to have a reasonable match of empirical and theoretical transfer function shapes. The empirical transfer functions also have a greater degree of event-to-event consistency than has been found previously in Japan. We were unsuccessful at diagnosing conditions that would indicate, *a priori*, whether ground response analyses are or are not effective for a particulate site.

Three damping models were considered in the ground response analyses – geotechnical models, models for quality factor (Q) based on seismological inversion, and models derived from the site-specific site diminutive parameter (κ_0). These models represent, to varying degrees, the attenuation of ground motions from two physical mechanisms – soil intrinsic (hysteretic) damping and wave scattering, both of which would be expected to be present to varying degrees at a given site. Despite the different mechanisms, the principle means by which to incorporate damping in ground response analysis is through the soil hysteretic damping considered in the analysis (D), which was the approach taken here. As expected, the effects of using different damping models are concentrated at high frequencies, specifically those higher that the frequency of the modelled soil column. Ground response analyses based on geotechnical models underestimate site attenuation, which has been observed previously and is expected because scattering effects are neglected. The models based on seismological inversion tend to overestimate site attenuation; this conclusion is likely not fully general, but applies to the considered data inventory. We describe a means by which to adjust geotechnical models for D using observations of κ_0, more specifically

the change of κ_0 across the depth range of vertical arrays. This approach yielded intermediate levels of site attenuation that modestly improved prediction accuracy and reduced the dispersion of residuals relative to the other damping models.

We use the residuals of ground response analysis predictions of site response, relative to observation, to quantify epistemic uncertainties. Our proposed methodology partitions prediction residuals into between- and within-site components, and takes the between-site standard deviation as a quantification of epistemic uncertainty. Our results suggest values ranging from 0.35-0.5 in natural log units, which is surprisingly consistent with related prior results from other investigators using Japanese data. We also find levels of event-to-event variability for a given site that are consistent with observations elsewhere, including Japan and Taiwan.

1 Introduction

Evaluating the role of local site conditions on ground shaking is an essential part of earthquake ground motion prediction, which can be done using ergodic models or site-specific (non-ergodic) analyses. One-dimensional (1D) simulation of shear waves propagating vertically through shallow soil layers, also known as ground response analysis (GRA), is a common approach for capturing the effects of site response on ground shaking. In GRA, different approaches have been used for modeling soil behavior, namely linear, equivalent-linear (EL), and various nonlinear (NL) methods. Much attention has been directed in recent research to which of these approaches is best suited to a particular problem, with the intention of guiding the selection of an appropriate method of analysis (e.g., choosing when NL is preferred to EL) (e.g., Kim et al., 2015; Kaklamanos et al, 2013, 2015; Zalachoris and Rathje, 2015). However, crucial issues that have received much less attention are the degree to which 1D simulations (the essential assumption behind all GRA methods) are effective and the epistemic uncertainties associated with their use in ground motion prediction.

While site response can include important contributions from the wave propagation mechanics simulated in GRA, site response as a whole is considerably more complex. True site response represents the difference between ground motions for a given site condition and what would have occurred had the site had a reference condition (typically rock with a particular V_{S30}). Processes that can control site response in this context include 1D ground response in combination with additional effects including surface waves, basin effects (including focusing and basin edge-generated surface waves), and topographic effects. Because GRA only simulates a portion of the physics controlling site response, there should be no surprise that it is not always effective at accurately predicting site effects.

When GRA are performed for engineering projects, it is usually with the expectation that they provide an unbiased, site-specific estimate of site response. The site response computed in this manner can be interpreted in the form of a site-specific amplification function, which in turn can be implemented in probabilistic seismic hazard analyses (PSHA) (e.g., McGuire et al., 2001; Stewart et al. 2017). If the ground response computed in this manner accurately reflects the primary physical mechanisms controlling site response, it provides the basis for a non-ergodic hazard analysis, which has appreciable benefits with regard to standard deviation and hazard reduction (e.g., Stewart et al., 2017). As a result, there is a considerable practical need to understand the degree to which GRA can be considered to provide an accurate (unbiased) estimate of site response and the appurtenant uncertainties associated with its use.

Validation and testing of 1D GRA is possible by studying recordings from vertical array sites. Vertical arrays are valuable tools for distinguishing the effects of shallow site conditions from the other effects (source, path, etc.) on ground motions. They allow for the observation of ground motions from the same source both at the surface and the depth at which the downhole sensor is installed. Therefore, a vertical array directly reveals the effects of site response between surface and downhole instruments. In addition to allowing for direct observation of site response effects, a well characterized vertical array site, which includes a high quality shear wave velocity (V_s) profile and possibly a geotechnical log, allows for validating numerical site response models.

Numerous studies of data from vertical arrays at individual sites have found reasonably good fits of data to GRA results (e.g., Borja et al., 1999; Elgamal et al., 2001; Lee et al., 2006; Tsai and Hashash, 2009; Yee et al., 2013). The KiK-net array in Japan (Aoi et al., 2000) provides a large inventory of vertical arrays that has been extensively used for validation purposes (Thompson et al., 2012; Kaklamanos et al, 2013, 2015; Zalachoris and Rathje, 2015), although the resolution and quality of the seismic velocity and geotechnical site descriptions is arguable sub-optimal. Nonetheless, as described in Chapter 4, when viewed as a whole, these KiK-net data challenge the notion that 1D GRA provides a reliable estimate of site response. Were this result found to be widely applicable, it would upend a good deal of current practice that relies on GRA to estimate first-order site response.

Our objectives in this study were to compile and analyze data from vertical arrays in California for the purpose of evaluating ground response analysis as a method of predicting non-

ergodic (site-specific) site response and to estimate epistemic uncertainties associated with its application. We utilize the growing body of vertical array data from California to assemble a database suitable for meeting these objectives.

Chapter 2 describes the database attributes, including available information on site conditions, the processing of ground motion data, and the range of conditions represented in the data set. Chapter 3 describes the methods of ground response analysis considered for each vertical array site, including alternate methods of accounting for the attenuation of seismic energy within the site under effectively visco-elastic conditions. Chapter 3 includes discussion of the manner in which site-specific diminutive parameter κ_0 was evaluated from available ground motion data as well as the change in κ_0 across the depth range of the arrays.

Chapter 4 describes analysis of the data in the form of transfer functions between the surface and downhole instruments and how these data attributes compare to estimates from ground response analysis, both for individual sites and in aggregate across the dataset. Chapter 5 describes analysis of the data from the perspective of 5%-damped pseudo spectral accelerations, in consideration of both model performance and associated uncertainties. The report is concluded in Chapter 6 with a summary of principal findings.

2 California Vertical Array Dataset

2.1 INTRODUCTION

A database of recordings from vertical arrays owned and operated by the California Strong Motion Instrumentation Program (CSMIP) and University of California at Santa Barbara (UCSB) has been compiled. A similar database from Japan was compiled by Dawood et al. (2016), which is comprised of data from the Kiban-Kyoshin network (KiK-net) (Aoi et al., 2001). The Dawood et al. database updates an earlier KiK-net database by Pousse (2005). In order to compile the large database of about 157,000 recordings, Dawood et al. (2016) developed a step-by-step automated protocol to systematically process the data, and produced a flatfile which is available at NEEShub (https://nees.org/resources/7849). Other major vertical array networks are operated in Taiwan (Downhole Earthquake Monitoring Network, http://scweb.cwb.gov.tw/Twenty.aspx?ItemId=41&loc=en) and Greece (EuroSeis test, Raptakis et al., 2000, Chavez-Garcıa et al., 2000 at http://euroseisdb.civil.auth.gr/).

2.2 ARRAY ATTRIBUTES

We have collected site data for 39 vertical arrays in California as listed in Table 2.1. Our main source of site properties and ground motion data is the Center for Engineering Strong Motion Data (CESMD) website (http://www.strongmotioncenter.org/). Velocity profile data is available for 30 sites, and ground motion time series can be downloaded through a search engine. In addition, CESMD maintains an FTP folder containing a database of weaker motions for all vertical array and surface-only sites. We have also considered four sites owned and maintained by the University

of California at Santa Barbara (UCSB). The site information and recorded motions for these sites are available at http://nees.ucsb.edu/.

Interestingly, a factor limiting the inventory of usable vertical array sites in California is the availability of V_S profile data; of the 39 vertical arrays, we have been able to collect usable V_S profile data for 30 sites (26 CESMD, 4 UCSB), and boring logs are available for 24 sites (20 CESMD and 4 UCSB). Given the relative cost of array installation (high) vs V_S profile development (low), a priority in future work should be to fill this data gap.

Boring logs for the sites were obtained from multiple sources. For two of the four sites owned by UCSB, the boring logs were available at http://nees.ucsb.edu/. For the Hollister Digital Array site and Borrego Valley Downhole Array site, boring logs were provided by J. Steidl (*personal communication*, Feb, 2016). For 17 CESMD sites located at California Department of Transportation bridges, we obtained logs from Javier V. Ortiz (personal communication, July, 2015). Three of CESMD sites have been part of calibration sites for validation of nonlinear geotechnical models project for which high quality boring logs are available. The V_S profiles and geotechnical logs are shown in Figures 4.5-4.25.

We utilize vertical array sites with measured V_S profiles and having at least four pairs of surface/downhole recordings to increase the statistical significance of the results. These data selection criteria resulted in 21 sites, of which 17 have available boring logs. The locations of those vertical array sites are shown in Figure 2.1. Figure 2.2 shows the histograms of V_{S30} for the KiK-net sites used by Thompson et al. (2012), all California sites listed in Table 2.1, and the California sites selected to be used in this study with a measured V_S profile and at least four surface/downhole recording pairs. The median V_{S30} is 413 m/s for the KiK-net sites, 309 m/s for all California sites, and 321 m/s for the California sites used in this study. The median values as well as the shape of the histograms in Figure 2.2 indicate that KiK-net sites are generally stiffer than the California sites. This may due to the KiK-net arrays having been installed with the primary purpose of source detection, for which installation of the base instrument in rock is preferred. This led to a large number of KiK-net vertical arrays being located on geology consisting of weathered rock or shallow soil overlying rock, often in mountainous areas. In contrast, most of the California sites are located next to bridges, which are generally located in topographically flat areas with relatively soft soils near the surface of deep sedimentary basins.

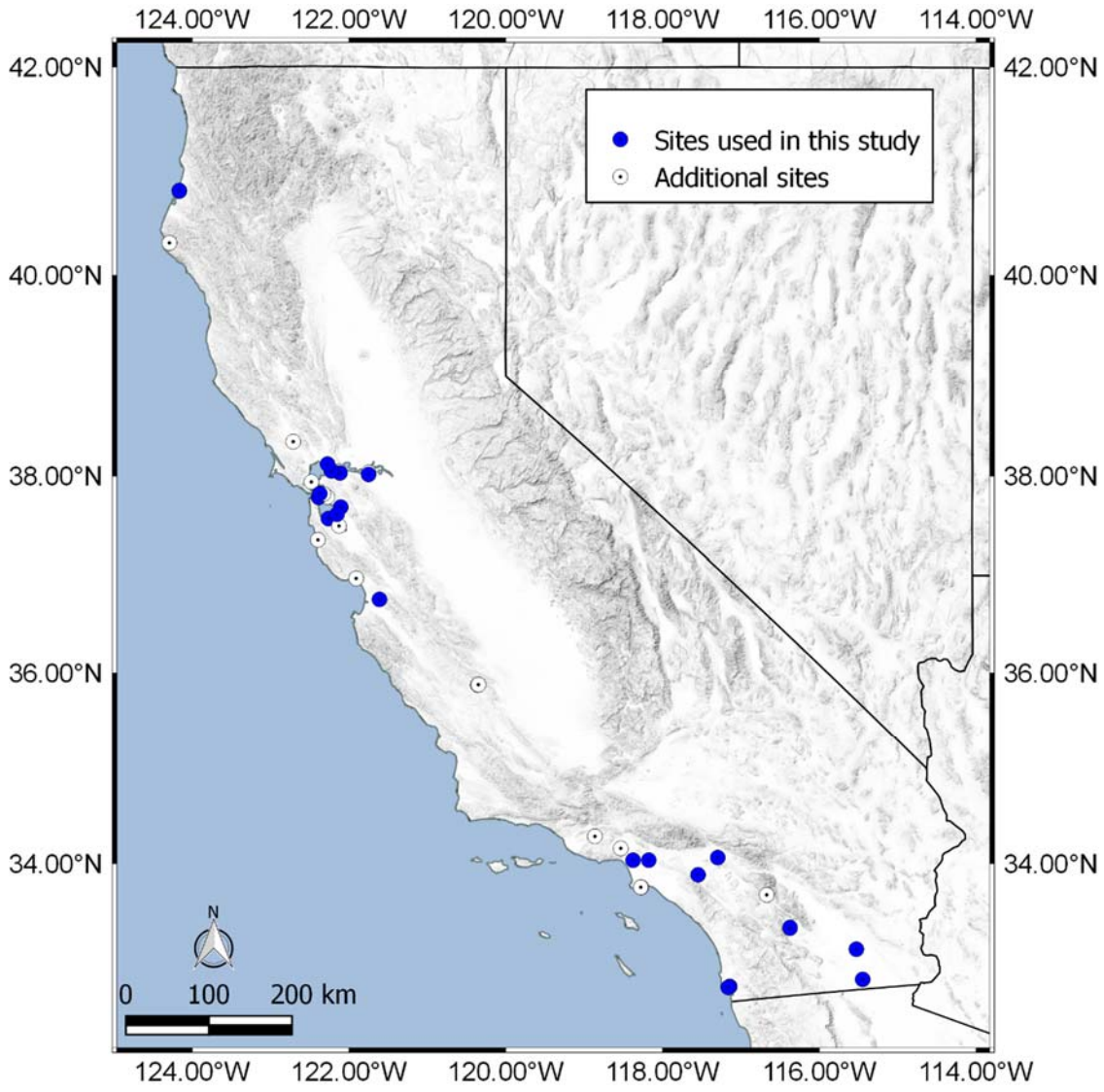

Figure 2.1. The location of vertical array sites in California (The sites used in this study are shown in blue)

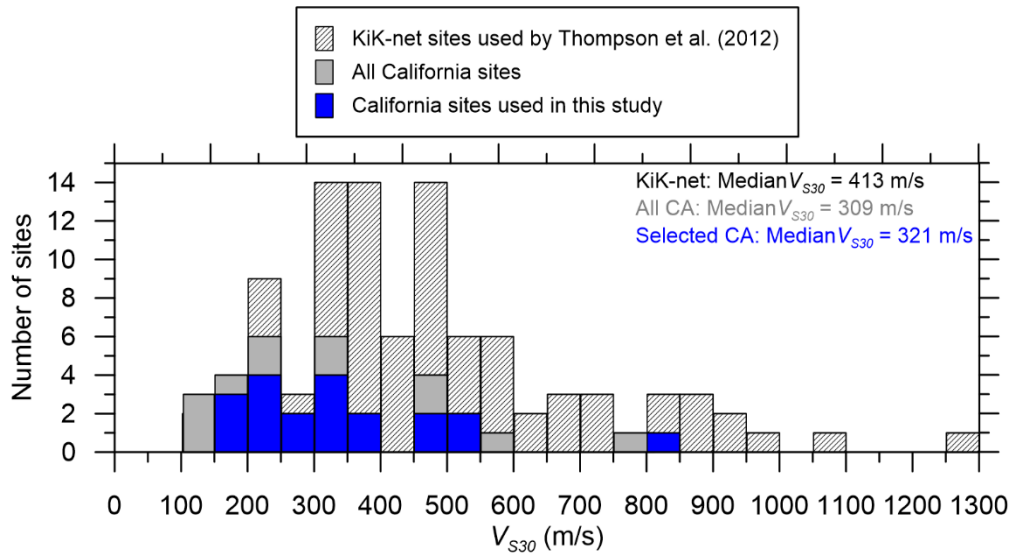

Figure 2.2. Histograms of V_{S30} for vertical array sites from Table 2.1, vertical array sites selected to be used in this study, and vertical arrays from KiK-net used by Thompson et al. (2012).

Table 2.1. Summary of site characteristics for California vertical arrays. Sites considered in present work are bolded

Site	Station NO (CSMIP)	Owner	No. of Rec	Latitude	Longitude	Site geology	V_{S30} (m/s)	$R_V = \frac{V_{SDH}}{V_{S5}}$	V_S profile available ?	Boring log available?	Source of boring log
Alameda - Posey & Webster	58137	CGS - CSMIP	7	37.790	-122.277	Deep alluvium	208 (inferred)	NA	N	Y	Caltrans[1]
Antioch-San Joaquin N	67265	CGS	4	38.0377	-121.7515	Deep Alluvium	Problematic measurements	NA	top 20 m missing	N	NA
Antioch-San Joaquin S	**67266**	**CGS**	**4**	**38.018**	**-121.752**	**Deep Alluvium**	**253**	**3.76**	**Y**	**Y**	**Caltrans**
Aptos - Seacliff Bluff	47750	CGS - CSMIP	4	36.972	-121.910	Alluvium	463 (profile not available)	NA	N	N	NA
Benicia North	68321	CGS - CSMIP	2	38.051	-122.128	Shallow fill over bay mud	582	Not measured	Y	Y	Caltrans
San Francisco - Bay Bridge	**58961**	**CGS - CSMIP**	**9**	**37.787**	**-122.389**	**Thin alluvium over soft rock**	**391**	**6.58**	**Y**	**N**	**NA**
Benicia-Martinez South	**68323**	**CGS - CSMIP**	**10**	**38.033**	**-122.117**	**Sediments underlain by slightly more competent rock**	**547**	**1.48**	**Y**	**Y**	**Caltrans**
Borrego Valley Digital Array	**NA**	**UCSB**	**16**	**33.322**	**-116.376**	**Shallow alluv over rock (granodiorite)**	**340**	**12.22**	**Y**	**Y**	**Jamison Steidle[2]**
Crockett-Carquinez Br #2	68259	CGS - CSMIP	4	38.055	-122.226	Shallow clay over rock (sed.)	--	NA	N	Y	Caltrans
Corona I15/Hwy 91	**13186**	**CGS - CSMIP**	**31**	**33.882**	**-117.549**	**Shallow clay over soft rock**	**321**	**16.68**	**Y**	**Y**	**Caltrans**
Coronado East	**3192**	**CGS - CSMIP**	**10**	**32.698**	**-117.145**	**Deep alluvium**	**329**	**1.89**	**Y**	**Y**	**Caltrans**
Coronado West	**3193**	**CGS - CSMIP**	**21**	**32.688**	**-117.164**	**Deep alluvium**	**214**	**4.53**	**Y**	**Y**	**Caltrans**
Half Moon Bay - Tunitas	58964	CGS - CSMIP	2	37.358	-122.398	Shallow alluv over rock (chert/greenstone)	309	Not measured	Y	Y	Caltrans
Crockett-Carquinez Br #1	**68206**	**CGS - CSMIP**	**8**	**38.054**	**-122.225**	**Alluvium over soft rock (granite)**	**335**	**3.08**	**Y**	**Y**	**Caltrans**

Site	Station NO (CSMIP)	Owner	No. of Rec	Latitude	Longitude	Site geology	V_{S30} (m/s)	$R_V = \frac{V_{SDH}}{V_{S5}}$	V_S profile available ?	Boring log available?	Source of boring log
El Centro - Meloland	**1794**	**CGS - CSMIP**	**19**	**32.774**	**-115.449**	**Alluvium over soft rock (siltstone)**	**238**	**4.45**	**Y**	**Y**	**Calibration sites[3]**
Eureka	**89734**	**CGS - CSMIP**	**14**	**40.819**	**-124.166**	**Deep alluvium**	**160**	**6.31**	**Y**	**Y**	**Caltrans**
Foster City-San Mateo	**58968**	**CGS - CSMIP**	**7**	**37.573**	**-122.264**	**Deep alluvium**	**810**	**22.40**	**Y**	**N**	**Caltrans**
Los Angeles – Vincent Thm Geo Array W1	14783	CGS - CSMIP	3	33.750	-118.275	Alluvium over crystalline rock	149	Not measured	Y	N	NA
Los Angeles – Vincent Thm Geo Array W2	14784	CGS - CSMIP	3	33.750	-118.278	Deep alluvium	149	Not measured	Y	N	NA
Los Angeles – Vincent Thos W	14786	CGS - CSMIP	2	33.750	-118.280	Deep alluvium over rock (sandstone)	149	Not measured	Y	Y	Caltrans
Moorpark - Hwy118/Arroyo Simi	24185	CGS - CSMIP	1	34.288	-118.865	Deep alluvium	--	NA	N	Y	Caltrans
Oakland – Bay Bridge	58204	CGS - CSMIP	3	37.821	-122.327	Deep alluvium	--	Not measured	top 20 m missing	N	NA
Palo Alto – Dumbarton Br W	58526	CGS	1	37.499	-122.129	Deep alluvium	--	Not measured	missing in website	Y	Caltrans
Parkfield – Turkey Flat #1	36529	CGS - CSMIP	1	35.878	-120.359	Shallow alluvium rock (sandstone)	907	Not measured	Y	N	NA
Parkfield – Turkey Flat #2	36520	CGS - CSMIP	0	35.882	-120.351	Alluvium (fill)	467	Not measured	Y	N	NA
Petrolia - Downhole [abandoned]	89289	CGS - CSMIP	1	40.317	-124.292	Deep alluvium	--	NA	N	N	NA
Rohnert Park - Hwy 101	68797	CGS - CSMIP	2	38.347	-122.713	Rock (sandstone)	223	Not measured	Y	N	NA
Garner Valley	**NA**	**UCSB**	**10**	**33.669**	**-116.674**	**Shallow alluvium over rock (sandstone)**	**241**	**14.08**	**Y**	**Y**	**NEES @ UCSB Website[4]**

Site	Station NO (CSMIP)	Owner	No. of Rec	Latitude	Longitude	Site geology	V_{S30} (m/s)	$R_V = \frac{V_{SDH}}{V_{S5}}$	V_S profile available ?	Boring log available?	Source of boring log
Hayward-580W	**58487**	**CGS**	**5**	**37.689**	**-122.107**	**Shallow alluvium over rock (greywacke)**	**489**	**0.94**	**Y**	**N**	**NA**
Hayward-San Mateo	**58798**	**CGS**	**5**	**37.617**	**-122.154**	**Alluvium**	**185**	**3.10**	**Y**	**N**	**NA**
Hollister Digital Array	**NA**	**UCSB**	**23**	**36.758**	**-121.613**	**Deep alluvium**	**385**	**10.36**	**Y**	**Y**	**Jamison Steidle**
San Rafael – Richmond Brdg	58267	CGS	1	37.943	-122.481	Shallow alluvium over soft rock (sandst)	921	Not measured	Y	N	NA
Tarzana – Cedar Hill B	24764	CGS - CSMIP	4	34.161	-118.535	Thin fill/alluv over soft rock (sandst)	302	NA	N	N	NA
La-Cienega	**24703**	**CGS - CSMIP**	**20**	**34.036**	**-118.378**	**Fill over shallow alluv over soft rock**	**242**	**3.62**	**Y**	**Y**	**Calibration sites**
Obregon Park	**24400**	**CGS - CSMIP**	**23**	**34.037**	**-118.178**	**Thin Alluvium over weathered rock (Franciscan)**	**452**	**1.28**	**Y**	**Y**	**Calibration sites**
San Bernardino	**23792**	**CGS - CSMIP**	**5**	**34.064**	**-117.298**	**Thin alluvium over shale**	**252**	**4.85**	**Y**	**Y**	**Caltrans**
Treasure Island	**58642**	**CGS - CSMIP**	**11**	**37.825**	**-122.374**	**Shallow fill over deep alluvium (Bay mud)**	**157**	**16.00**	**Y**	**Y**	**Caltrans**
Vallejo - Hwy 37/Napa River	**68310**	**CGS - CSMIP**	**17**	**38.122**	**-122.275**	**Bay mud**	**528**	**1.54**	**Y**	**Y**	**Caltrans**
Wildlife Liquefaction Array	**NA**	**UCSB**	**21**	**33.097**	**-115.530**	**Silty clay with a granular layer**	**200**	**1.44**	**Y**	**Y**	**NEES @ UCSB Website**

[1] Caltrans: California Department of Transportation (Javier V. Ortiz, personal communication).
[2] Jamison Steidle: Personal communication with Jamison Steidle of UCSB.
[3] Calibration sites: Calibration sites for validation of nonlinear geotechnical models project (http://www.seas.ucla.edu/~jstewart/CalibrationSites/Webpage/main.htm).
[4] NEES @ UCSB Website: http://nees.ucsb.edu/

The sites as shown in Figure 2.1 are primarily located in the San Francisco Bay Area in northern California, and the Los Angeles, San Diego, and Imperial Valley regions of southern California. Due to the diverse geological conditions at the sites, the vertical arrays selected for this study cover site classes from rock (NEHRP class B) to soft soil (NEHRP class E). There are also differences in the stiffness of the soil/rock at the depth of the downhole instrument, as well as differences in the relative change in the stiffness between surface and downhole. In order to quantify the latter conditions, we define a surface/downhole shear wave velocity ratio (R_V) as the ratio of the time-averaged V_S at the top 5 meters (V_{S5}) to the time-averaged V_S at the 5 meter interval below the downhole instrument (V_{SDH}):

$$R_V = \frac{V_{SDH}}{V_{S5}} \tag{2.1}$$

A high value of R_V indicates a large change of stiffness from downhole to surface, which is indicative of either a steep gradient in the V_S profile and/or a large impedance contrast, either of which causes large ground response. Low values of R_V (close to 1) indicate a small gradient and lack of impedance contrast, which in turn should produce little amplification. Small R_V values tend to occur when the downhole instrument in a vertical array is within the sediment stack and not within underlying bedrock materials, which is typical of arrays in deep basins (e.g., Los Angeles, Imperial Valley). A histogram of R_V values is shown in Figure 2.3, and the spatial distribution of R_V is shown in Figure 2.4.

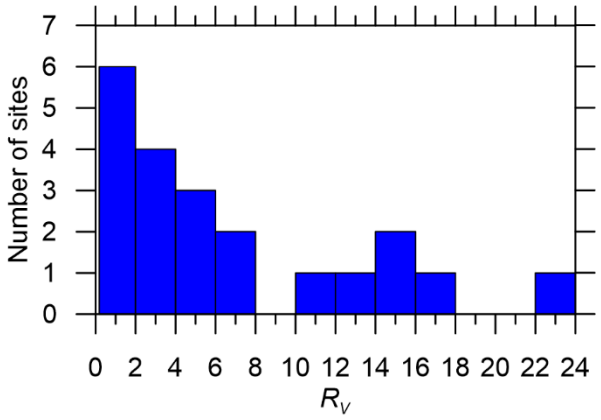

Figure 2.3. Histograms of R_V for vertical array sites used in this study.

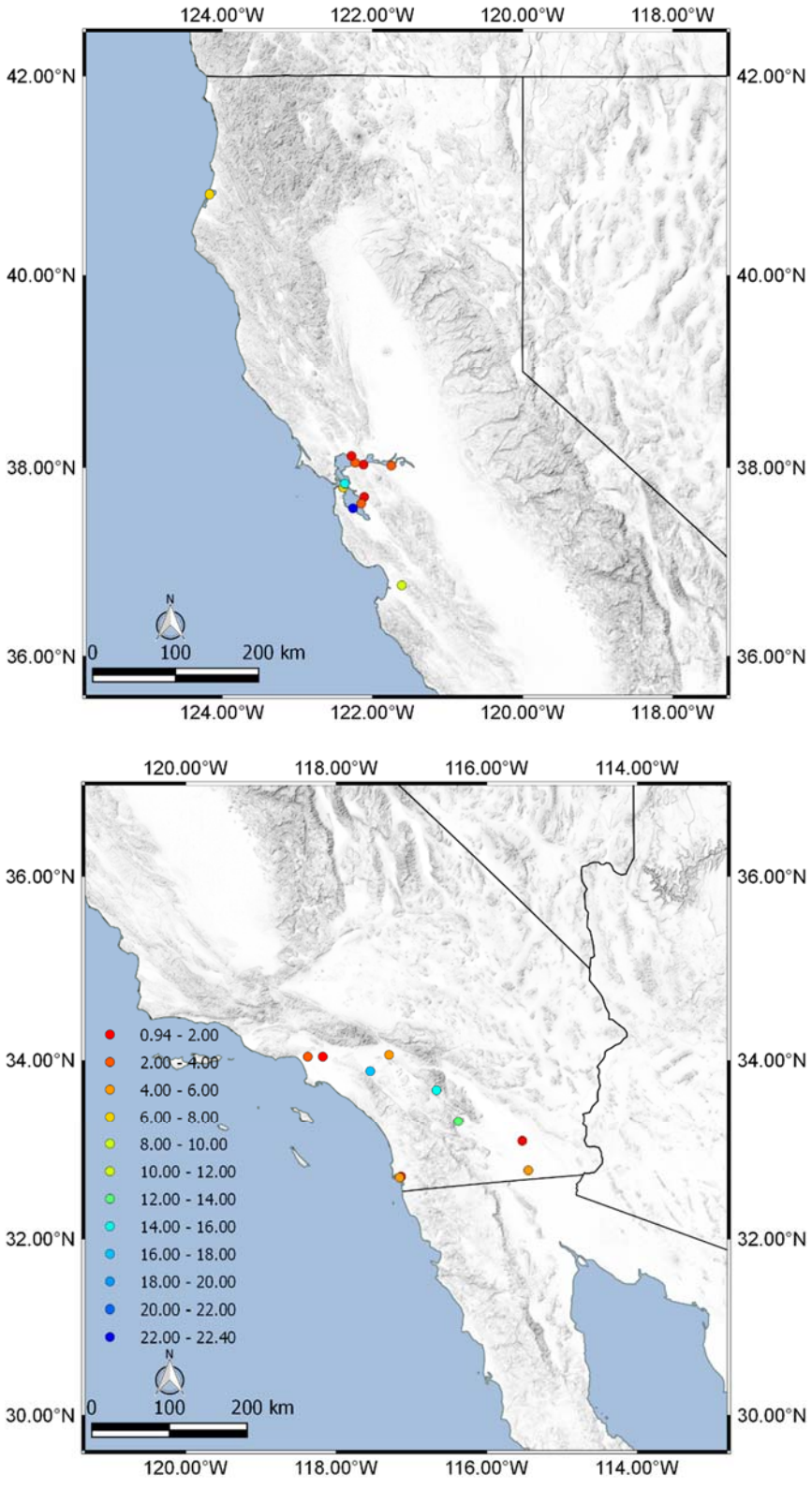

Figure 2.4. The location of vertical array sites in California used for this study in (a) northern California and (b) southern California (Red: Low values of R_V, blue: High values of R_V).

2.3 DATA ATTRIBUTES

In this section, we describe a dataset of 287 surface/downhole processed recording pairs from 207 events. The times of the events have been extracted from the unprocessed data files, and the characteristics of the events (magnitude and epicenter location) are found on a USGS website (https://earthquake.usgs.gov/earthquakes/search/). Event magnitudes vary from small (**M**2.5) to large (**M**7.2 El Mayor Cucapah earthquake). Epicenter locations are shown in Figure 2.5 with circle diameters proportional to magnitude. Also shown in Figure 2.5 are station locations.

2.3.1 Available recordings

The 287 surface/downhole recording pairs used in this study include two horizontal components recorded at the surface and two horizontal components recorded downhole (total of four individual recordings). The vertical array sites often have instruments at multiple levels to record ground motions at different depths. In the case of multiple downhole instruments, we have chosen the deepest level in order to capture the effects of site response over a longest path for upcoming shear waves, therefore the recordings at the intermediate depths were not processed for inclusion in this database.

Figure 2.6 shows the distribution of the data with respect to magnitude and epicentral distance, with the plot symbol size being proportional to the RotD50 peak ground velocity (*PGV*) at the surface. We choose *PGV* because it can be related to maximum shear strain in the profile caused by the ground motions (i.e., peak strain is roughly related to PGV/V_S). We also show the histogram of strain index (I_γ) in Figure 2.7 which is defined by Kim et al. (2016) as the ratio of input motion *PGV* to V_{S30}. This parameter can be used as an index correlated to the maximum shear strain in the soil profile.

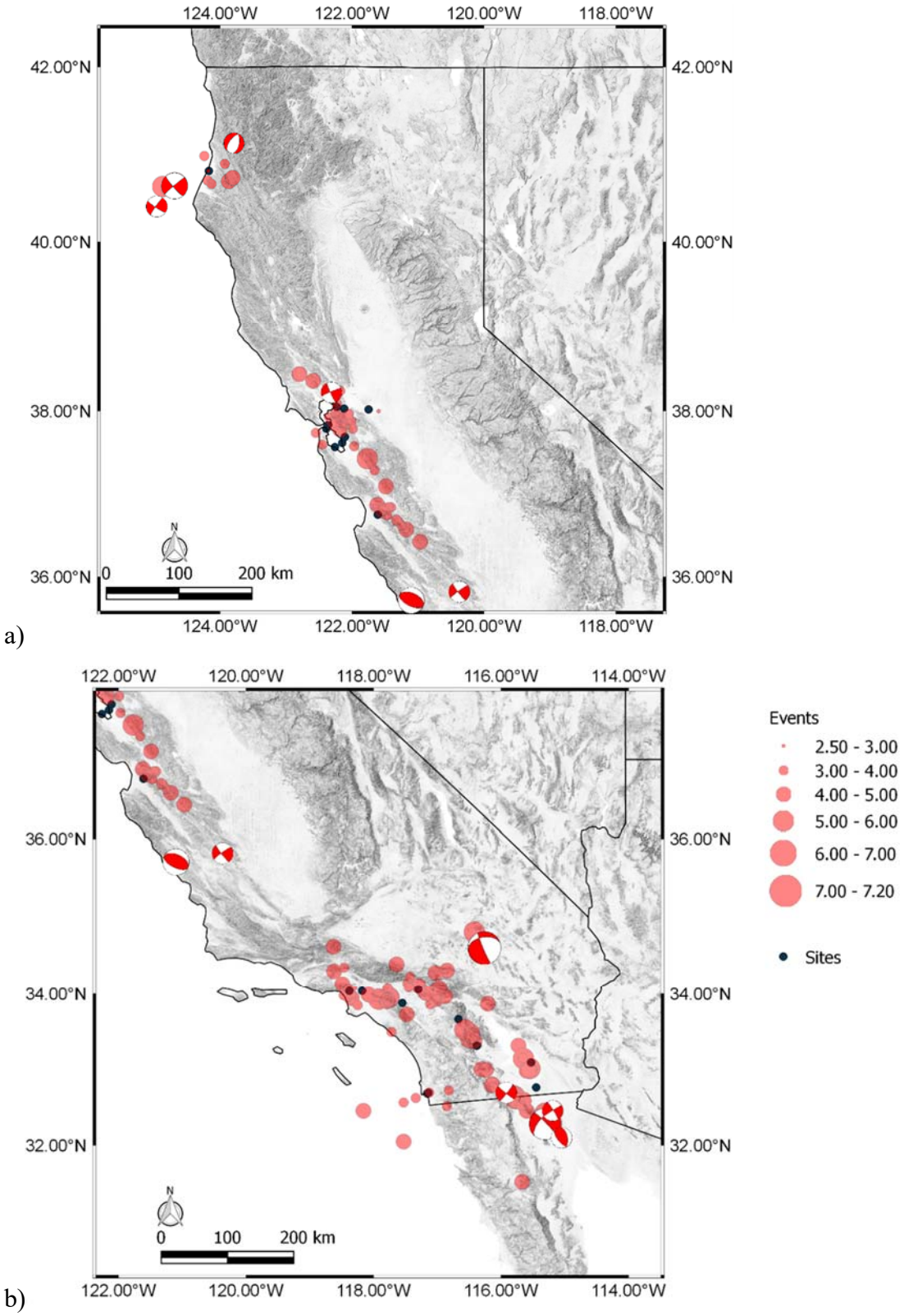

Figure 2.5. The location of events vertical array sites in California used for this study in (a) Northern California and (b) Southern California (Moment tensors are shown for M>5.5 events).

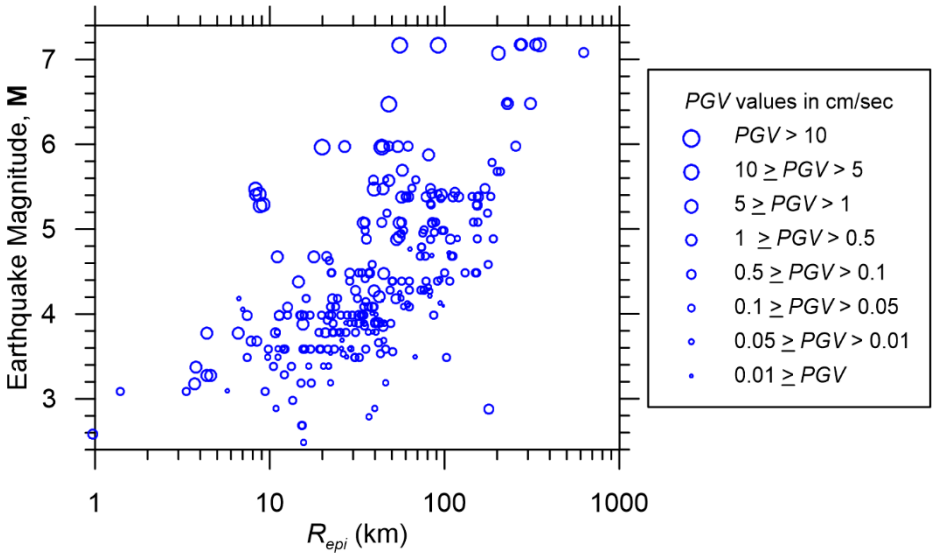

Figure 2.6. Magnitude and distance distribution of data used in the current work; the size of the symbols represent the *PGV* of the surface recording.

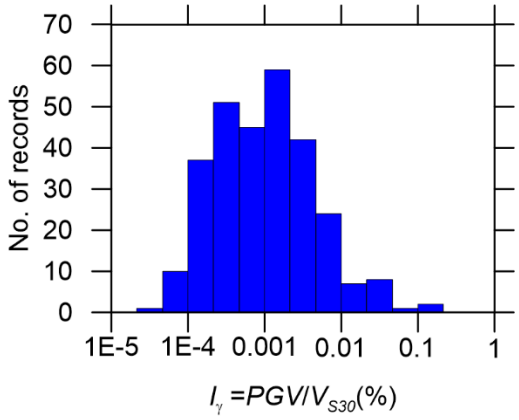

Figure 2.7. Histogram of strain index (I_γ) for the recordings from California Vertical arrays.

2.3.2 Data processing

Unprocessed records for the sites identified in the previous section were downloaded from CESMD and the nees.ucsb websites. Acceleration time series were visually inspected to identify and exclude low-quality, noise-dominated records. The data were processed using procedures developed in the NGA-West2 research project (Ancheta et al., 2014) and coded into an R routine (T. Kishida, *personal communication*, 2015). Low-cut and high-cut corner frequencies have been identified for each record by visual inspection, and low- and high-pass acausal Butterworth filters

are used for filtering high and low frequency noise in the frequency domain. Baseline correction is also applied as needed.

Error! Reference source not found. shows the number of usable records as a function of period; the decrease as period increases is due to application of low-cut corner frequencies in the record processing. The longest usable period is taken as $(0.877/f_c)$, where f_c is the low-cut corner frequency selected in record processing. Figure 2. shows an example of a record processed using the NGA procedures, including time series (acceleration, velocity, displacement for processed record) and Fourier amplitude spectra and pseudo-acceleration response spectra at 5% damping for the unprocessed and processed versions of the record. Based on the records we have been able to access and process, the usable database currently includes 21 sites and 287 record pairs.

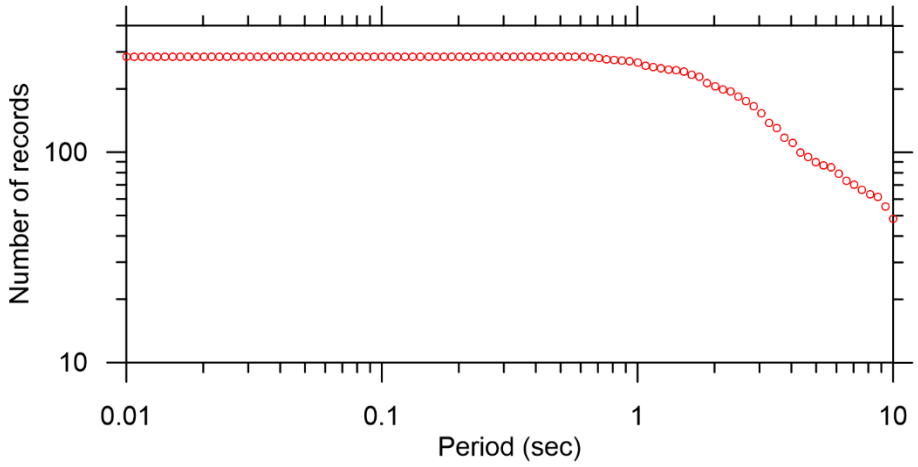

Figure 2.8. Number of available record pairs in the database according to their longest usable periods.

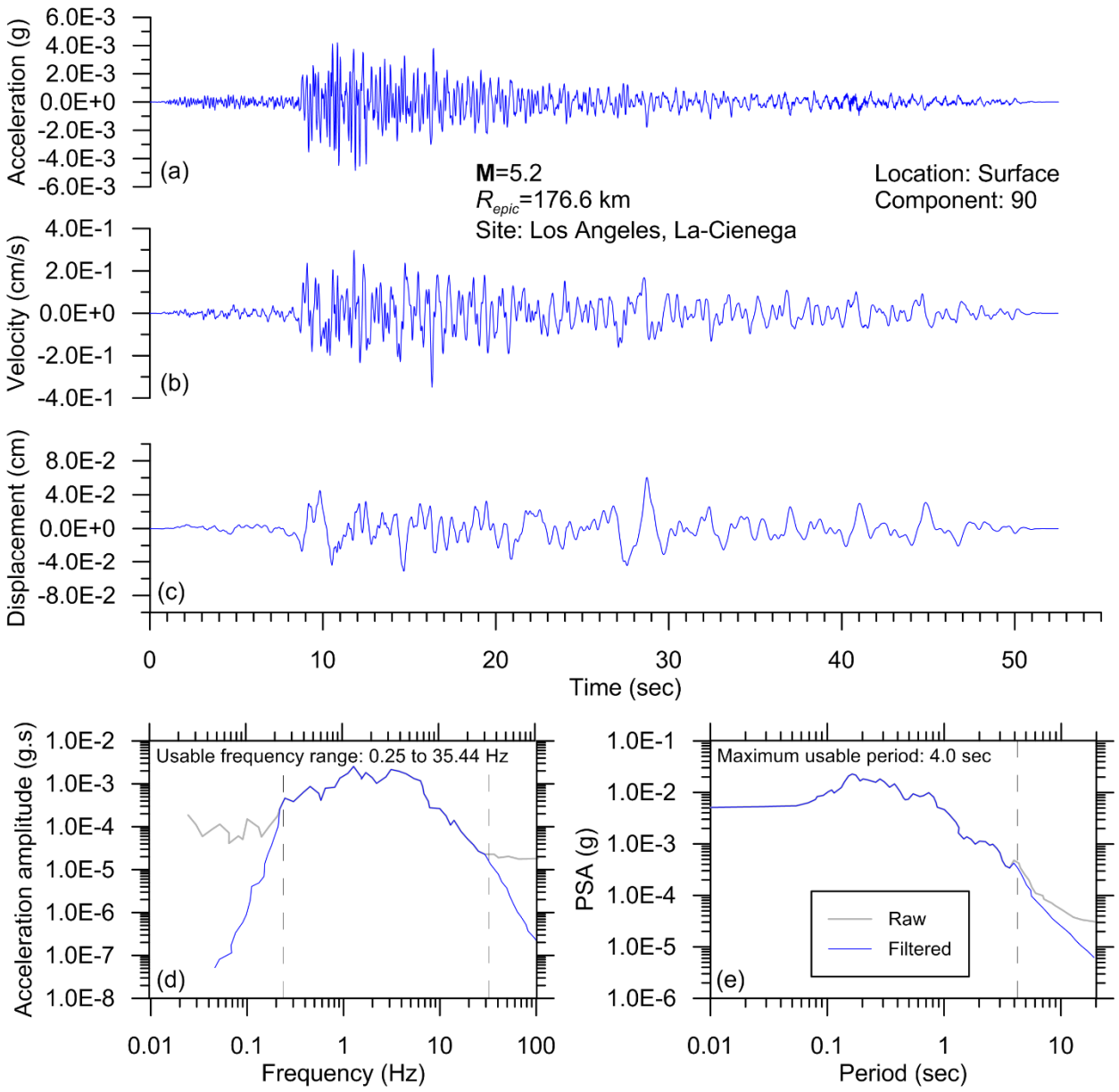

Figure 2.9. Example of record processed using PEER protocols developed in NGA-West2 project (Ancheta et al., 2014), including (a) acceleration time series, (b) velocity time series, (c) displacement time series, as well as (d) Fourier amplitude spectra and (e) pseudo-acceleration response spectra (*PSA*) at 5% damping for raw and filtered records.

3 Analysis Tools and Parameter Selection Procedures

3.1 INTRODUCTION

One-dimensional (1D) simulation of shear waves propagating vertically through shallow soil layers, also known as ground response analysis (GRA), is a common approach for capturing the effects of site response on ground shaking. In this chapter, we describe how GRA was performed for the vertical array sites discussed in Chapter 2. This includes the selected analysis platform and three alternate procedures by which small-strain hysteretic damping was assigned. Chapters 4 and 5 compare observed and predicted transfer functions and 5% damped pseudo spectral acceleration (*PSA*).

3.2 GROUND RESPONSE ANALYSIS PROCEDURES

3.2.1 Ground Response Analysis Methods

There are many options for performing 1D GRA. Different procedures for GRA can be used depending on the level of nonlinearity that is expected in the profile. The principal alternatives for GRA are linear (more specifically, visco-elastic), Equivalent-Linear (EL), and Nonlinear (NL) methods. Linear methods require only a shear wave velocity profile, unit weights, and a soil damping profile. Additional soil properties required for EL are relationships for modulus reduction and damping vs. shear strain. The NL procedures require these same inputs, but will often incorporate shear strength and other parameters related to viscous damping and rules for unload-reload relationships.

As one example, Thompson et al. (2012) used the GRA program NRATTLE, which is a part of the ground motion simulation program SMSIM (Boore, 2005). Linear GRA is performed in NRATTLE using the Thomson–Haskell matrix (Thomson, 1950; Haskell, 1953). Kaklamanos et al. (2013) used NRATTLE for linear GRA and SHAKE (Schnabel et al. 1972) for EL GRA. Kaklamanos et al. (2015) used SHAKE for EL and DEEPSOIL (Hashash et al., 2016) for NL analysis to compare the effectiveness of different GRA methods for problems involving various levels of nonlinearity. Zalachoris and Rathje (2015) used STRATA (Kottke and Rathje, 2009) for EL and DEEPSOIL for NL analysis.

In this study, we model the soil as linearly visco-elastic because almost all of the recordings compiled in our database are not strong enough to cause soil nonlinearity, as discussed further below. Therefore, we only perform linear analysis similar to Thompson et al. (2012) in order to validate GRA under small levels of ground shaking. We have chosen to use the linear option in the Frequency Domain Analysis module in DEEPSOIL for linear analysis. We acknowledge there are several other GRA programs which are capable of performing linear GRA, including NRATTLE, SHAKE, and STRATA. We examined results from DEEPSOIL and STRATA, and found them to provide essentially identical results for a common set of input variables. We ultimately selected DEEPSOIL in consideration of its user-friendliness.

We applied parameter selection protocols for GRA as given by Stewart at al. (2014). An exception is small strain damping (D_{min}), the selection of which is discussed in Sections 3.2.2-3.2.3.

Methods of analysis for EL and NL are familiar to geotechnical engineers and are well documented elsewhere (e.g., NCHRP, 2012; Stewart et al. 2014). Hence, we do not describe such methods here. We next describe quarter-wavelength theory, because this approach is less familiar to engineers (although it is well documented, Joyner et al. 1981, Boore, 2013). While this method of GRA is not directly used for comparison to data in this study, the approach is nonetheless important for the present discussion because it provides the context in which site diminutive parameter κ_0 is used.

Quarter wave length theory is based on a simple equation for evaluating amplification of Fourier Amplitude Spectra for a vertical ray path:

$$A_0(f) = \left(\frac{\rho_R V_R}{\overline{\rho}\,\overline{V}} \right)^{0.5} \tag{3.1}$$

where A_0 is the amplification, ρ_R and V_R are density and shear wave velocity at the reference (downhole condition), and $\overline{\rho}$ and $\overline{V}$ are average density and shear wave velocity for a depth interval corresponding to the top quarter wavelength of the profile. While this method is simple and efficient, it cannot capture the effects of resonance and nonlinearity. Moreover, in the form represented by Eq. (3.1), it does not include the effects of damping, which is evident by the amplification value at high frequencies approaching a plateau. This plateau feature is unrealistic because actual amplification functions slope downward with frequency at high frequencies beyond the primary modal peaks in the spectrum. Although the shape shown in Figure 3.1 is strictly applicable to site amplification, similar features are observed in simulated Fourier amplitude spectra using stochastic methods (e.g., Boore, 2003).

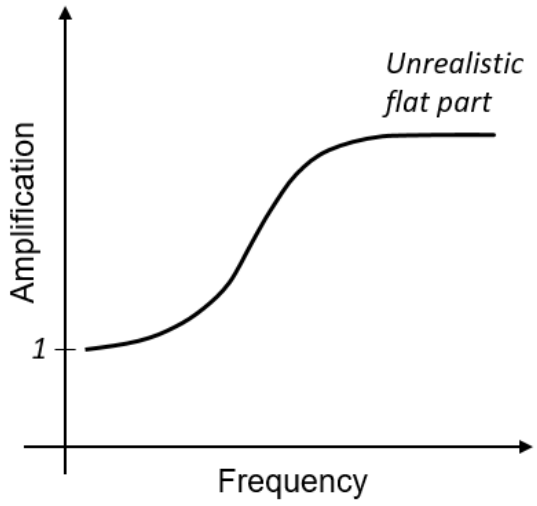

Figure 3.1. Unrealistic plateau of amplification at high frequencies when using quarter wave length theory without application of diminutive parameter κ.

In order to overcome the problem of unrealistic Fourier amplitude spectral shapes at high frequencies, a spectral decay, or diminutive, parameter (κ) is introduced.

$$X(f) = X_0(f) \times \exp(-\pi \kappa f) \tag{3.2}$$

where X indicates Fourier amplitude. The effect on spectral shape of applying this parameter is shown in Figure 3.2. The value of κ applicable to a particular ground motion recording can be

partitioned into two components, namely a zero distance κ or site κ (κ_0), and the attenuation with distance ($\kappa_R R$) (adapted from Anderson, 1991):

$$\kappa = \kappa_0 + \kappa_R R \tag{3.3}$$

where R is the source-site distance, and κ_R is the rate with which the decay parameter (κ) increases with distance, capturing the effects of anelastic attenuation. As shown subsequently, the site component can be used to constrain small-strain damping in the soil profile.

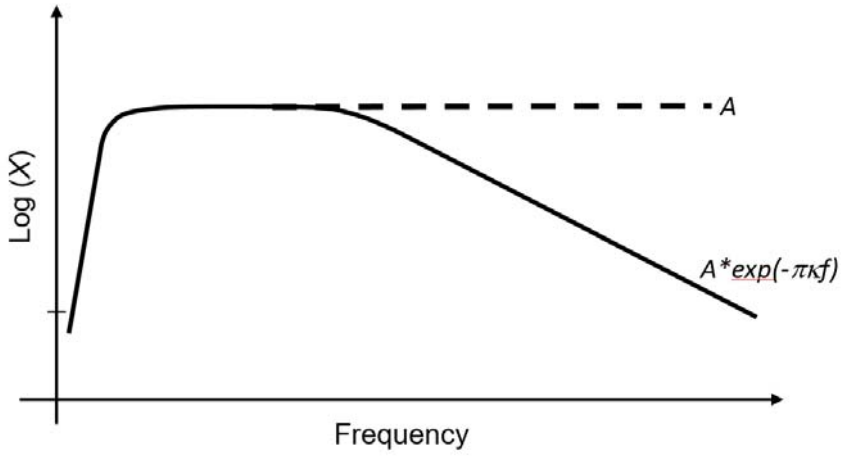

Figure 3.2. Modifying simulated ground motions at high frequencies by introducing κ.

3.2.2 Small Strain Damping from Models

Small-strain damping is required in GRA, including those employing linear soil properties. Even under elastic conditions, damping occurs because of the intrinsic damping within soil elements and scattering of waves off of subsurface irregularities (e.g., Rodriguez-Castellanos et al. 2006).

We consider two classes of models for small strain damping in soils, both of which are frequency-independent (hysteretic). The first class of models are collectively referred to as geotechnical models, because they are derived from advanced cyclic testing performed in geotechnical labs. These models account for intrinsic damping. The second are V_S-based models originally developed from calibration of stochastic ground motion simulations in central and eastern North America. To the extent that the calibration is accurate for a given application, these models incorporate the effects of both intrinsic material damping and scattering.

The geotechnical models relate small-strain damping as measured from geotechnical laboratory cyclic testing, denoted D_{min}^{L}, to various predictor variables related to soil type and confining pressure. We estimate laboratory-based D_{min}^{L} using Darendeli (2001) relations for clays and silts, and Menq (2003) relations for granular soils. The input parameters for the D_{min}^{L} models are plasticity index (*PI*), overconsolidation ratio (*OCR*), and effective stress for Darendeli (2001), and mean grain size (D_{50}), coefficient of uniformity (C_u), and effective stress for Menq (2003). The D_{min}^{L} relations can only be used when geotechnical log and/or description of soil conditions are available for the site.

The second class of models draw from the seismology literature. Seismological simulations often convolve ground motions derived from source and path models, which apply for a reference rock site condition, with a site amplification function derived from an assumed (or measured) soil column V_S profile. The site amplification function is typically derived using quarter wavelength procedures (Sec. 3.2.1) that evaluate impedance effects from the V_S profile (Eq. 3.1). The contribution of site damping to high frequency attenuation is captured by the κ_0 diminutive parameter (Eq. 3.3). The κ_0 parameter represents the cumulative effect of damping through the soil column, which is commonly represented by (Hough and Anderson 1988; Chapman et al. 2003; Campbell 2009):

$$\kappa_0 = \int_0^z \frac{dz}{Q_{ef}(z) V_S(z)} \tag{3.4}$$

where z is the soil column depth and Q_{ef} is the depth-dependent effective material quality factor, representing both the effects of frequency-dependent wave scattering and frequency-independent soil damping. Quantity Q_{ef} can be readily converted to an effective soil damping as follows (Campbell, 2009):

$$D_{eff}(\%) = \frac{100}{2Q_{\text{ef}}} \tag{3.5}$$

In order to facilitate ground motion prediction in central and eastern U.S., several investigators have developed models for either depth-dependent Q_{ef} or κ_0 in particular regions

(e.g., Boore and Joyner 1991, Gomberg et al. 2003, Cramer et al. 2004). Campbell (2009) reviewed many of these studies and proposed a suite of models relating Q_{ef} to V_S, one of which is given by

$$Q_{ef} = 7.17 + 0.0276V_S \tag{3.6}$$

Eq. (3.6) is one of four models proposed by Campbell (2009) and has seen application in a number of subsequent studies (Hashash et al., 2014; E. Rathje, personal communication) (more so than the other three models). We choose to use this model over an older model by Olsen et al. (2003) which is intended for long periods (>2 sec). An advantage of this approach for modeling D_{eff} is that it is only based on V_S as an input parameter, and therefore it does not require a geotechnical log. We apply this approach for all 21 sites used in this study.

3.2.3 Kappa-Informed Small Strain Damping

The use of site diminutive parameter κ in ground response prediction was introduced in Section 3.2.1. In this section we describe how the site component of κ (i.e, κ_0) can be used for sites with ground motion recordings to adjust values of small-strain damping derived from models like those in Section 3.2.2 to represent site-specific effects. Whether such adjustments are effective for ground motion prediction is investigated in Section 5.3.

The expression for κ_0 given in Eq. (3.4) strictly applies when the full crustal profile is considered in the depth integral. A more practical alternative is to evaluate the site diminutive parameter for reference rock, $\kappa_{0,ref}$, and then modify it for damping through the soil column as (Campbell, 2009):

$$\kappa_0 = \kappa_{0,ref} + \int_0^z \frac{dz}{Q_{ef}(z)V_S} \tag{3.3}$$

The integral in this case represents the contribution from the geologic column above the reference rock. Note that $\kappa_{0,ref}$ as used in simulations may not match the site condition at the downhole sensor. However, for the present application, we take $\kappa_{0,ref}$ as applying for the downhole geologic condition. Adopting this definition and using Eq. (3.5) to convert Q_{ef} to D_{min}, we re-write Eq. (3.7) as:

$$\kappa_0 = \kappa_{0,ref} + \int_0^z \frac{2D_{eff}(z)}{100} V_S^{-1}(z)dz \tag{3.4}$$

The following sub-sections describe how vertical array data can be used to estimate the integral in Eq. (3.8), which in turn can be used to adjust model-based D_{min} to reflect site-specific conditions.

3.2.3.1 Inference of profile contribution to κ_0 from vertical array data

Using recordings from vertical arrays, κ_0 and $\kappa_{0,ref}$ cannot be measured directly because the source-site distance component ($\kappa_R R$) still exists in κ measured from the surface and downhole recordings. However, if we take the distance component ($\kappa_R R$) as identical for the surface and downhole κ as observed for a given event, the difference ($\Delta\kappa$) in total κ becomes a profile attribute:

$$\Delta\kappa = \kappa - \kappa_{ref} = \left(\kappa_0 + \kappa_R R\right) - \left(\kappa_{0,ref} + \kappa_R R\right) = \kappa_0 - \kappa_{0,ref} \tag{3.5}$$

where κ_{ref} is the total κ for the downhole recording. Combining Eqs (3.8) and (3.9), we can relate $\Delta\kappa$ to D_{eff} as:

$$\Delta\kappa = \int_0^z \frac{2D_{eff}(z)}{100} V_S^{-1}(z)dz \tag{3.6}$$

The conceptually simplest way to estimate $\Delta\kappa$ from vertical array recordings is to evaluate κ_{ref} and κ from the recorded Fourier amplitude spectra (FAS) of downhole and surface recordings, and take the difference (per Eq. 3.9). It is recognized that the downhole recording is a 'within' record that contains attributes of reflected waves from the ground surface, and hence is different from the outcropping condition at the surface. However, the differences between outcropping and within motions are localized at site frequencies, and hence are unlikely to significantly affect the downhole κ_{ref} measurement.

We measure κ using procedures introduced by Anderson and Hough (1984), in which a line is fit to the decaying part of the FAS in semi-log space, as shown for example recordings in Figure 3.3. As shown in the figure, it is necessary to pick a frequency range over which the line is fit. The lower and upper limit of the fit frequency range are denoted f_e and f_x, respectively. We adopt the criteria below for choosing the frequency range (similar to Cabas and Rodriguez-Marek, 2017 and Xu et al. 201x). It is acknowledged that there are other approaches for measuring κ in the literature (Ktenidou et al., 2014).

- Avoid the 1st site response peak in the transfer function.

- Avoid the flat part of the high frequency ETF which is not expected to be dominated by shear waves.

- Avoid frequencies outside of the usable frequency rage chosen for filtering in the processing stage.

In order to select f_e and f_x values producing the most stable κ, we initially select a reasonable range for both f_e and f_x based on the above criteria, and then use a search module to pick the combination of f_e and f_x producing the least variability with azimuth for Δκ (Eq. 3.9). Note that one set of f_e and f_x is chosen for all four components of a recording (two horizontal components each for surface and downhole). In order to compute variability with azimuth, the search module uses the two horizontal components of Δκ for a range of orientations, and then computes the coefficient of variation (COV) across Δκ values from all orientations. The COV is computed for every combination of f_e and f_x inside the introduced range, and the combination that generates the smallest COV for Δκ is selected and then applied to all four components. The summary of findings on measuring Δκ from surface and downhole recordings in our dataset as the difference between κ and κ_{ref} is shown in Table 3.1. In the table, the average and limits of f_e and f_x chosen for κ measurements are summarized for each site.

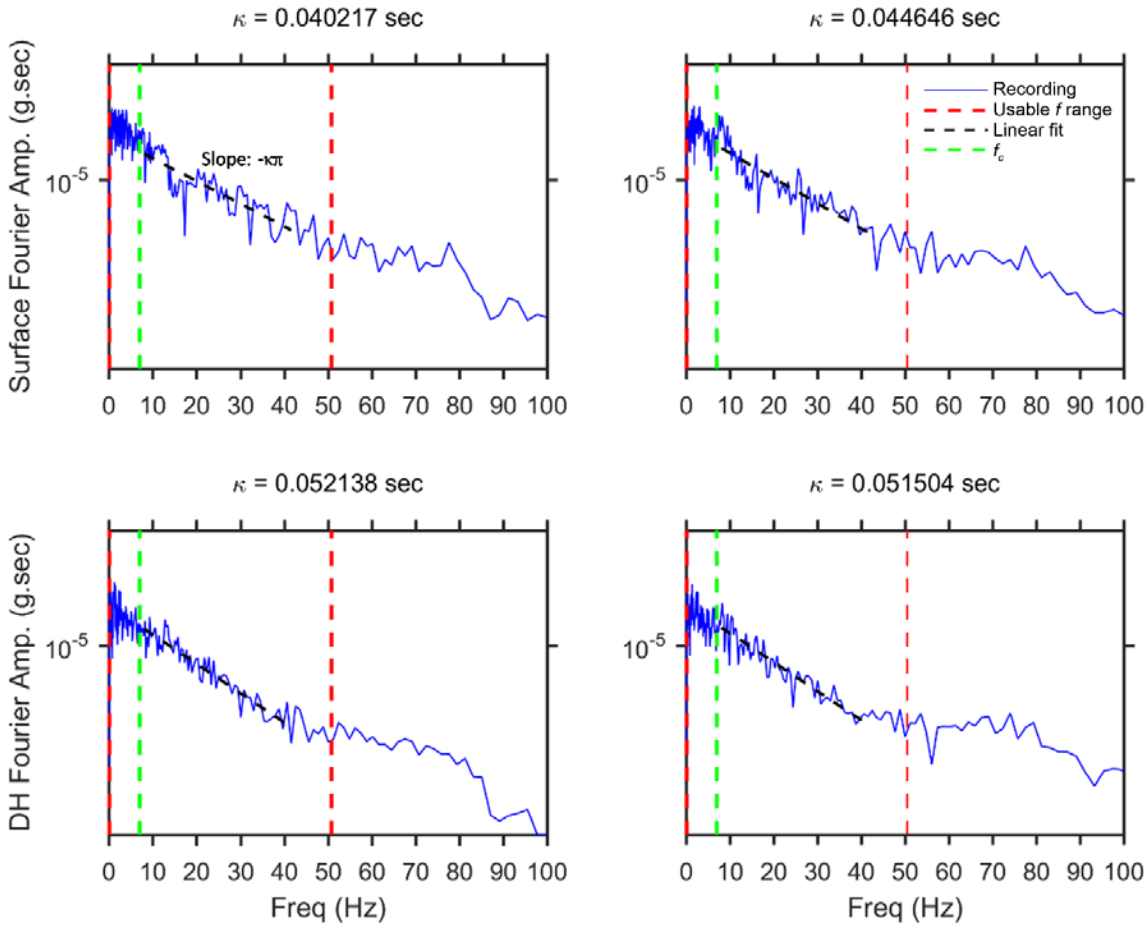

Figure 3.3. The customary approach of measuring $\Delta\kappa$ by directly fitting a line to the two components of surface (top) and downhole (bottom) FAS, where f_c is the corner frequency of the event.

When the above approach of separately evaluating κ for surface and downhole records was applied, the results were found to be somewhat 'noisy' due to sensitivities to limiting frequencies, and the differences between surface and downhole κ were often small. As a result of these issues, Δκ values were negative for a substantial number of cases (35% of recordings) as shown in Table 3.1, which is a spurious result. Accordingly, we considered a different approach in which Δκ is evaluated directly from surface/downhole transfer functions. Because the line is fit in semi-logarithmic space, the slope of the transfer function is the difference between the slopes of respective FAS. An advantage of this approach is that the transfer function lacks peaks and valleys from effects other than surface-downhole site response, which allows the line to be fit over lower frequency ranges than is possible for κ measurements (Figure 3.3.). An example of Δκ inference from a transfer function is shown in Figure 3.4.

We measure Δκ by directly fitting a line to the ETF over a frequency range that is expected to be dominated by shear waves. The protocols for selecting that frequency range are similar to those described above (for FAS). However, in addition to those criteria, we find the surface/downhole ratio of FFT for background noise useful in order to identify the frequency ranges less influenced by noise. For this purpose, we compute the ETF for the first 5 seconds of the raw recordings, which occurs within a pre-event time window (before seismic shaking). For the example in Figure 3.4, for frequencies above approximately 22 Hz, the ETF of noise becomes similar to that for the full signals, which could explain the rise in transfer function ordinates as that frequency is approached (i.e., the increase begins at about 16 Hz). Processes of this sort guide the selection of f_x for the fitting of Δκ to the ETF.

Summary results obtained by measuring Δκ in this manner are shown in Table 3.2. Summary statistics of directly measuring Δκ for the vertical array sites from transfer functions. In this case, only two sites (less than 10%) produced negative Δκ. Comparing the limiting frequencies in Tables 4.1 and 4.2, the ETF-fitting approach produces lower values of f_e and f_x.

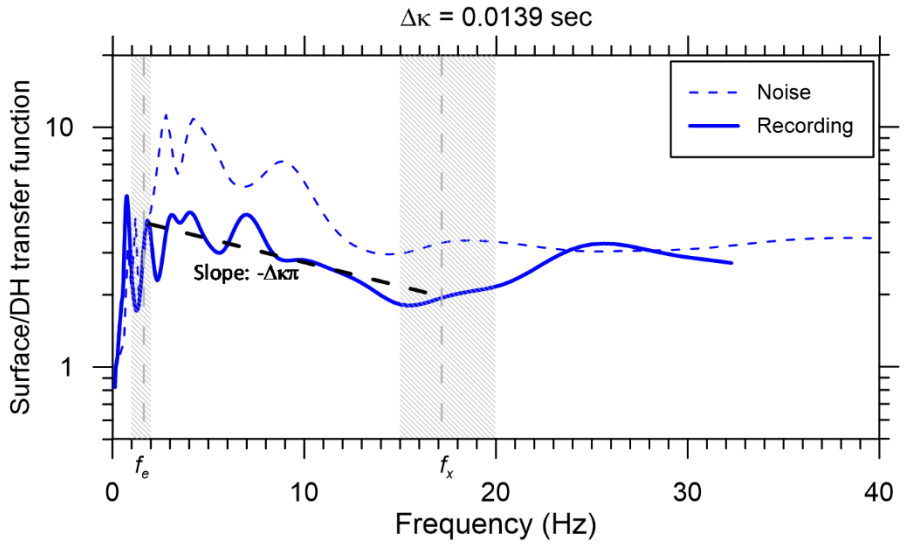

Figure 3.4. Approach for measuring Δκ by directly fitting a line to ETF for each recording. The shaded areas show the frequency ranges used for choosing f_e and f_x.

Table 3.1. Summary statistics of measuring Δκ for the vertical array sites as the difference between κ and κ_{ref}.

Site	Station NO (CSMIP)	No. of Rec	$\overline{f_e}$ (Hz)	$\overline{f_x}$ (Hz)	f_e range (Hz) min, max	f_x range (Hz) min, max	$\overline{\kappa}$ (sec)	κ range (sec) min, max	$\overline{\kappa_{ref}}$ (sec)	κ_{ref} range (sec) min, max	$\overline{\Delta\kappa}$ (sec)	Δκ range (sec) min, max
Antioch-San Joaquin S	67266	4	3.1	13.0	2.0, 5.0	10, 17	0.121	0.105, 0.133	0.109	0.092, 0.133	0.0119	-0.0005, 0.0213
Bay Bridge	58961	9	7.9	21.4	5.5, 10	15.3, 27.2	0.069	0.038, 0.113	0.051	0.03, 0.074	0.0184	0.0034, 0.0387
Benicia South	68323	10	8.6	28.8	6.1, 10	21.9, 44.7	0.049	0.026, 0.085	0.050	0.023, 0.104	-0.0006	-0.0183, 0.0162
Borrego Valley	NA	16	8.1	33.4	4.0, 20.9	20.0, 50.5	0.042	0.016, 0.069	0.048	0.028, 0.0616	-0.0057	-0.0147, 0.0084
Corona	13186	31	10.4	55.2	4.0, 23.7	10.0, 79.5	0.024	0.009, 0.084	0.028	0.009, 0.0987	-0.0035	-0.0354, 0.0181
Coronado East	3192	10	8.0	29.6	2.9, 16.6	23.9, 51.3	0.040	0.019, 0.055	0.048	0.025, 0.073	-0.0080	-0.0321, 0.0236
Coronado West	3193	21	6.4	23.5	3.3, 14.5	10.8, 45	0.063	0.025, 0.096	0.057	0.014, 0.094	0.0060	-0.0214, 0.0459
Crockett-1	68206	8	10.6	31.7	5.3, 14.7	21.1, 46.8	0.041	0.027, 0.052	0.056	0.024, 0.072	-0.0150	-0.0276, 0.0227
El Centro-Meloland	1794	19	10.0	31.6	5.5, 14.8	17.3, 51.3	0.049	0.013, 0.074	0.049	0.035, 0.073	0.0004	-0.0253, 0.0185
Eureka	89734	14	7.3	24.3	2.0, 9.5	15.0, 30.0	0.073	0.046, 0.093	0.045	0.026, 0.057	0.0285	0.0018, 0.0502

Site	Station NO (CSMIP)	No. of Rec	$\overline{f_e}$ (Hz)	$\overline{f_x}$ (Hz)	f_e range (Hz) min, max	f_x range (Hz) min, max	$\overline{\kappa}$ (sec)	κ range (sec) min, max	$\overline{\kappa_{ref}}$ (sec)	κ_{ref} range (sec) min, max	$\overline{\Delta\kappa}$ (sec)	$\Delta\kappa$ range (sec) min, max
Foster City	58968	7	7.2	25.7	3.0, 12.0	13.2, 42.6	0.034	0.008, 0.069	0.052	0.003, 0.114	-0.0173	-0.0445, 0.0043
Garner Valley	NA	10	12.6	53.4	7.1, 19.5	42.6, 70.0	0.028	0.018, 0.046	0.011	0.001, 0.030	0.0178	0.0146, 0.0223
Hayward-580W	58487	5	11.9	44.4	5.8, 26.8	25.0, 63.2	0.042	0.015, 0.084	0.038	0.018, 0.065	0.0040	-0.0120, 0.0185
Hayward-San Mateo	58798	5	8.0	22.1	6.9, 9.7	18.0, 32.4	0.051	0.024, 0.079	0.043	0.002, 0.073	0.0080	-0.049, 0.072
Hollister digital	NA	23	10.9	28.3	5.7, 22.4	17.0, 47.9	0.060	0.013, 0.111	0.048	0.009, 0.0100	0.0122	-0.0576, 0.0554
La-Cienega	24703	20	13.0	43.6	5.0, 35.8	22.0, 80.0	0.040	0.007, 0.096	0.032	0.008, 0.084	0.0076	-0.0162, 0.0179
Obregon Park	24400	23	12.9	34.0	4.8, 19.5	16.2, 75.0	0.067	0.032, 0.118	0.046	0.019, 0.101	0.0214	0.0089, 0.0380
San Bernardino	23792	5	7.6	23.8	2.0, 11.8	12.0, 32.0	0.059	0.025, 0.130	0.060	0.031, 0.119	-0.0008	-0.0171, 0.0111
Treasure Island	58642	11	9.9	38.4	9.5, 10.0	20.0, 60.0	0.049	0.029, 0.072	0.033	0.021, 0.068	0.0157	0.0036, 0.0332
Vallejo	68310	17	12.1	31.2	5.5, 19.3	20.0, 45.0	0.053	0.035, 0.077	0.049	0.025, 0.059	0.0043	-0.0139, 0.0180
Wildlife Liquefaction	NA	21	7.4	38.1	5.0, 10.0	7.0, 63.2	0.043	0.000, 0.079	0.049	0.029, 0.066	-0.0051	-0.0665, 0.0244

Table 3.2. Summary statistics of directly measuring Δκ for the vertical array sites from transfer functions.

Site	Station NO (CSMIP)	No. of Rec	$\overline{f_e}$ (Hz)	$\overline{f_x}$ (Hz)	f_e range (Hz) min, max	f_x range (Hz) min, max	$\overline{\Delta\kappa}$ (sec)	Δκ range (sec) min, max
Antioch-San Joaquin S	67266	4	2.8	12.8	2.0, 3.0	8.0, 17.0	0.0116	-0.0014, 0.0197
Bay Bridge	58961	9	7.4	18.3	7.0, 8.0	17.0, 20.0	0.0085	-0.0023, 0.0174
Benicia South	68323	10	4.4	24.3	4.0, 5.0	17.0, 35.0	0.0044	0.0005, 0.0120
Borrego Valley	NA	16	1.5	16.3	1.0, 2.0	8.0, 20.0	0.0053	0.0003, 0.0159
Corona	13186	31	3.8	18.2	3.0, 5.0	15.0, 22.9	0.0078	-0.0223, 0.0264
Coronado East	3192	10	1.6	15.8	1.0, 2.5	10.0, 24.5	0.0133	0.0044, 0.0295
Coronado West	3193	21	2.0	14.9	1.0, 3.0	4.0, 21.9	0.0063	-0.0175, 0.0490
Crockett-1	68206	8	3.2	16.2	2.0, 5.0	6.0, 19.9	0.0016	-0.0094, 0.0154
El Centro-Meloland	1794	19	1.1	12.0	1.0, 2.0	5.0, 24.1	0.0013	-0.0053, 0.0119
Eureka	89734	14	1.4	18.1	1.0, 1.8	8.1, 19.9	0.0203	0.0115, 0.0276

Site	Station NO (CSMIP)	No. of Rec	$\overline{f_e}$ (Hz)	$\overline{f_x}$ (Hz)	f_e range (Hz) min, max	f_x range (Hz) min, max	$\overline{\Delta\kappa}$ (sec)	$\Delta\kappa$ range (sec) min, max
Foster City	58968	7	1.5	14.6	1.0, 2.0	6.9, 21.4	-0.0033	-0.0475, 0.0148
Garner Valley	NA	10	1.9	21.2	1.3, 3.0	12, 24.5	0.0136	-0.0185, 0.0239
Hayward-580W	58487	5	2.3	16.1	1.0, 3.0	11.8, 20.0	0.0234	0.0126, 0.0304
Hayward-San Mateo	58798	5	1.4	12.9	1.0, 2.0	4.0, 24.5	0.0330	0.0053, 0.0802
Hollister digital	NA	23	1.5	16.6	1.0, 3.0	15.0, 19.5	0.0236	0.0097, 00413
La-Cienega	24703	20	2.1	18.2	1.0, 3.0	5.0, 23.9	0.0042	-0.1216, 0.0354
Obregon Park	24400	23	2.1	23.4	1.0, 3.0	17.0, 24.5	0.0074	-0.0200, 0.0156
San Bernardino	23792	5	2.7	22.6	2.2, 3.0	20.0, 24.5	0.0000	-0.0162, 0.0168
Treasure Island	58642	11	2.6	17.8	1.0, 3.0	15.0, 20.0	0.0118	0.0040, 0.0182
Vallejo	68310	17	5.3	23.9	4.0, 6.0	15.0, 29.5	-0.0080	-0.0191, 0.0046
Wildlife Liquefaction	NA	21	1.7	16.5	1.5, 2.0	15.0, 18.7	0.0167	0.0068, 0.0309

3.2.3.2 Modifying damping profiles based on measured $\Delta\kappa$

The laboratory-based estimate of the soil damping profile (D_{min}^{L}) is multiplied by a constant value (F_D) at all layers to obtain D_{eff}. As a result, Eq. (3.10) is modified as:

$$\overline{\Delta\kappa} = \int_0^z \frac{2D_{min}^{L}(z)F_D}{100} V_S^{-1}(z)dz \tag{3.7}$$

where $\overline{\Delta\kappa}$ is the mean $\Delta\kappa$ for all recordings at the site and F_D is the multiplicative modification factor. For sites without a geotechnical log we are unable to produce a detailed D_{min}^{L} profile – in these cases we assume D_{min}^{L}= 1% for use with the above procedures. This application as well as the other two approaches for estimation of damping are shown for all sites in Figure 3.5-3.25. In the figures the damping profiles are shown even if they are available for that site. The multiplication of D_{min}^{L} by a constant factor is the simplest modification and perhaps is sub-optimal. Some studies have shown that the variation of κ with depth is weaker than suggested by Eq. (3.11) (Xu et al. 201x), so a weighting factor that scales with depth (decreasing as depth increases) may be advisable to consider in future work.

Table 3.3 summarizes for each site values of $\overline{\Delta\kappa}$ as measured from ETFs, $\Delta\kappa$ implied by the D_{min}^{L} profile without any modification (F_D=1), and F_D values computed using Eq. (3.11). The latter two are not shown for sites without a geotechnical log.

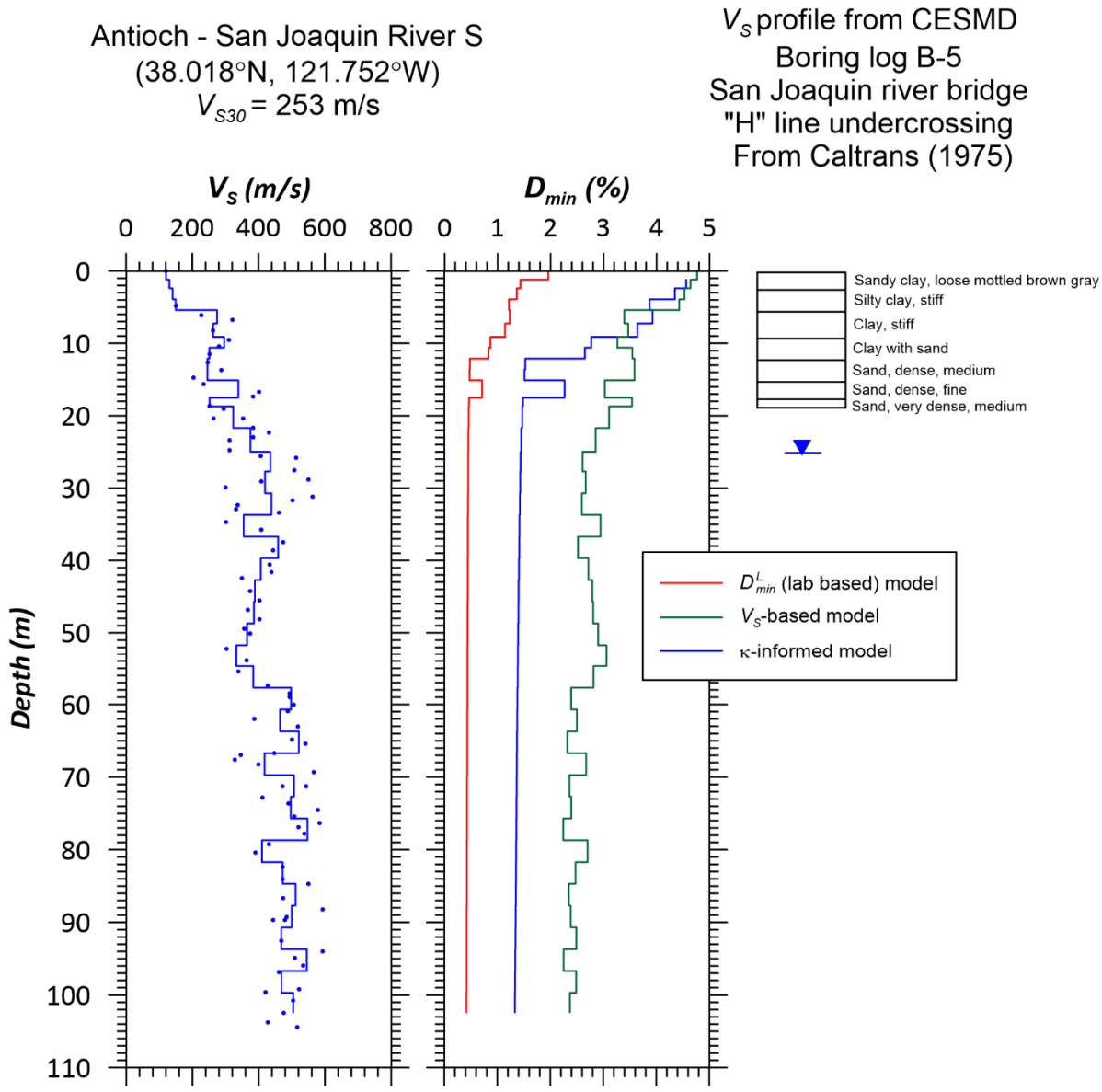

Figure 3.5. V_S profile and D_{min} profiles based on geotechnical models for laboratory damping (D^L_{min}), Campbell (2009) model for Q_{ef}, and Δκ for Antioch-San Joaquin site.

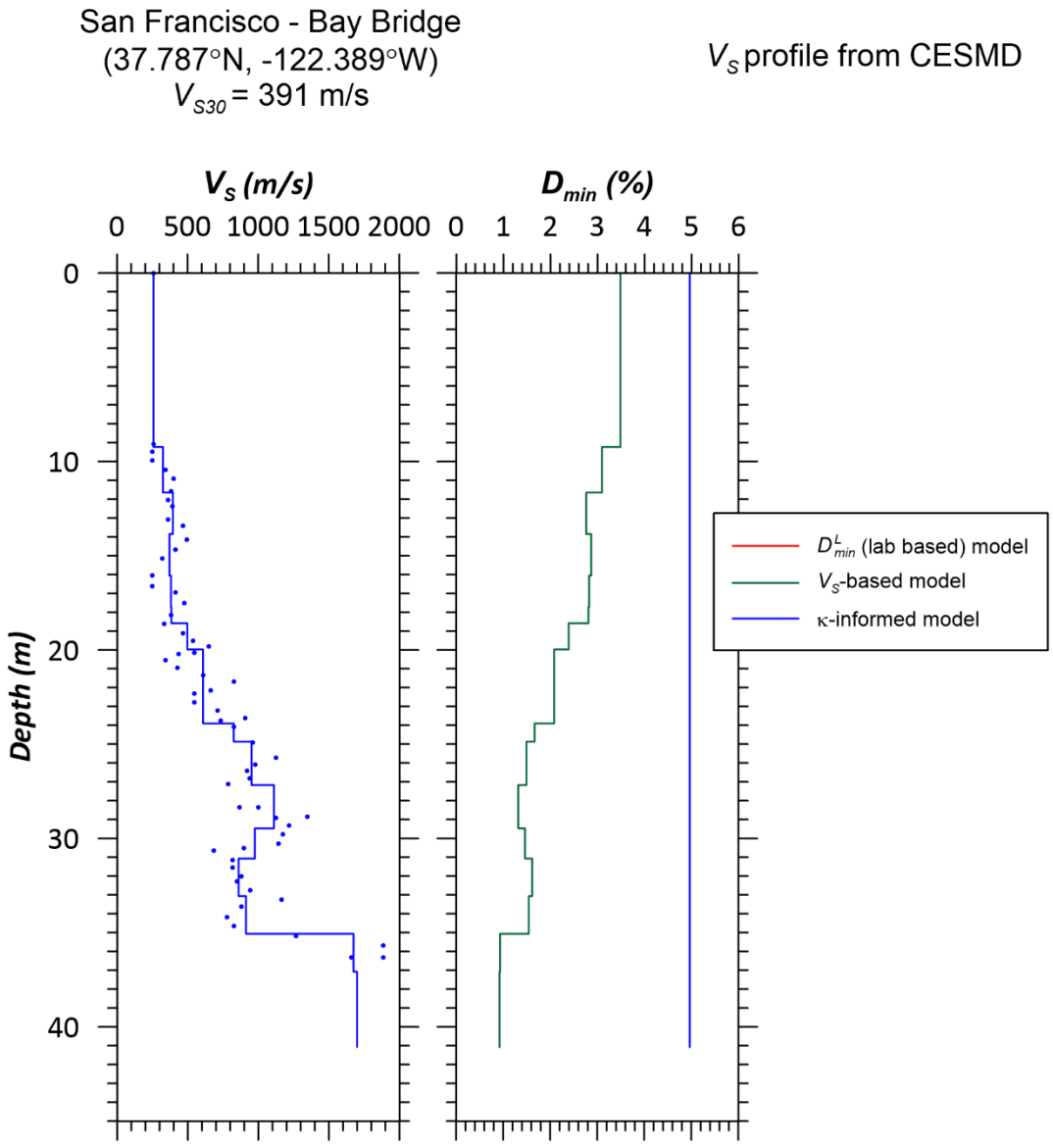

Figure 3.6. V_S profile and D_{min} profiles based on geotechnical models for laboratory damping (D^L_{min}), Campbell (2009) model for Q_{ef}, and $\Delta\kappa$ for San Francisco Bay Bridge site.

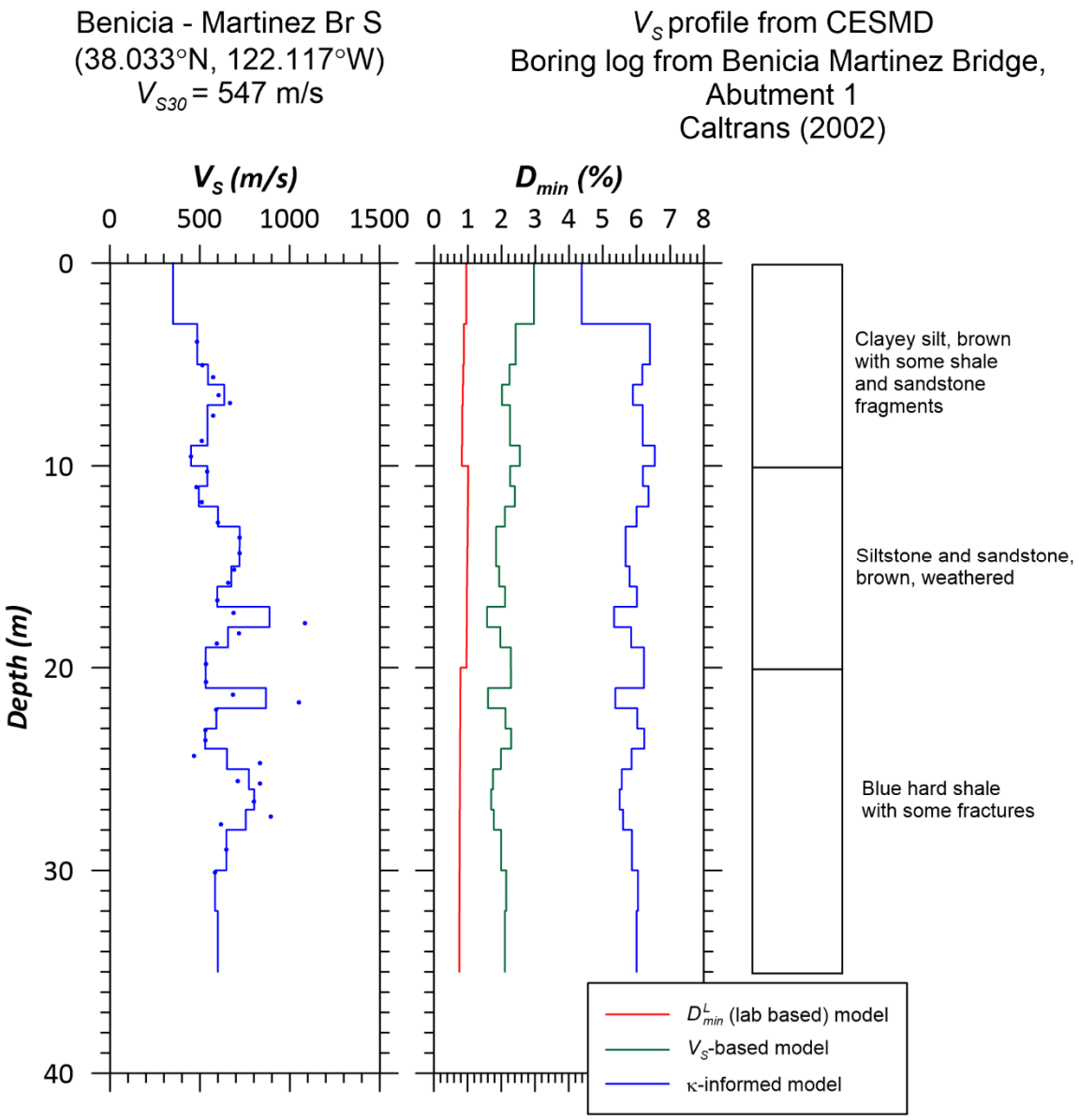

Figure 3.7. V_S profile and D_{min} profiles based on geotechnical models for laboratory damping (D^L_{min}), Campbell (2009) model for Q_{ef}, and $\Delta\kappa$ for Benicia-Martinez South site.

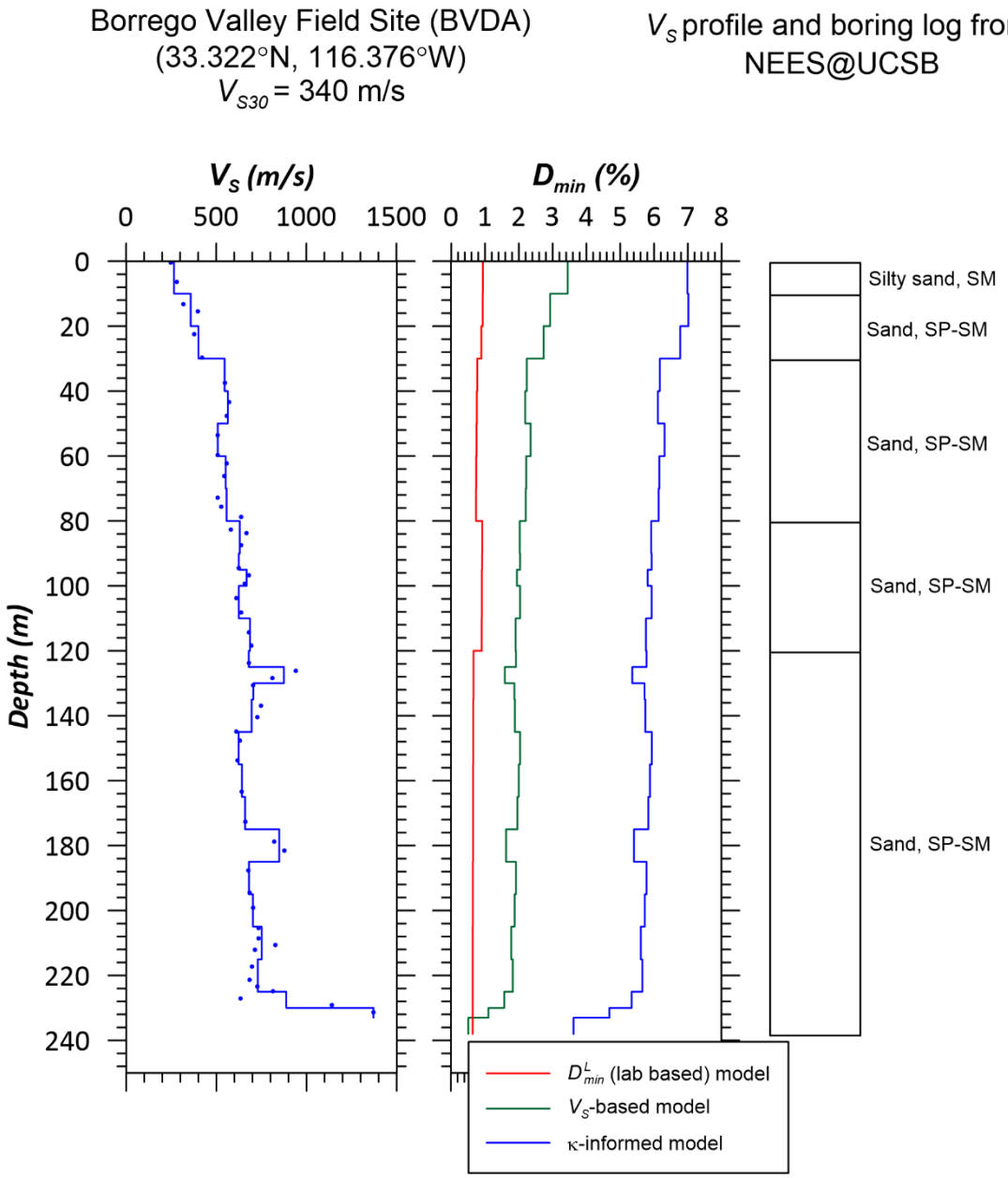

Figure 3.8. V_S profile and D_{min} profiles based on geotechnical models for laboratory damping (D^L_{min}), Campbell (2009) model for Q_{ef}, and $\Delta\kappa$ for Borrego Valley Downhole Array site.

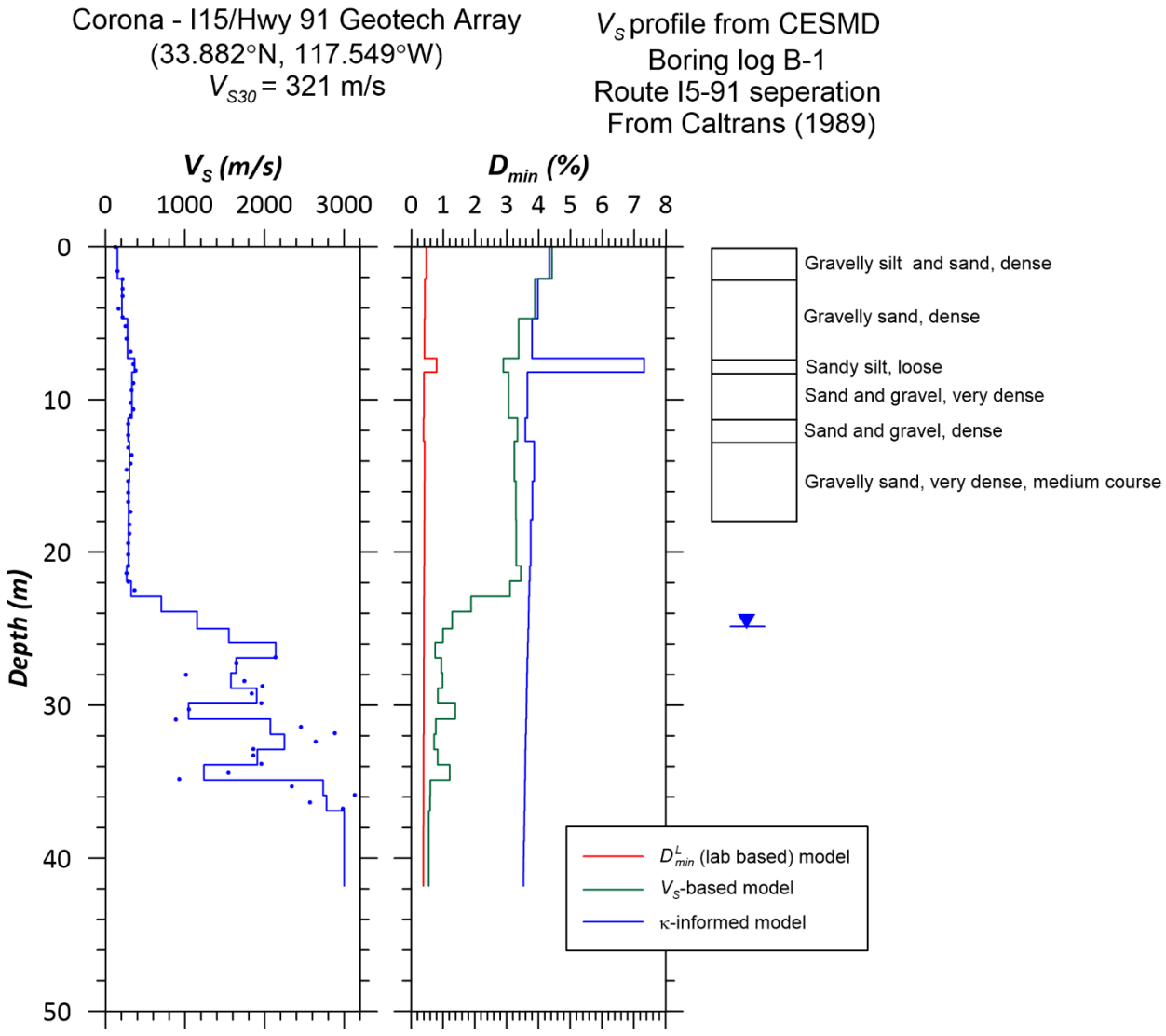

Figure 3.9. V_S profile and D_{min} profiles based on geotechnical models for laboratory damping (D^L_{min}), Campbell (2009) model for Q_{ef}, and Δκ for Corona vertical array site.

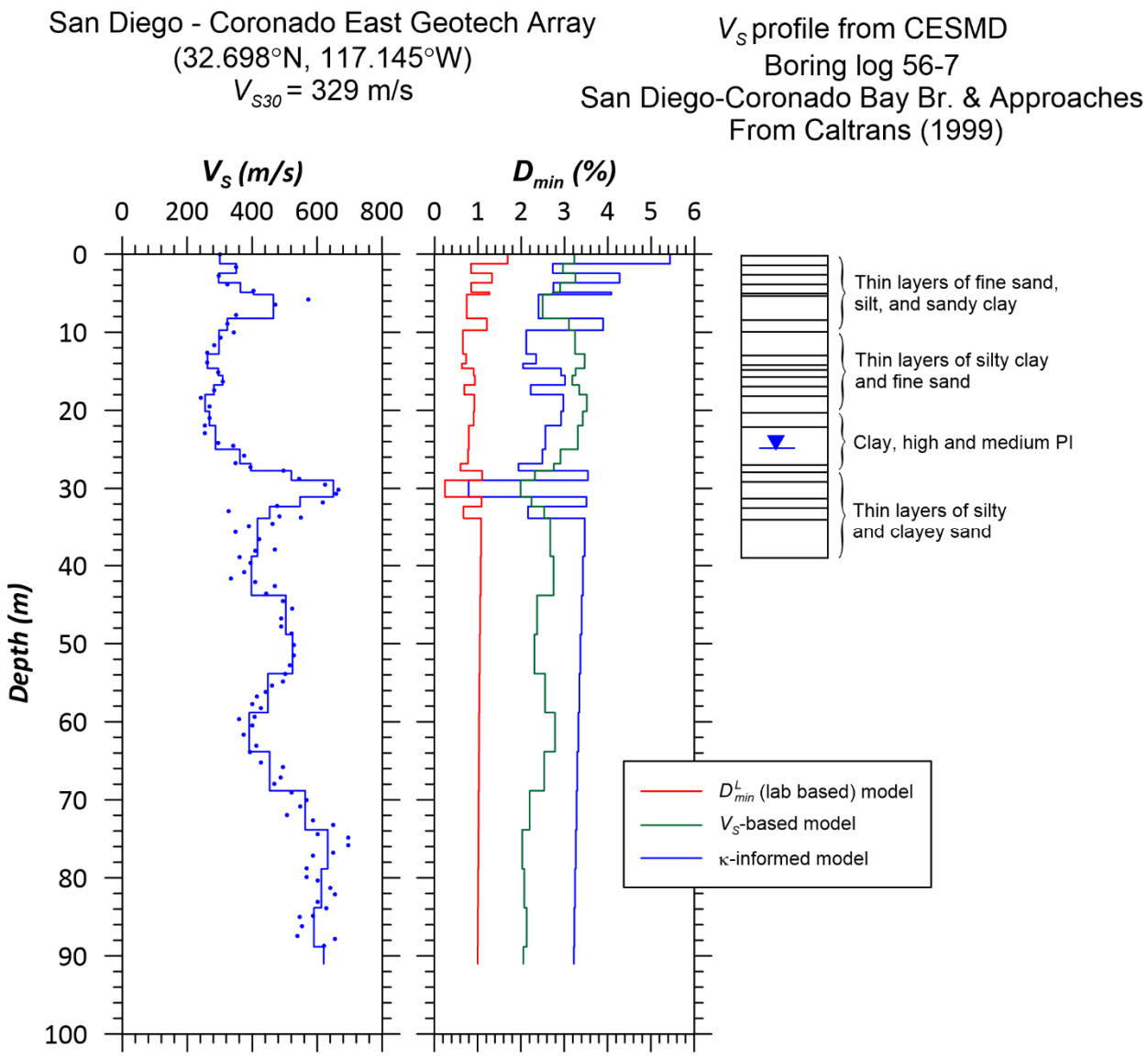

Figure 3.10. V_S profile and D_{min} profiles based on geotechnical models for laboratory damping (D^L_{min}), Campbell (2009) model for Q_{ef}, and $\Delta\kappa$ for Coronado East site.

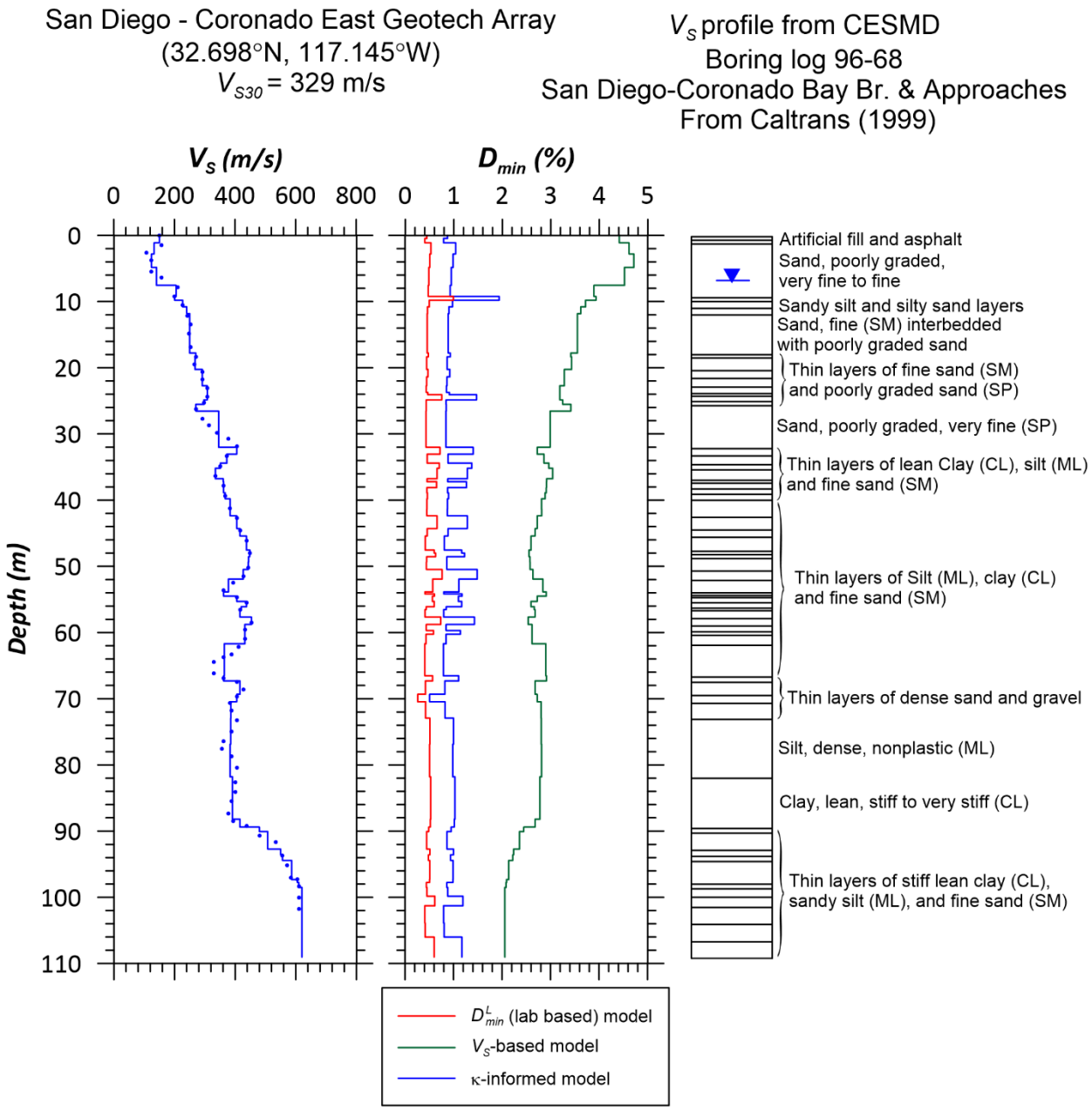

Figure 3.11. V_S profile and D_{min} profiles based on geotechnical models for laboratory damping (D^L_{min}), Campbell (2009) model for Q_{ef}, and $\Delta\kappa$ for Coronado West site.

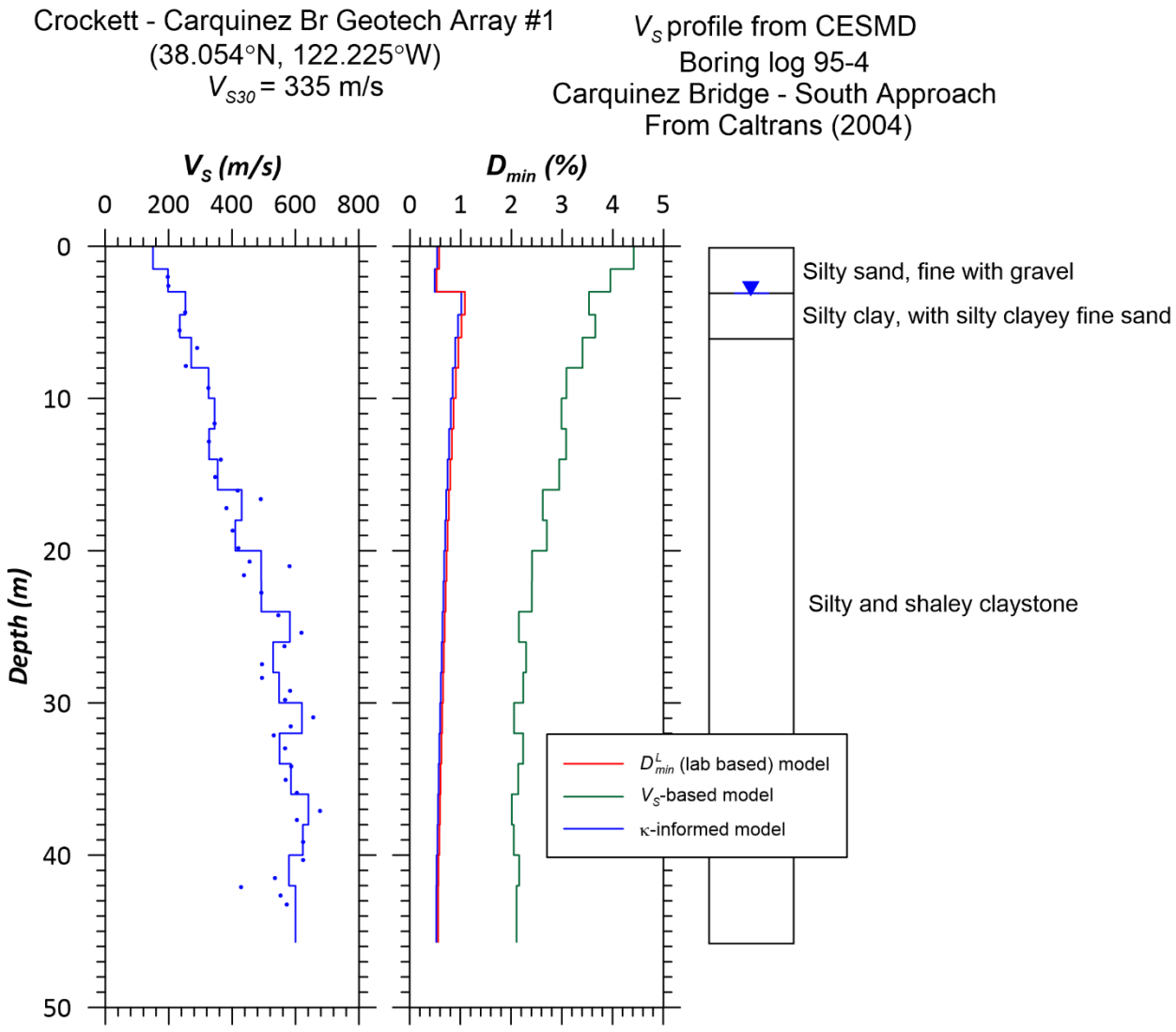

Figure 3.12. V_S profile and D_{min} profiles based on geotechnical models for laboratory damping (D^L_{min}), Campbell (2009) model for Q_{ef}, and Δκ for Crockett-Carquinez Br site.

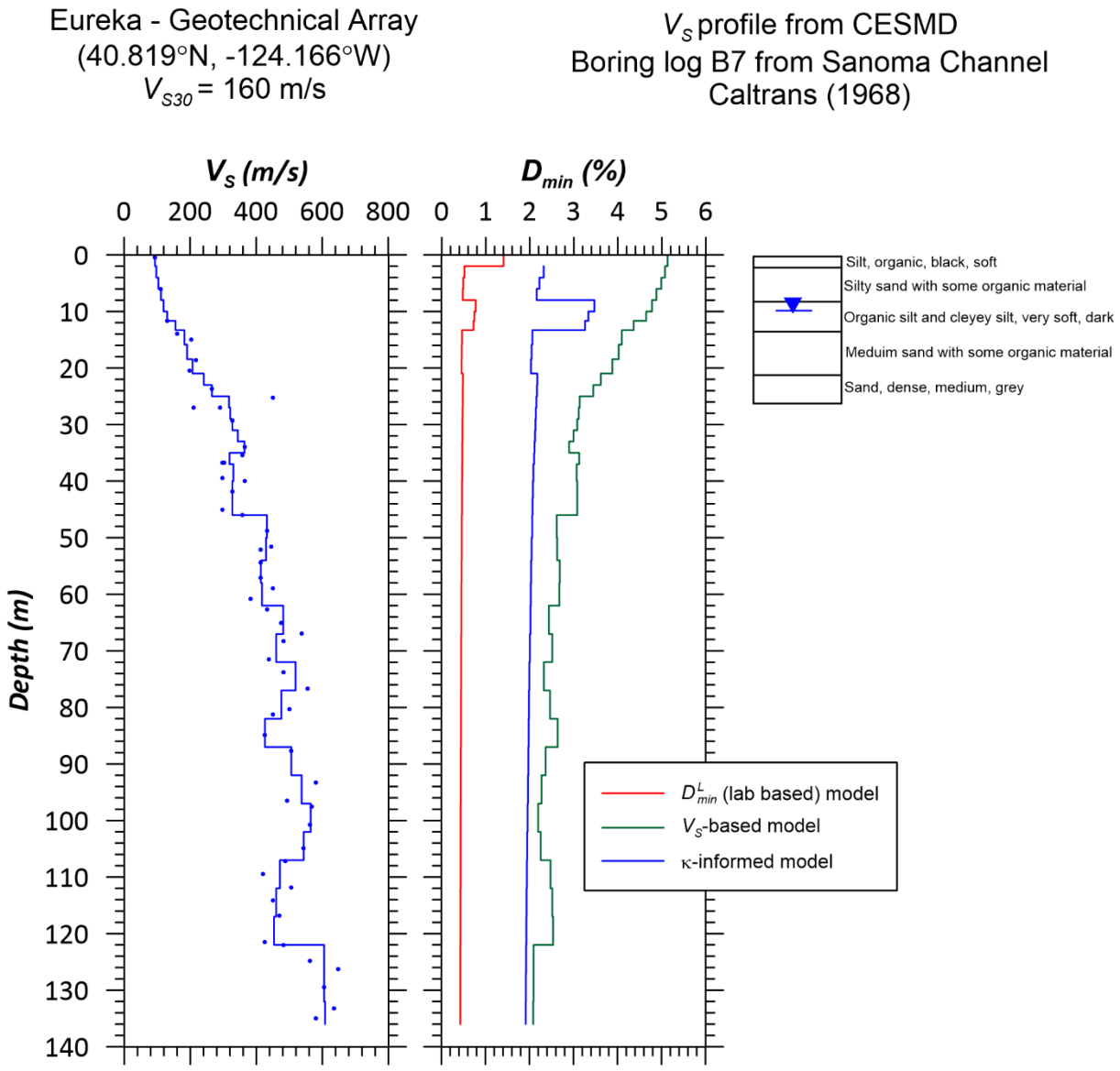

Figure 3.13. V_S profile and D_{min} profiles based on geotechnical models for laboratory damping (D^L_{min}), Campbell (2009) model for Q_{ef}, and $\Delta\kappa$ for Eureka site.

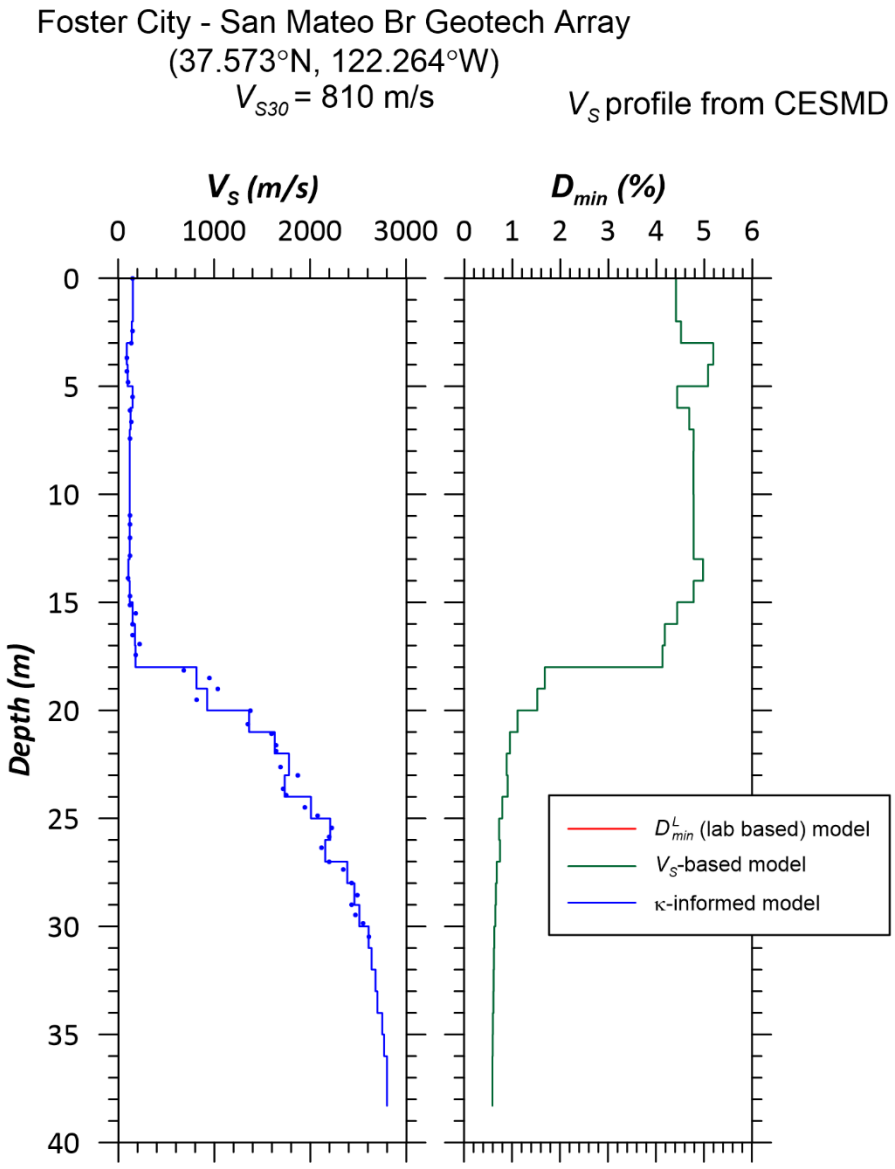

Figure 3.14. V_S profile and D_{min} profiles based on geotechnical models for laboratory damping (D^L_{min}), Campbell (2009) model for Q_{ef}, and $\Delta\kappa$ for Foster City-San Mateo site.

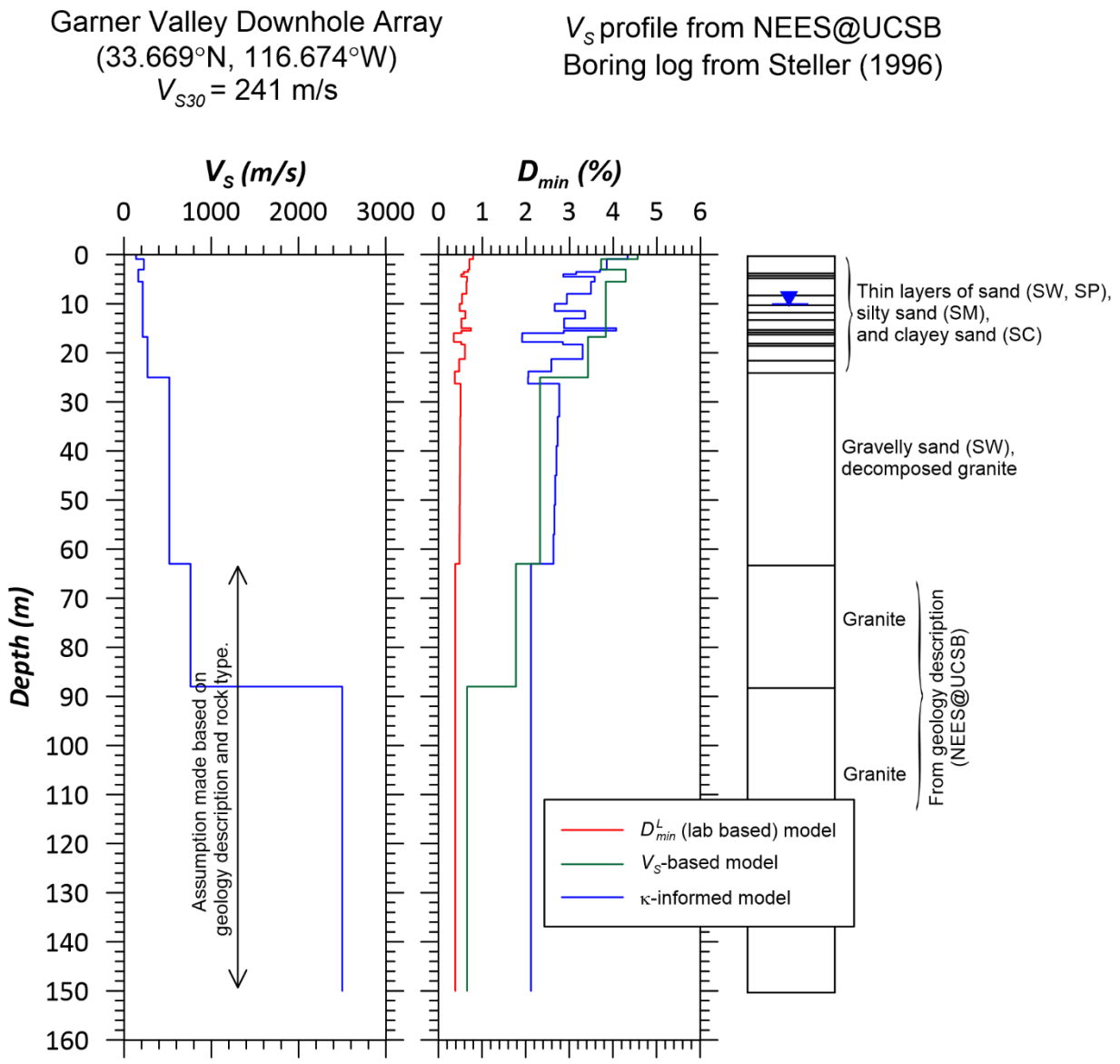

Figure 3.15. V_S profile and D_{min} profiles based on geotechnical models for laboratory damping (D^L_{min}), Campbell (2009) model for Q_{ef}, and $\Delta\kappa$ for Garner Valley site.

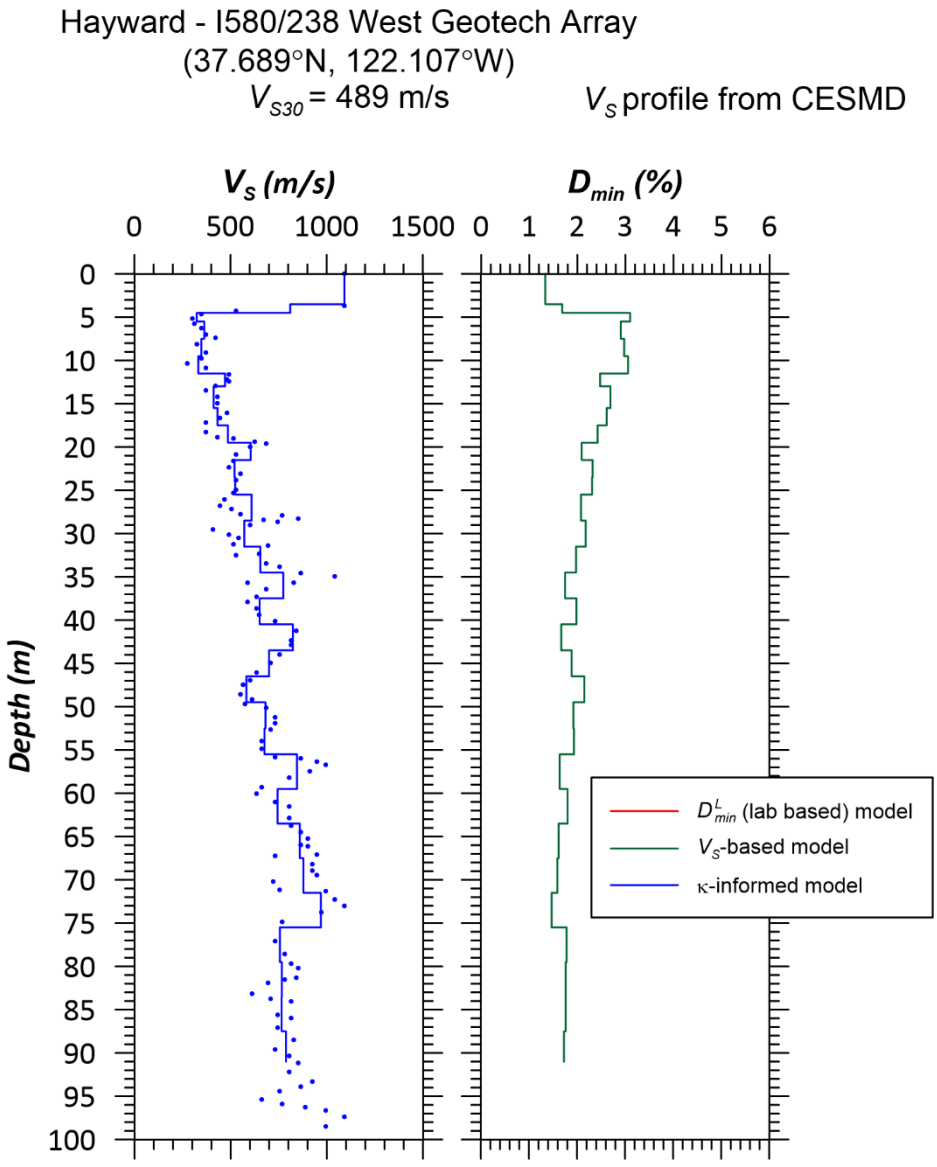

Figure 3.16. V_S profile and D_{min} profiles based on geotechnical models for laboratory damping (D^L_{min}), Campbell (2009) model for Q_{ef}, and Δκ for Hayward-I580/238 site.

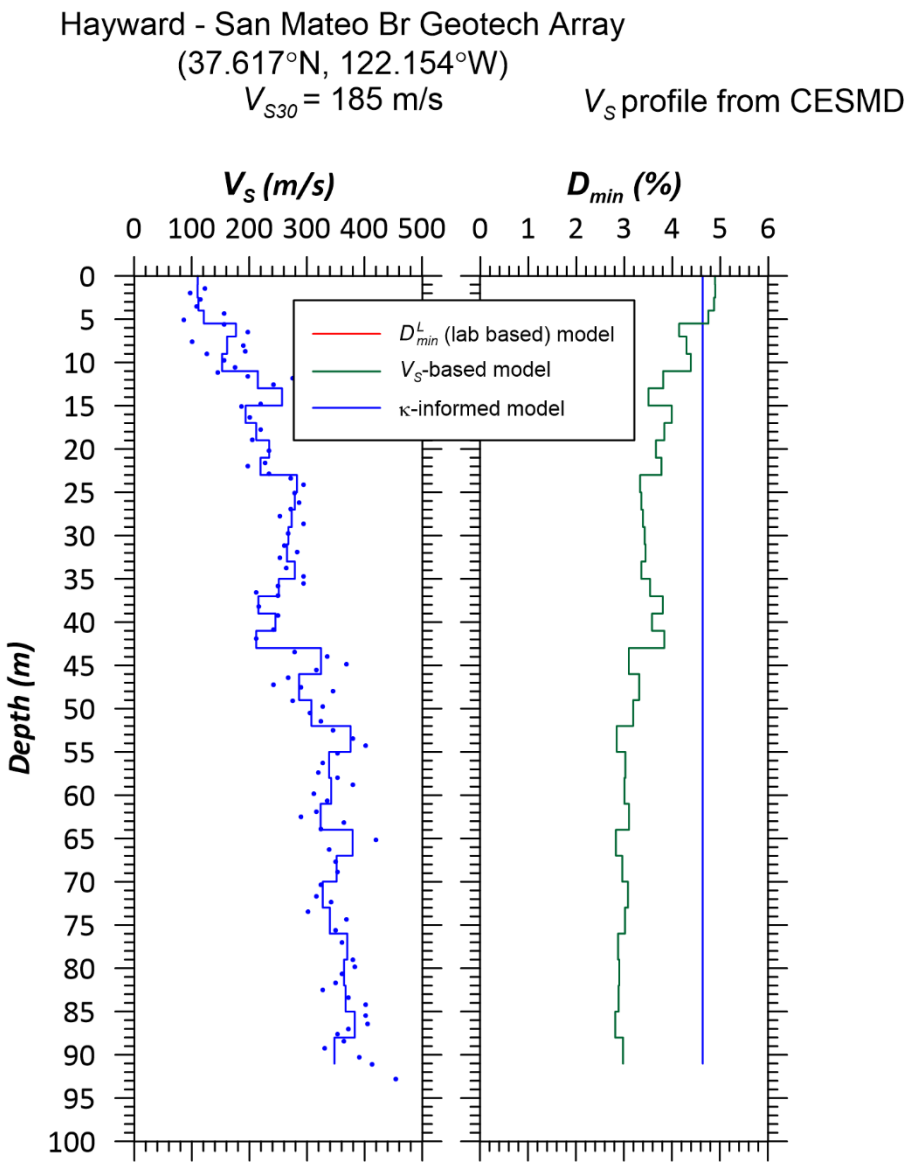

Figure 3.17. V_S profile and D_{min} profiles based on geotechnical models for laboratory damping (D^L_{min}), Campbell (2009) model for Q_{ef}, and Δκ for Hayward-San Mateo site.

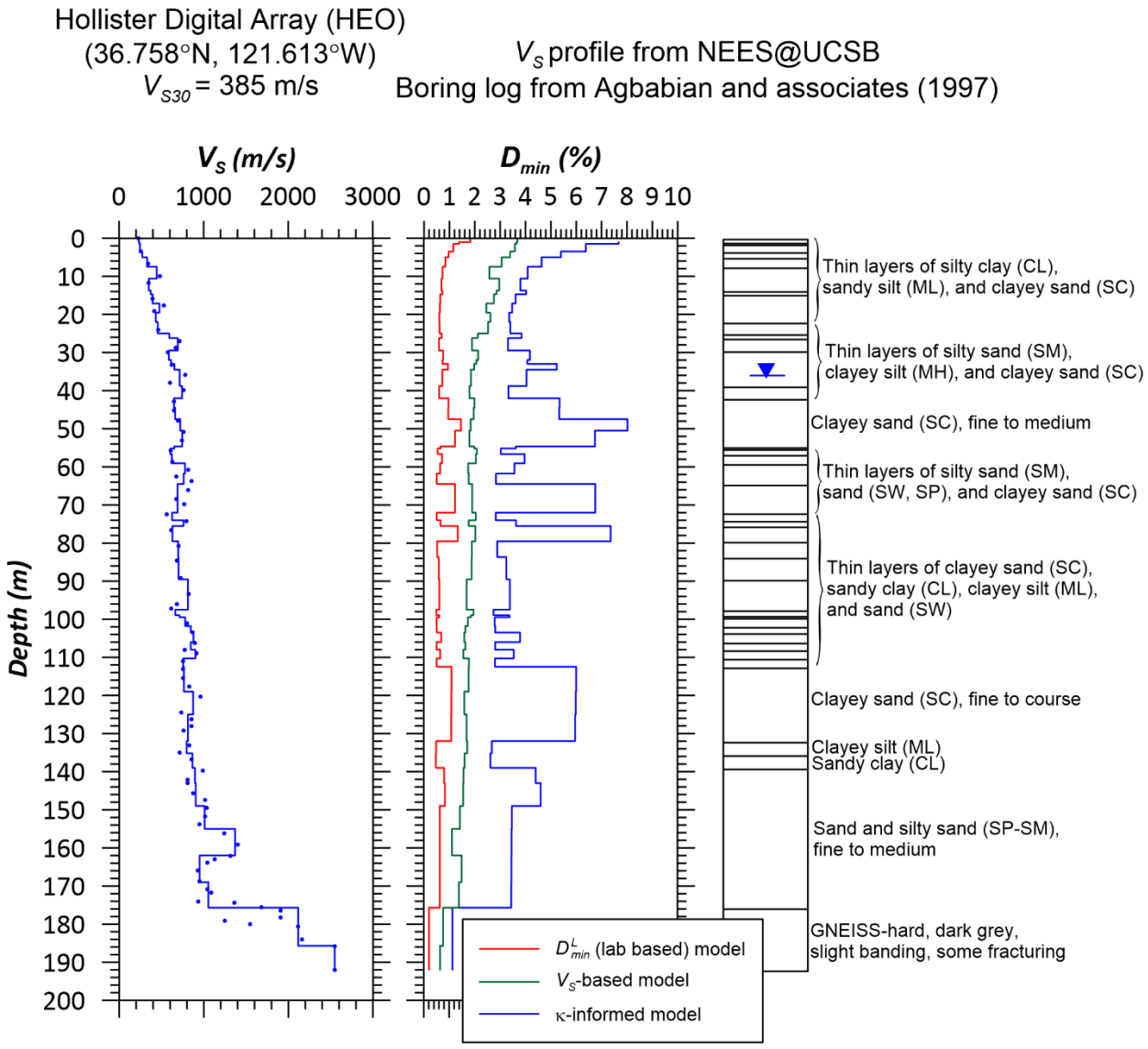

Figure 3.18. V_S profile and D_{min} profiles based on geotechnical models for laboratory damping (D^L_{min}), Campbell (2009) model for Q_{ef}, and $\Delta\kappa$ for Hollister Digital Array site.

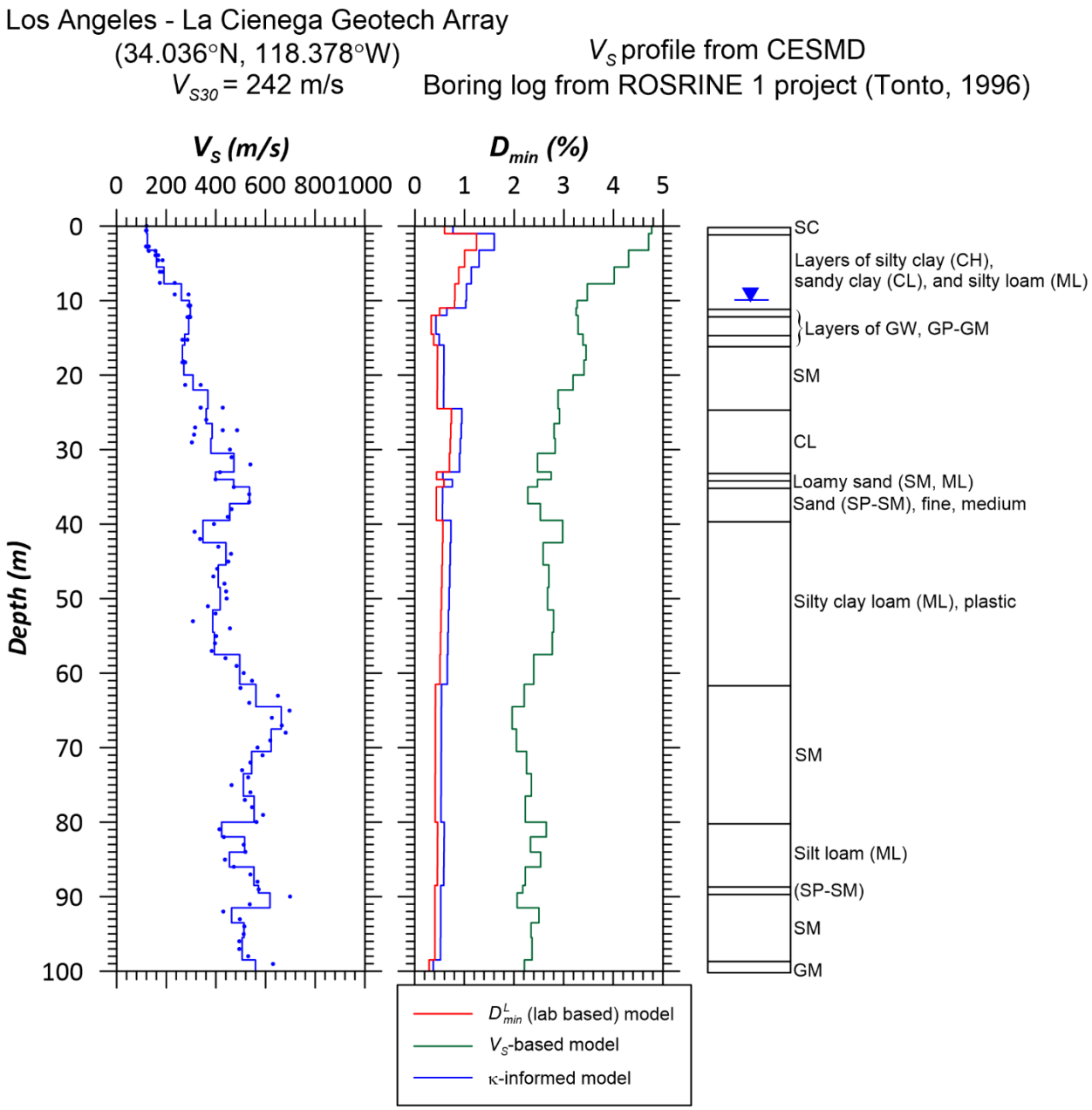

Figure 3.19. V_S profile and D_{min} profiles based on geotechnical models for laboratory damping (D^L_{min}), Campbell (2009) model for Q_{ef}, and $\Delta\kappa$ for Los Angeles-La Cienega site.

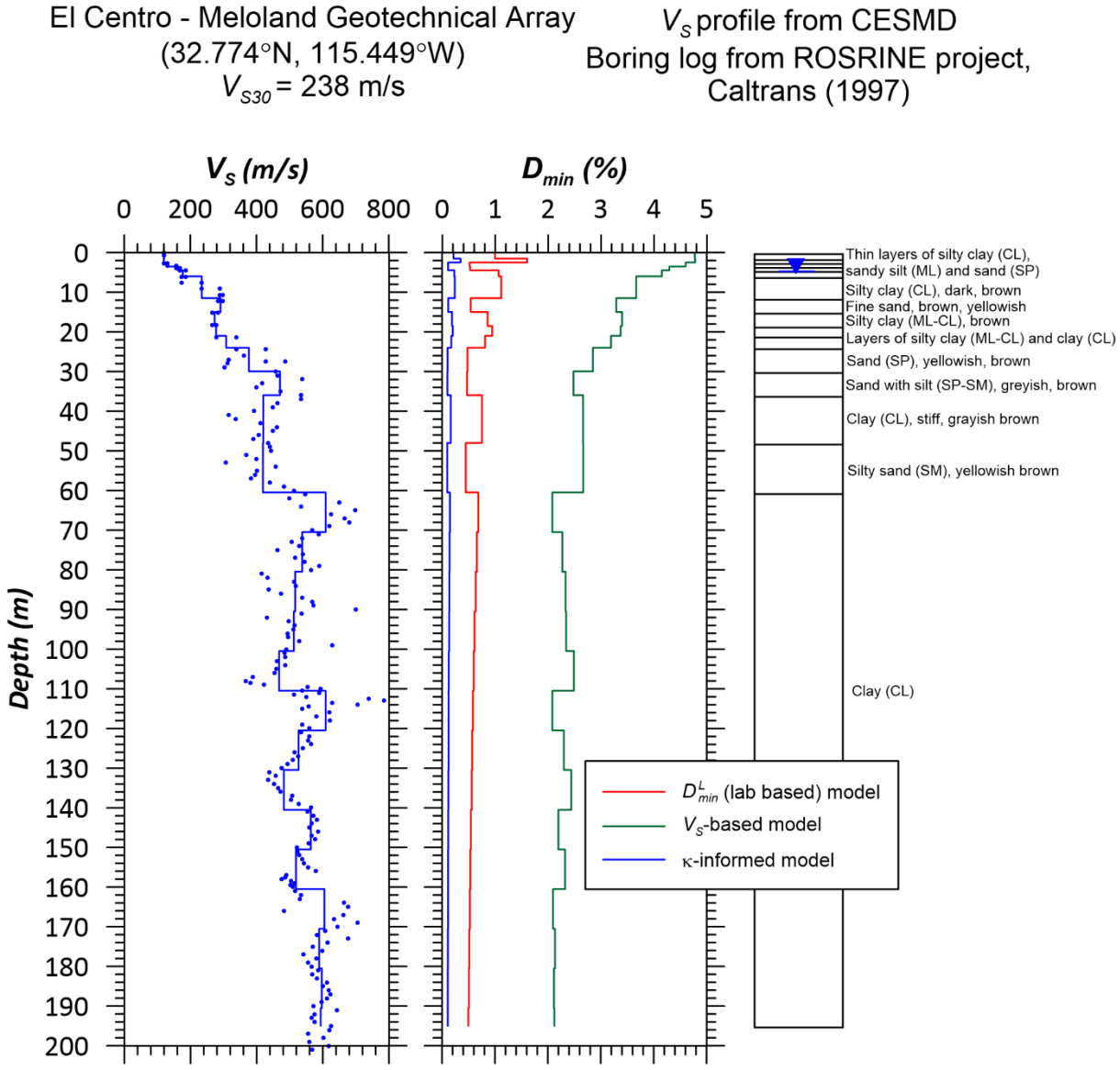

Figure 3.20. V_S profile and D_{min} profiles based on geotechnical models for laboratory damping (D^L_{min}), Campbell (2009) model for Q_{ef}, and $\Delta\kappa$ for El Centro-Meloland vertical array site.

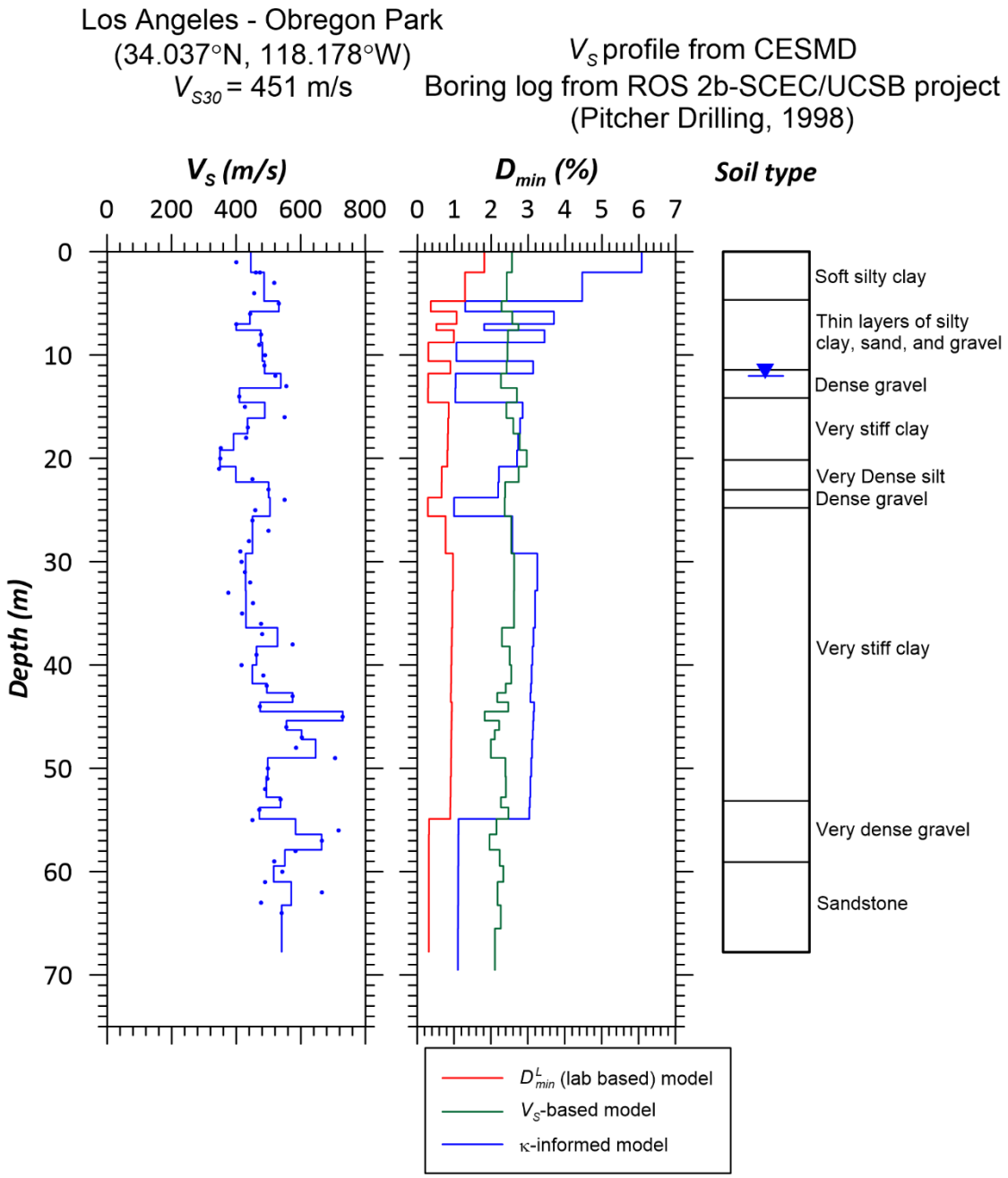

Figure 3.21. V_S profile and D_{min} profiles based on geotechnical models for laboratory damping (D^L_{min}), Campbell (2009) model for Q_{ef}, and $\Delta\kappa$ for Los Angeles-Obregon Park site.

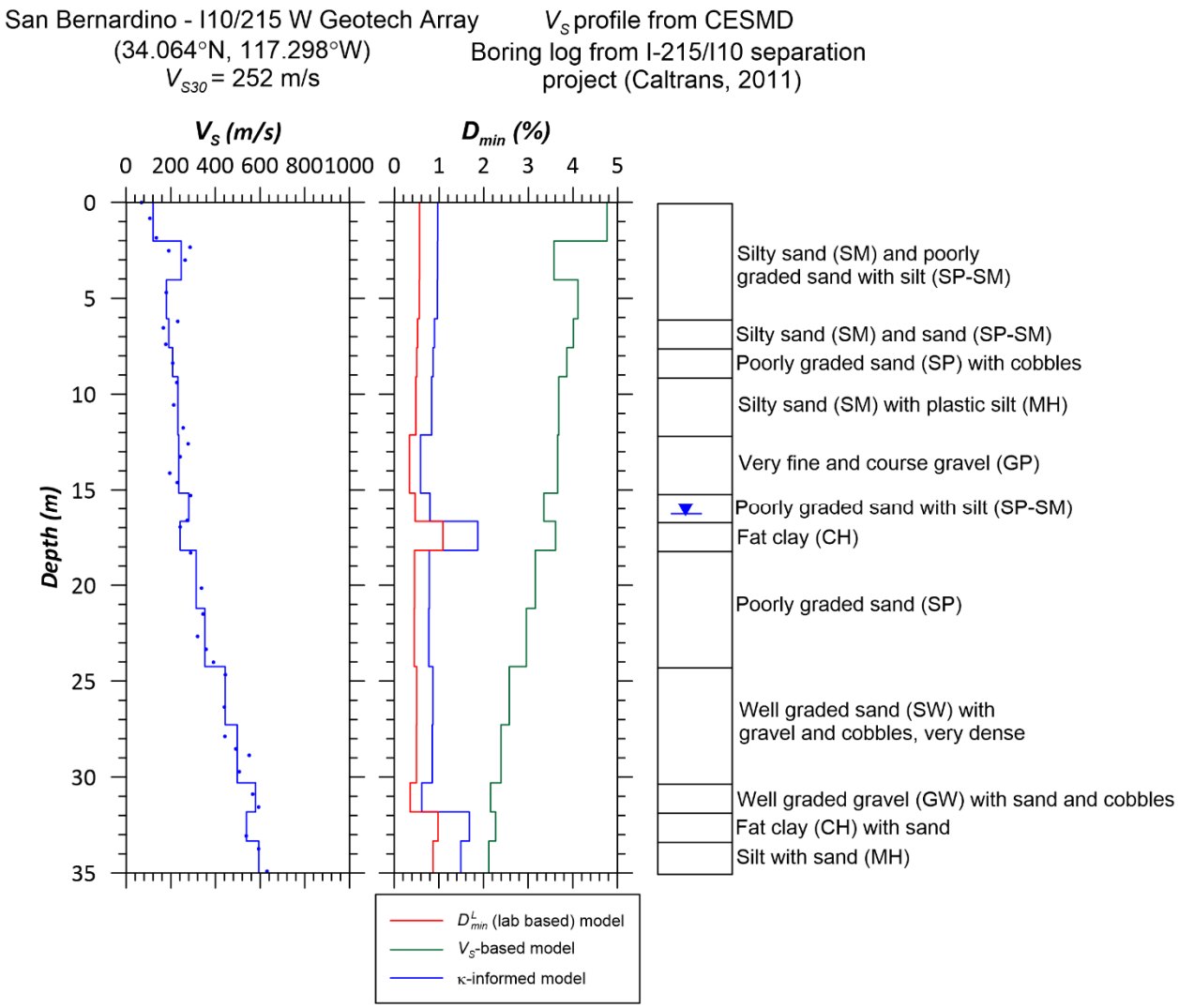

Figure 3.22. V_S profile and D_{min} profiles based on geotechnical models for laboratory damping (D^L_{min}), Campbell (2009) model for Q_{ef}, and $\Delta\kappa$ for San Bernardino vertical array site.

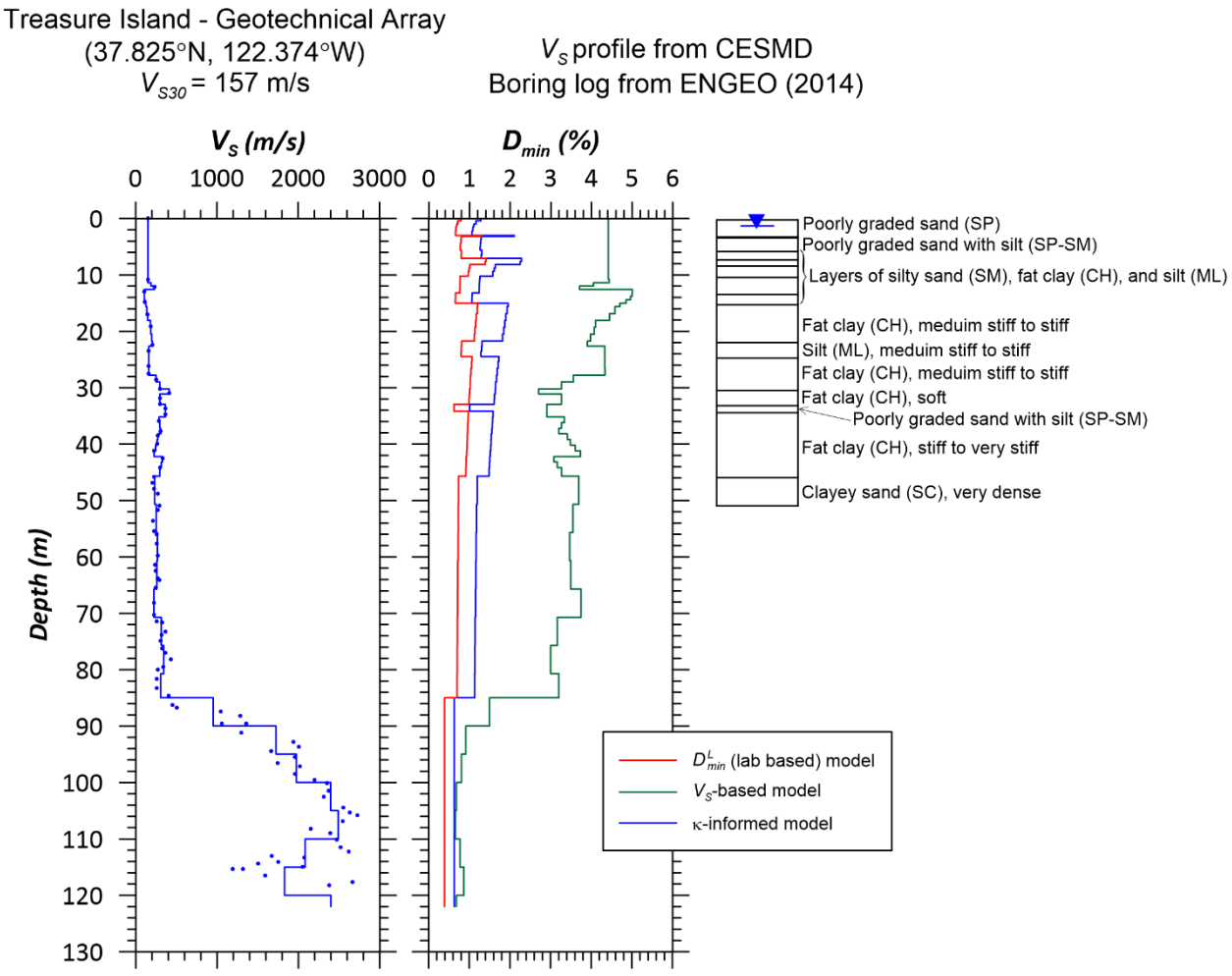

Figure 3.23. V_S profile and D_{min} profiles based on geotechnical models for laboratory damping (D^L_{min}), Campbell (2009) model for Q_{ef}, and $\Delta\kappa$ for Treasure Island vertical array site.

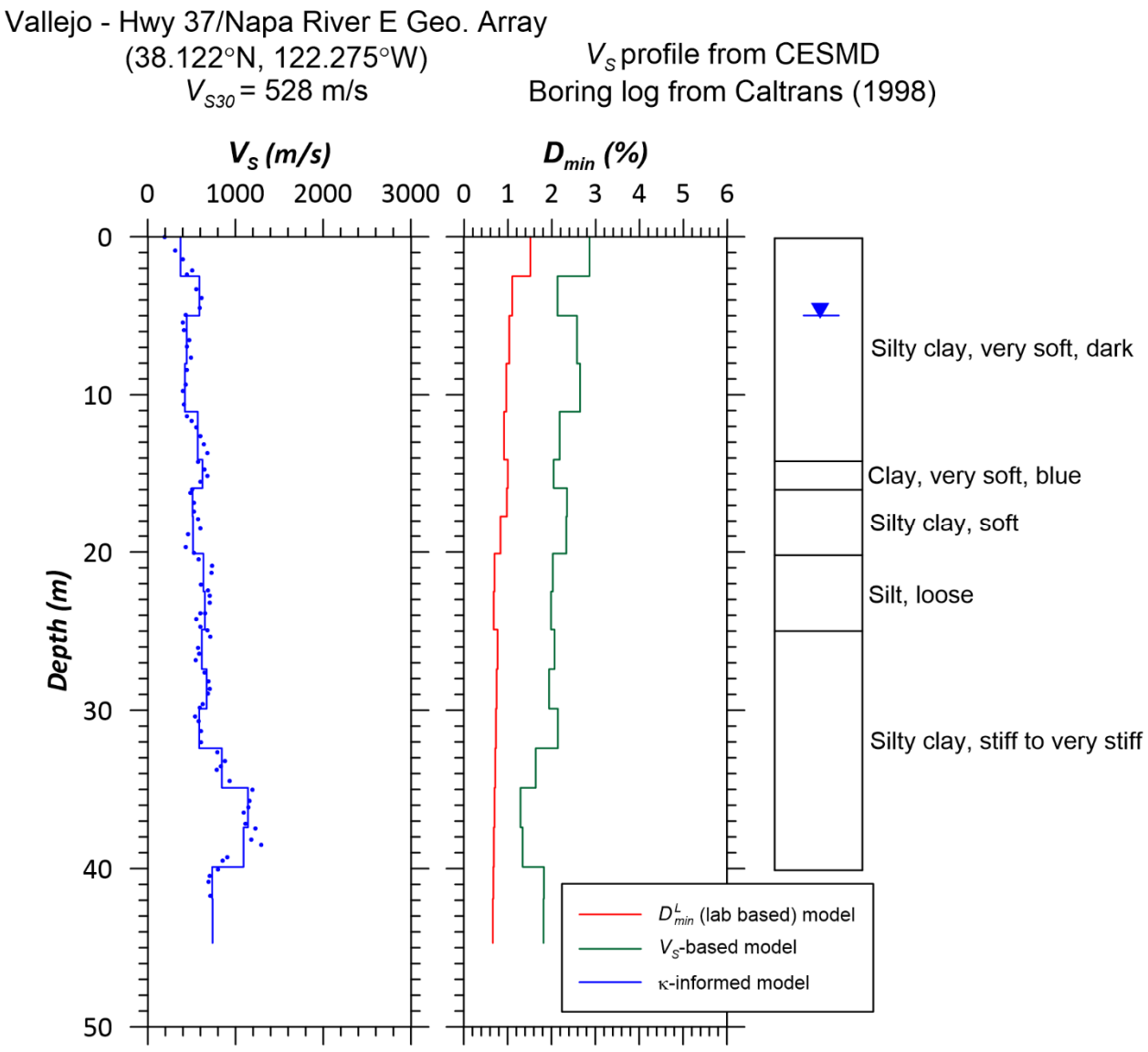

Figure 3.24. V_S profile and D_{min} profiles based on geotechnical models for laboratory damping (D^L_{min}), Campbell (2009) model for Q_{ef}, and $\Delta\kappa$ for Vallejo-Hwy 37/Napa River E. site.

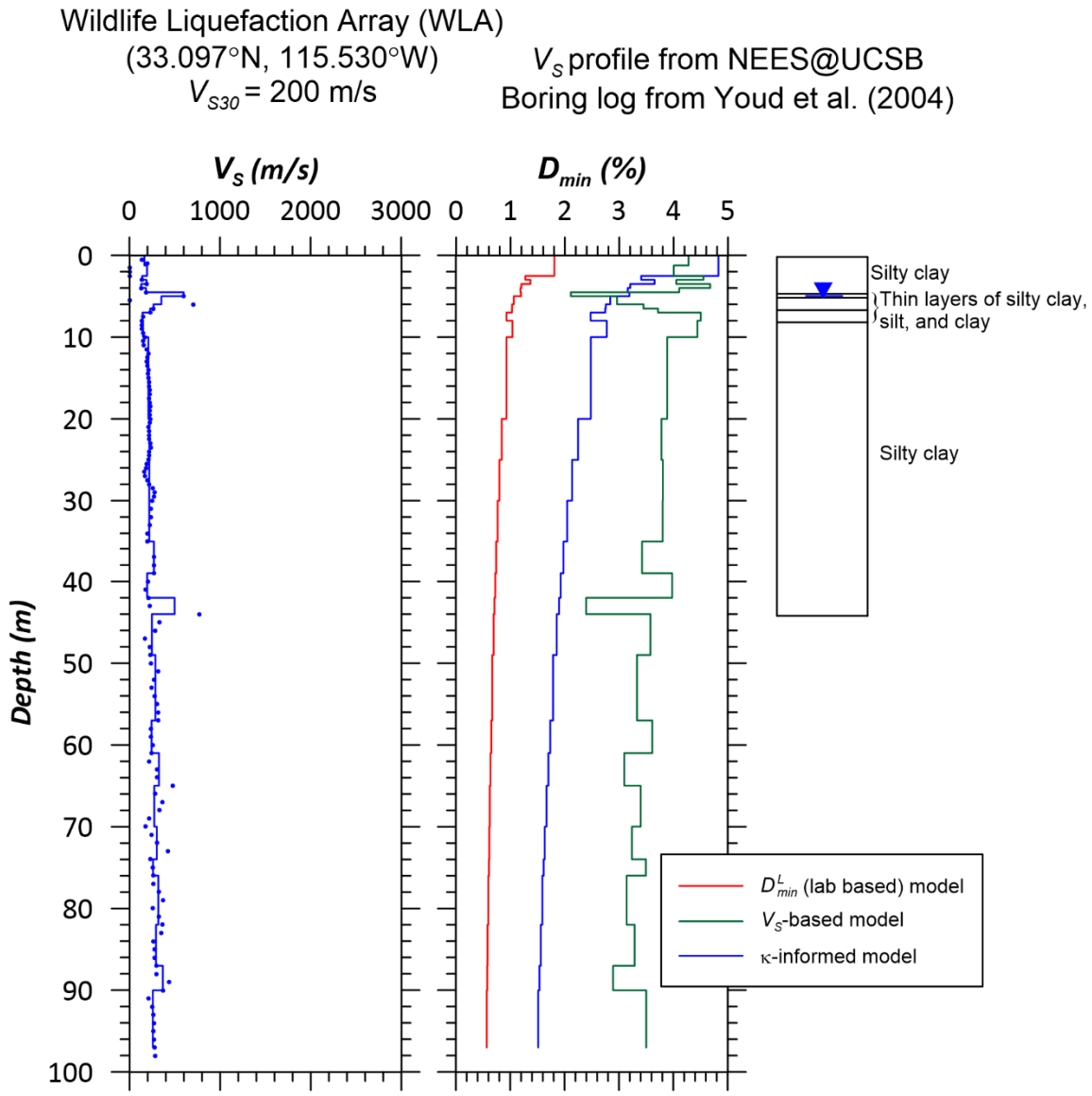

Figure 3.25. V_S profile and D_{min} profiles based on geotechnical models for laboratory damping (D^L_{min}), Campbell (2009) model for Q_{ef}, and $\Delta\kappa$ for Wildlife Liquefaction Array (WLA) site.

Table 3.3. Summary statistics of Δκ (measured from ETF), Δκ implied from D_{min}^{L} profiles, and F_D. for the vertical array sites.

Site	Station No. (CSMIP)	$\overline{\Delta\kappa}$ (sec)	Δκ implied by D_{min}^{L} (sec)	F_D
Antioch-San Joaquin S	67266	0.0116	0.00366	3.18
Bay Bridge	58961	0.0085	NA	4.97
Benicia South	68323	0.0044	NA	4.53
Borrego Valley	NA	0.0053	0.00632	0.74
Corona	13186	0.0078	0.00085	9.15
Coronado East	3192	0.0133	0.00415	3.21
Coronado West	3193	0.0063	0.00324	1.95
Crockett-1	68206	0.0016	0.00121	0.94
El Centro-Meloland	1794	0.0013	0.00656	0.22
Eureka	89734	0.0203	0.00456	4.46
Foster City	58968	-0.0033	NA	NA
Garner Valley	NA	0.0136	0.0025	5.43
Hayward-580W	58487	0.0234	NA	8.19
Hayward-San Mateo	58798	0.0330	NA	4.64
Hollister digital	NA	0.0236	0.00429	5.50

Site	Station No. (CSMIP)	$\overline{\Delta\kappa}$ (sec)	$\Delta\kappa$ implied by D_{min}^{L} (sec)	F_D
La-Cienega	24703	0.0042	0.00325	1.29
Obregon Park	24400	0.0074	0.00212	3.48
San Bernardino	23792	0.0000	0.00139	1.72
Treasure Island	58642	0.0118	0.00684	1.62
Vallejo	68310	-0.0080	0.00136	NA
Wildlife Liquefaction	NA	0.0167	0.00628	2.67

4 Inferences of Site Response from Transfer Functions and Implications for the Effectiveness of Ground Response Analysis

4.1 INTRODUCTION

In this chapter, we study the effectiveness of 1D Ground Response Analysis (GRA) by comparing observed (empirical) and predicted (theoretical) transfer functions representing site response between the downhole and surface accelerometers. Transfer functions reveal the position of site response resonance peaks more clearly than the alternative of 5% damped Pseudo-Spectral Acceleration (*PSA*) ratios. The performance of GRA is investigated by plotting and quantifying misfits between the shapes of empirical and theoretical transfer functions, especially with respect to the positions of resonant peaks.

4.2 CALCULATION OF TRANSFER FUNCTIONS

Empirical transfer functions (ETFs) representing site response between the downhole and surface accelerometers are computed from ratios of Fourier amplitudes as follows:

$$H(f) = \frac{Z(f, x_1)}{X(f, x_2)} \tag{4.1}$$

where $H(f)$ is the ETF, $Z(f,x_1)$ is the surface FAS and $X(f,x_2)$ is the downhole FAS. ETFs are only considered over the usable frequency range based on record processing. The ETF is taken as the geometric-mean of ETFs for the two horizontal components of the recordings (at their as-recorded azimuths) for each site. The results shown subsequently are smoothed through the use of a logarithmic window function proposed by Konno and Ohmachi (1998) with the coefficient for bandwidth frequency (b) equal to 20.

Theoretical transfer functions (TTF) are a direct outcome of linear and equivalent-linear analysis (Section 3.2.1). In other words, the calculation of TTFs does not require analysis of ground motions and their Fourier amplitudes as in Eq. (4.1). When time-domain procedures are used, the ground motions must be calculated, their FAS computed, and then TTF can be taken using Eq. (4.1).

Before proceeding further, it should be pointed out that the ETF (and TTF) represent the surface/downhole ratio in which the surface motion is outcropping and the downhole motion is 'within'. The 'within' term indicates that the motion includes the effects of down-going waves that have reflected from the ground surface, whereas outcropping motions are twice the amplitude of the incident wave due to full reflection at a free-surface. The analysis of data in the form of spectral accelerations, discussed subsequently in Chapter 5, is based on direct evaluation of surface recordings in lieu of surface/downhole ratios.

4.3 TRANSFER FUNCTION COMPARISONS FROM KIK-NET ARRAY IN JAPAN

Thompson et al. (2012) studied 100 KiK-net sites in Japan in order to assess the variability in site amplification and the performance of linear 1D GRA. These sites have recorded a large number of surface and downhole recordings. For GRA, they used the program NRATTLE, which is a part of the ground motion simulation program SMSIM (Boore, 2005). NRATTLE performs linear GRA using Thomson–Haskell matrix method (Thomson, 1950; Haskell, 1953). The input parameters for NRATTLE include shear wave velocity (V_S), soil density, and the intrinsic attenuation of shear-waves (Q_S^{-1}) which represents damping. Soil density was estimated from P-wave velocity using the procedures suggested by Boore (2008), and $Q_S^{-1}$was estimated using a grid-search algorithm to optimize the fit to $H(f)$. Note that by optimizing damping in this manner, Thompson et al. (2012) do not assess the performance of alternative damping models, as described in Section 3.2.3. Moreover, this optimization would not be possible to perform in a forward sense when vertical array recordings from a site are not available.

Thompson et al. (2012) computed ETFs with Eq. (4.1) using available data meeting certain selection requirements. In order to minimize the potential for nonlinear effects, only records having a ground surface PGA < 0.1 g were selected. In total, 3714 records from 1573 earthquakes were considered for the 100 KiK-net sites. The mean and 95% confidence intervals were computed

across all selected recordings at a given site, with the example results (for two sites) given in Figure 4.1. TTFs from the GRA are also shown in Figure 4.1.

Figure 4.1 (a) provides an example of poor fit between the ETF and TTF whereas Figure 4.1 (b) shows a good fit. Goodness-of-fit was quantified using Pearson's sample correlation coefficient (r) as a measure of how well the model predictions and the data are correlated. Parameter r quantifies how well the transfer functions align, including the locations and shapes of peaks. Parameter r is insensitive to relative overall levels of amplification, which is better quantified in the next subsection in *PSA* amplifications. Thompson et al. (2012) calculated the Pearson's sample correlation coefficient for i^{th} earthquake and j^{th} analysis (based on damping estimation approach) as follows for a given site:

$$r_{ij} = \frac{\sum \left(\mathrm{ETF}_i(f) - \overline{\mathrm{ETF}_i} \right) \left(\mathrm{TTF}_j(f) - \overline{\mathrm{TTF}_j} \right)}{\sqrt{\sum \left(\mathrm{ETF}_i(f) - \overline{\mathrm{ETF}_i} \right)^2} \sqrt{\sum \left(\mathrm{TTF}_j(f) - \overline{\mathrm{TTF}_j} \right)^2}} \tag{4.2}$$

The summations in Eq. 4.2 are taken over a frequency range with a lower bound f_{min} corresponding to the first peak in the TTF and an upper bound f_{max} that is the minimum of the frequency of the fourth peak of the TTF or 20 Hz. The summation is performed over all frequency points between f_{min} and f_{max}, which are equally spaced in logarithmic units. The mean value of r across all events (r_j) for a given site is denoted $\overline{r}$.

A value of r=0.6 was taken by Thompson et al. as the threshold for good fit. The corresponding r values for the two sites in Figure 4.1 are 0.10 for the poor fit site and 0.79 for the good fit site. Dispersion curves (phase velocity vs. frequency) for the two example sites are shown in Figure 4.1. The results indicate that there is a large degree of variability in the dispersion curves for the poor fit site and consistency in the dispersion curves for the good fit site. Multiple dispersion curves are only available for two of the 100 sites considered by Thompson et al. (2012). Nonetheless, the limited available data hint at the possibility that geologic complexity, as reflected by spatial variability in the Rayleigh wave velocity structure, may correlate to the accuracy of GRA prediction. More complex geologic structure would be expected to produce 3D site effects that are not captured by GRA.

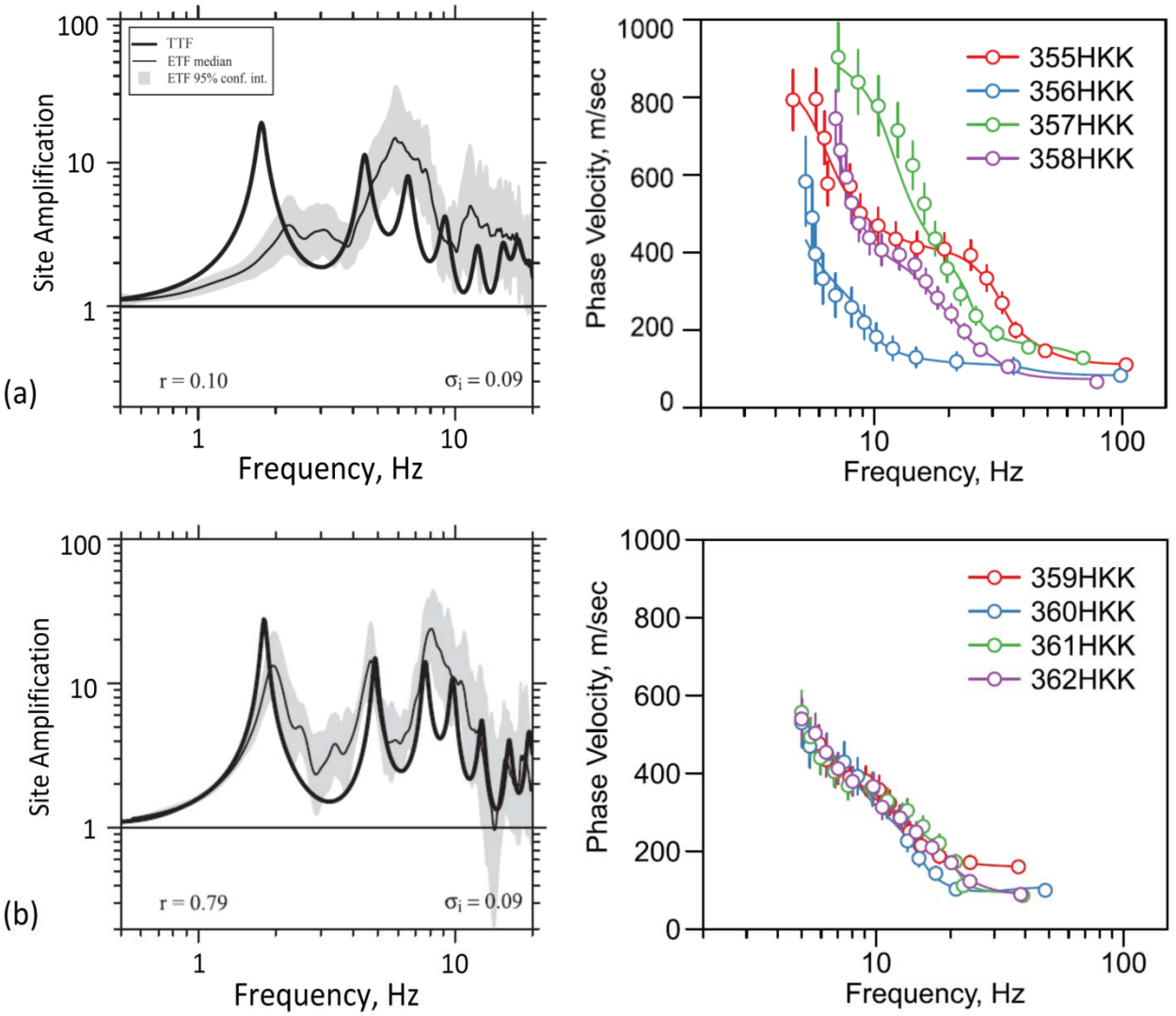

Figure 4.1. Examples of a poor fit (a) and good fit (b) between ETF and TTF at two KiK-net sites along with the dispersion curves from multiple SASW tests for both sites (adapted from Thompson et al., 2012).

Results for the 100 considered sites show that only 18% have a good fit between ETFs and TTFs, indicating 1D GRA fails to provide an accurate estimation of site response for a large majority of KiK-net sites.

A second metric considered by Thompson et al. (2012) concerns the inter-event variability of transfer function ordinates, which they computed as a median value of the standard deviations computed across the frequencies within the range to compute *r*. Large values of this standard deviation indicate large event-to-event differences in observed site amplification, suggesting potential complexities from 3D geologic structure. The two sites shown in Figure 4.4 have low

levels of variability (0.09); results for full list of 100 sites and a comparison to California data is presented in the next section.

4.4 TRANSFER FUNCTION COMPARISONS FOR CALIFORNIA VERTICAL ARRAY DATA

Using the data set described in Chapter 2, we compute ETF ordinates for each of the 21 selected California vertical array sites. In this sense our approach is similar to that of Thompson et al. (2012) – we 'cast the net widely' to study site response performance over a wide range of conditions. Unlike several studies conducted since Thompson et al. (2012), we do not screen sites to identify those for which the ETF matches the shape of a TTF; instead we seek to understand how frequently such a match is achieved in relatively weak motion data from California vertical array sites.

Similar to Thompson et al. (2012), we exclude recordings with strong ground shaking (*PGA* at surface instrument > 0.1 g) so as to minimize nonlinear effects. Figure 4.2 shows histograms of *PGA* and *PGV* for the downhole instrument records used in the present work.

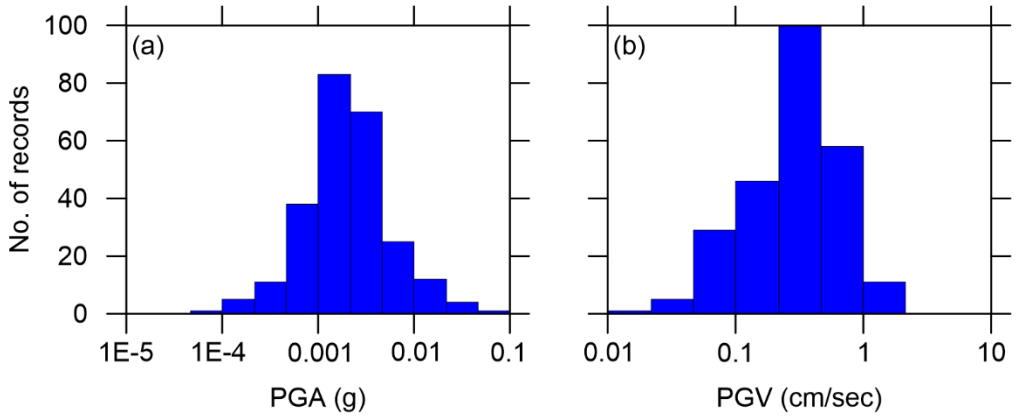

Figure 4.2. Histograms of PGA (a) and PGV (b) for downhole recordings used in this study.

We assume a log-normal distribution for ETF ordinates and compute for each site the median ($\mu_{\ln}$) (equivalent to the exponent of the natural log mean) and the natural log standard deviation of ETF ($\sigma_{\ln}$) at each frequency using all available record pairs. Figure 4.3 shows example ETFs for all record pairs at the San Bernardino and Obregon Park sites along with the median and 95% confidence intervals of ETF ordinates. For plotting purposes, we show results over a frequency range between 0.5 and 10 Hz. The all-inclusive usable frequency range is 0.2-28 Hz for

San Bernardino site recordings, and 1.4-18 Hz for Obregon Park. Therefore, the range shown focuses attention on frequencies that significantly contribute to *PSA* ordinates. The median ETF and its standard deviation are shown for all sites in plots in the Appendix.

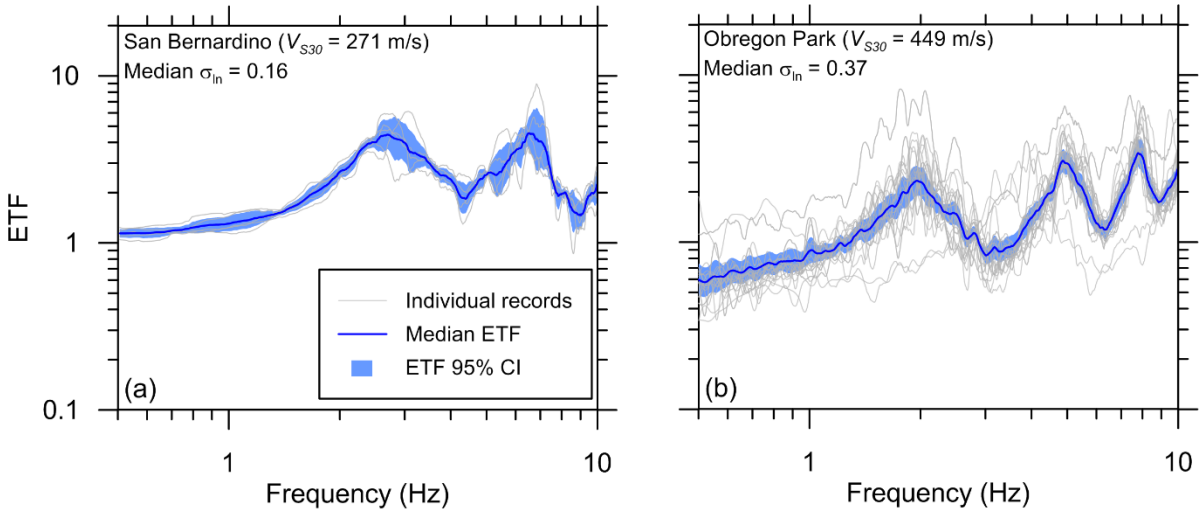

Figure 4.3. Empirical transfer functions plots for (a) San Bernardino site with low ETF variability, and (b) Obregon park with high ETF variability.

Theoretical transfer functions (TTFs) are computed by linear visco-elastic 1D GRA in DEEPSOIL. As the downhole sensor is recording both up-going and down-going waves, we take the boundary condition at the base of the model as rigid (Kwok et al., 2008). The visco-elastic analysis in DEEPSOIL is performed in the frequency domain, and the transfer function predicted by the model is independent of the input motion. Similar to ETFs, the TTFs are smoothed by Konno and Ohmachi (1998) function with b=20. We utilize alternate approaches for estimating small-strain soil damping as described in Section 3.2.2-3.2.3 to provide insight and guidance on best practices for selection of effective small-strain damping (D_{eff}). Note that this aspect of our analysis departs from the prior work of Thompson et al. (2012), who back-calculated damping to optimize the ETF-TTF fit.

Figures 4.4-4.13 show model-data comparisons by plotting together TTFs and ETFs. Unlike the amplification of *PSA* which is discussed in Chapter 5, transfer functions are able to show multiple modal frequencies for the soil column from both recordings and simulations. The match (or lack thereof) of the positions of the first several peaks in ETFs and TTFs are a good indicator of consistency between the transfer functions. In the example of El Centro-Meloland site (Figure 4.12), the simulations are not able to capture the position of any of the visible five peaks

seen in ETF plot. This is an indication that 1D GRA is unable to simulate the site response between surface and downhole regardless of damping model. On the contrary, for the Treasure Island site (Figure 4.10), the position of all six peaks in the ETF are captured by GRA, which is an indication that the 1D assumption implicit to GRA is valid for this site.

In addition to the above qualitative assessments of goodness of fit, it is also useful to consider quantitative metrics. One such metric is the Pearson's sample correlation coefficient r (also used by Thompson et al., 2012), which was computed in the manner described in Section 4.2. We use the mean value over all recordings at a given site, $\bar{r}$, which is shown in Figure 4.14. Generally, sites with qualitatively good fit between ETF and TTF have values of $\bar{r} > 0.6$ (e.g., Treasure Island site in Figure 4.10) and sites with poor fit have $\bar{r} < 0$ (e.g., El Centro-Meloland site).

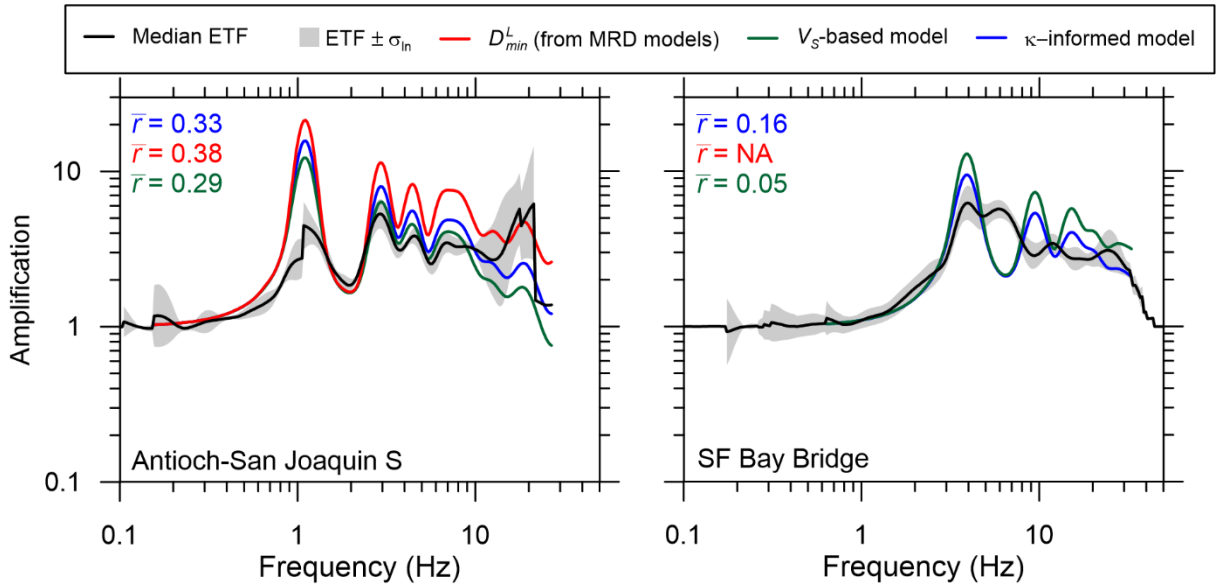

Figure 4.4. Comparison of ETF and TTFs for Antioch-San Joaquin S and San Francisco Bay Bridge. Values of $\bar{r}$ for each damping model are shown in different colors (red: D_{min}^{L}, green: *Vs*-based, blue: κ-informed).

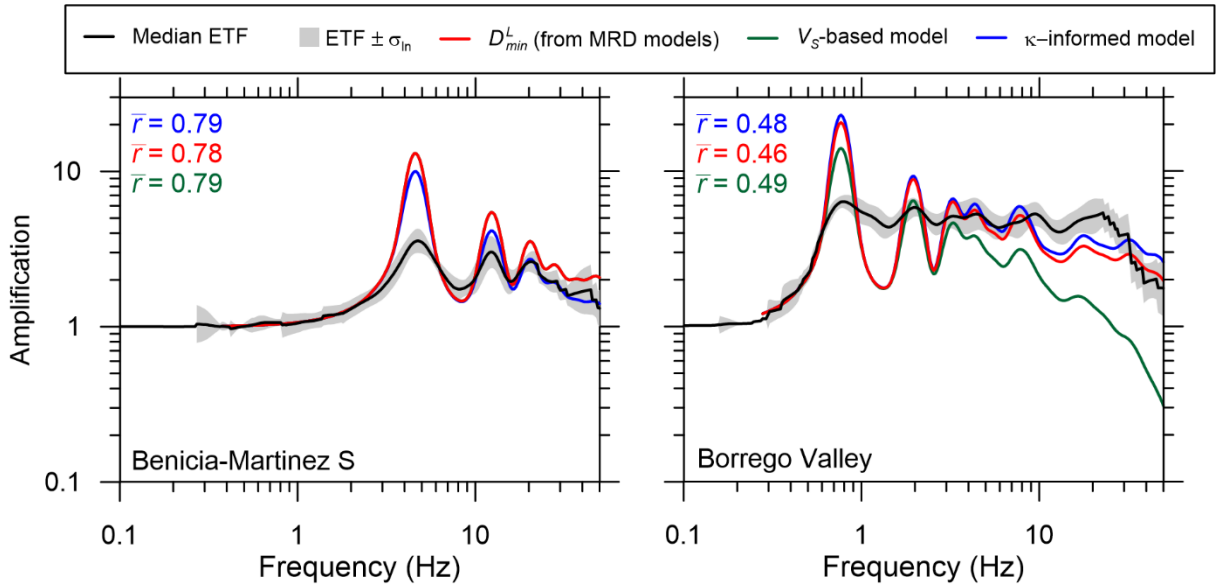

Figure 4.5. Comparison of ETF and TTFs for Benicia-Martinez S and Borrego Valley (BVDA). Values of $\bar{r}$ for each damping model are shown in different colors (red: D_{min}^{L}, green: V_S-based, blue: κ-informed).

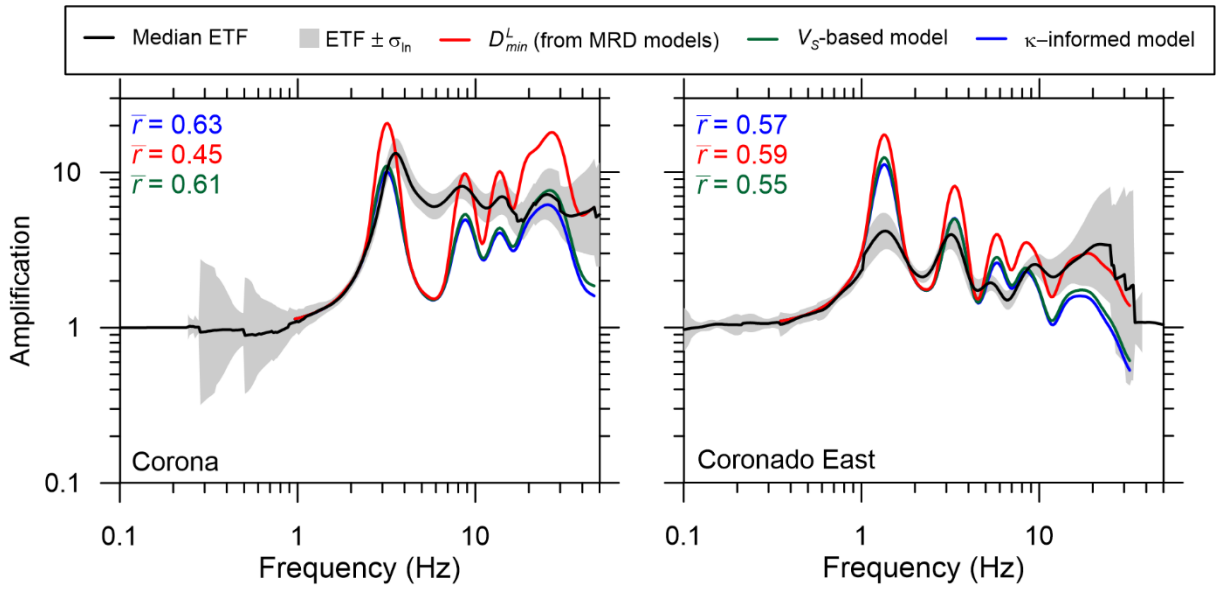

Figure 4.6. Comparison of ETF and TTFs Corona and Coronado East. Values of $\bar{r}$ for each damping model are shown in different colors (red: D_{min}^{L}, green: V_S-based, blue: κ-informed).

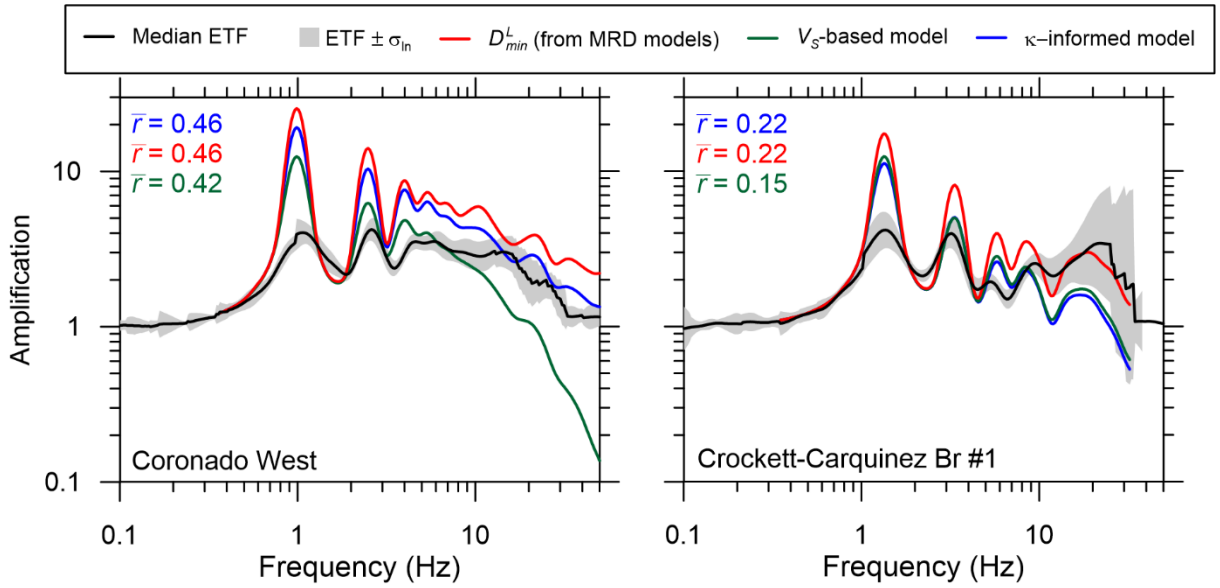

Figure 4.7. Comparison of ETF and TTFs for Coronado West and Crockett-Carquinez Br #1. Values of $\bar{r}$ for each damping model are shown in different colors (red: D_{min}^{L}, green: *Vs*-based, blue: κ-informed).

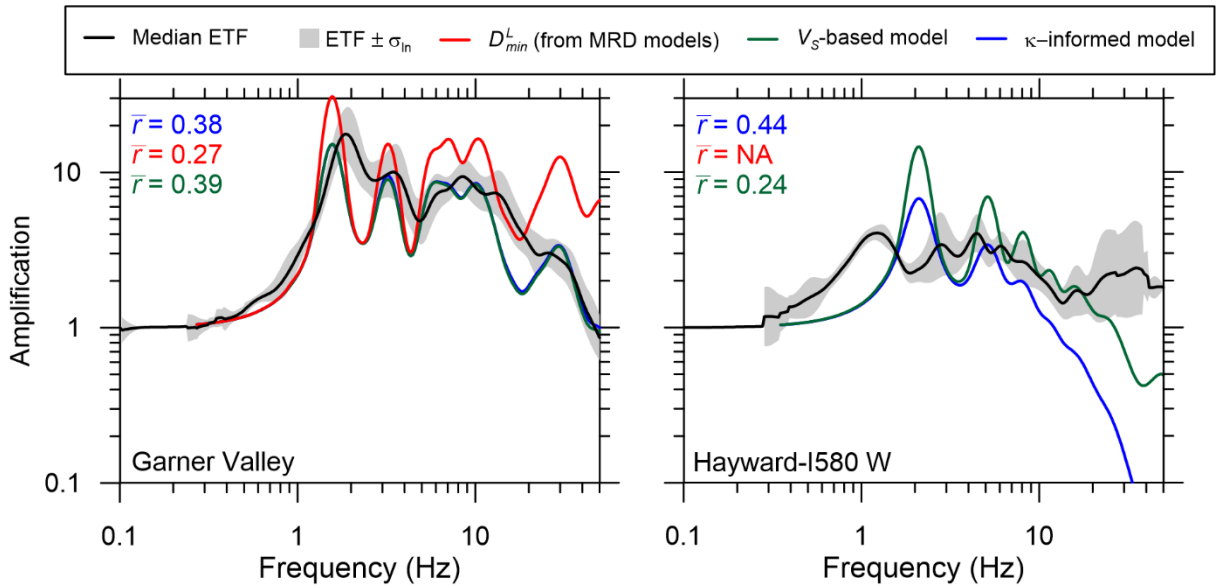

Figure 4.8. Comparison of ETF and TTFs for Garner Valley and Hayward-I580W. Values of $\bar{r}$ for each damping model are shown in different colors (red: D_{min}^{L}, green: *Vs*-based, blue: κ-informed).

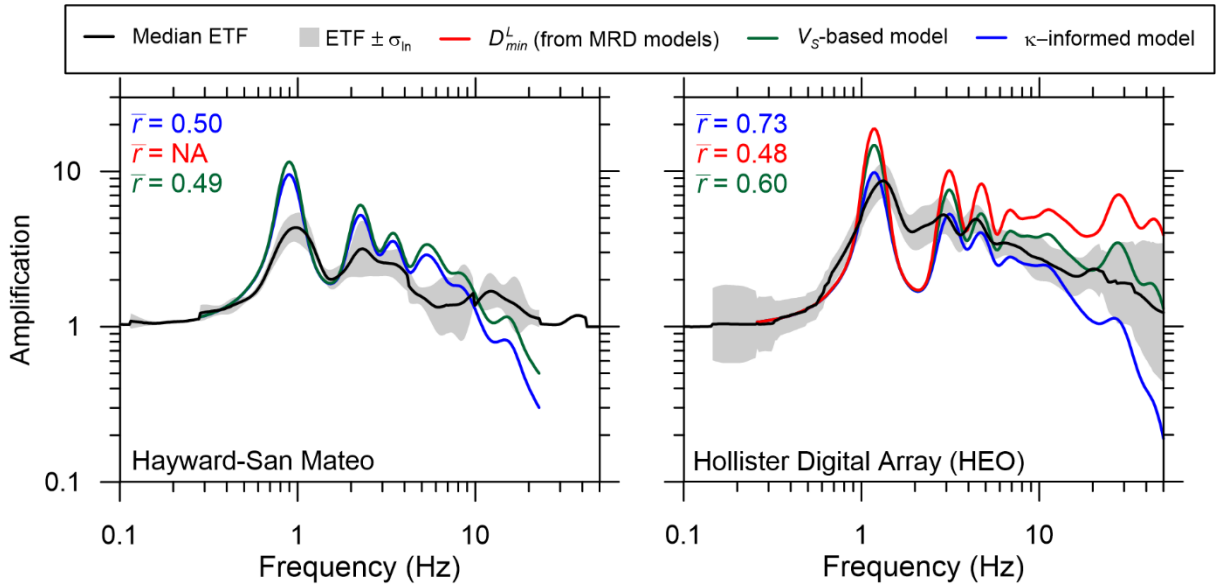

Figure 4.9. Comparison of ETF and TTFs for Hayward-San Mateo and Hollister Digital Array (HEO). Values of $\bar{r}$ for each damping model are shown in different colors (red: D_{min}^{L}, green: *Vs*-based, blue: κ-informed).

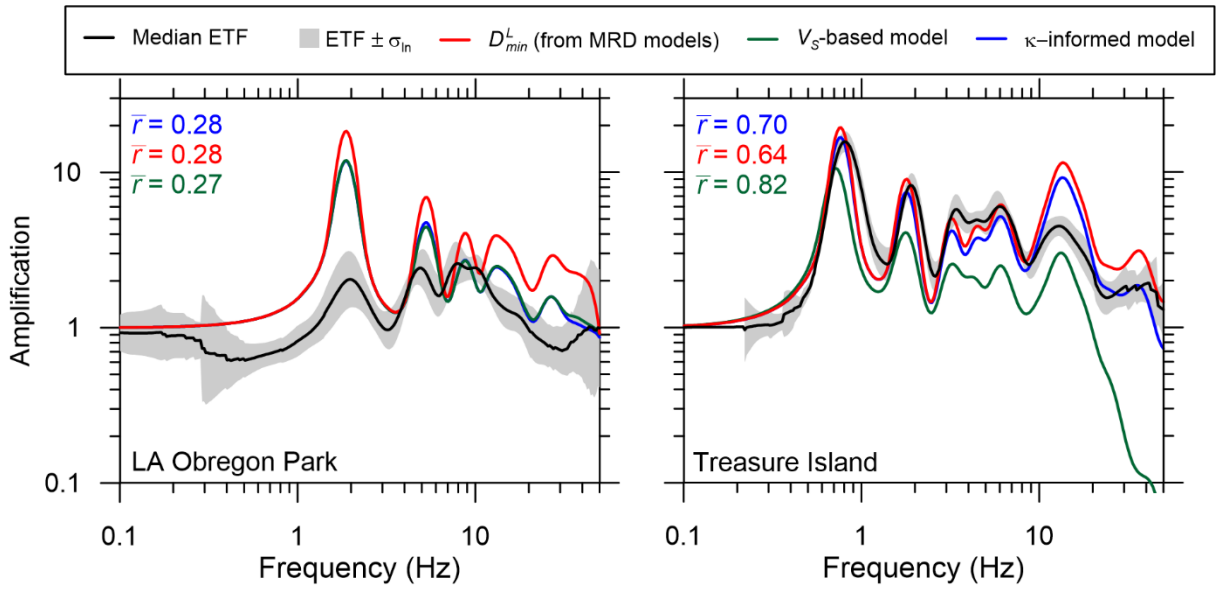

Figure 4.10. Comparison of ETF and TTFs for LA Obregon Park and Treasure Island. Values of $\bar{r}$ for each damping model are shown in different colors (red: D_{min}^{L}, green: *Vs*-based, blue: κ-informed).

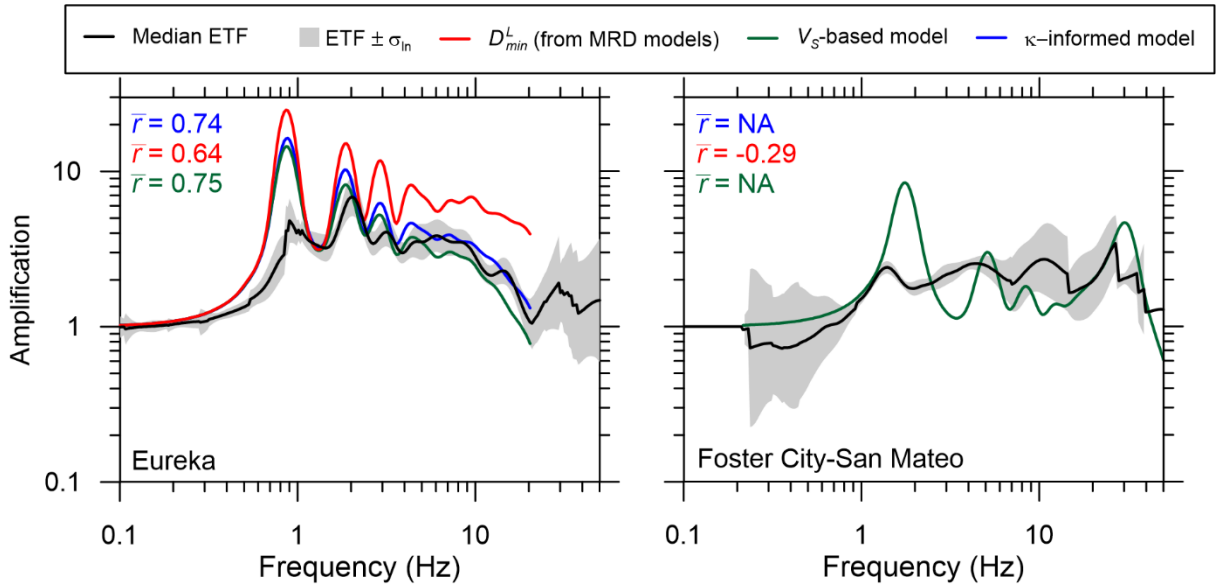

Figure 4.11. Comparison of ETF and TTFs for Eureka and Foster City-San Mateo. Values of $\bar{r}$ for each damping model are shown in different colors (red: D_{min}^{L}, green: V_S-based, blue: κ-informed).

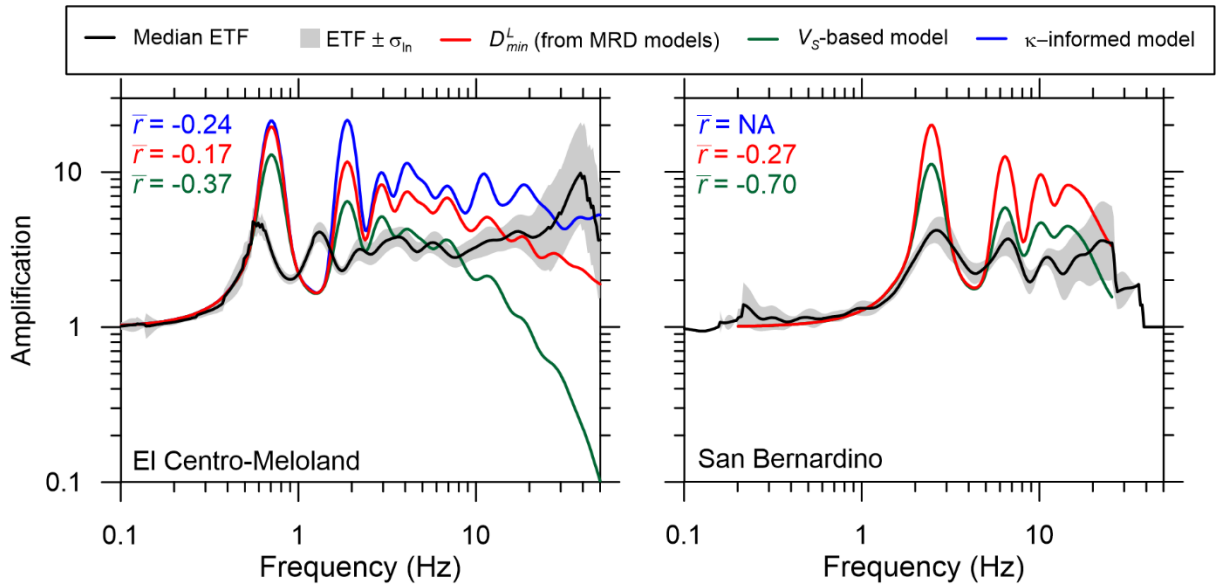

Figure 4.12. Comparison of ETF and TTFs for El Centro-Meloland and Treasure Island. Values of $\bar{r}$ for each damping model are shown in different colors (red: D_{min}^{L}, green: V_S-based, blue: κ-informed).

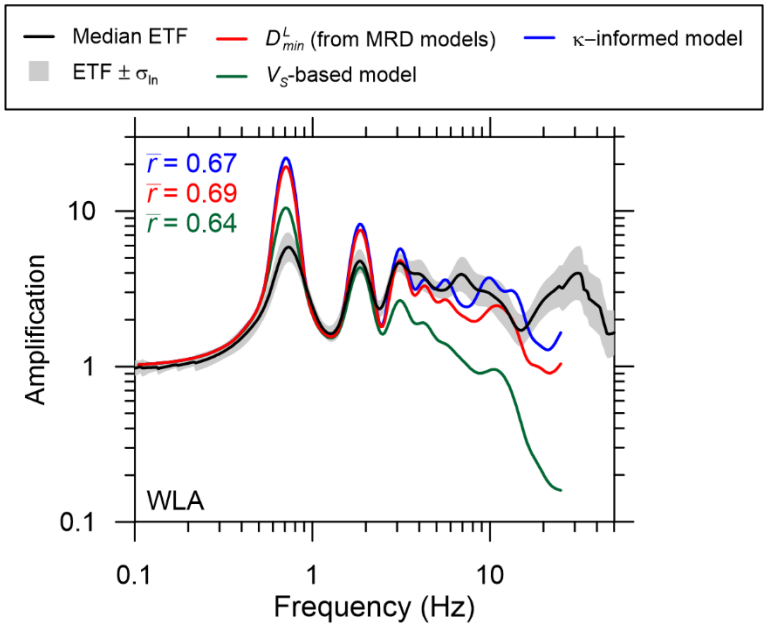

Figure 4.13. Comparison of ETF and TTFs for Wildlife Liquefaction array (WLA). Values of $\bar{r}$ for each damping model are shown in different colors (red: D_{min}^{L}, green: V_S-based, blue: κ-informed).

Figure 4.14 shows histograms of $\bar{r}$ from the California vertical array sites using the three damping models (geotechnical, Vs-based, κ-informed). Also shown for comparison is the distribution from Thompson et al. (2012) for KiK-net sites, although the optimization of damping performed in that study makes the comparison somewhat 'apples-to-oranges', with Japan sites expected to have higher $\bar{r}$ than they would have had without optimization. We see that California sites have higher values of $\bar{r}$ in aggregate, with a higher population median and lower standard deviation. There is also a higher percentage of sites with strong correlation ($\bar{r} > 0.6$) in comparison to their counterparts for the KiK-net arrays in Japan for all damping models. This suggests that the ability of GRAs to match observation is better for the California vertical arrays than for KiK-net sites. Furthermore, the comparison of $\bar{r}$ histograms for California sites suggests a slight increase in $\bar{r}$ when using the κ-informed model indicating a slightly better performance of the κ-informed damping model in capturing the shape of site response transfer functions.

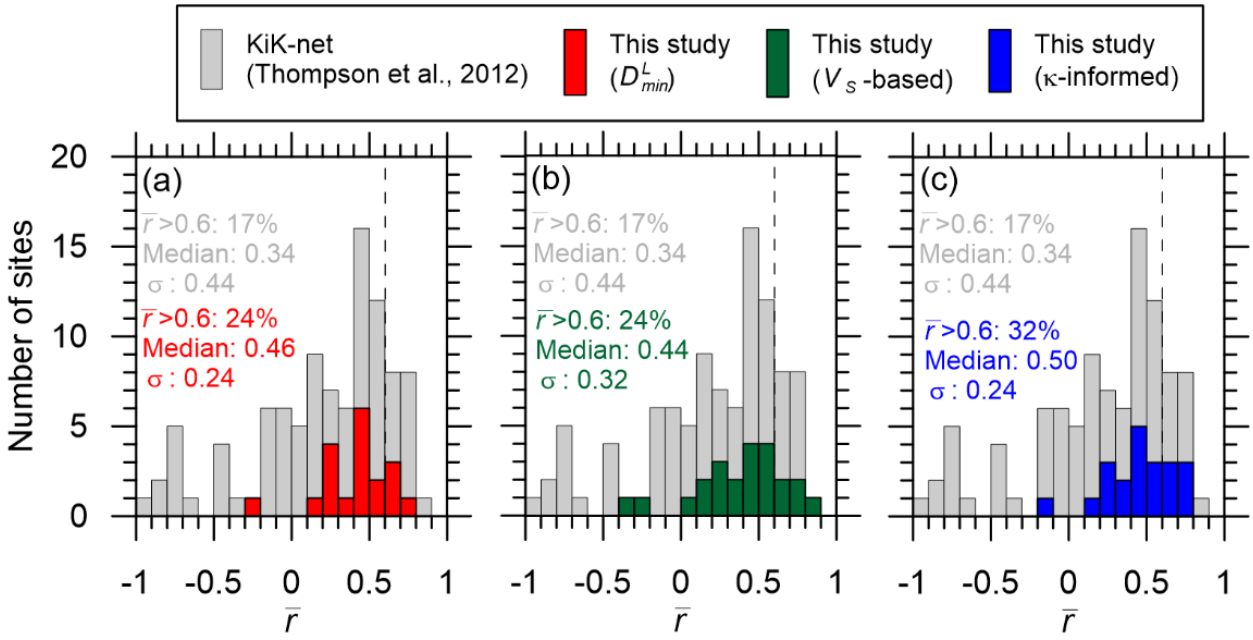

Figure 4.14. Histograms of $\bar{r}$ for California and KiK-net sites as well as their medians and standard deviations. Values and summary statistics of $\bar{r}$ for each damping model are shown in different colors for California sites (red: D^L_{min}, green: V_S-based, blue: κ-informed model).

As described in Section 4.2, Thompson et al. (2012) introduced a metric of ETF variability that is useful to consider in combination with $\bar{r}$ because it quantifies event-to-event variability in observed site response across a particular vertical array. This metric is computed by first taking the natural log standard deviation of ETF ordinates for each of the frequencies considered in the analysis of $\bar{r}$ (i.e., between the lower and upper bound frequencies f_{min} and f_{max}). Then the median across those standard deviations is taken, which is denoted σ^M_{ln}. Figure 4.15 shows the distribution of σ^M_{ln} for the California vertical array sites, with the values reported by Thompson et al. (2012) for the KiK-net sites also shown for comparison (the method of computation is the same in both cases). The inter-event dispersion is notably smaller for the California sites, with only two (10%) exceeding the value of 0.35 considered as 'high dispersion' by Thompson et al. (2012).

The better fit and smaller ETF dispersion encountered for the California sites as compared to the KiK-net sites may result from the former mostly being located within large sedimentary basins and relatively flat areas, whereas the later are often on firmer ground conditions (often weathered rock or thin soil over rock) with uneven ground conditions. The geologic conditions at the KiK-net sites are such that horizontal layering of sediments is less likely to be an acceptable

assumption, with the site response being strongly influenced by 2D and 3D effects associated with irregular stratigraphy and (in some cases) topography. The 2D and 3D effects in site response in KiK-net sites has been studied by De Martin et al. (2013), who suggests the period and amplitude of site response peaks are significantly sensitive to 2D and 3D effects due to non-horizontal layering. Another possible factor resulting in a better fit for California sites is the quality of V_S measurements. The vertical arrays in California used in this study have high-resolution suspension logging measurements (with Garner Valley being the only exception), while the KiK-net sites are characterized with lower-resolution downhole measurements.

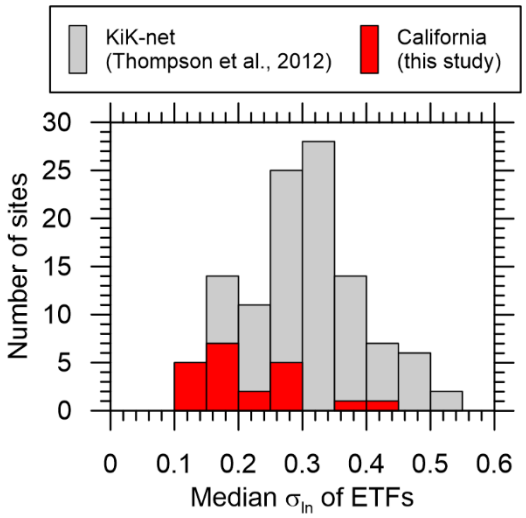

Figure 4.15. Histogram of ETF between-event standard deviation term σ_{ln}^{M} for California and KiK-net vertical array sites.

5 Analysis of Spectral Amplification and Epistemic Uncertainty of Ground Response Analysis Predictions

5.1 INTRODUCTION

In this chapter, we examine features of site amplification for the inventory of California vertical array sites from Chapter 2 in the form of *PSA* amplification. The objective of the analysis presented here is in part complimentary to the analysis of transfer function results in Chapter 4, in that we seek insight into GRA model effectiveness for the three considered damping models described in Section 3.2.2-3.2.3. However, in addition, we describe an approach that can be used to quantify uncertainty in the prediction of site response as estimated from GRA. This uncertainty quantification is of interest for PSHA in which site terms are taken from the results of GRA, in which case epistemic uncertainties in the site response should be considered using a logic tree (or similar) framework (Bommer et al. 2005).

Subsequent sections describe the methodology for statistical analysis of the data to infer bias and uncertainty, present results as derived from the California data, and compare to comparable results obtained previously for KiK-net sites (Kaklamanos et al., 2013).

5.2 RESIDUALS ANALYSIS TO QUANTIFY BIAS AND UNCERTAINTY OF SITE RESPONSE PREDICTIONS FROM GRA

Our analysis of epistemic uncertainty is based on comparing observations (in this case, the surface recordings at California vertical array sites) to predictions. We use 5%-damped *PSA* of the recorded and predicted surface ground motions. We use the RotD50 parameter which is the median single-component horizontal ground motion across all non-redundant azimuths (Boore 2010). In

order to quantify the misfits between the predictions and recordings, we compute the residuals between the recorded and predicted *PSA* in natural logarithmic units:

$$R_{G,kj} = \ln\left(Z_{kj}^{obs}\right) - \ln\left(Z_{kj}^{pre}\right) \tag{5.1}$$

where $R_{G,kj}$ is the residual for recording j at site k, Z_{kj}^{obs} is the observed intensity measure (generally *PSA* at a certain oscillator period), and Z_{kj}^{pre} is the predicted intensity measure. It should be emphasized that the residual is computed based on the surface ground motion, not the site amplification, which is done because (1) it avoids the need to adjust the computed within motion to an equivalent outcropping motion and (2) both terms on the right side of Eq. (5.1) can be viewed as the sum of the amplification and input (in ln units), and the inputs are common and will cancel through the subtraction. Hence, in effect the residual is on the difference between observed and computed site amplification.

5.3 RESULTS FROM CALIFORNIA DATA

One example of predicted/recorded *PSA* plots and the computed residual is shown in Figure 5.1. Positive residuals indicate underprediction and negative residuals indicate overprediction of the recorded ground motion by GRA. Because the downhole recording is used in the calculation of Z_{kj}^{pre}, any misfit in the prediction of the surface motions is attributed to the misfits in site response.

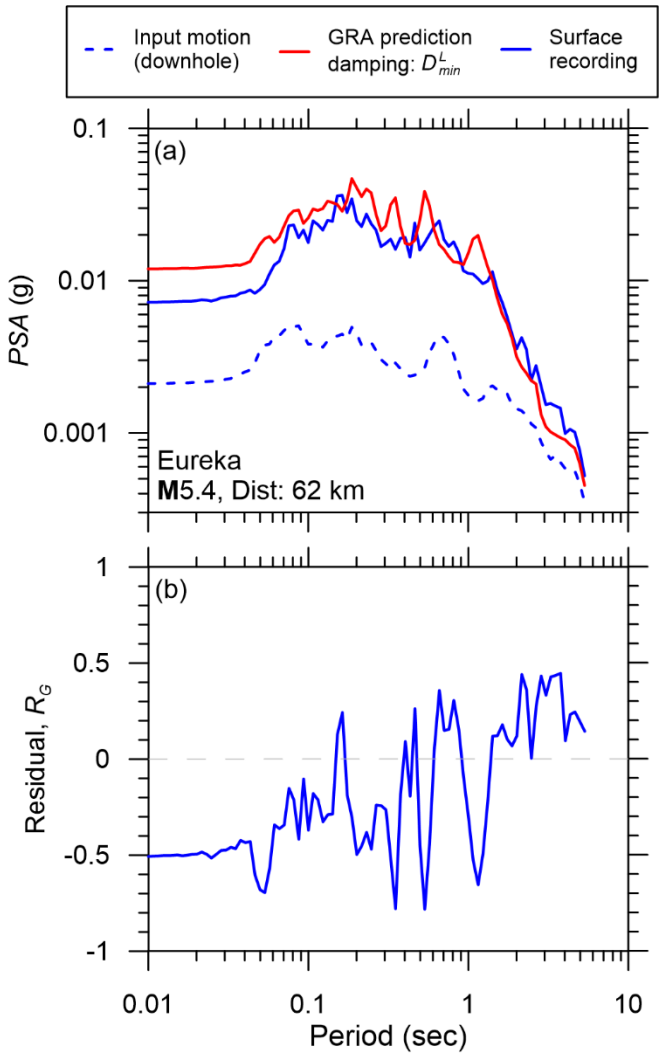

Figure 5.1. An example of (a) response spectrum plots of the downhole motion, surface recorded motion, and surface predicted motion at Eureka (M5.4, epicenteral distance: 62 km); (b) The plot of residuals between observed and predicted ground motions.

Because one objective of our analysis is to assess the performance of alternative small-strain damping models, we sought to identify recordings for which the dynamic soil behavior could, as a first approximation, be represented by layer-specific small-strain shear moduli (G_{max}) and damping (D_{min} or D_{eff}). Kaklamanos et al. (2015) recommend that linear, visco-elastic GRA procedures can be used when the maximum shear strain in a soil column, $\gamma_{max} < 0.01$-0.1%. In the selection of recordings used in these analyses, we sought record sets with $\gamma_{max}<0.01\%$, to ensure that soil nonlinearity is not appreciably affecting the GRA and resulting findings on damping models. In order to exclude strong recordings which are dominated by the effects of soil

nonlinearity, we use shear strain index (I_γ) defined by Kim et al. (2016) as the ratio of input motion *PGV* to V_{S30} in order to approximate the maximum shear strain (γ_{max}) in the soil profile. After applying this screening, the data set consists of 250 recordings at 21 stations.

We perform mixed-effects regression with the LME routine in program R (Pinheiro et al., 2013) to partition the residuals into multiple components:

$$R_{G,kj} = c_{G,l} + \eta_{G,S,k} + \varepsilon_{G,kj} \tag{5.2}$$

where $c_{G,l}$ is the overall model bias, $\eta_{G,S,k}$ is the between-site residual (site term) for site *k*, which represents the average deviation from the prediction for an individual site, and $\varepsilon_{G,ij}$ is the within-site residual, which is the remaining misfit after removing the overall bias and the between-site residual. It should be noted that there is no event-to-event variability in the computed residuals because for the predicted motion (Z_{kj}^{pre}), the actual downhole recording has been used as the input motion. The lack of event-to-event variability eliminates any contribution from the variability in source effects (event terms). This makes Eq. (5.2) different from what is customary in the analysis of residuals when utilizing ground motion data only from surface recordings.

The term $\eta_{G,S,k}$ is the indicator of how well GRA is predicting site response for site *k*, with large absolute values of $\eta_{G,S}$ indicating poor prediction of site response. Two examples of $\eta_{G,S}$ plots for a site with good fit (La Cienega) and poor fit (Corona) are shown in Figure 5.2.

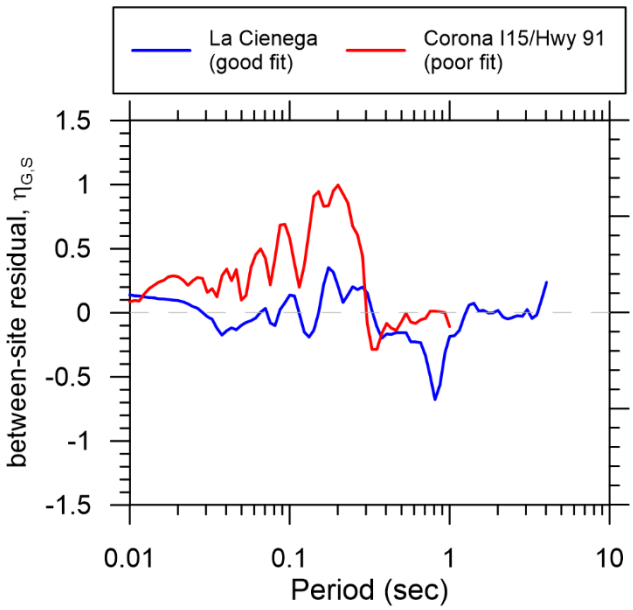

Figure 5.2. Plots of between-site residuals ($\eta_{G,S}$) for La Cienega with a good fit; and Corona with a poor fit between recordings and predictions. The smaller values of ($\eta_{G,S}$) indicate a better fit.

The overall bias is plotted in Figure 5.3 for the three different damping models used in this study. The c_I for the three damping models have relatively similar trends with period, each having a relatively flat trend with period for T >~0.1 sec and negative residuals (indicating over-prediction) at short periods. The geotechnical model exhibits the least bias for T >~0.1 sec and the largest over-prediction bias at shorter periods. The V_S-based model tends to produce the largest damping, and has bias terms 0.2-0.4 larger than the geotechnical model. The κ-informed model provides intermediate results.

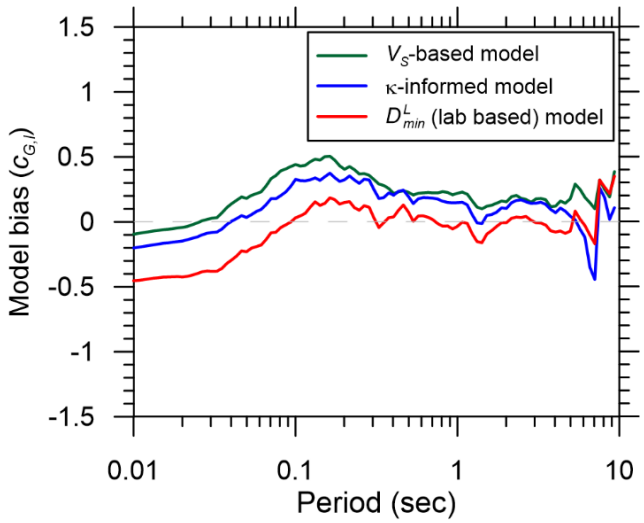

Figure 5.3. The overall bias ($c_{G,l}$) of GRA models in prediction of site response.

Figure 5.4-5.10 show the average total residuals ($c_{G,l}+\eta_{G,S,k}$) for all sites starting from the ones with lowest $R_V=V_{SDH}/V_{S5}$. The site period (T_{site}) labelled in these plots is taken from the period of the fundamental mode from GRA. In these figures, the site-specific bias can be studied for each individual site. In these plots, we looked for common features shared across multiple sites. The figures show that the bias plots have a decrease (valley) near the site period, and do not show any trend with R_V. For example, both Wildlife Liquefaction array ($R_V=1.44$) and Borrego Valley ($R_V=12.22$) have a similar behavior despite very different levels of impedance contrast. The decrease at the site period indicates over-prediction of resonance in GRA, which is a commonly observed result in prior work (e.g,, Zalachoris and Rathje, 2015).

We do not find any significant trend between the behavior of sites (in consideration of average total residuals) with the depth of the array. This is somewhat surprising, as errors in damping models would be expect to produce increasing misfit as the thickness of the modeled soil profile increases, especially at high frequencies. For example, La Cienega and Borrego Valley are the deepest arrays (depth: 245 and 235 m, respectively), however the mean residuals trend is not systematically different from those for the shallowest arrays, Benicia South and Bay Bridge (depth: 35 and 40 m, respectively). The only appreciable differences between these pairs of sites is that the dip in the mean residuals occurs (as expected) near the different site periods.

Figure 5.4-5.10 also show no significant pattern in the performance of damping models with the impedance ratio R_V. The general pattern of overprediction and underprediction with the

three damping models are similar to what is indicated in Figure 5.3. Arguably the κ-informed model has the best overall performance when both short and long periods are considered. The geotechnical model tends to produce more negative residuals at short periods, indicating model over-prediction (site attenuation is too low). The V_S-based model tends to produce positive residuals at periods shorter than the fundamental period, indicating model underprediction (site attenuation too high). These are the overall trends, and are not necessarily descriptive of features for individual sites.

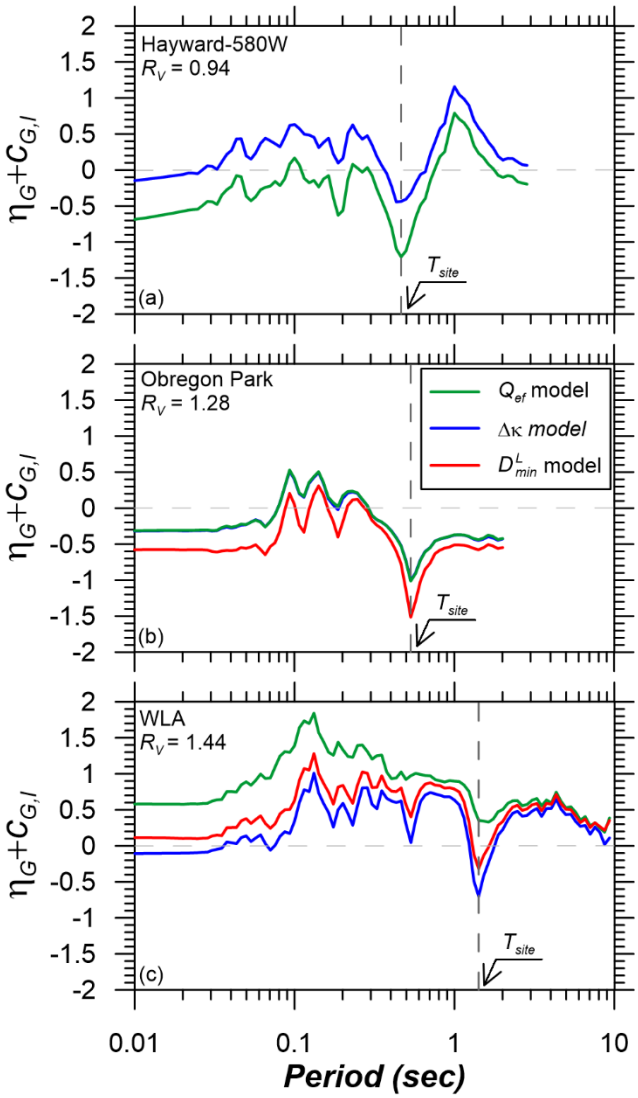

Figure 5.4. Comparison of total residuals (bias+site term) using the three models for damping for sites with different values of *Rv*: (a) Hayward-580 W, (b) Obregon Park, and (c) Wildlife Liquefaction Array (WLA).

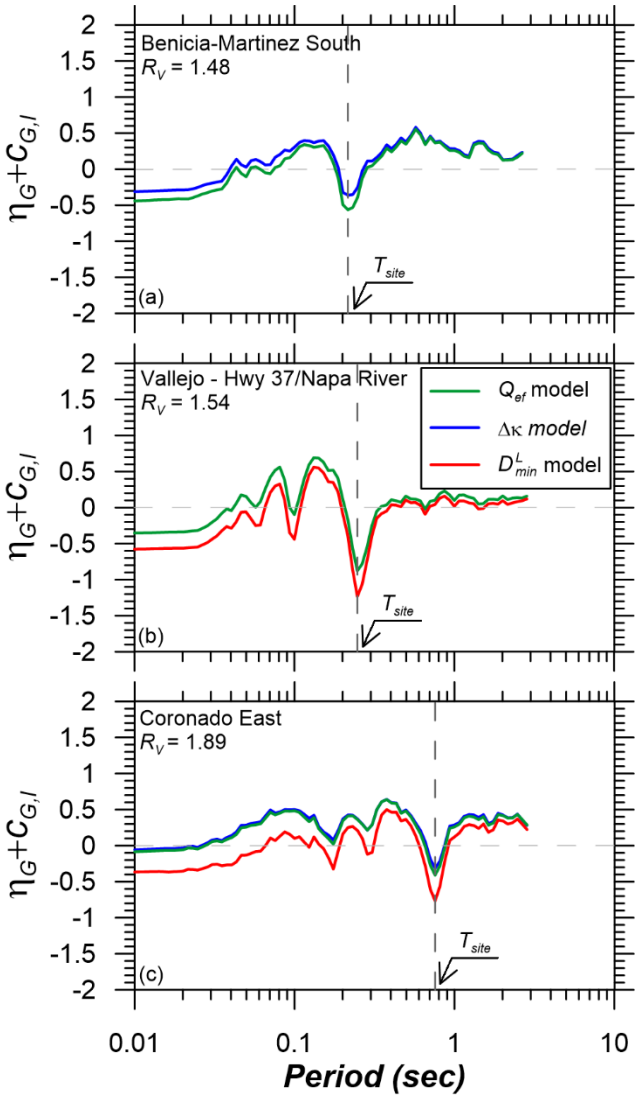

Figure 5.5. Comparison of total residuals (bias+site term) using the three models for damping for sites with different values of R_V: (a) Benicia-Martinez South, (b) Vallejo - Hwy 37/Napa River, and (c) Coronado East.

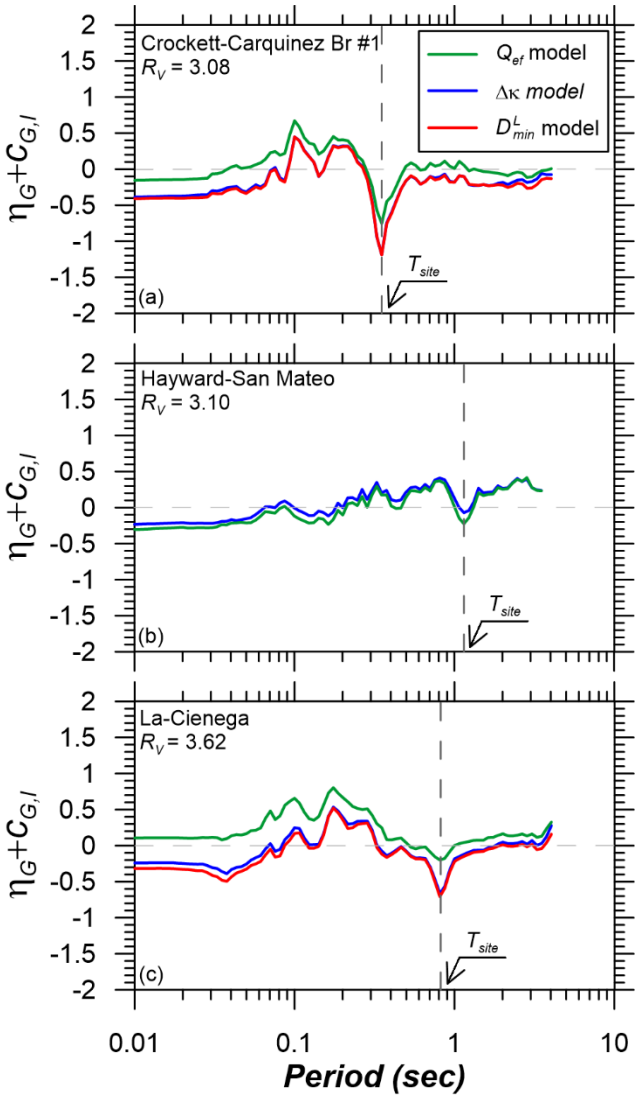

Figure 5.6. Comparison of total residuals (bias+site term) using the three models for damping for sites with different values of R_V: (a) Crockett-Carquinez Br #1, (b) Hayward-San Mateo, and (c) La-Cienega.

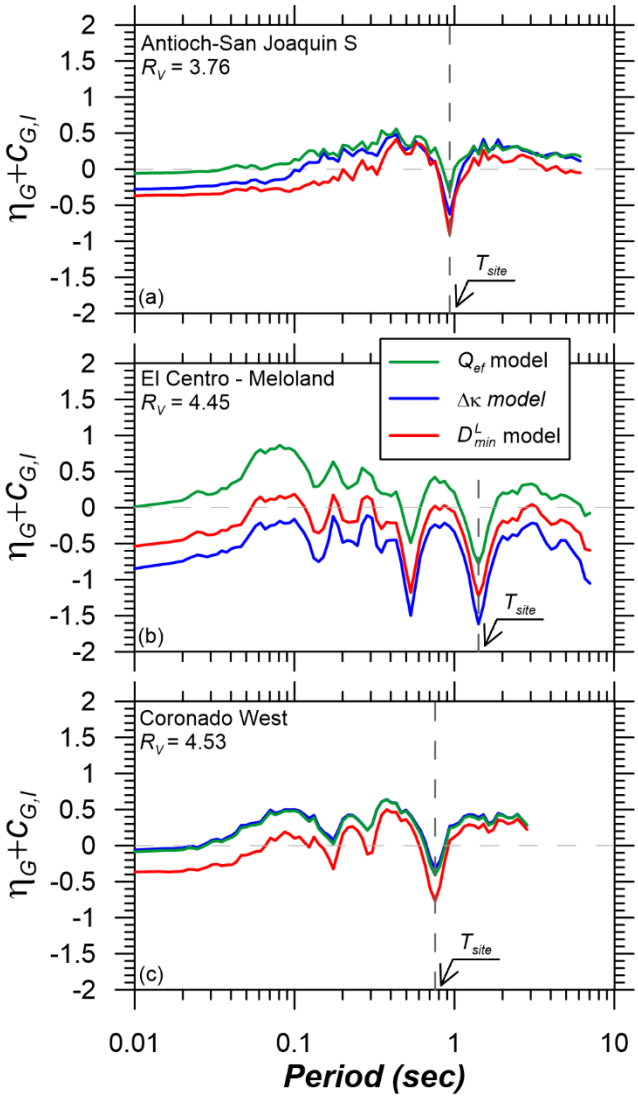

Figure 5.7. Comparison of total residuals (bias+site term) using the three models for damping for sites with different values of R_V: (a) Antioch-San Joaquin S, (b) El Centro - Meloland, and (c) Coronado West.

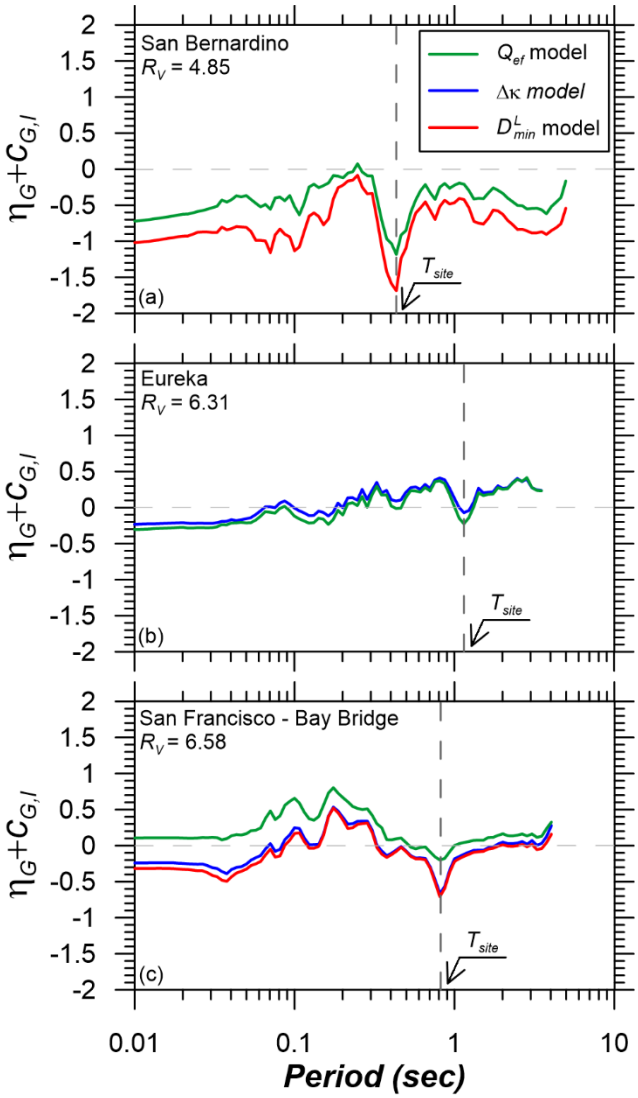

Figure 5.8. Comparison of total residuals (bias+site term) using the three models for damping for sites with different values of R_V: (a) San Bernardino, (b) Eureka, and (c) San Francisco - Bay Bridge.

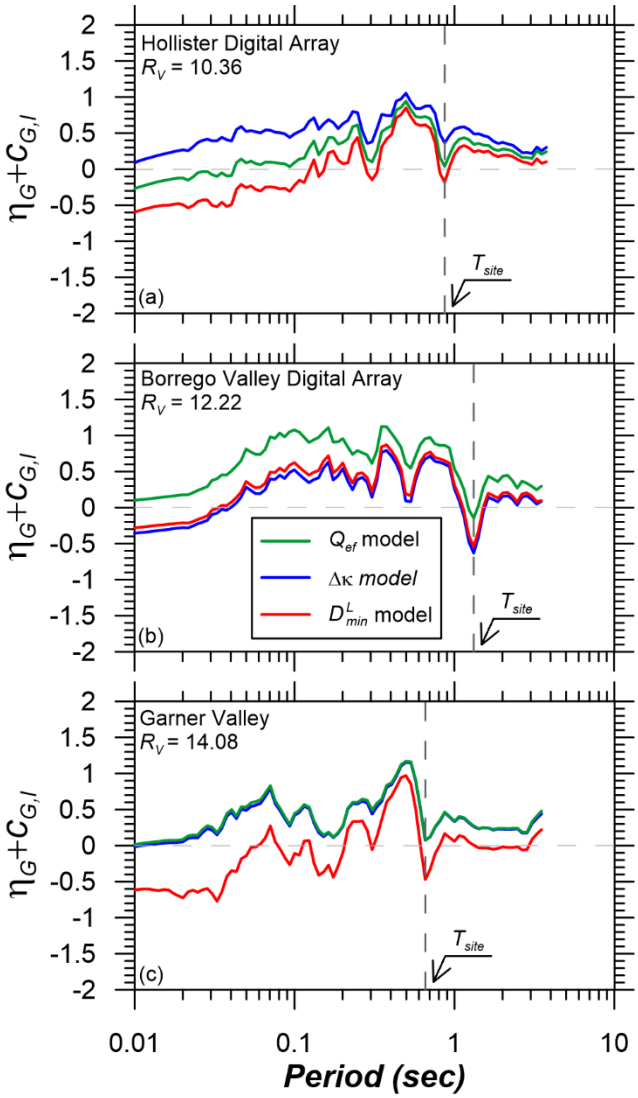

Figure 5.9. Comparison of total residuals (bias+site term) using the three models for damping for sites with different values of R_V: (a) Hollister Digital Array, (b) Borrego Valley Digital Array, and (c) Garner Valley.

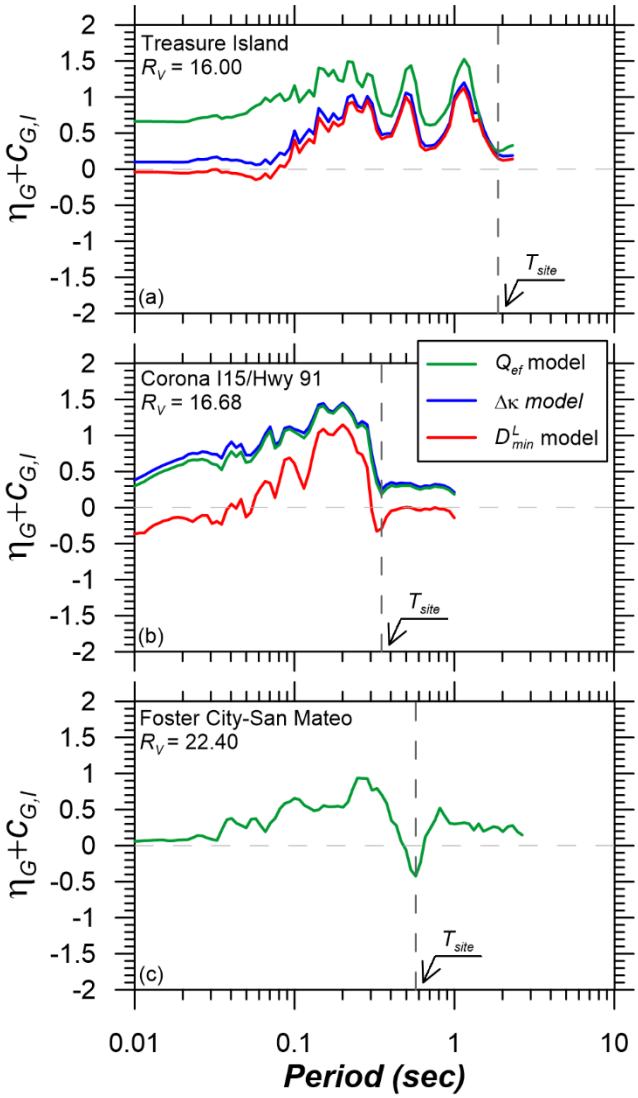

Figure 5.10. Comparison of total residuals (bias+site term) using the three models for damping for sites with different values of R_V: (a) Treasure Island, (b) Corona I15/Hwy 91, and (c) Foster City-San Mateo.

The standard deviations of the residuals are computed as follows:

$$\sigma_Y^2 = \tau_{G,S}^2 + \phi_{\mathrm{G,ln}Y}^2 \tag{5.3}$$

where σ_Y, $\tau_{G,S}$, and $\phi_{G,lnY}$ are the standard deviations of $R_{G,kj}$, $\eta_{G,S,k}$, and $\varepsilon_{G,ij}$, respectively. Our principal interest is in $\tau_{G,S}$, which represents the site-to-site variability of the misfit in the prediction of ground motion using GRA. In other words, the epistemic uncertainty about how well GRA is able to predict the effects of site response is quantified by $\tau_{G,S}$. Figure 5.11a shows the period-dependence of $\tau_{G,S}$ for the three considered damping models, with a result for Kik-net sites also shown for comparative purposes.

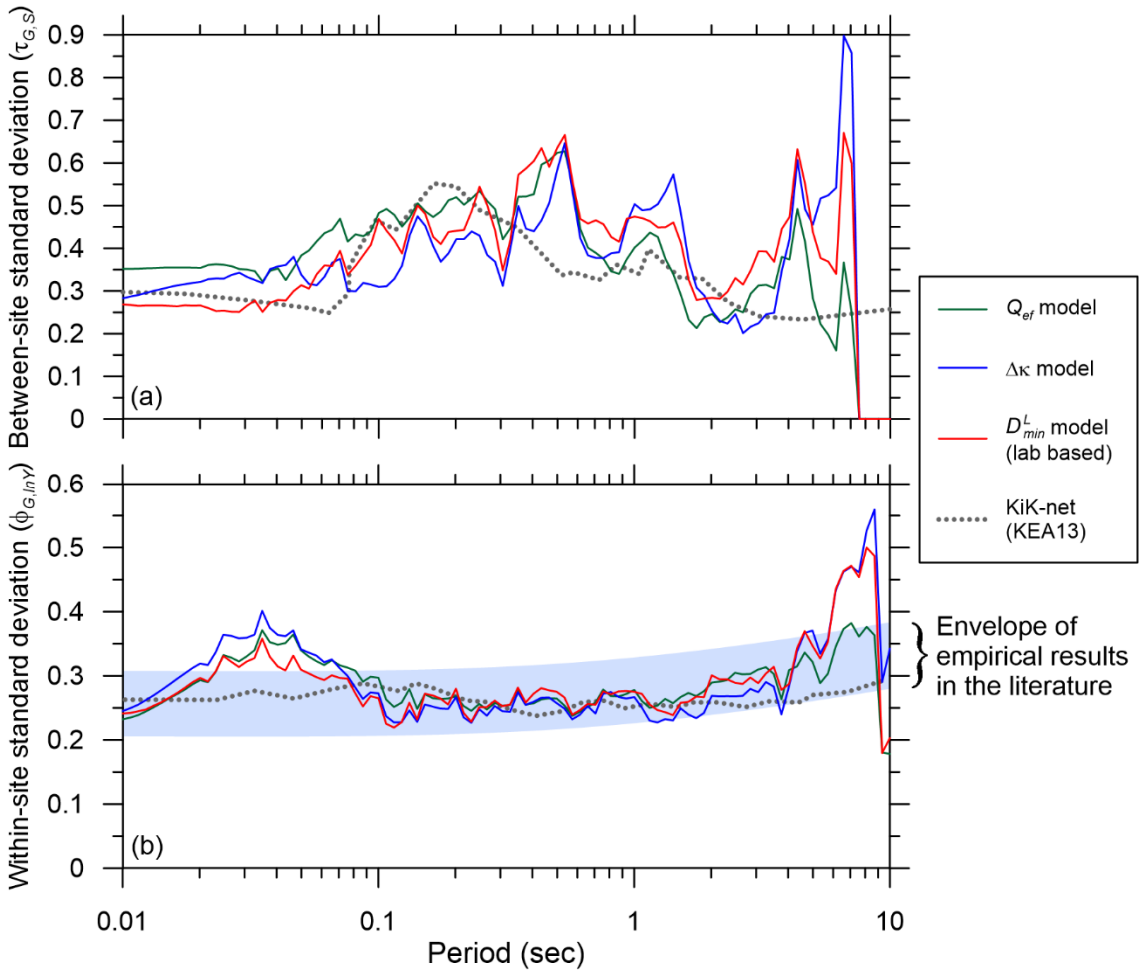

Figure 5.11. Comparison of (a) between-site standard deviation (τ_S), and (b) within-site standard deviation ($\phi_{G,lnY}$) for sites in California and KiK-net sites studied by KEA13 (Kaklamanos et al., 2013). The range of $\phi_{G,lnY}$ shown in Part (b) is presented in Stewart et al. (2017).

The mean of the site periods for the considered California sites is about 0.8 sec. At longer periods, the $\tau_{G,S}$ results have little meaning. Arguably the most important period range in Figure

5.11a is for periods shorter than 0.8 sec and longer than where saturation to PGA occurs (about 0.03-0.05 sec); this period range would be expected to be the most sensitive to changes in damping models. Within that period range, the κ-informed model generally has the smallest values of $\tau_{G,S}$, indicating a nominally greater ability to capture site-specific effects and thereby reduce site-to-site variability. However, the differences from other models are small. The comparison to results in Japan is presented in the next section. Figure 5.11b shows results for within-site variability $\phi_{G,lnY}$, which is also discussed in the next section.

5.4 COMPARISON TO PRIOR RESULTS

5.4.1 Bias

Several prior studies have investigated the potential for bias in site response estimated from GRA using laboratory-based material damping models (denoted here as D_{min}^{L}). Most of those studies, but not all, have found that the use of D_{min}^{L} underestimates site attenuation.

Tsai and Hashash (2009) used vertical array data from the Lotung, Taiwan, (soft silts) and La Cienega, California, (soft clay) arrays in a neural network based inverse analysis to extract soil properties. Based on previous work, these sites are considered to be reasonably well represented by 1D models. Their inverse analyses were not constrained by model-based assumptions of soil behavior. Shear-wave velocity models were slightly adjusted from data in the "learning" process and stress-strain loops were extracted. Modulus reduction and damping curves were then computed from the loops, which demonstrate stronger nonlinearity than laboratory-based curves (i.e., lower modulus reduction and higher damping). The observation of higher damping is in agreement with system identification results obtained from Lotung data by Elgamal et al. (2001). Yee et al. (2013) analyzed vertical array data from the Kashiwazaki, Japan, Service Hall Array site (stiff deep soil) under relatively weak and strong shaking conditions. The weak motion data showed that D_{min}^{L} should be increased by 2-5% for GRA results to adequately capture observations. In summary, various studies of three individual sites (Lotung, La Cienega, Service Hall Array) support the need for greater site attenuation than is provided by material damping models to capture observed behavior. The discrepancy is likely caused by wave scattering effects that are not included in D_{min}^{L} models.

Kaklamanos and Bradley (2016) used recordings from two KiK-net sites, and observed positive (under-prediction) bias in linear GRA with damping set from laboratory-based models (D_{min}^{L}). In order to improve the results, they used a depth-dependent gradient for the V_S profile for eliminating unrealistically large steps in the V_S profiles, and decreased D_{min}^{L} by 50%. This reduction of geotechnical model damping to achieve fit to data is contrary to observations from Tsai and Hashash (2009), Elgamal et al. (2001), and Yee et al. (2013).

Because all of these studies are based on analyzing only one or two sites, and there is a significant degree of site-to-site variability, it is not surprising that there is not a clear consensus on the issue of how to adjust D_{min}^{L} in the available literature. By considering multiple sites in the present work, we anticipate the findings from California vertical arrays will be valuable.

5.4.2 Variability

We compare our results for $\tau_{G,S}$ and $\phi_{G,lnY}$ with prior studies in the literature in Figure 5.11a and 5.11b, respectively. The only applicable study of which we are aware is Kaklamanos et al. (2013), who used the same KiK-net sites used by Thompson et al. (2012). Similar to Thompson et al. (2012), Kaklamanos et al. (2013) optimize damping for each site and recording, which improves fit to data relative to the application of damping models as in the present application.

The values of $\tau_{G,S}$ shown in Figure 5.11a indicate levels of variability in California comparable to KiK-net sites. Although we observe little regional dependence in dispersion of residuals when using *PSA* amplifications, we recognize the potential for countering trends: (1) the KiK-net site-to-site dispersion is likely reduced by the damping optimization, at least for high frequencies, and (2) the KiK-net dispersion would otherwise be expected to be higher than in California due to the relatively poor fit of 1D models to the observations.

In Figure 5.11b, the within-site dispersion ($\phi_{G,lnY}$) plot from California is slightly higher than $\phi_{G,lnY}$ for KiK-net sites, but interestingly, the California results fit inside the approximate range for ϕ_{lnY} recommended by Stewart et al. (2017). Taken as a whole, the global results for within-site dispersion have a flat trend with period, and are remarkably consistent despite having been developed using different data sets and different methods of analysis.

6 Conclusion and Recommendations

In this study, we prepared a database of recordings from vertical array sites in California in order to (1) study the performance of 1D GRA in predicting site response effects between the downhole and surface instruments, (2) assess the relative performance of different models for small strain material damping, including one derived from site-specific attributes (κ-informed model), and (3) quantify the epistemic uncertainty associated with site response estimates derived from GRA for low to modest strain levels.

The performance of the 1D assumption was studied by computing theoretical and empirical transfer functions, and a goodness of fit parameter (r) was used as an indicator of how well the shapes of theoretical and empirical site response transfer functions match. The shape of the transfer functions are mainly controlled by the positions of peaks, and a good match (r>0.6) indicates the 1D model is able to predict the frequencies of different resonance modes. We also quantified the dispersion in empirical transfer functions with the assumption of a log-normal distribution for the transfer function. The goodness of fit parameter (r) and the median standard deviation (σ_{ln}) of the transfer functions from California vertical array sites were compared to the similar results from Thompson et al. (2012) study on KiK-net sites. We observed a better goodness of fit and less dispersion for California sites, which indicates better predictability of site response transfer functions using GRA procedures. Moreover, we find that the site-specific damping estimate (κ-informed) provides improved fits to data relative to two alternatives (a geotechnical material damping model and a model for quality factor Q derived from seismological inversion) when the data set as a whole is considered. These improved fits are quantified as, on average, higher values of r and lower values of σ_{ln}.

These results on the suitability of GRA are encouraging, but there are caveats related to limitations of the dataset. A goodness of fit for a vertical array that is judged as suitable by some criteria does not necessarily indicate that GRA will accurately predict the surface ground motion at the site. The suitability of vertical arrays for validation of GRA is limited by their depth if the array does not go deep enough to reach a stiff bedrock representing "reference" conditions. For example, the high value of the goodness of fit parameter ($\overline{r}$) for the WLA site (Figure 4.13) is an indicator of good performance of 1D GRA for predicting site response between the surface and the downhole sensor, which is 100 m deep. However, the site is located in a large basin which is several kilometers deep, and the downhole sensor is located in a soil layer with V_S=257 m/s. In this case, the effects of the deep basin on surface waves and the amplification of long period ground motions are expected, but the amplification would affect the motions both at the surface and the downhole, therefore the amplification of long periods cannot be observed using the recordings from the vertical array. As a result, GRA can be effective for site response between surface and downhole, but it may or may not be effective for site response between the deep bedrock and the surface. Therefore, caution needs to be exercised when using GRA for deep basin sites, which is discussed further in Stewart et al. (2017).

Another example of a deep basin site (La Cienega) is shown in Figure 6.1. In this case, the seismic velocity measurements are compared to an estimated profile from SCEC Community velocity model version 4 (Magistrale et al., 2000; Small et al., 2017). The SCEC model extends to greater depth and reaches more competent materials that are located far below the downhole sensor (note that in Figure 6.1 depth is shown on a logarithmic axis). As such, we do not expect the vertical array to capture the global site response modal frequencies.

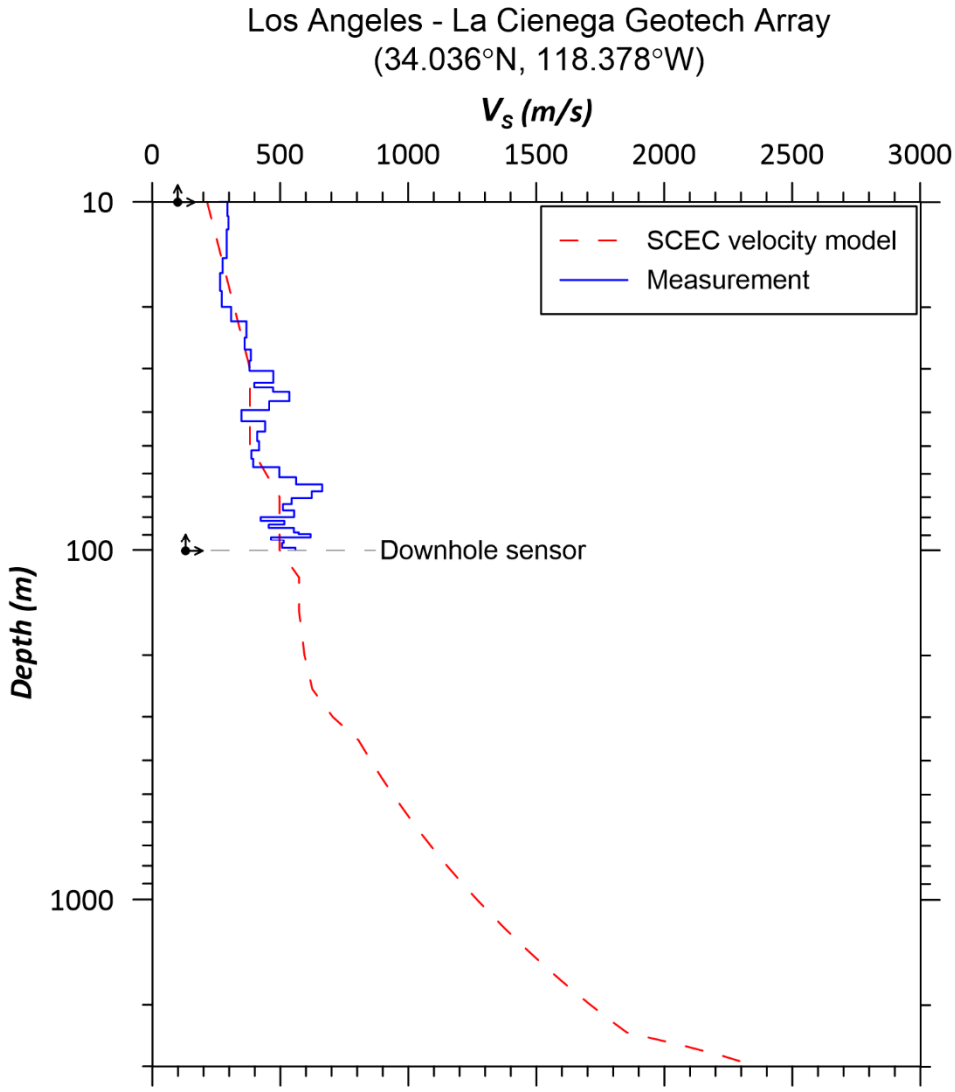

Figure 6.1. Shear wave velocity measurements for La Cienega site and comparison to the prediction by SCEC velocity model (Magistrale et al., 2000; Small et al., 2017)

We also quantified the bias and dispersion of GRA predictions of *PSA* amplifications. We consider bias to evaluate the effectiveness of the three damping models. For most of the period range (T >~0.1 sec) the lab-based damping provides an unbiased estimate of site response, and the V_S-based model is unbiased for very short periods (T <~0.02 sec). The bias from the κ-informed model falls between the others and arguably provides the best overall result. The improved fit of the κ-informed model could be anticipated, because it incorporates attributes of on-site recordings, whereas the laboratory-based and V_S-based models do not. As a result, the κ-informed model is site-specific, leading to reduced values of site-to-site variability ($\eta_{G,S}$), reflecting lowered

epistemic uncertainty. This indicates a potential predictive power of κ for estimating effective small strain damping, D_{eff}, in GRA.

We compared the between-site and within site standard deviations of *PSA* amplification residuals for California sites to the results from KiK-net sites in Japan (Kaklamanos et al., 2013). We also compare within site standard deviations to a previously identified empirical range. Comparing Japan and California, we find no significant regional dependence of dispersion for *PSA* amplification.

References

Afshari, K. and Stewart, J. P., 2015a. Effectiveness of 1D ground response analyses at predicting site response at California vertical array sites, *Proc. SMIP2015 Seminar on Utilization of Strong Motion Data*, California Strong Motion Instrumentation Program, Sacramento, CA.

Afshari, K. and Stewart, J. P., 2015b. Uncertainty of site amplification derived from ground response analysis, *Proc. 6th Int. Conf. Earthquake Geotech. Eng.*, Christchurch, New Zealand, Paper No. 227.

Amir-Faryar, B., Aggour, M. S., and McCuen, R. S., 2016. Universal model forms for predicting the shear modulus and material damping of soils. *Geomechanics and Geoengineering*. 1-12. 10.1080/17486025.2016.1162332.

Ancheta, T. D., Darragh, R. B., Stewart, J. P., Seyhan, E., Silva, W. J., Chiou, B. S.-J., Wooddell, K. E., Kottke, A. R., Boore, D. M., Kishida, T., and Donahue, J. L., 2014. NGA-West2 database, *Earthquake Spectra*, **30**, 989–1005.

Anderson, J. G., 1991. A preliminary descriptive model for the distance dependence of the spectral decay parameter in Southern California, *Bull. Seismol. Soc. Am*., **81**, 1969-1993.

Anderson, J. G., and Hough, S. E., 1984. A model for the shape of the Fourier amplitude spectrum of acceleration at high frequencies, *Bull. Seismol. Soc. Am*., **74**, 1969-1993.

Aoi, S. ,Obara, K., Hori, S., Kasahara, K., Okada, Y., 2000. New Japanese uphole–downhole strong-motion observation network: KiK-Net, Seismological Research Letters *Seism. Res. Lett.*, **72**, p 239.

Boore, D.M., 2003. Simulation of ground motion using the stochastic method, *Pure and Applied Geophysics*, **160**, 635-675.

Boore, D. M., 2005. SMSIM—Fortran programs for simulating ground motions from earthquakes: Version 2.3—A Revision of OFR 96- 80-A, *Open-File Rpt. 00-509*, U.S. Geological Survey, revised 15 August 2005, 55 pp.

Boore, D.M., 2008. Some thoughts on relating density to velocity <http://quake.wr.usgs.gov/boore/daves_notes/daves_notes_on_relating_density_to_velocity_v1.2.pdf>

Boore, D. M., 2010. Orientation-independent, nongeometric-mean measures of seismic intensity from two horizontal components of motion, *Bull. Seismol. Soc. Am*., **100**, 1830–1835.

Boore, D. M., 2013. The uses and limitations of the square-root-impedance method for computing site amplication. *Bull. Seismol. Soc. Am*., **103**, 2356-2368.

Boore, D. M. and Bommer, J. J., 2005. Processing of strong-motion accelerograms: needs, options and consequences, *Soil Dyn. Eqk. Eng.*, **25**, 93–115.

Boore, D. M., and W. B. Joyner, 1991. Estimation of ground motion at deep-soil sites in eastern North America, *Bull. Seismol. Soc. Am.*, **81**, 2167–2185.

Boore, D. M., Stewart, J. P., Seyhan, E., and Atkinson, G. M, 2014. NGA-West 2 equations for predicting PGA, PGV, and 5%-damped PSA for shallow crustal earthquakes, *Earthquake Spectra*, **30**, 1057–1085.

Boore, D. M., Stewart, J. P., Seyhan, E., and Atkinson, G. M., 2013. *NGA-West2 Equations for Predicting Response Spectral Accelerations for Shallow Crustal Earthquakes*, PEER Report No. 2013/05, Pacific Earthquake Engineering Research Center, UC Berkeley, CA.

Bommer, J. J. and Scherbaum, F., 2008. The use and misuse of logic trees in probabilistic seismic hazard analysis. *Earthquake Spectra*, **24**, 997–1009.

Bommer, J. J., Scherbaum, F., Bungum, H., Cotton, F., Sabetta, F., and Abrahamson, N. A., 2005. On the use of logic trees for ground-motion prediction equations in seismic hazard analysis, *Bull. Seismol. Soc. Am.*, **95**, 377–389.

Borja, R. I., Chao, H.-Y., Montans, F. J., and Lin, C.-H., 1999. Nonlinear ground response at Lotung LSST site, *J. Geotech. Geoenviron. Eng.*, **125**, 187–197.

Cabas, A., and Rodriguez-Marek, a., 2017. What can we learn from kappa (κ) to achieve a better characterization of damping in geotechnical site response models?, *Geotechnical Frontiers 2017*, March 12–15, 2017, Orlando, Florida

Campbell, K.W., 2009. Estimates of shear-wave Q and κ_0 for unconsolidated and semiconsolidated sediments in Eastern North America, *Bull. Seismol. Soc. Am*., **99**, 2365-2392.

Chavez-Garcia, F. J., Raptakis, D., Makra, K., Pitilakis, K., 2000. Site effects at Euroseistest—II. Results from 2D numerical modeling and comparison with observations, *Soil Dyn & Earthquake Eng,* **19**, 23–39.

Cramer, C. H., Gomberg, J. S., Schweig, J. S., Waldron, B. A., and Tucker, K., 2004. The Memphis, Shelby Country, Tennessee, seismic hazard maps, *U.S. Geol. Surv.* Open-File Rept. 04-1294.

Darendeli, M. B., 2001. Development of a New Family of Normalized modulus reduction and material damping curves, PhD Thesis, Department of Civil Engineering, University of Texas, Austin, TX.

Dawood, H., Rodriguez-Marek, A., Bayless, J., and Thompson, E. M., 2016. A Flatfile for the KiK-net Database Processed Using an Automated Protocol, *Earthquake Spectra*, **32**, 1281-1302.

Elgamal, A., Lai, T., Yang, Z., He, L., 2001. Dynamic soil properties, seismic downhole arrays and applications in practice, *Proceedings, 4th International Conference on Recent Advances in Geotechnical Earthquake Engineering and Soil Dynamics*, S. Prakash, ed., San Diego, CA.

Gomberg, J., Waldron, B., Schweig, E., Hwang, H., Webbers, A., Van Arsdale, R., Tucker, K., Williams, R., Street, R., Mayne, P., Stephenson, W., Odum, J., Cramer, C., Updike, R., Hutson, S., and Bradley, M., 2003. Lithology and shear-wave velocity in Memphis, Tennessee, *Bull. Seismol. Soc. Am*., **93**, 986–997.

Hancock, J., and Bommer, J. J., 2007. Using spectral matched records to explore the influence of strong-motion duration on inelastic structural response, *Soil Dyn. Earthquake Eng.* **27**, 291–299.

Hashash, Y. M. A., Musgrove, M. I., Harmon, J. A., Groholski, D. R., Phillips, C. A., and Park, D., 2016. DEEPSOIL 6.1, User Manual.

Haskell, N.A., 1953. The dispersion of surface waves on multilayered media. *Bull. Seismol. Soc. Am*., **72**, 17–34.

Kaklamanos, J., Bradley, B. A., Thompson, E. M., and Baise, L. G., 2013. Critical parameters affecting bias and variability in site-response analyses using KiK-net downhole array data, *Bull. Seismol. Soc. Am*., **103**, 1733–1749.

Kaklamanos, J., Baise, L. G., Thompson, E. M., and Dorfmann, L., 2014. Comparison of 1D linear, equivalent-linear, and nonlinear site response models at six KiK-net validation sites, *Soil Dyn. Eqk. Eng.*, **69**, 435–460.

Kaklamanos, J., Baise, L. G., Thompson, E. M., Dorfmann, L., 2015. Comparison of 1D linear, equivalent-linear, and nonlinear site response models at six KiK-net validation sites, *Soil Dyn. Earthq. Eng.*, **69**, 207-215.

Kaklamanos, J., Bradley, B. A., Thompson, E. M., and Baise, L. G., 2013. Critical parameters affecting bias and variability in site-response analyses using KiK-net downhole array data, *Bull. Seismol. Soc. Am*., **103**, 1733–1749.

Kim, B., and Hashash, Y. M. A., 2013. Site response analysis using downhole array recordings during the March 2011 Tohoku-Oki Earthquake and the effect of long-duration ground motions." *Earthquake Spectra*, **29**, S37–S54.

Kim, B., Hashash, Y. M. A., Stewart, J. P., Rathje, E. M., Harmon, J. A., Musgrove, M. I., Campbell, K. W, and Silva, W. J., 2015. Relative differences between nonlinear and equivalent-linear 1D site response analyses, *Earthquake Spectra*, **32**, 1845-1865.

Ktenidou, O-J., Cotton, F., Abrahamson, N. A., and Anderson, J. G., 2014. Taxonomy of κ: A review of definitions and estimation approaches targeted to applications. *Seismological Research Letters*, **85**, 135-146.

Kottke, A. R., and Rathje, E. M., 2009. Technical Manual for Strata, *PEER Report No. 2008/10*, Pacific Earthquake Engineering Research Center, UC Berkeley, CA.

Kwok, A. O. L., Stewart, J. P., Hashash, Y. M. A, 2008. Nonlinear ground-response analysis of Turkey Flat shallow stiff-soil site to strong ground motion, *Bull. Seismol. Soc. Am.*, **98**, 331–343.

Lee, C.-P., Tsai, Y.-B., and Wen, K. L., 2006. Analysis of nonlinear site response using the LSST downhole accelerometer array data, *Soil Dyn. Eqk. Eng.*, **26**, 435–460.

Li X.-S., Wang Z.-L., Shen C-.K. (1992). *SUMDES: A Nonlinear Procedure for Response Analysis of Horizontally-Layered Sites Subjected to Multi-Directional Earthquake Loading*, Department of Civil Engineering, University of California, Davis, CA.

Matasovic, N., 2006. *D-MOD_2: A Computer Program for Seismic Response Analysis of Horizontally Layered Soil Deposits, Earthfill Dams, and Solid Waste Landfills, User's Manual*, GeoMotions, LLC, Lacey, Washington.

McGuire, R. K., Silva, W. J., and Costantino, C. J., 2001. Technical basis for revision of regulatory guidance on design ground motions: Hazard-and risk-consistent ground motion spectra guidelines. *NUREG/CR-6728*, United States NRC.

McKenna F., Fenves G. L., 2001. *The OpenSees Command Language Manual, Version 1.2*., Pacific Earthquake Engineering Research Center, University of California, Berkeley, CA.

Menq, F. Y., 2003. Dynamic Properties of Sandy and Gravelly Soils, PhD Thesis, Department of Civil Engineering, University of Texas, Austin, TX.

Mikami, M., Stewart, J. P., Kamiyama, M., 2008. Effects of time series analysis protocols on transfer functions calculated from earthquake accelerograms, *Soil Dyn. Earthquake Eng*., **28**, 695-706.

NCHRP, 2012. *Practices and Procedures for Site-Specific Evaluations of Earthquake Ground Motions, Synthesis 428* (N Matasovic and YMA Hashash), National Cooperative Highway Research Program, Transportation Research Board, Washington D.C.

Olsen, K., Day, S., Bradley, C., 2003. Estimation of Q for long-period (> 2 sec) waves in the Los Angeles basin. *Bull. Seismol. Soc. Am.*, **93**, 627–638.

Pinheiro, H., Bates, D., DebRoy, S., Sarkar, D., and the R Development Core Team, 2013. NLME: Linear and Nonlinear Mixed Effects Models, R package version 3.1-108.

Pousse, G., 2005. Analyse des données accélérométriques de K-net et KiK-net implicationspour la prédiction du mouvement sismique'accélérogrammes et spectres de réponse'et laprise en compte des effets de site non linéaires, Ph.D. Thesis, Université Joseph Fourier,France.

Raptakis, D., Chavez-Garcia, F. J., Makra, K., Pitilakis, K., 2000. Site effects at Euroseistest—I. Determination of the valley structure and confrontation of observations with 1D analysis, *Soil Dyn & Earthquake Eng,* **19**, 1–22.

Rodriguez-Castellanos, A, FJ Sánchez-Sesma, F Luzon, R Martin, 2006. Multiple scattering of elastic waves by subsurface fractures and cavities, *Bull. Seismol. Soc. Am.*, **96**, 1359-1374

Small, P., Gill, D., Maechling, P. J., Taborda, R., Callaghan, S., Jordan, T. H., Ely, G. P., Olsen, K. B., and Goulet, C. A., 2017. The SCEC Unified Community Velocity Model Software Framework. *Seismological Research Letters*. **88**, 1469–1478.

Stafford, P. J, 2012 Evaluation of structural performance in the immediate aftermath of an earthquake: a case study of the 2011 Christchurch earthquake, *Int. J. Forensic Engineering*, **1**, 58–77.

Stafford, P. J., Mendis R., and Bommer, J. J., 2008. The dependence of spectral damping ratios on duration and number of cycles. *J. Structural Eng.* **134**, 1364–1373.

Stafford, P. J., 2012. Evaluation of structural performance in the immediate aftermath of an earthquake: A case study of the 2011 Christchurch earthquake, *Int. J. Forensic Engrg.*, **1**, 58-77.

Star, L. M., Stewart, J. P., and Graves, R. W., 2011. Comparison of ground motions from hybrid simulations to NGA prediction equations, *Earthquake Spectra*, **27,** 331–350.

Stewart, J.P., Afshari, K., and Hashash, Y. M. A., 2014. Guidelines for performing hazard-consistent one-dimensional ground response analysis for ground motion prediction, *PEER Report No. 2014/16*, Pacific Earthquake Engineering Research Center, UC Berkeley, CA.

Stewart, J.P., Afshari, K., and Goulet, C. A., 2017. Non-ergodic site response in seismic hazard analysis, *Earthquake Spectra***, 33**, 1385-1414.

Thompson, E. M., Baise, L. G., Tanaka, Y., and Kayen, R. E., 2012. A taxonomy of site response complexity, *Soil Dyn. Earthq. Eng.*, **41**, 32–43.

Thomson, W. T., 1950. Transmission of elastic waves through a stratified solid, Journal of Applied Physics, **21**, 89–93.

Tsai, C. C. and Hashash, Y. M. A., 2009. Learning of dynamic soil behavior from downhole arrays, *J. Geotech. Geoenv. Eng.*, **135**, 745–757.

Van Houtte, C., Drouet, S., Cotton, F., 2011. Analysis of the origins of κ (kappa) to compute hard rock to rock adjustment factors for GMMs, *Bull. Seismol. Soc. Am.*, **101**, 2926-2941.

Xu, B., E.M. Rathje, Y. Hashash, J.P. Stewart, K.W. Campbell, W.J. Silva, 201x, κ_0 for soil sites: Observations from Kik-net sites and their use in constraining small-strain damping profiles for site response analysis, in preparation for submission to *Earthquake Spectra*.

Yee, E., Stewart, J. P., and Tokimatsu, K., 2013. Elastic and large-strain nonlinear seismic site response from analysis of vertical array recordings, *J. Geotech. Geoenv. Eng.*, **139**, 1789–1801.

Youngs, R. R., 2004. Software validation report for SHAKE04, Geomatrix Consultants, Oakland, CA.

Zalachoris, G., and Rathje E. M., 2015. Evaluation of one-dimensional site response techniques using borehole arrays, *J. Geotech. Geoenviron. Eng.*, **141**, 04015053.

7 Appendix: Output Plots of Site Response at Vertical Arrays

In this appendix, the results of site response transfer function and *PSA* amplification for all 21 vertical array sites using the three damping models are shown. The figures show the empirical and theoretical transfer functions, empirical and theoretical *PSA* amplifications as well as their standard deviations. The amplification residuals are also shown. The following figures are the output of a program in MATLAB which was developed as a part of this research.

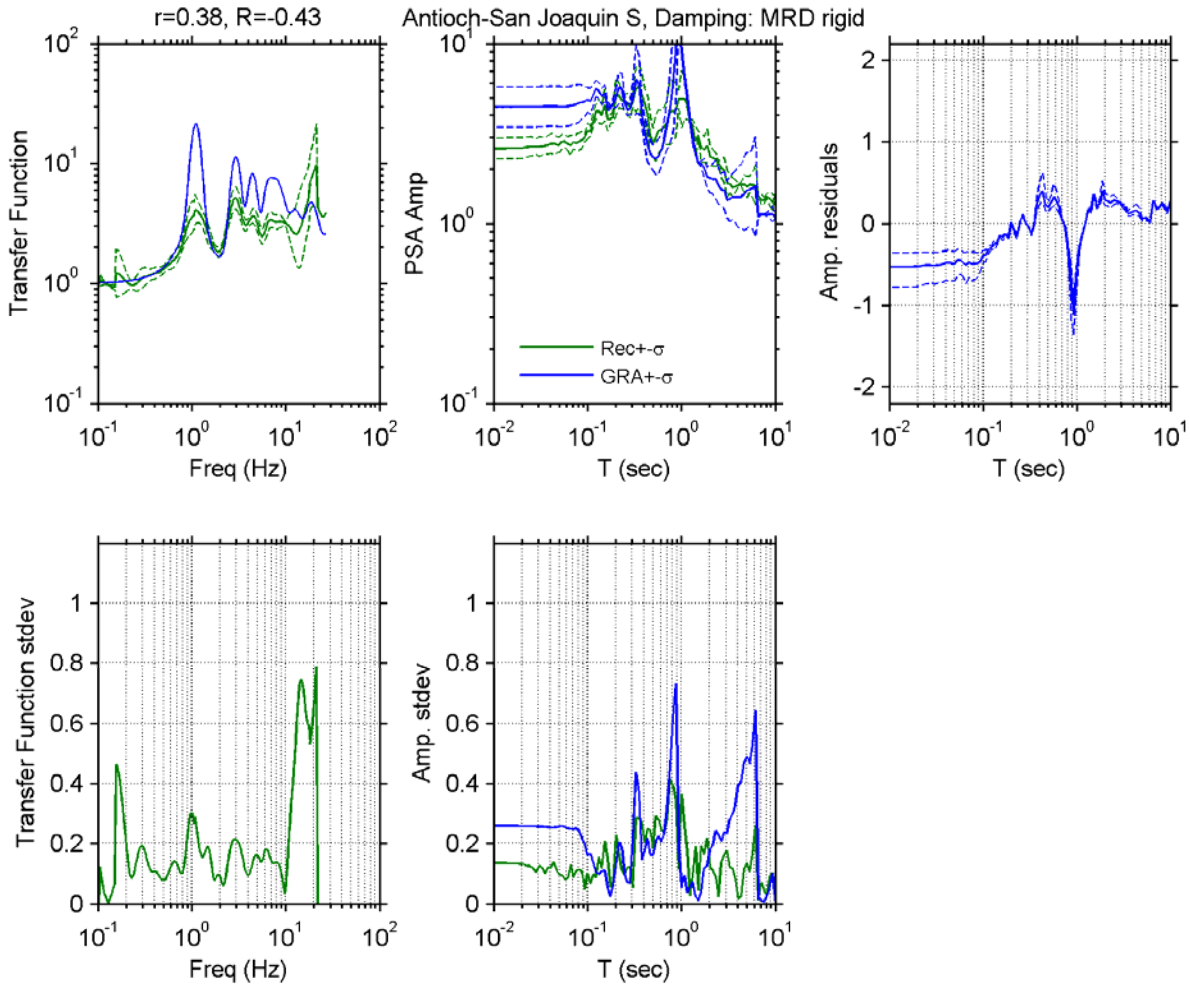

Figure A 1. Observed and simulated site response for Antioch-San Joaquin S site with $D^{L}_{\min}$ model for damping; Top left: Theoretical and median ± standard deviation of empirical transfer functions, Top middle: observed and predicted median ± standard deviation of *PS*A amplification, Top right: median ± standard deviation of *PS*A amplification residuals, Bottom left: standard deviation of empirical transfer functions, Bottom middle: standard deviation of observed and predicted *PS*A amplification residuals.

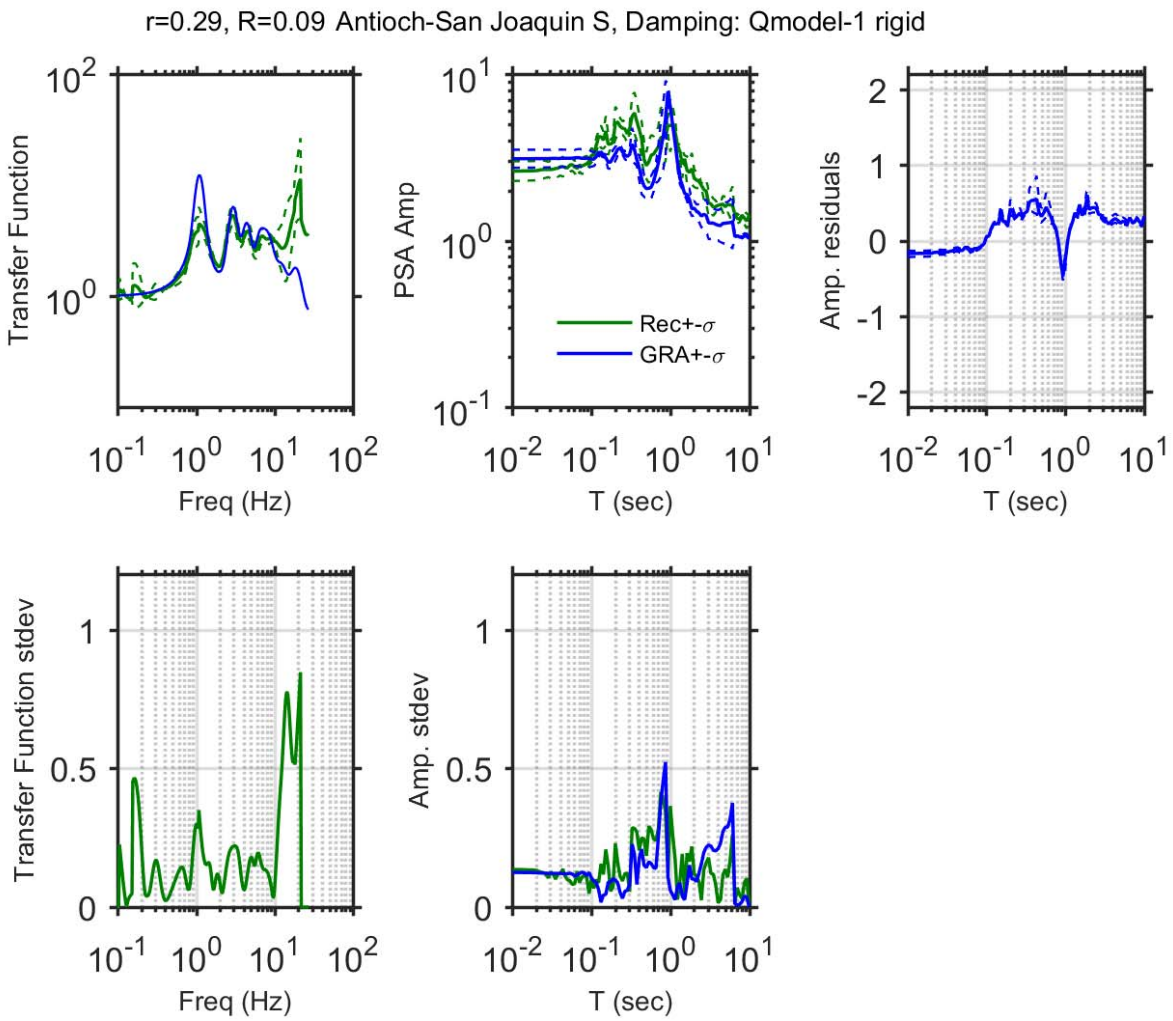

Figure A 2. Observed and simulated site response for Antioch-San Joaquin S site with V_S-based model for damping; Top left: Theoretical and median ± standard deviation of empirical transfer functions, Top middle: observed and predicted median ± standard deviation of *PS*A amplification, Top right: median ± standard deviation of *PS*A amplification residuals, Bottom left: standard deviation of empirical transfer functions, Bottom middle: standard deviation of observed and predicted *PS*A amplification residuals.

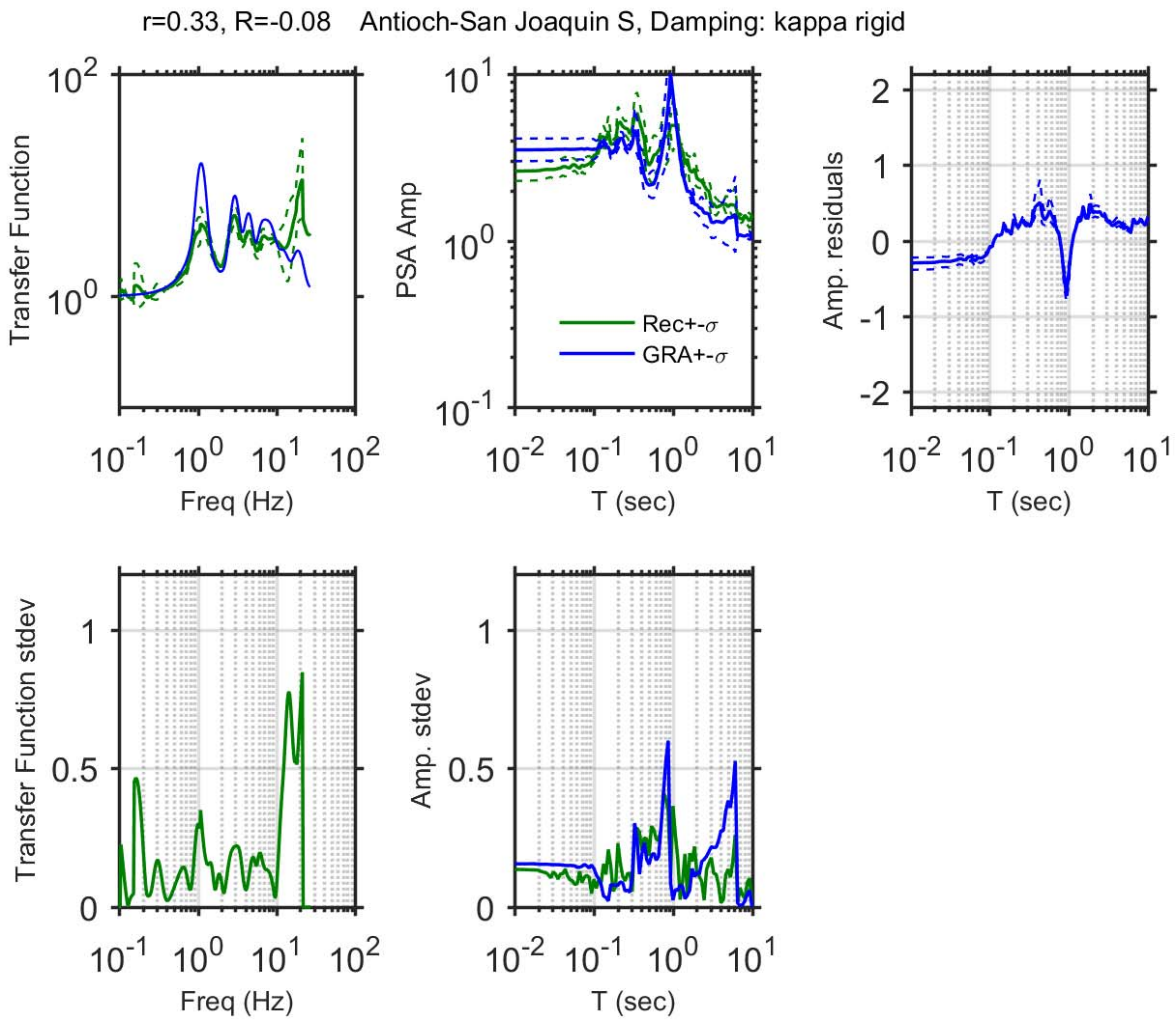

Figure A 3. Observed and simulated site response for Antioch-San Joaquin S site with κ-informed model for damping; Top left: Theoretical and median ± standard deviation of empirical transfer functions, Top middle: observed and predicted median ± standard deviation of *PS*A amplification, Top right: median ± standard deviation of *PS*A amplification residuals, Bottom left: standard deviation of empirical transfer functions, Bottom middle: standard deviation of observed and predicted *PS*A amplification residuals.

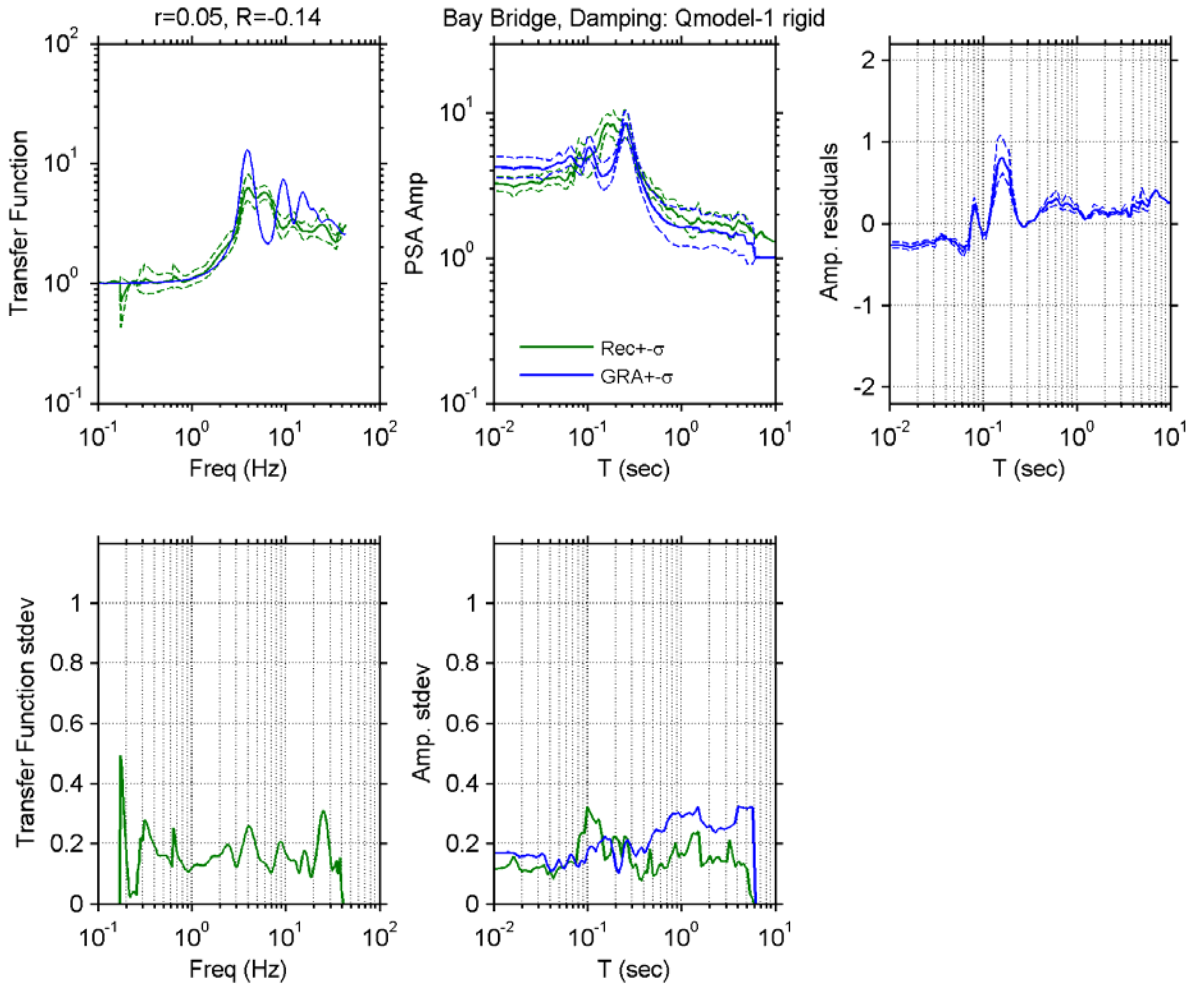

Figure A 4. Observed and simulated site response for San Francisco Bay Bridge site with V_S-based model for damping; Top left: Theoretical and median ± standard deviation of empirical transfer functions, Top middle: observed and predicted median ± standard deviation of *PS*A amplification, Top right: median ± standard deviation of *PS*A amplification residuals, Bottom left: standard deviation of empirical transfer functions, Bottom middle: standard deviation of observed and predicted *PS*A amplification residuals.

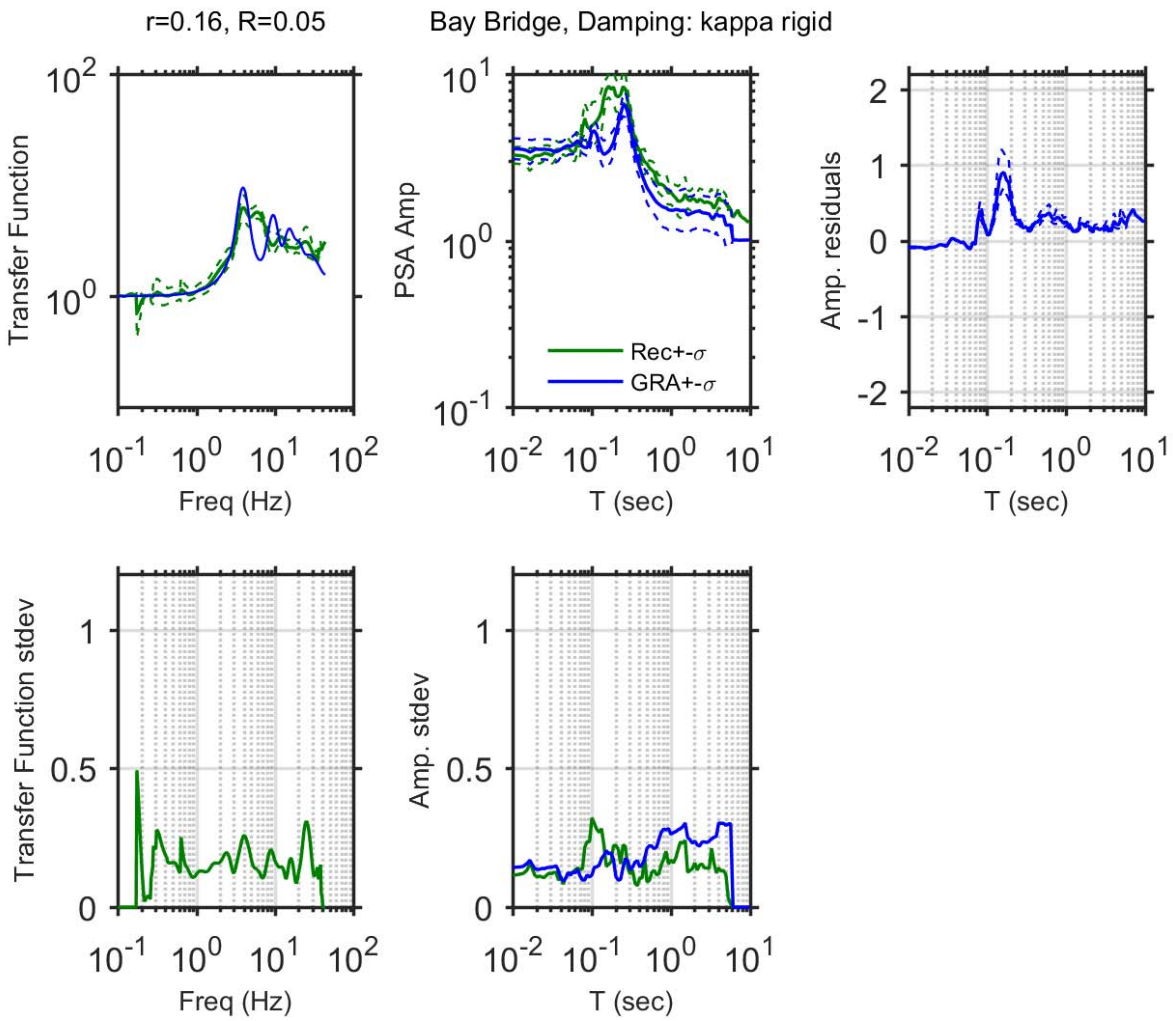

Figure A 5. Observed and simulated site response for San Francisco Bay Bridge site with κ-informed model for damping; Top left: Theoretical and median ± standard deviation of empirical transfer functions, Top middle: observed and predicted median ± standard deviation of *PS*A amplification, Top right: median ± standard deviation of *PS*A amplification residuals, Bottom left: standard deviation of empirical transfer functions, Bottom middle: standard deviation of observed and predicted *PS*A amplification residuals.

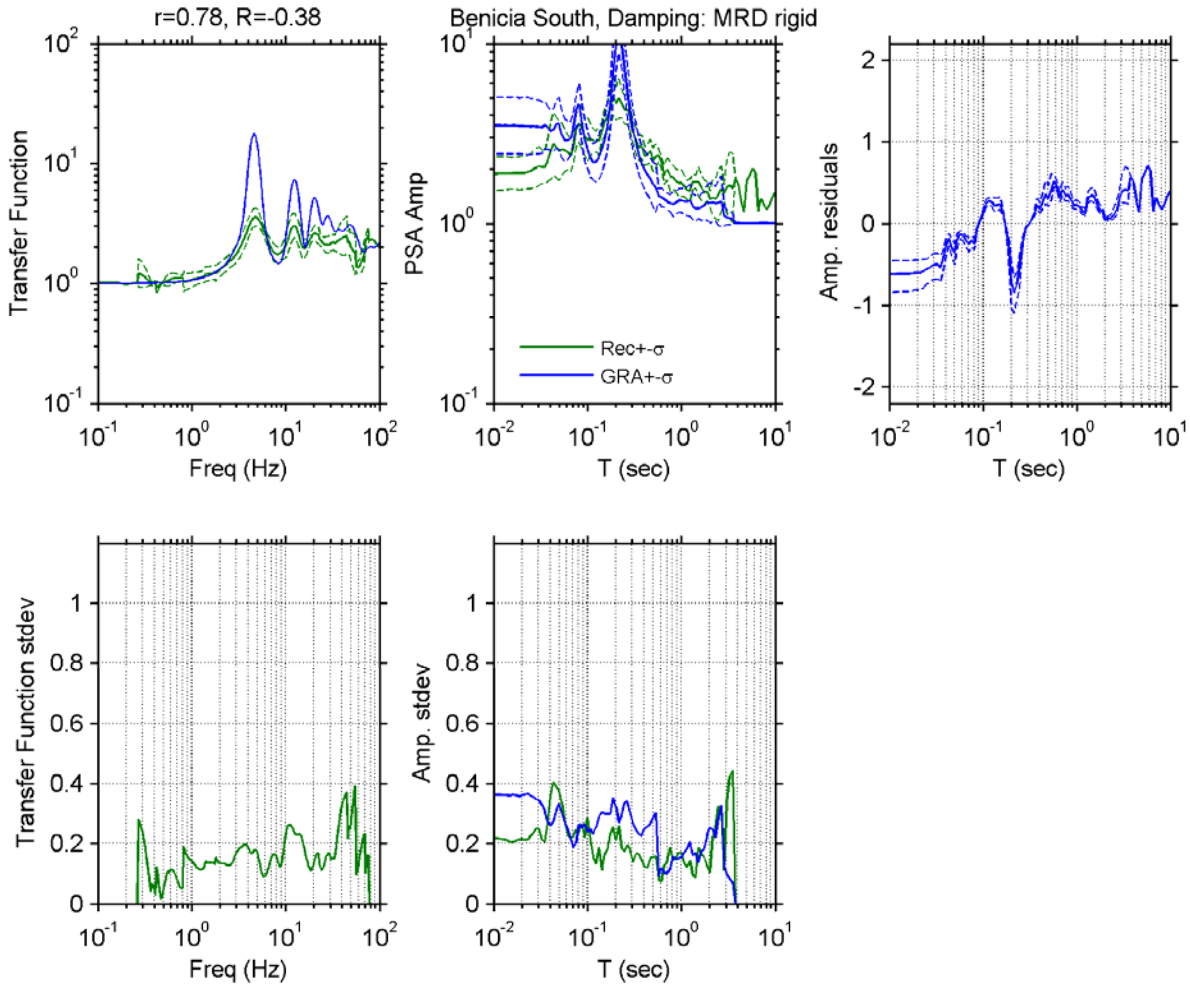

Figure A 6. Observed and simulated site response for Benicia-Martinez S site with $D^{L}_{\min}$ model for damping; Top left: Theoretical and median ± standard deviation of empirical transfer functions, Top middle: observed and predicted median ± standard deviation of *PS*A amplification, Top right: median ± standard deviation of *PS*A amplification residuals, Bottom left: standard deviation of empirical transfer functions, Bottom middle: standard deviation of observed and predicted *PS*A amplification residuals.

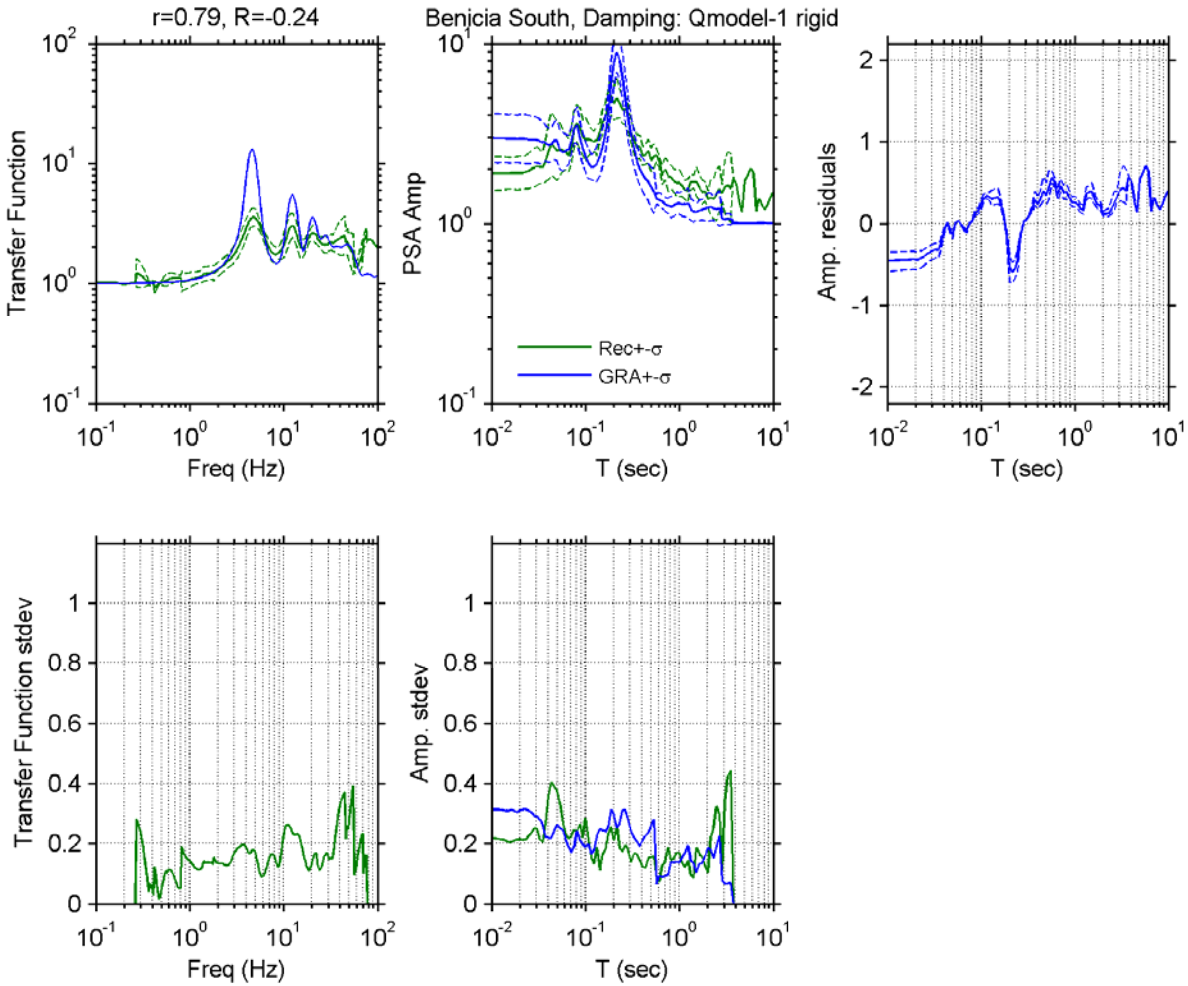

Figure A 7. Observed and simulated site response for Benicia-Martinez S site with V_S-based model for damping; Top left: Theoretical and median ± standard deviation of empirical transfer functions, Top middle: observed and predicted median ± standard deviation of *PSA* amplification, Top right: median ± standard deviation of *PSA* amplification residuals, Bottom left: standard deviation of empirical transfer functions, Bottom middle: standard deviation of observed and predicted *PSA* amplification residuals.

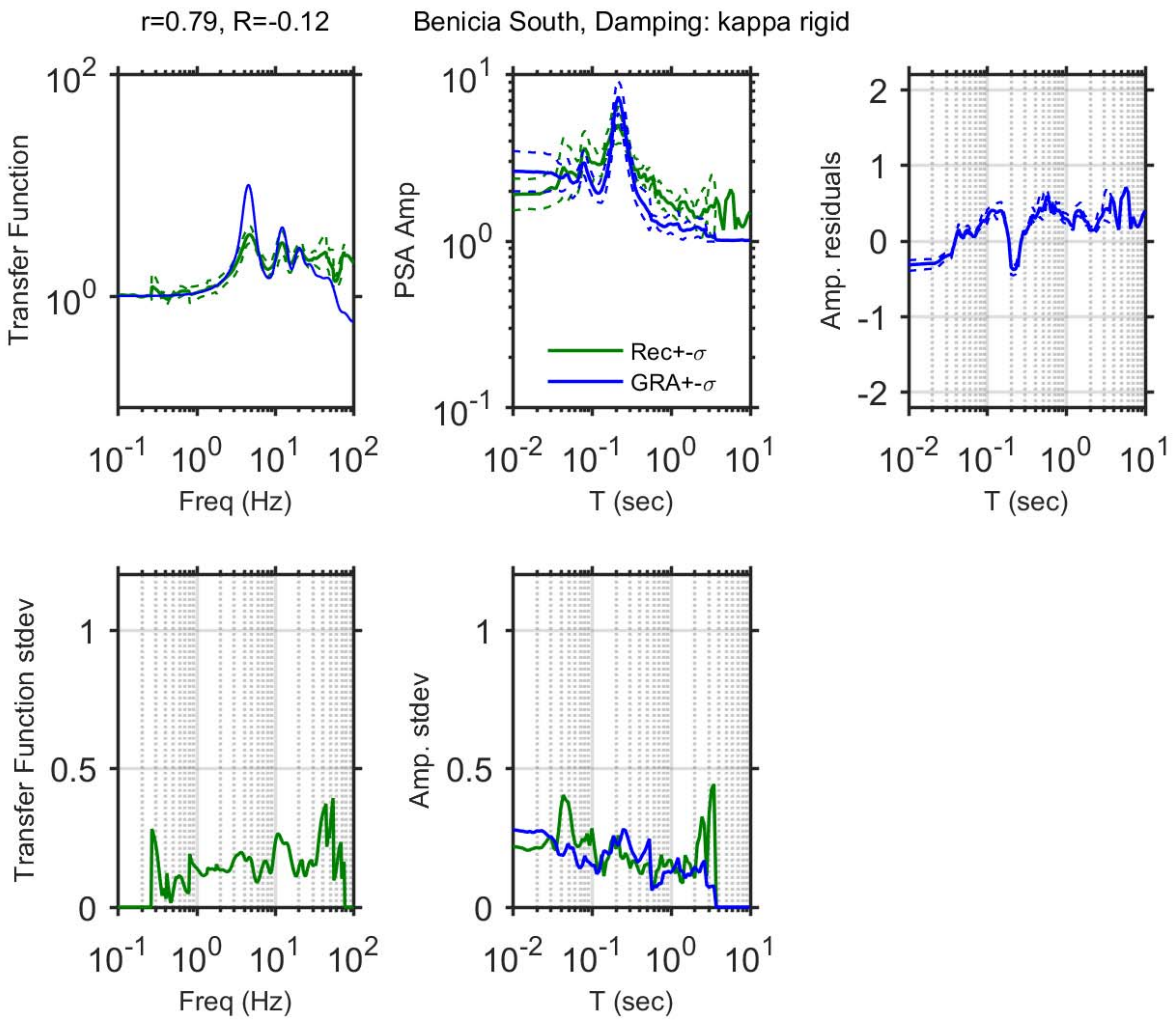

Figure A 8. Observed and simulated site response for Benicia-Martinez S site with κ-informed model for damping; Top left: Theoretical and median ± standard deviation of empirical transfer functions, Top middle: observed and predicted median ± standard deviation of *PS*A amplification, Top right: median ± standard deviation of *PS*A amplification residuals, Bottom left: standard deviation of empirical transfer functions, Bottom middle: standard deviation of observed and predicted *PS*A amplification residuals.

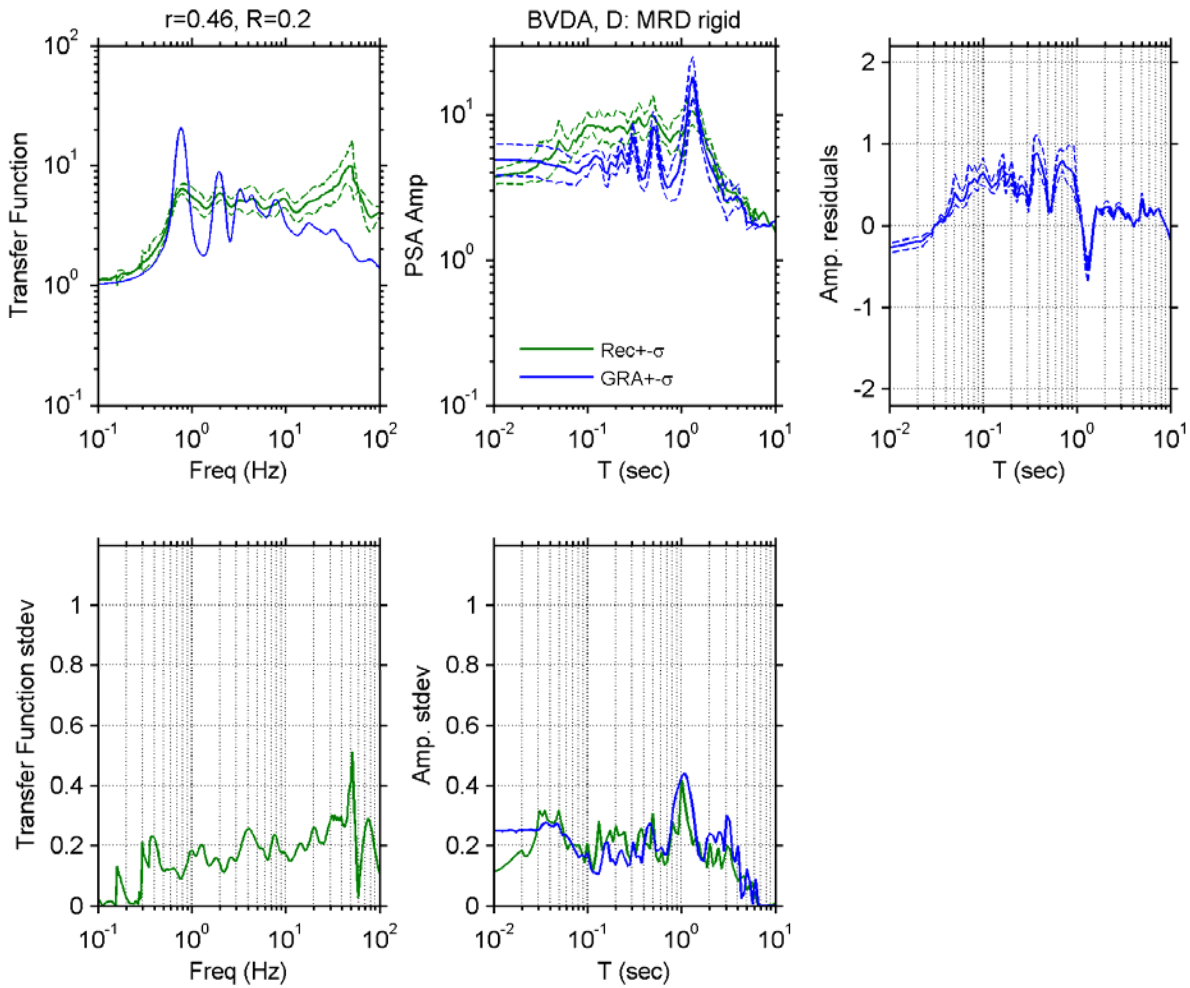

Figure A 9. Observed and simulated site response for Borrego Valley site with $D^{L}_{\min}$ model for damping; Top left: Theoretical and median ± standard deviation of empirical transfer functions, Top middle: observed and predicted median ± standard deviation of *PS*A amplification, Top right: median ± standard deviation of *PS*A amplification residuals, Bottom left: standard deviation of empirical transfer functions, Bottom middle: standard deviation of observed and predicted *PS*A amplification residuals.

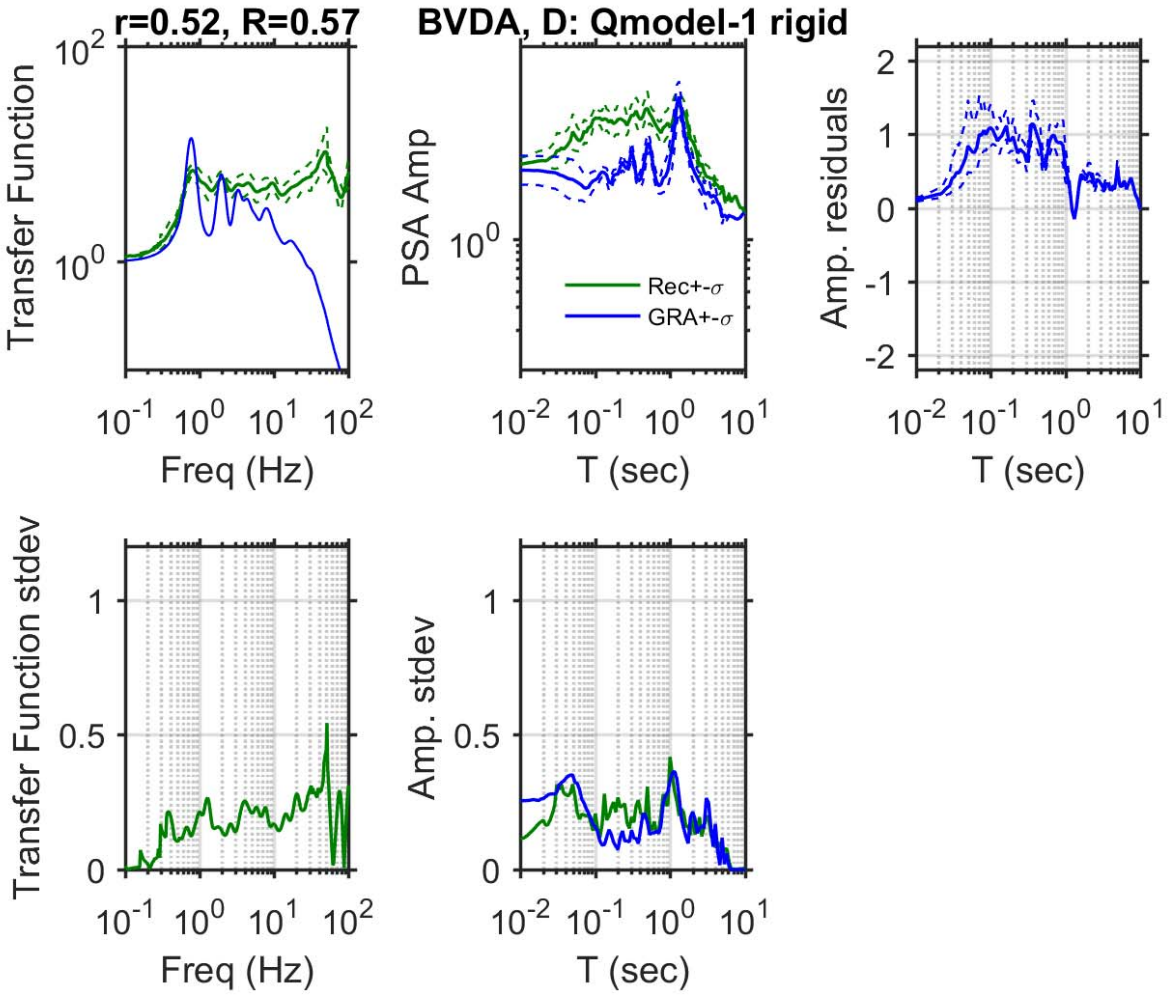

Figure A 10. Observed and simulated site response for Borrego Valley site with V_S-based model for damping; Top left: Theoretical and median ± standard deviation of empirical transfer functions, Top middle: observed and predicted median ± standard deviation of *PS*A amplification, Top right: median ± standard deviation of *PS*A amplification residuals, Bottom left: standard deviation of empirical transfer functions, Bottom middle: standard deviation of observed and predicted *PS*A amplification residuals.

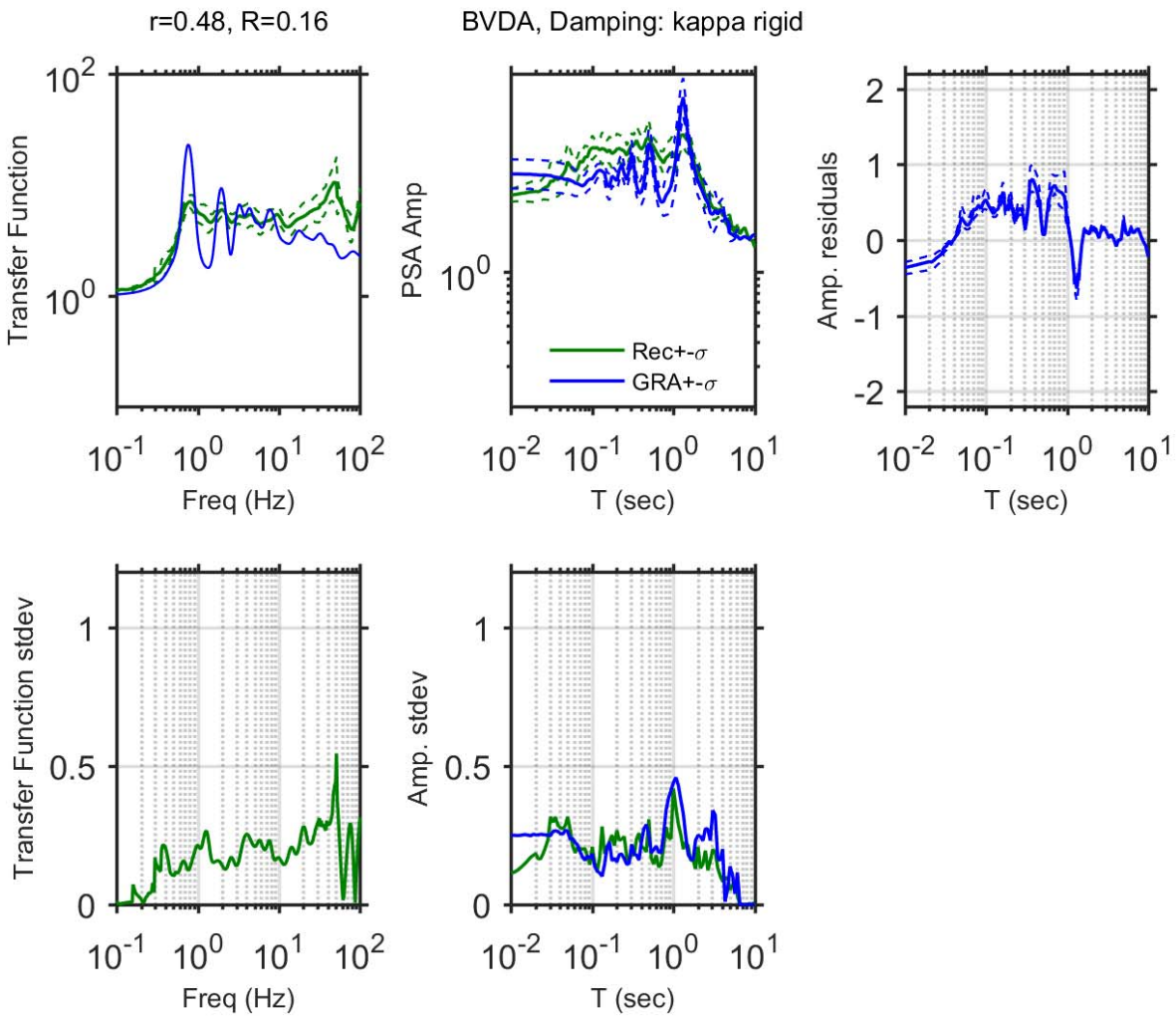

Figure A 11. Observed and simulated site response for Borrego Valley site with κ-informed model for damping; Top left: Theoretical and median ± standard deviation of empirical transfer functions, Top middle: observed and predicted median ± standard deviation of *PS*A amplification, Top right: median ± standard deviation of *PS*A amplification residuals, Bottom left: standard deviation of empirical transfer functions, Bottom middle: standard deviation of observed and predicted *PS*A amplification residuals.

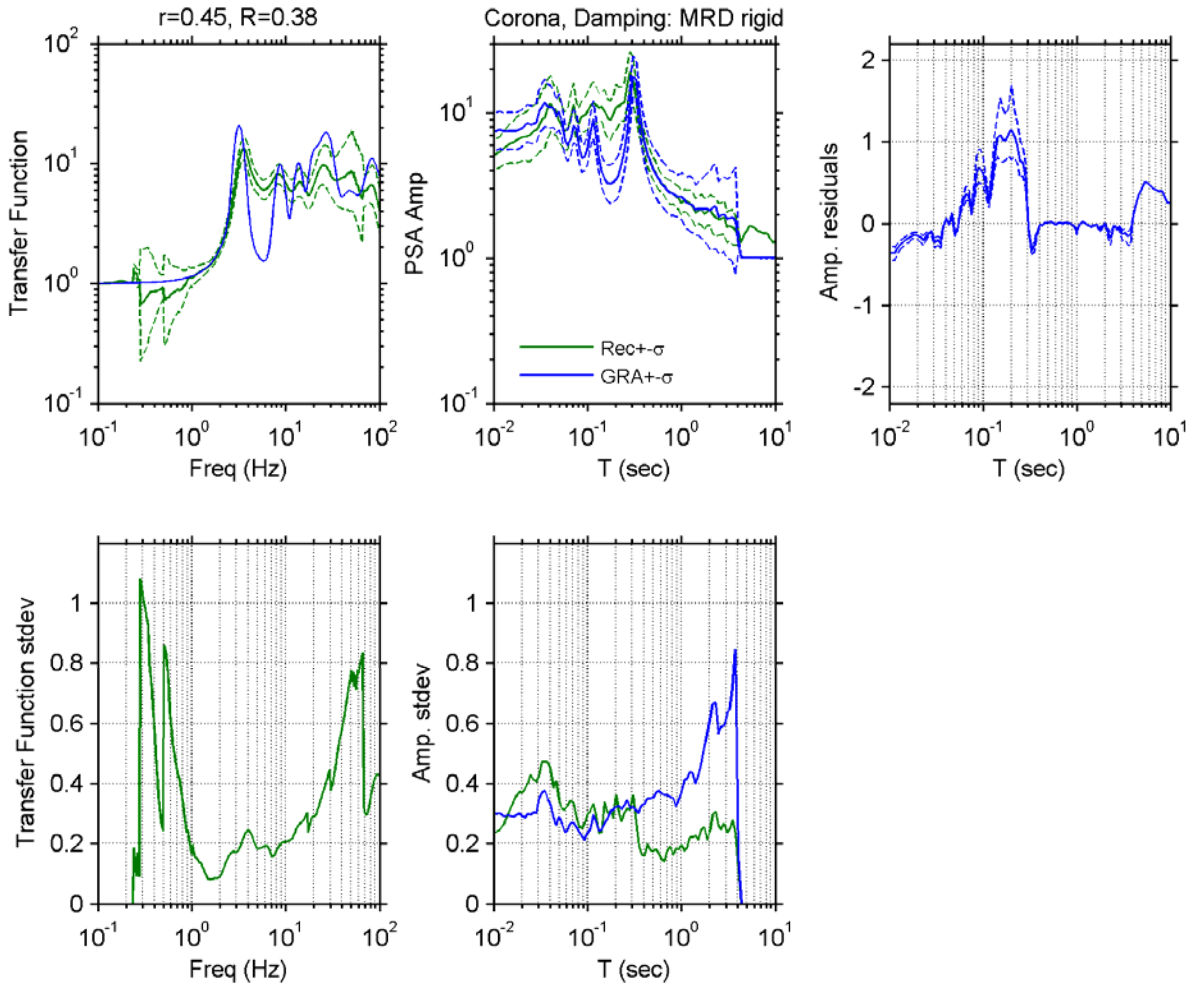

Figure A 12. Observed and simulated site response for Corona-I15/Hwy 91 site with $D^{L}_{\min}$ model for damping; Top left: Theoretical and median ± standard deviation of empirical transfer functions, Top middle: observed and predicted median ± standard deviation of *PS*A amplification, Top right: median ± standard deviation of *PS*A amplification residuals, Bottom left: standard deviation of empirical transfer functions, Bottom middle: standard deviation of observed and predicted *PS*A amplification residuals.

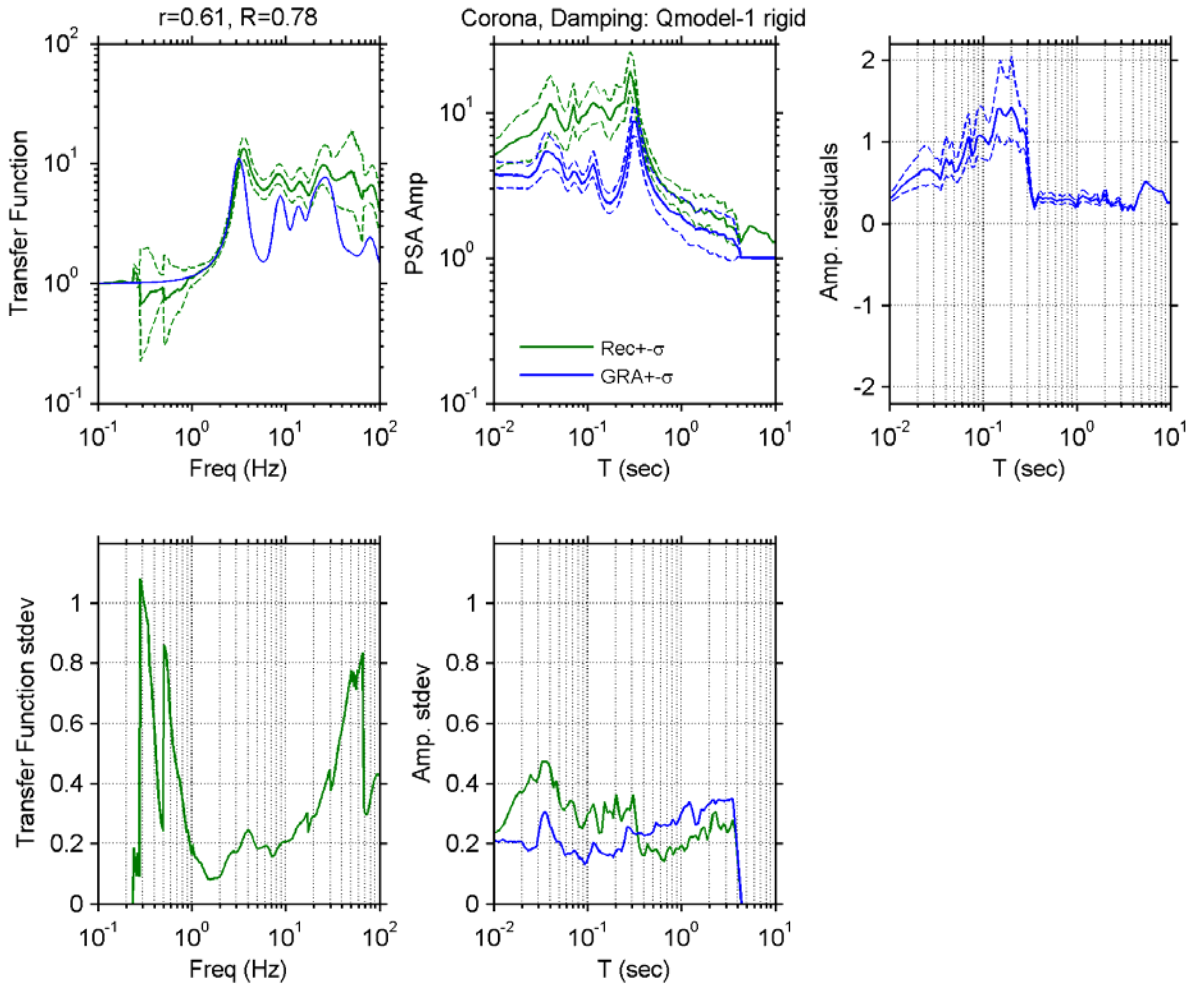

Figure A 13. Observed and simulated site response for Corona-I15/Hwy 91 site with V_S-based model for damping; Top left: Theoretical and median ± standard deviation of empirical transfer functions, Top middle: observed and predicted median ± standard deviation of *PSA* amplification, Top right: median ± standard deviation of *PSA* amplification residuals, Bottom left: standard deviation of empirical transfer functions, Bottom middle: standard deviation of observed and predicted *PSA* amplification residuals.

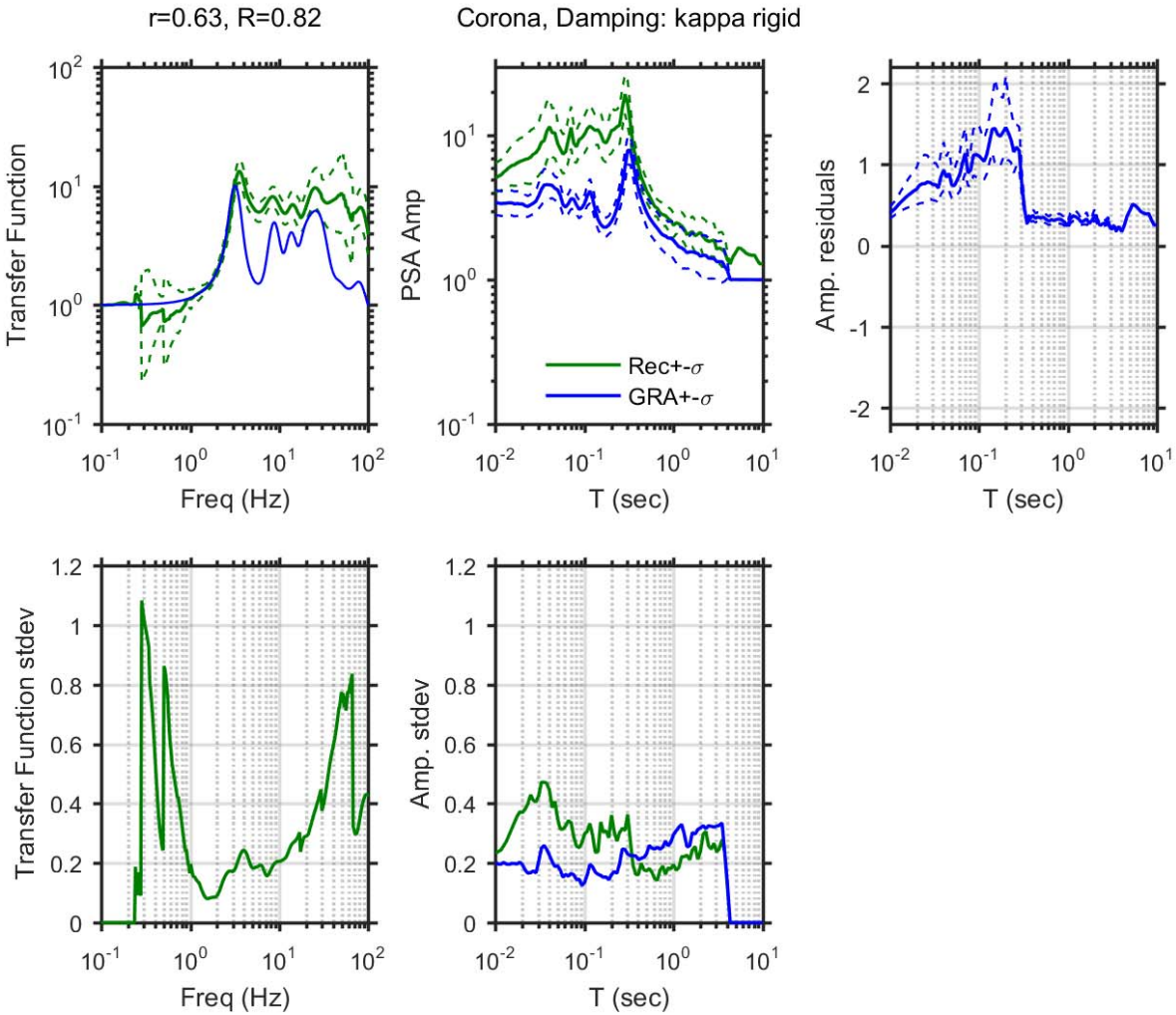

Figure A 14. Observed and simulated site response for Corona-I15/Hwy 91 site with κ-informed model for damping; Top left: Theoretical and median ± standard deviation of empirical transfer functions, Top middle: observed and predicted median ± standard deviation of *PS*A amplification, Top right: median ± standard deviation of *PS*A amplification residuals, Bottom left: standard deviation of empirical transfer functions, Bottom middle: standard deviation of observed and predicted *PS*A amplification residuals.

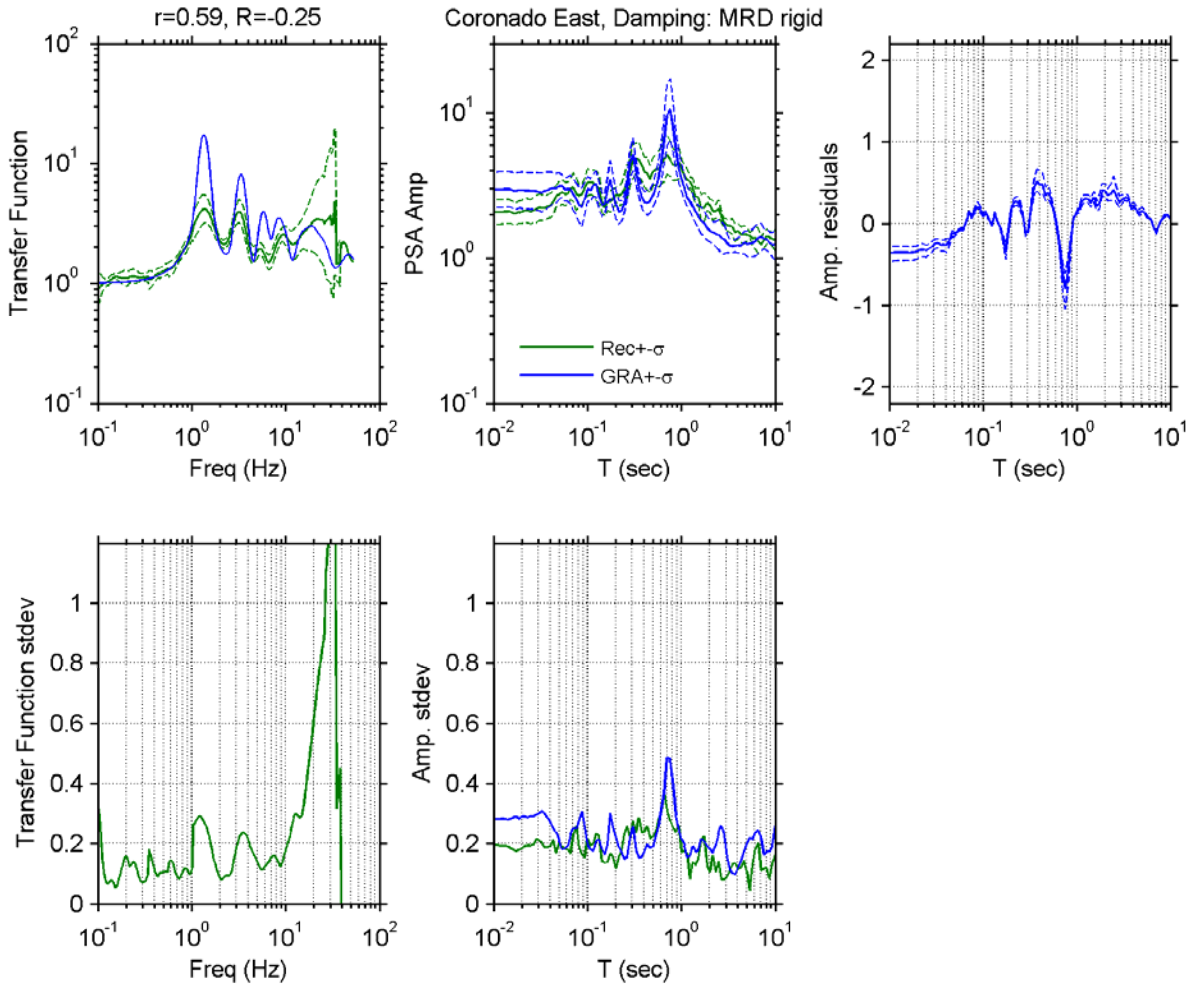

Figure A 15. Observed and simulated site response for Corona-I15/Hwy 91 site with $D^{L}_{\min}$ model for damping; Top left: Theoretical and median ± standard deviation of empirical transfer functions, Top middle: observed and predicted median ± standard deviation of *PS*A amplification, Top right: median ± standard deviation of *PS*A amplification residuals, Bottom left: standard deviation of empirical transfer functions, Bottom middle: standard deviation of observed and predicted *PS*A amplification residuals.

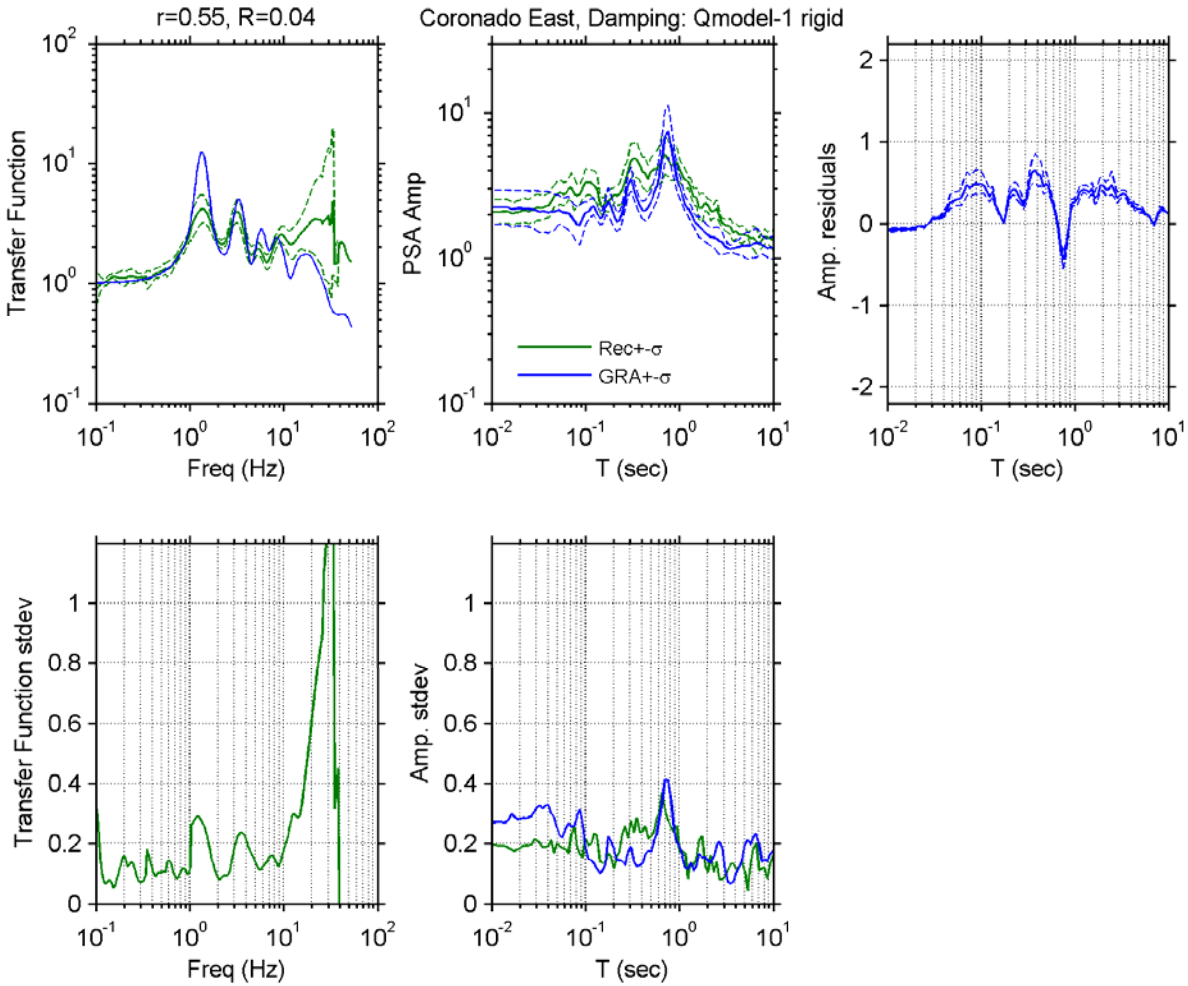

Figure A 16. Observed and simulated site response for Corona-I15/Hwy 91 site with V_S-based model for damping; Top left: Theoretical and median ± standard deviation of empirical transfer functions, Top middle: observed and predicted median ± standard deviation of *PS*A amplification, Top right: median ± standard deviation of *PS*A amplification residuals, Bottom left: standard deviation of empirical transfer functions, Bottom middle: standard deviation of observed and predicted *PS*A amplification residuals.

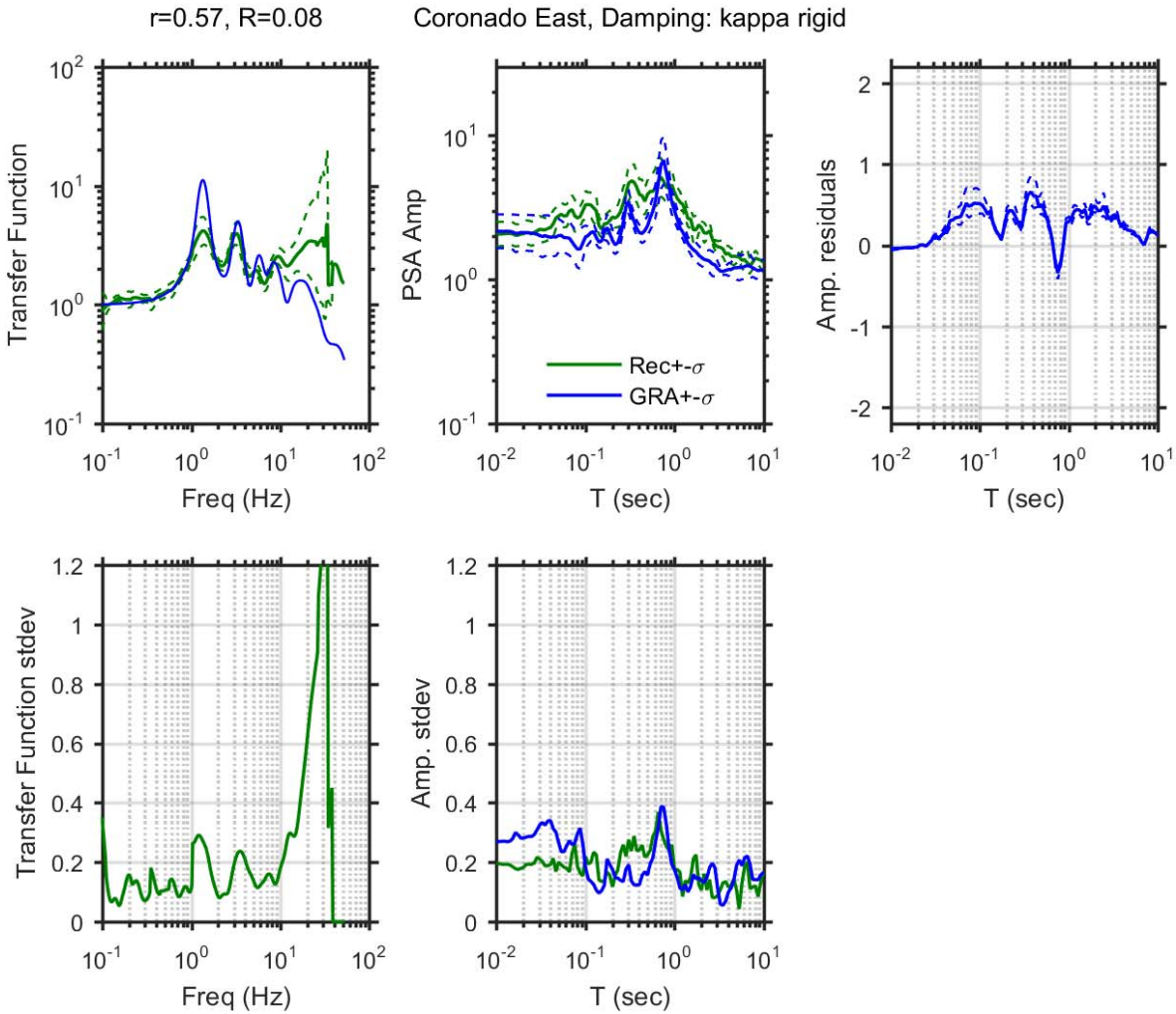

Figure A 17. Observed and simulated site response for Corona-I15/Hwy 91 site with κ-informed model for damping; Top left: Theoretical and median ± standard deviation of empirical transfer functions, Top middle: observed and predicted median ± standard deviation of *PS*A amplification, Top right: median ± standard deviation of *PS*A amplification residuals, Bottom left: standard deviation of empirical transfer functions, Bottom middle: standard deviation of observed and predicted *PS*A amplification residuals.

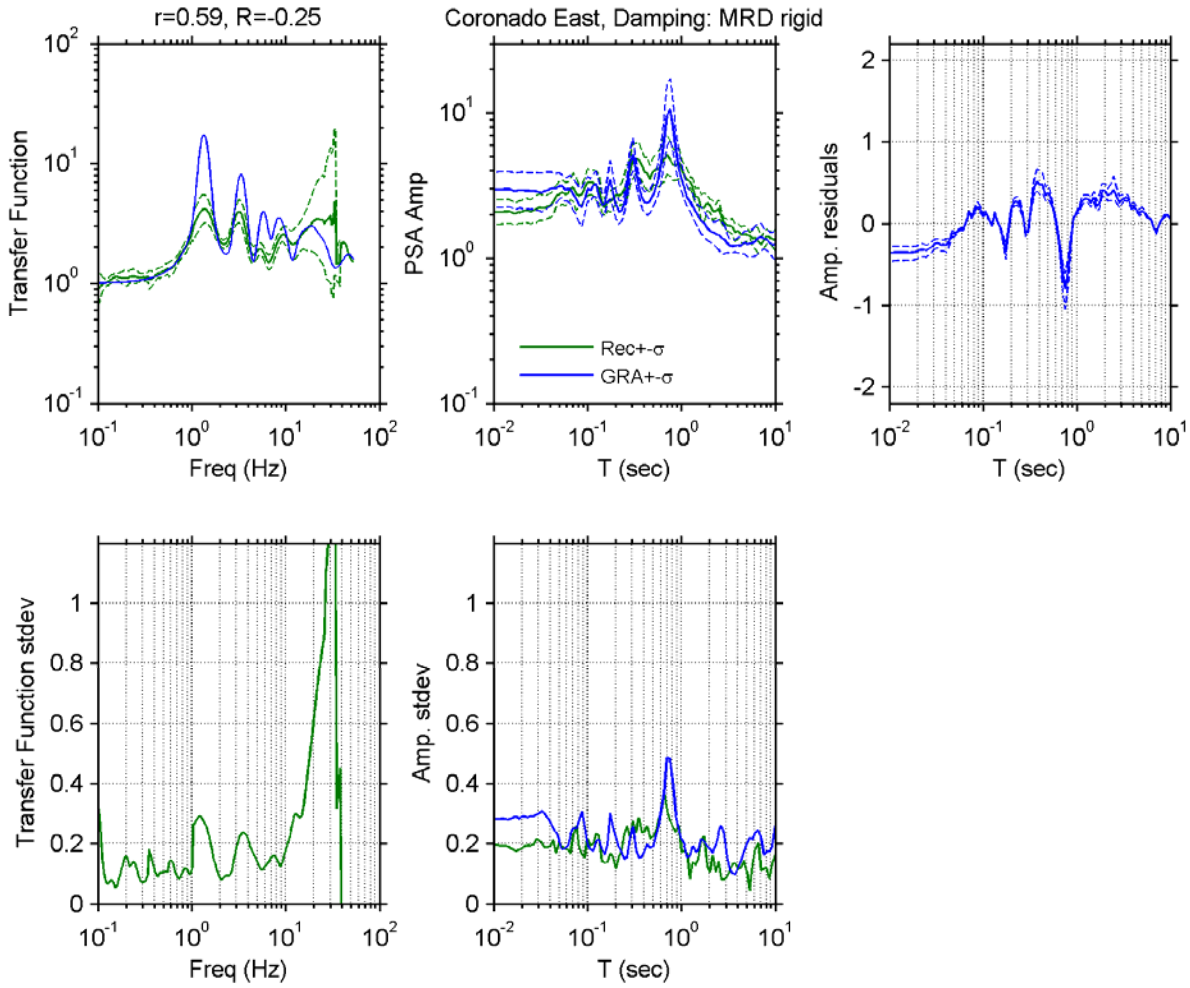

Figure A 18. Observed and simulated site response for Coronado East site with $D^{L}_{\min}$ model for damping; Top left: Theoretical and median ± standard deviation of empirical transfer functions, Top middle: observed and predicted median ± standard deviation of *PS*A amplification, Top right: median ± standard deviation of *PS*A amplification residuals, Bottom left: standard deviation of empirical transfer functions, Bottom middle: standard deviation of observed and predicted *PS*A amplification residuals.

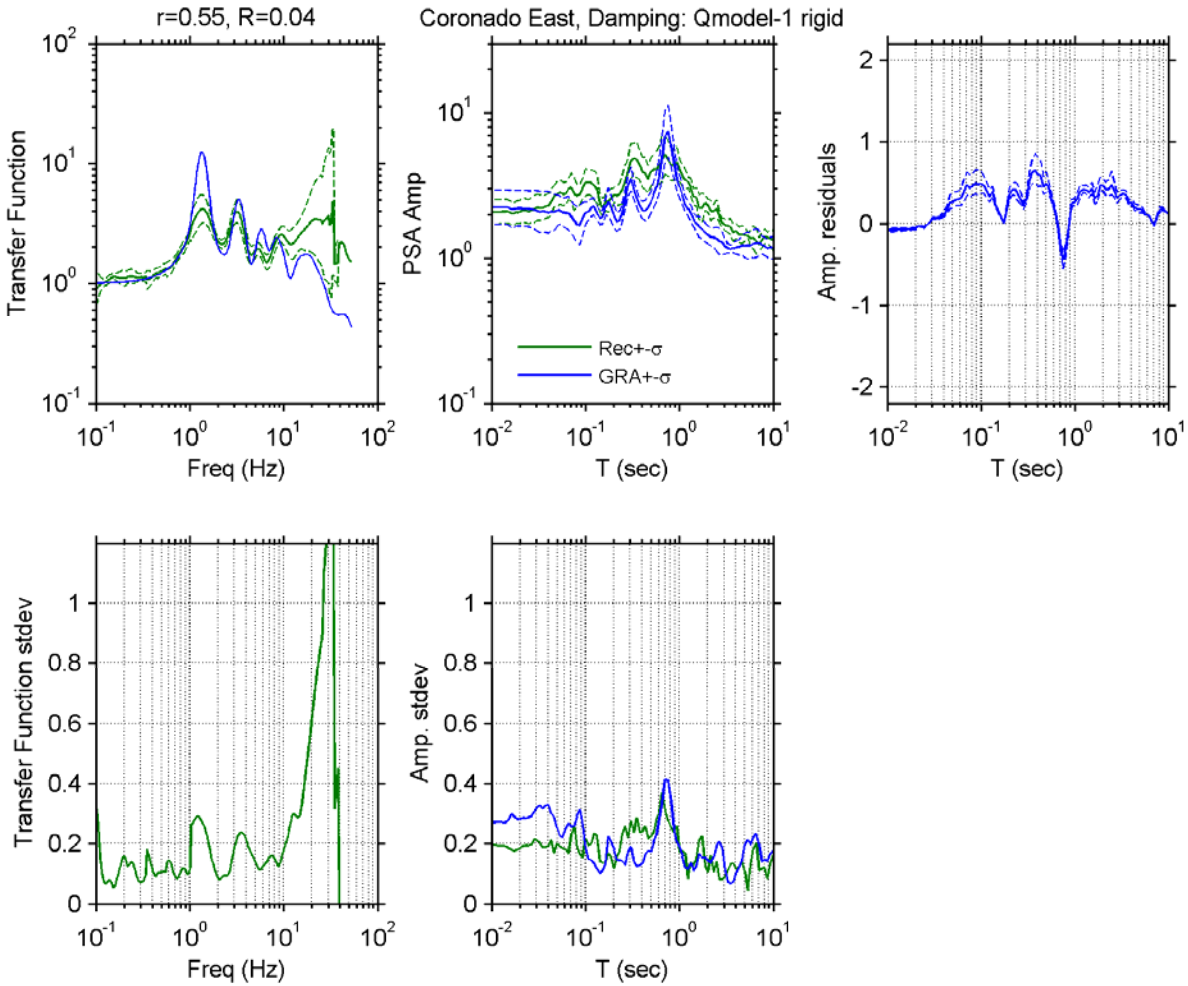

Figure A 19. Observed and simulated site response for Coronado East site with V_S-based model for damping; Top left: Theoretical and median ± standard deviation of empirical transfer functions, Top middle: observed and predicted median ± standard deviation of *PSA* amplification, Top right: median ± standard deviation of *PSA* amplification residuals, Bottom left: standard deviation of empirical transfer functions, Bottom middle: standard deviation of observed and predicted *PSA* amplification residuals.

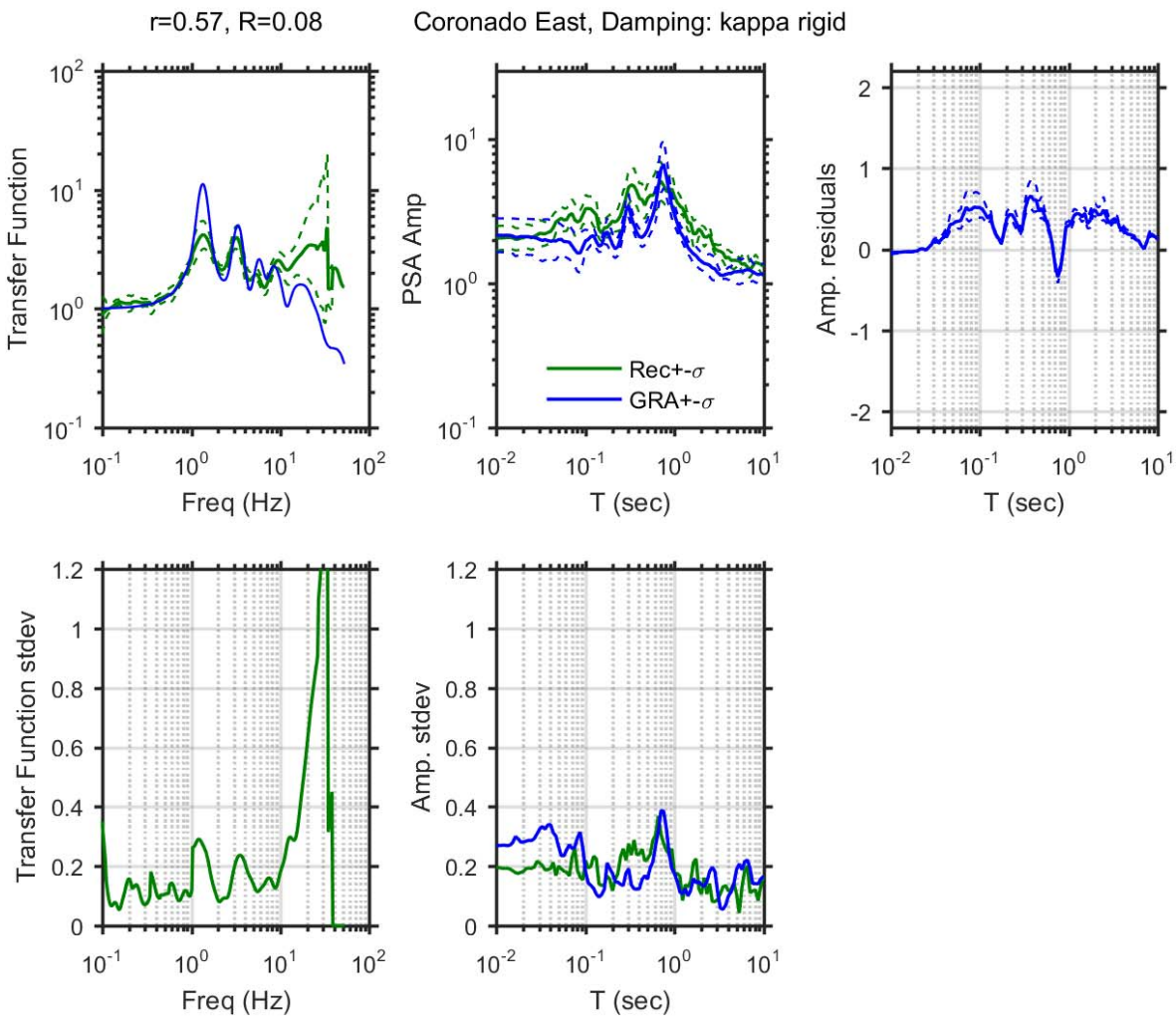

Figure A 20. Observed and simulated site response for Coronado East site with κ-informed model for damping; Top left: Theoretical and median ± standard deviation of empirical transfer functions, Top middle: observed and predicted median ± standard deviation of *PS*A amplification, Top right: median ± standard deviation of *PS*A amplification residuals, Bottom left: standard deviation of empirical transfer functions, Bottom middle: standard deviation of observed and predicted *PS*A amplification residuals.

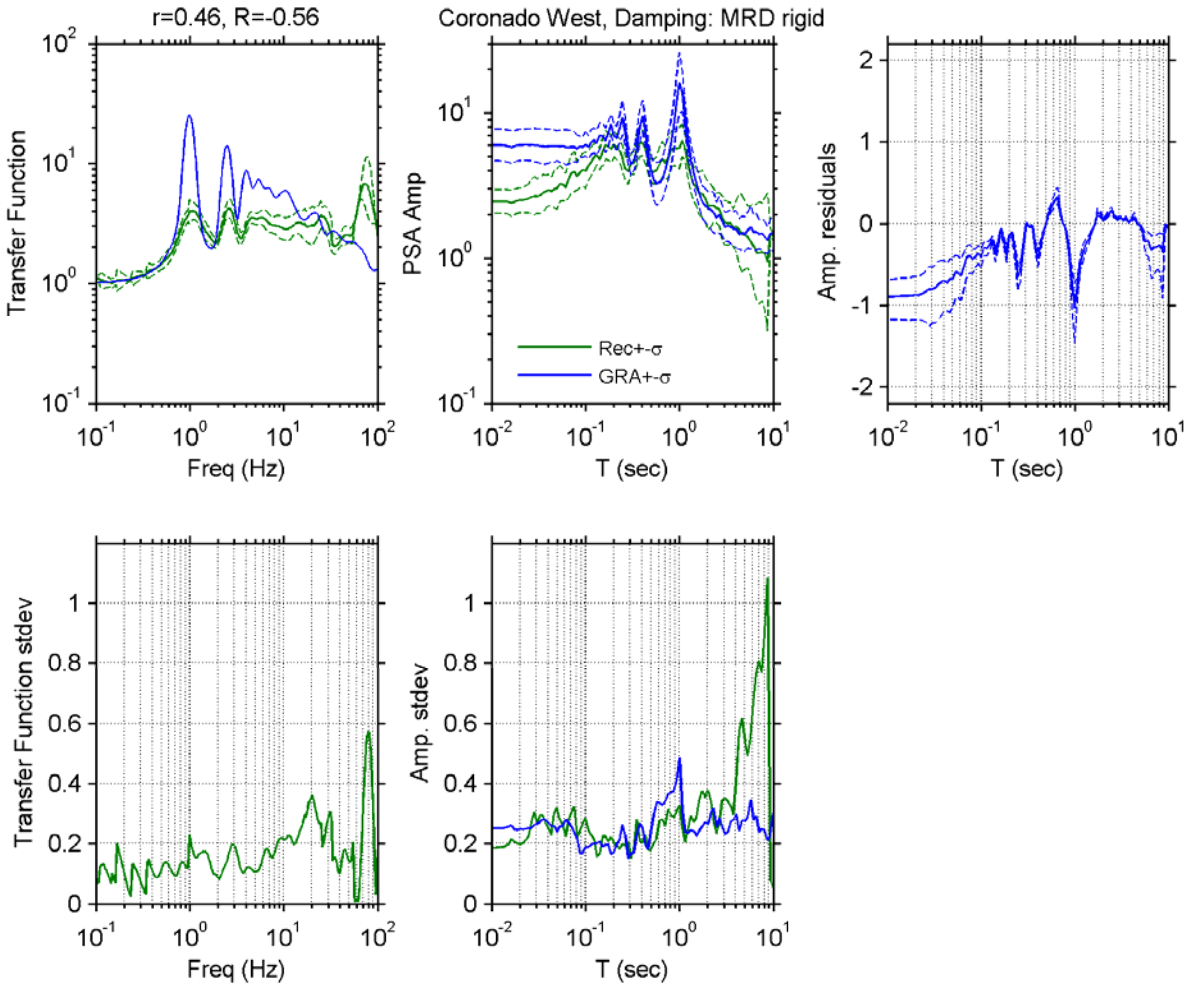

Figure A 21. Observed and simulated site response for Coronado West site with $D^{L}_{\min}$ model for damping; Top left: Theoretical and median ± standard deviation of empirical transfer functions, Top middle: observed and predicted median ± standard deviation of *PS*A amplification, Top right: median ± standard deviation of *PS*A amplification residuals, Bottom left: standard deviation of empirical transfer functions, Bottom middle: standard deviation of observed and predicted *PS*A amplification residuals.

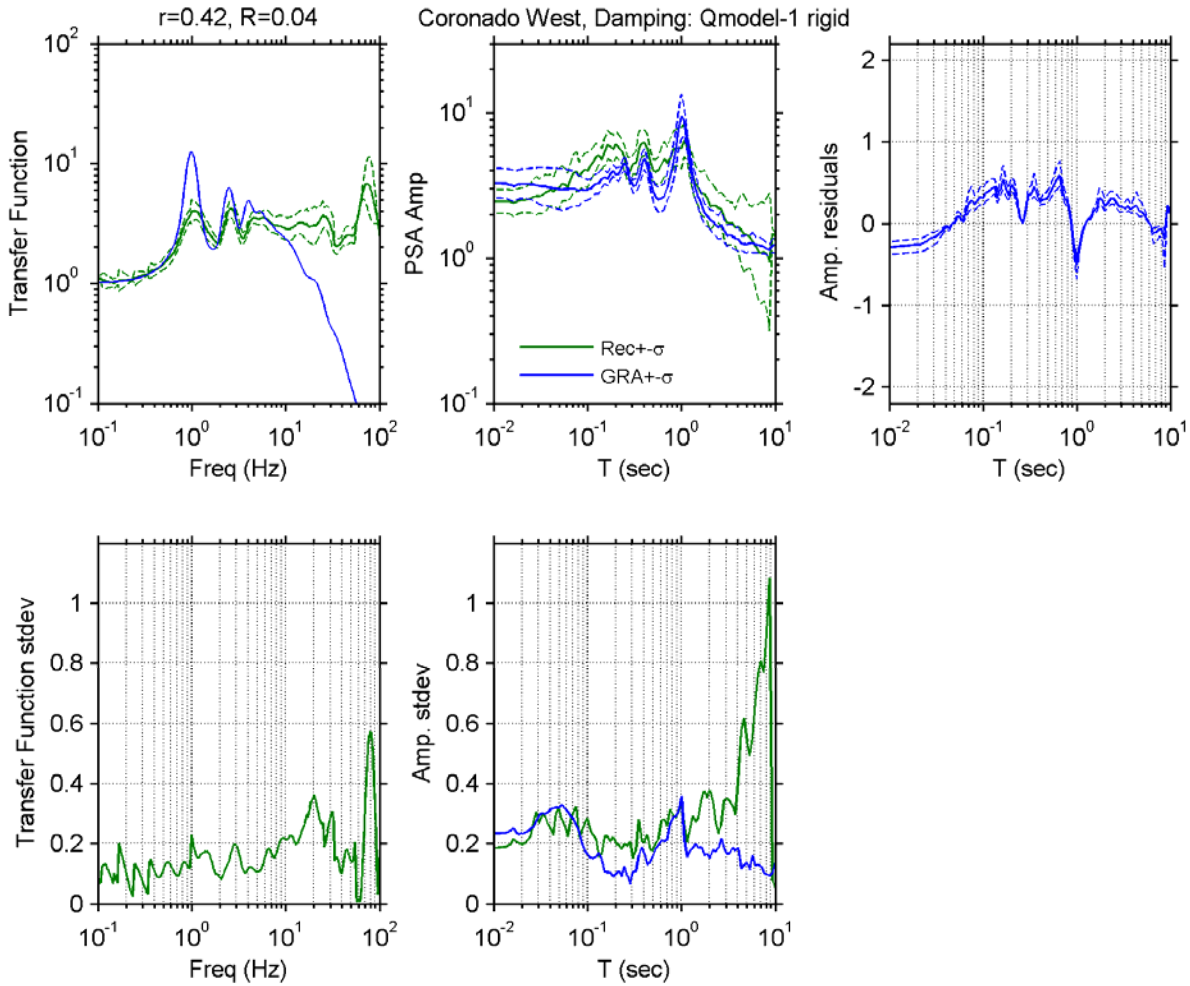

Figure A 22. Observed and simulated site response for Coronado West site with V_S-based model for damping; Top left: Theoretical and median ± standard deviation of empirical transfer functions, Top middle: observed and predicted median ± standard deviation of *PSA* amplification, Top right: median ± standard deviation of *PSA* amplification residuals, Bottom left: standard deviation of empirical transfer functions, Bottom middle: standard deviation of observed and predicted *PSA* amplification residuals.

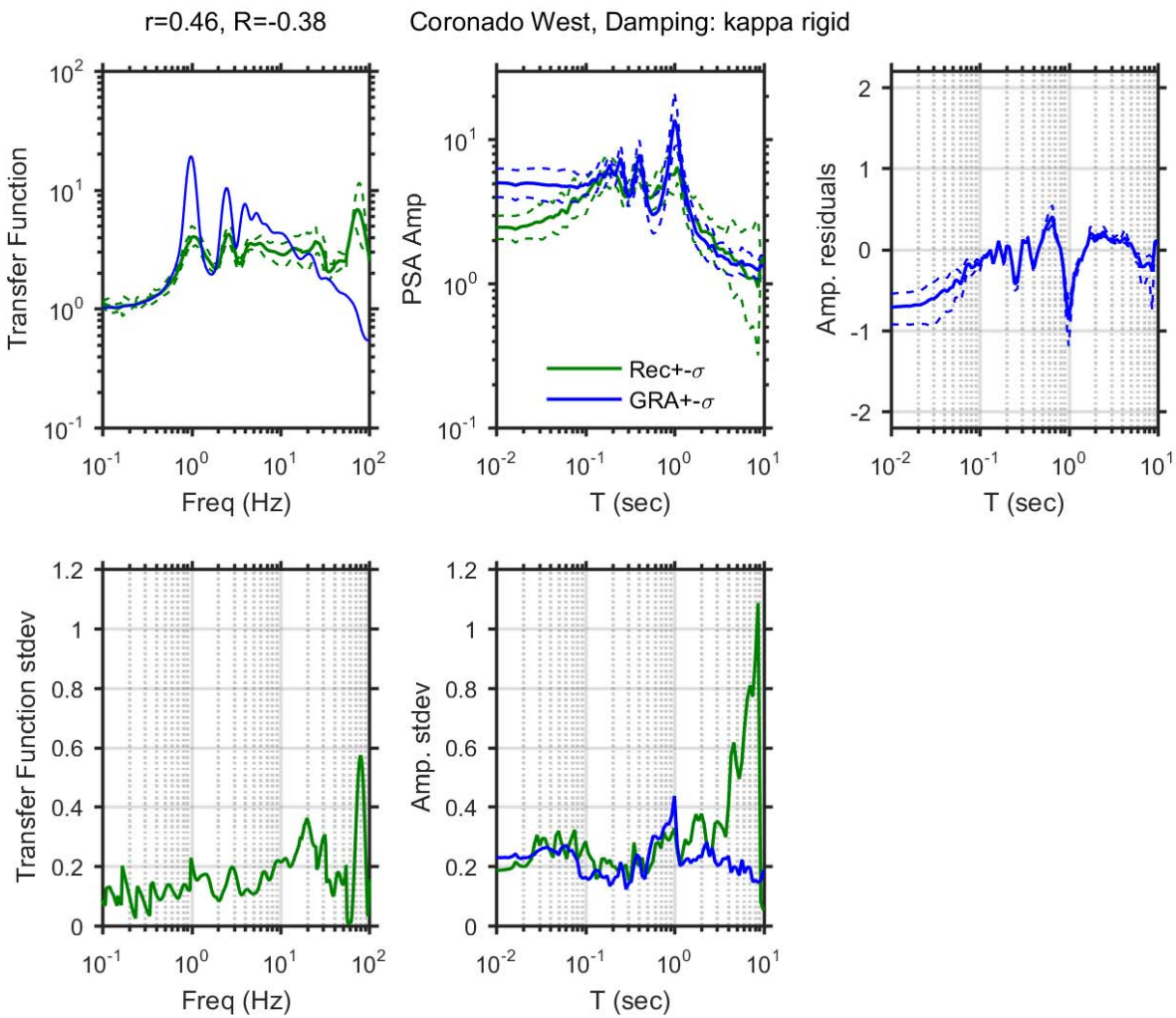

Figure A 23. Observed and simulated site response for Coronado West site with κ-informed model for damping; Top left: Theoretical and median ± standard deviation of empirical transfer functions, Top middle: observed and predicted median ± standard deviation of *PS*A amplification, Top right: median ± standard deviation of *PS*A amplification residuals, Bottom left: standard deviation of empirical transfer functions, Bottom middle: standard deviation of observed and predicted *PS*A amplification residuals.

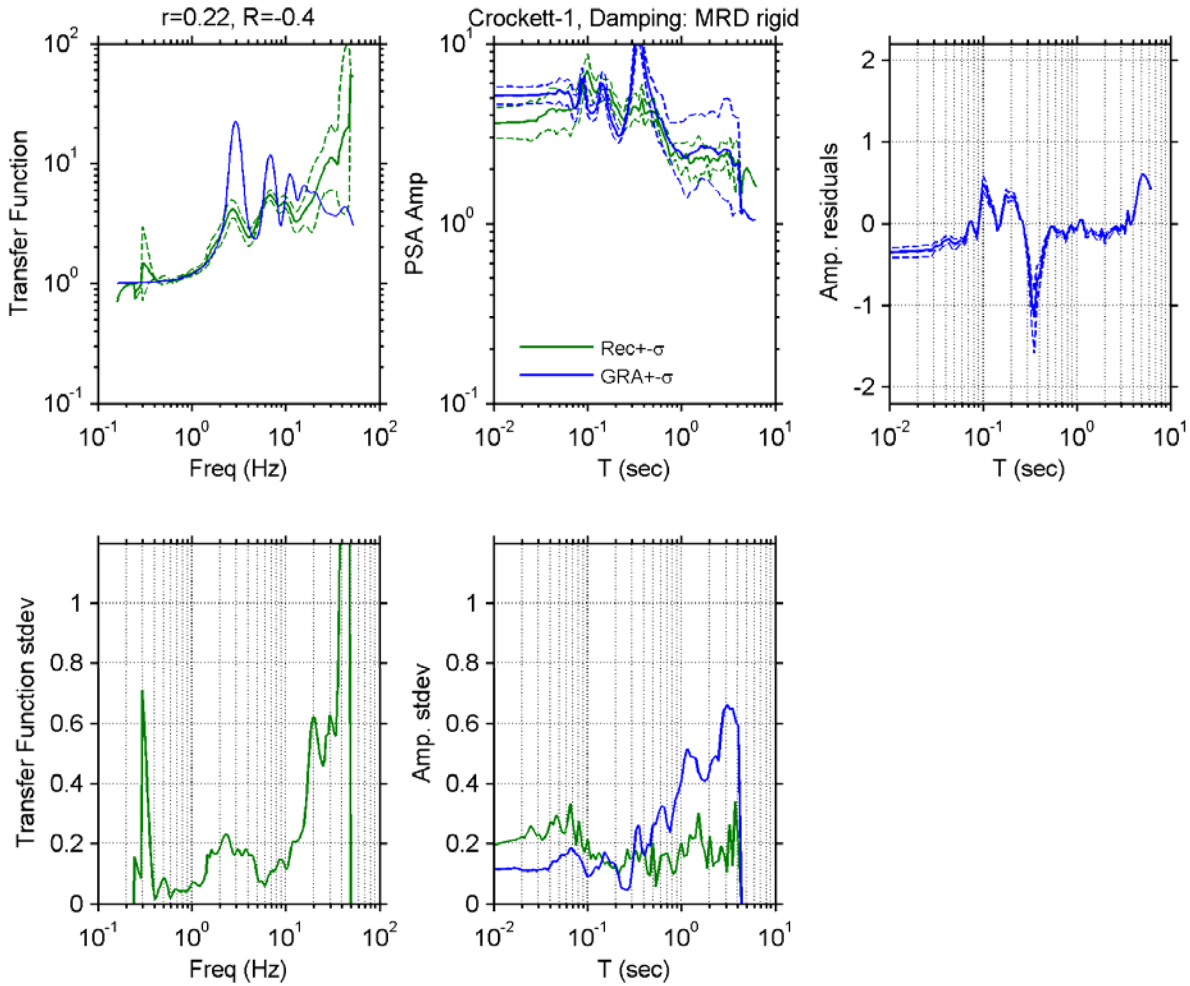

Figure A 24. Observed and simulated site response for Crockett-Carquinez Br #1 site with $D_{\min}^{L}$ model for damping; Top left: Theoretical and median ± standard deviation of empirical transfer functions, Top middle: observed and predicted median ± standard deviation of *PS*A amplification, Top right: median ± standard deviation of *PS*A amplification residuals, Bottom left: standard deviation of empirical transfer functions, Bottom middle: standard deviation of observed and predicted *PS*A amplification residuals.

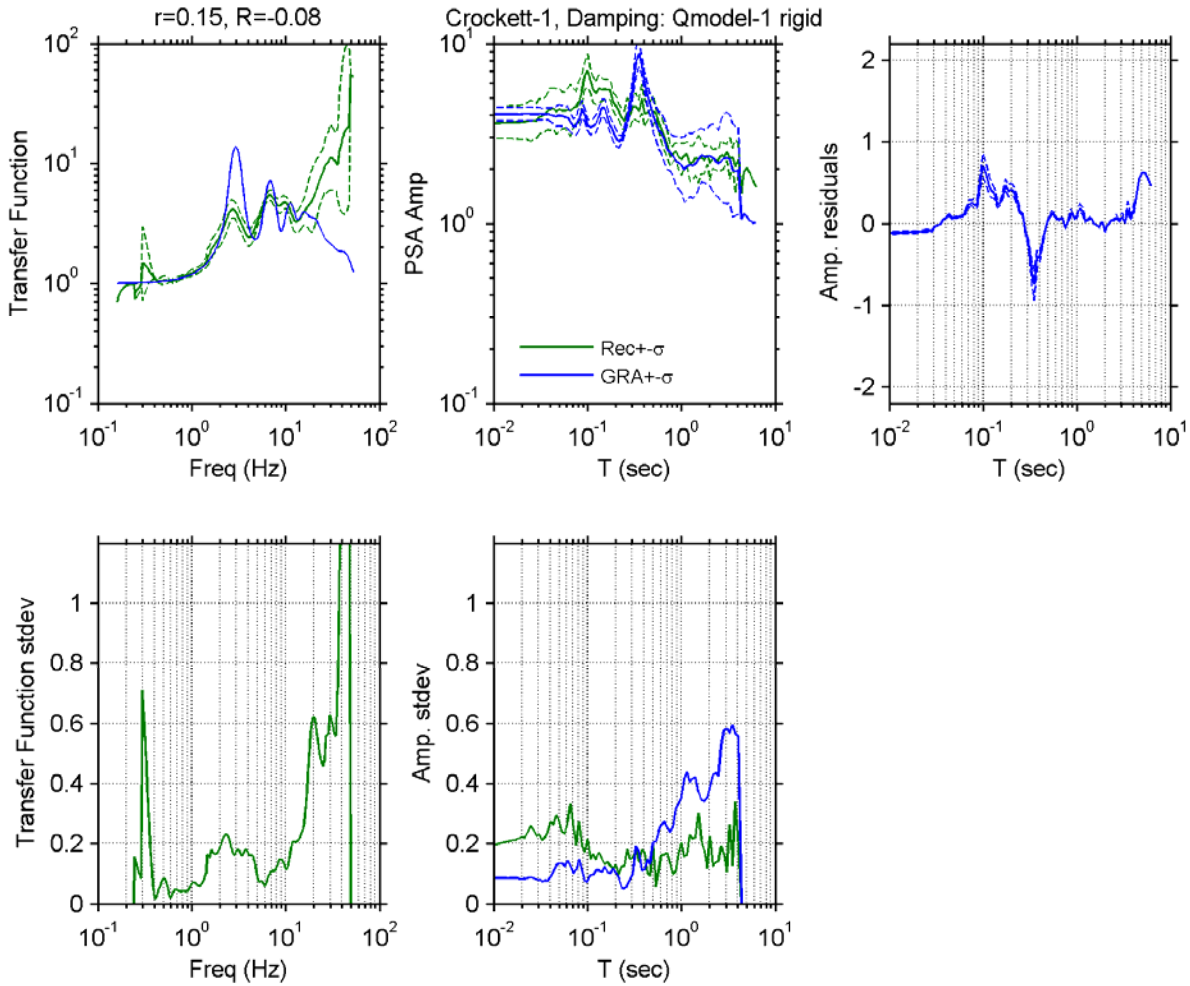

Figure A 25. Observed and simulated site response for Crockett-Carquinez Br #1 site with V_S-based model for damping; Top left: Theoretical and median ± standard deviation of empirical transfer functions, Top middle: observed and predicted median ± standard deviation of *PS*A amplification, Top right: median ± standard deviation of *PS*A amplification residuals, Bottom left: standard deviation of empirical transfer functions, Bottom middle: standard deviation of observed and predicted *PS*A amplification residuals.

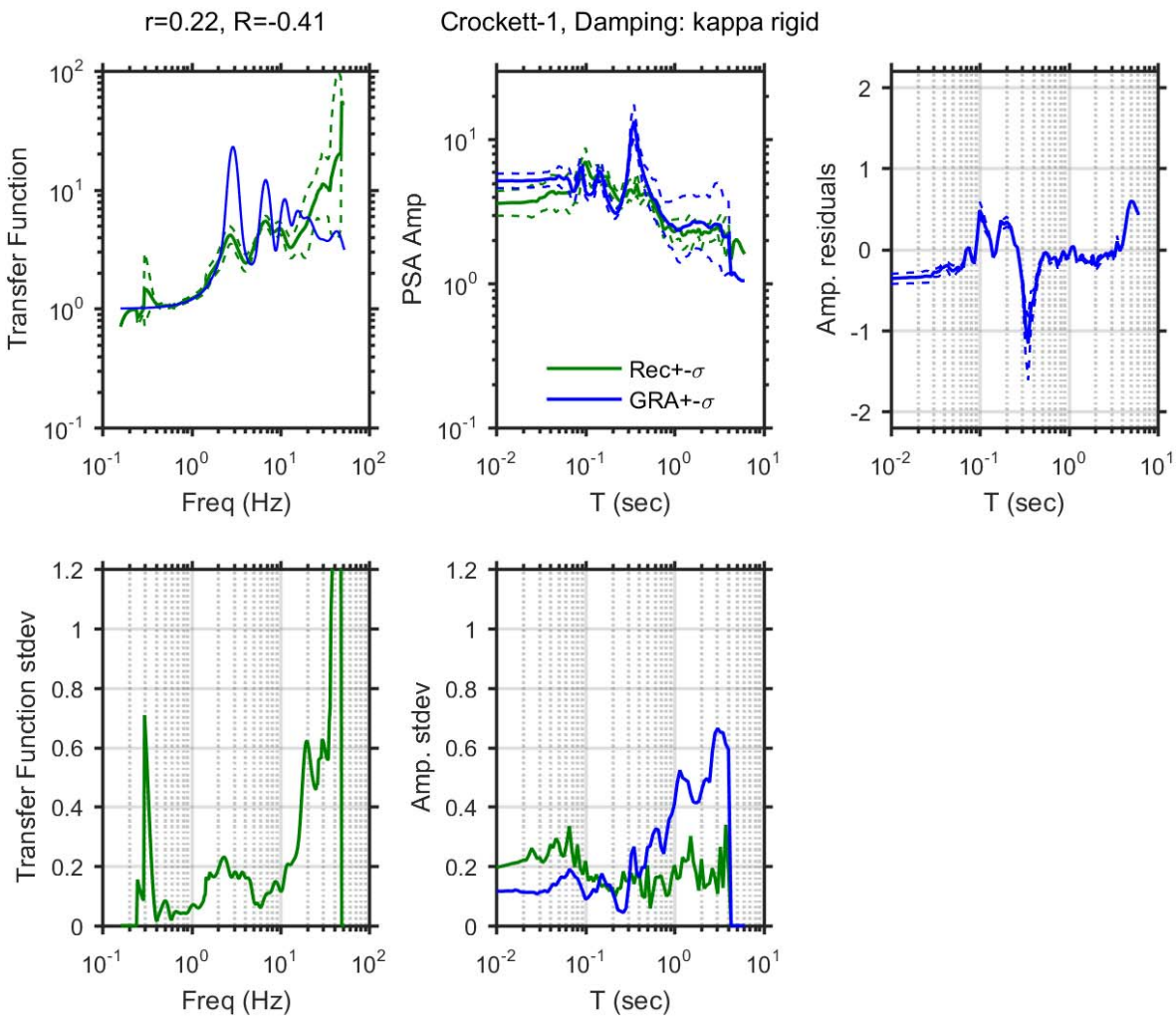

Figure A 26. Observed and simulated site response for Crockett-Carquinez Br #1 site with κ-informed model for damping; Top left: Theoretical and median ± standard deviation of empirical transfer functions, Top middle: observed and predicted median ± standard deviation of *PS*A amplification, Top right: median ± standard deviation of *PS*A amplification residuals, Bottom left: standard deviation of empirical transfer functions, Bottom middle: standard deviation of observed and predicted *PS*A amplification residuals.

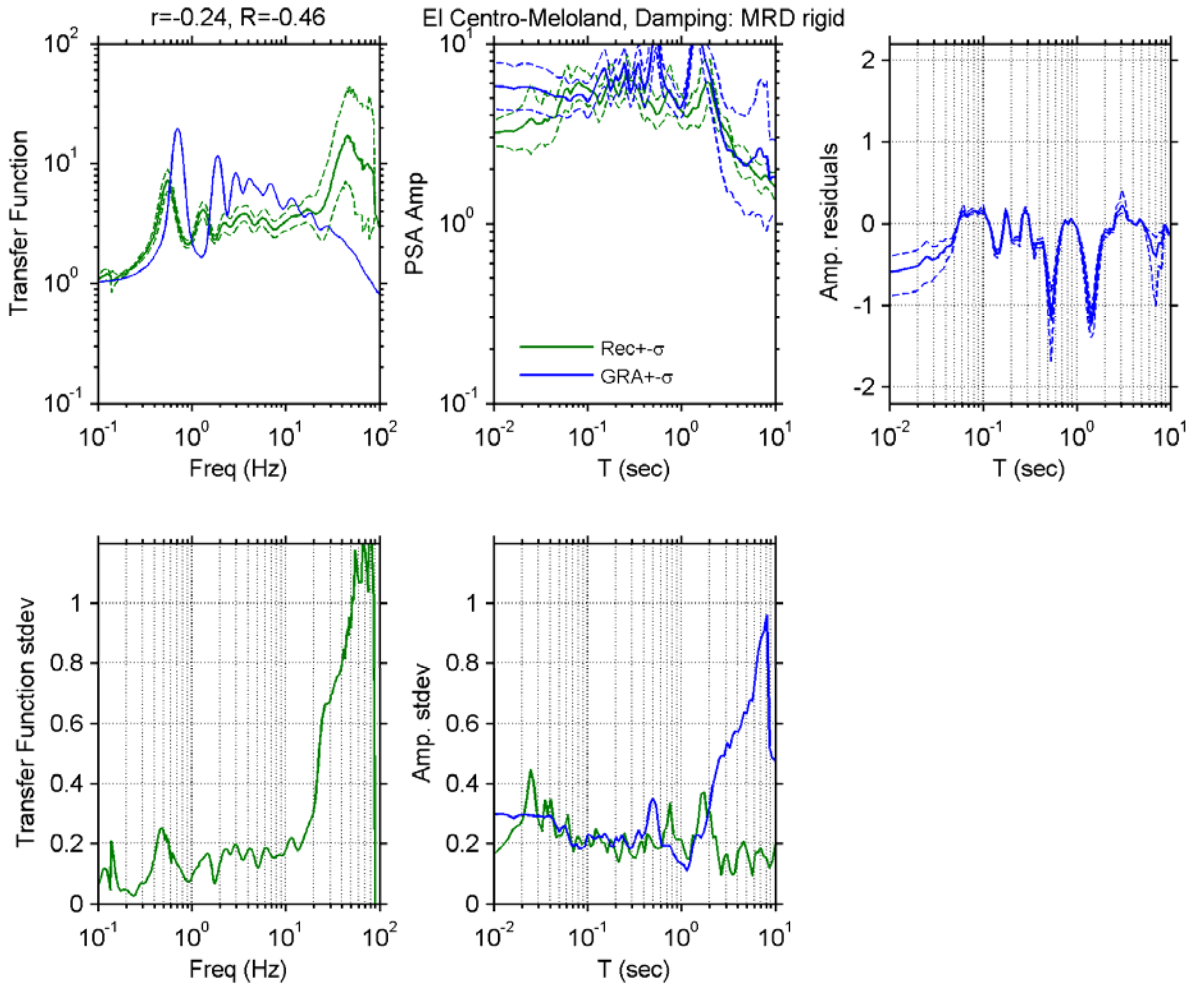

Figure A 27. Observed and simulated site response for El Centro-Meloland site with $D^{L}_{\min}$ model for damping; Top left: Theoretical and median ± standard deviation of empirical transfer functions, Top middle: observed and predicted median ± standard deviation of *PS*A amplification, Top right: median ± standard deviation of *PS*A amplification residuals, Bottom left: standard deviation of empirical transfer functions, Bottom middle: standard deviation of observed and predicted *PS*A amplification residuals.

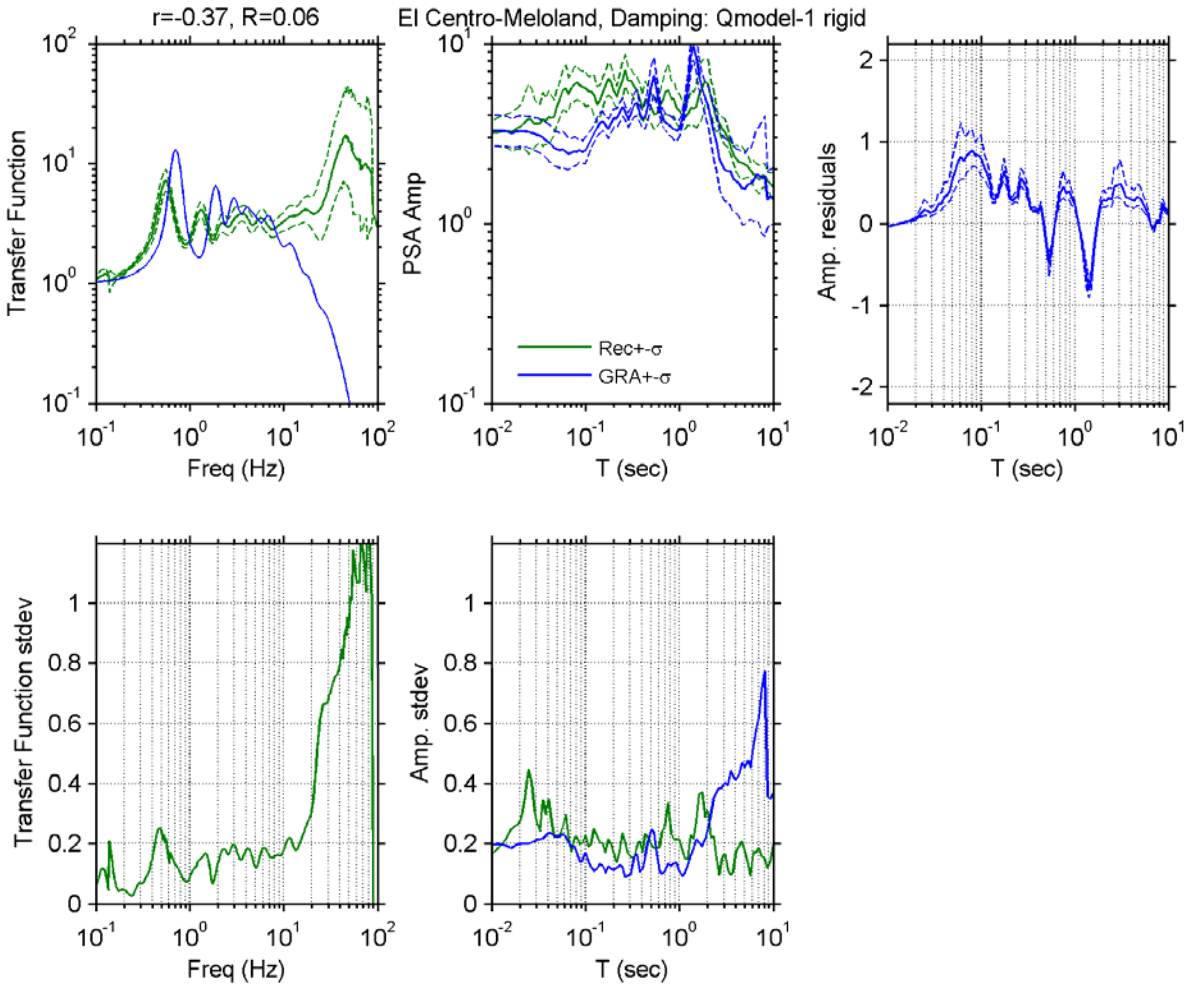

Figure A 28. Observed and simulated site response for El Centro-Meloland site with V_S-based model for damping; Top left: Theoretical and median ± standard deviation of empirical transfer functions, Top middle: observed and predicted median ± standard deviation of *PS*A amplification, Top right: median ± standard deviation of *PS*A amplification residuals, Bottom left: standard deviation of empirical transfer functions, Bottom middle: standard deviation of observed and predicted *PS*A amplification residuals.

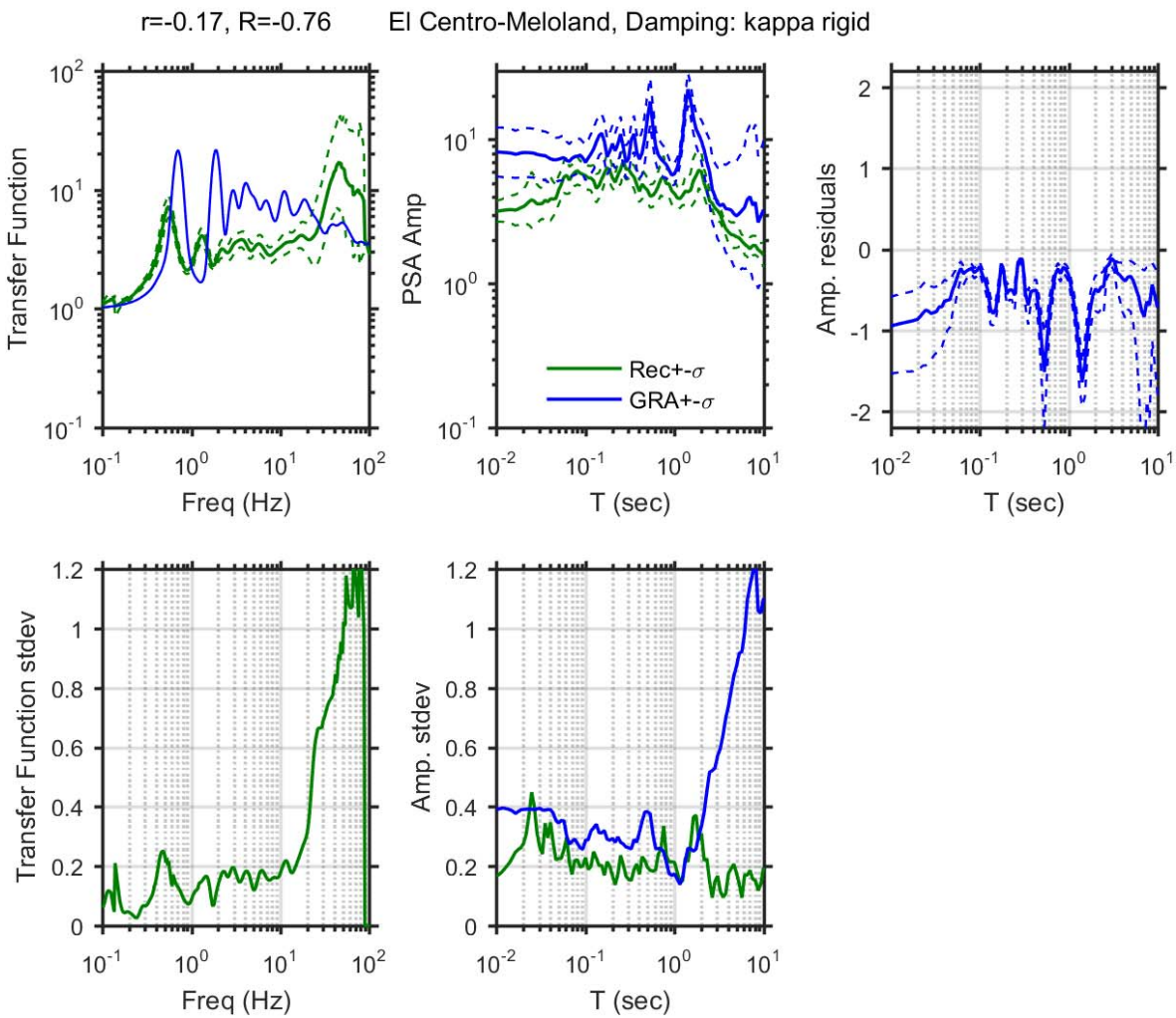

Figure A 29. Observed and simulated site response for El Centro-Meloland site with κ-informed model for damping; Top left: Theoretical and median ± standard deviation of empirical transfer functions, Top middle: observed and predicted median ± standard deviation of *PS*A amplification, Top right: median ± standard deviation of *PS*A amplification residuals, Bottom left: standard deviation of empirical transfer functions, Bottom middle: standard deviation of observed and predicted *PS*A amplification residuals.

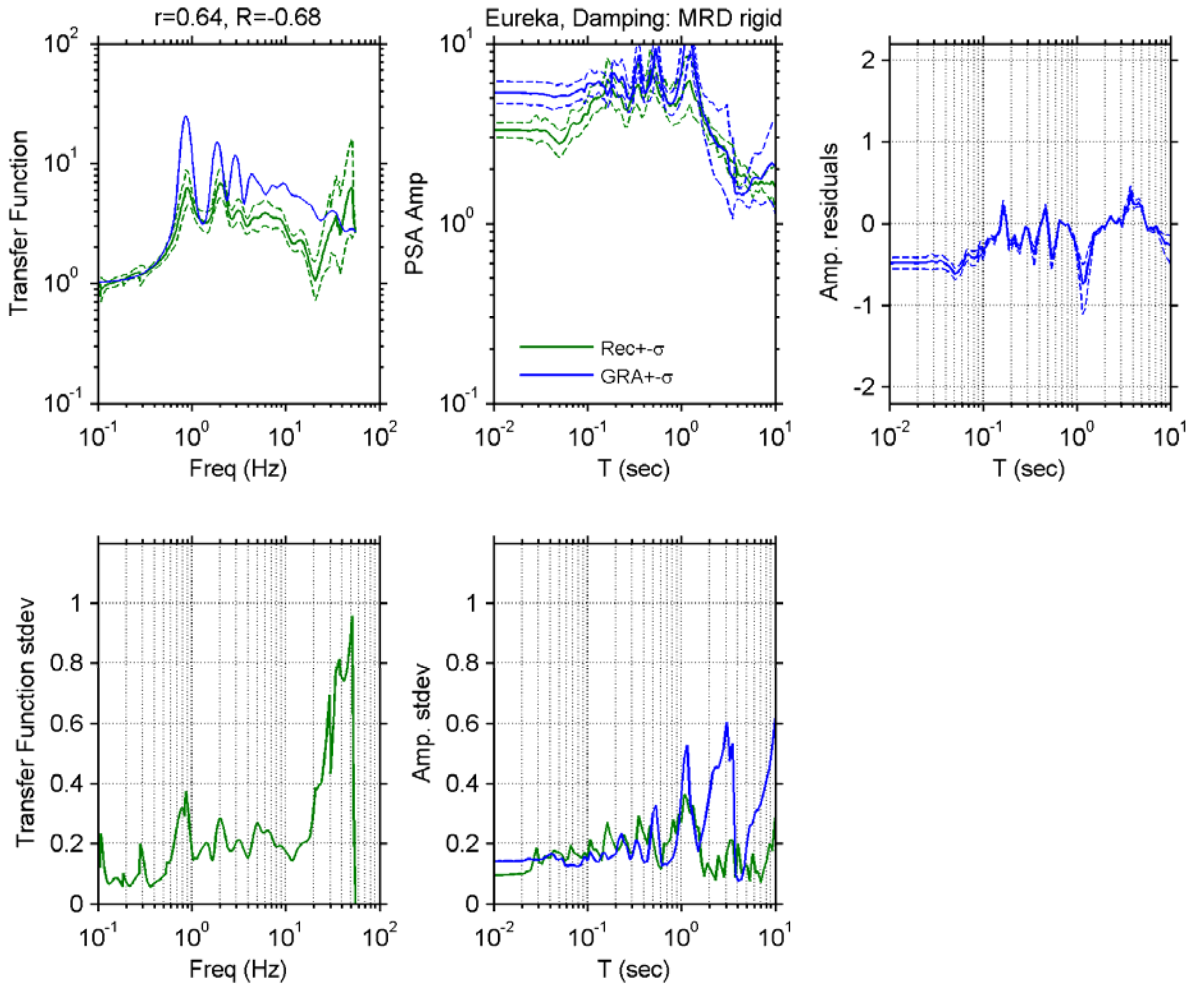

Figure A 30. Observed and simulated site response for Eureka site with $D^{L}_{\min}$ model for damping; Top left: Theoretical and median ± standard deviation of empirical transfer functions, Top middle: observed and predicted median ± standard deviation of *PS*A amplification, Top right: median ± standard deviation of *PS*A amplification residuals, Bottom left: standard deviation of empirical transfer functions, Bottom middle: standard deviation of observed and predicted *PS*A amplification residuals.

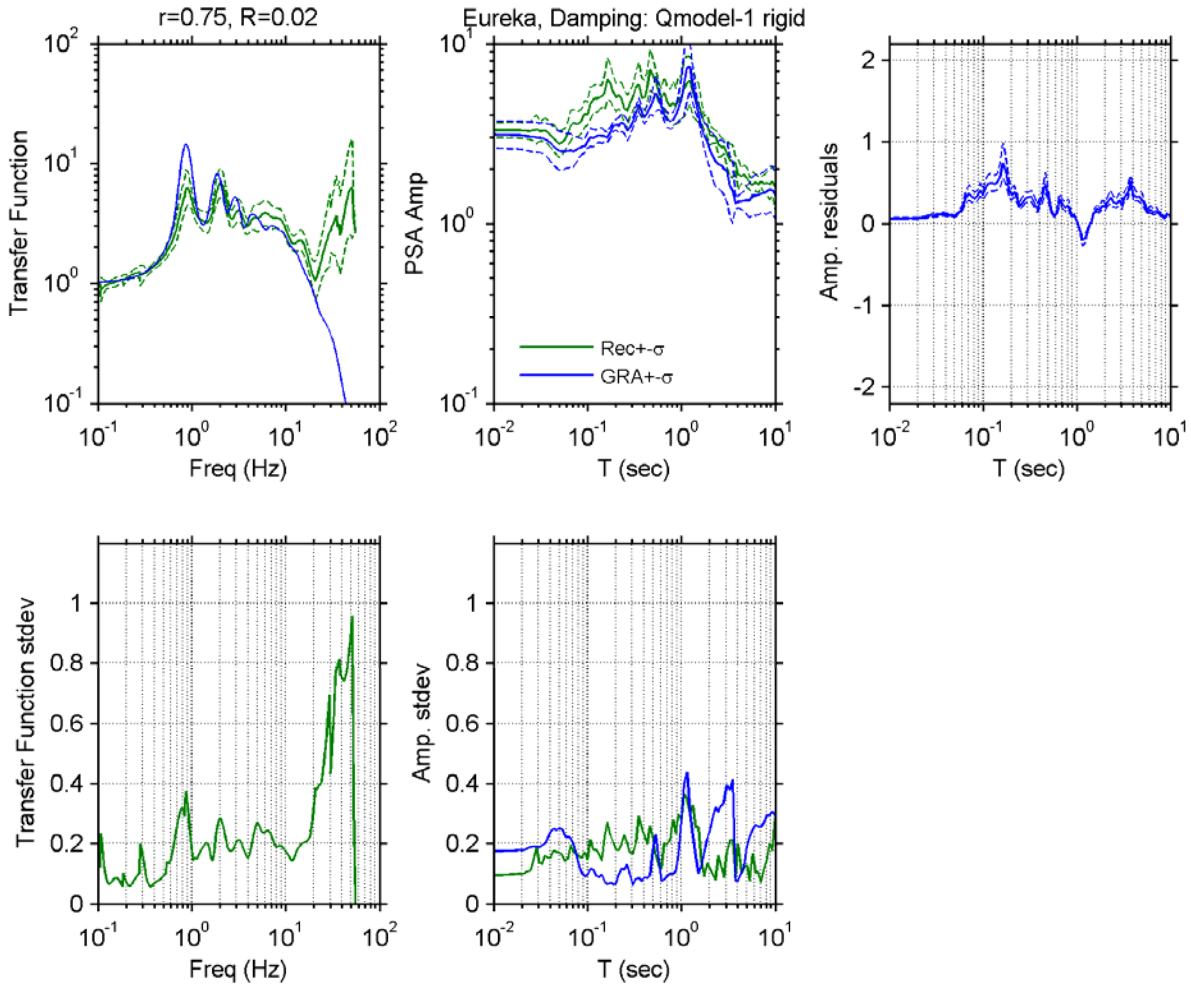

Figure A 31. Observed and simulated site response for Eureka site with V_S-based model for damping; Top left: Theoretical and median ± standard deviation of empirical transfer functions, Top middle: observed and predicted median ± standard deviation of *PS*A amplification, Top right: median ± standard deviation of *PS*A amplification residuals, Bottom left: standard deviation of empirical transfer functions, Bottom middle: standard deviation of observed and predicted *PS*A amplification residuals.

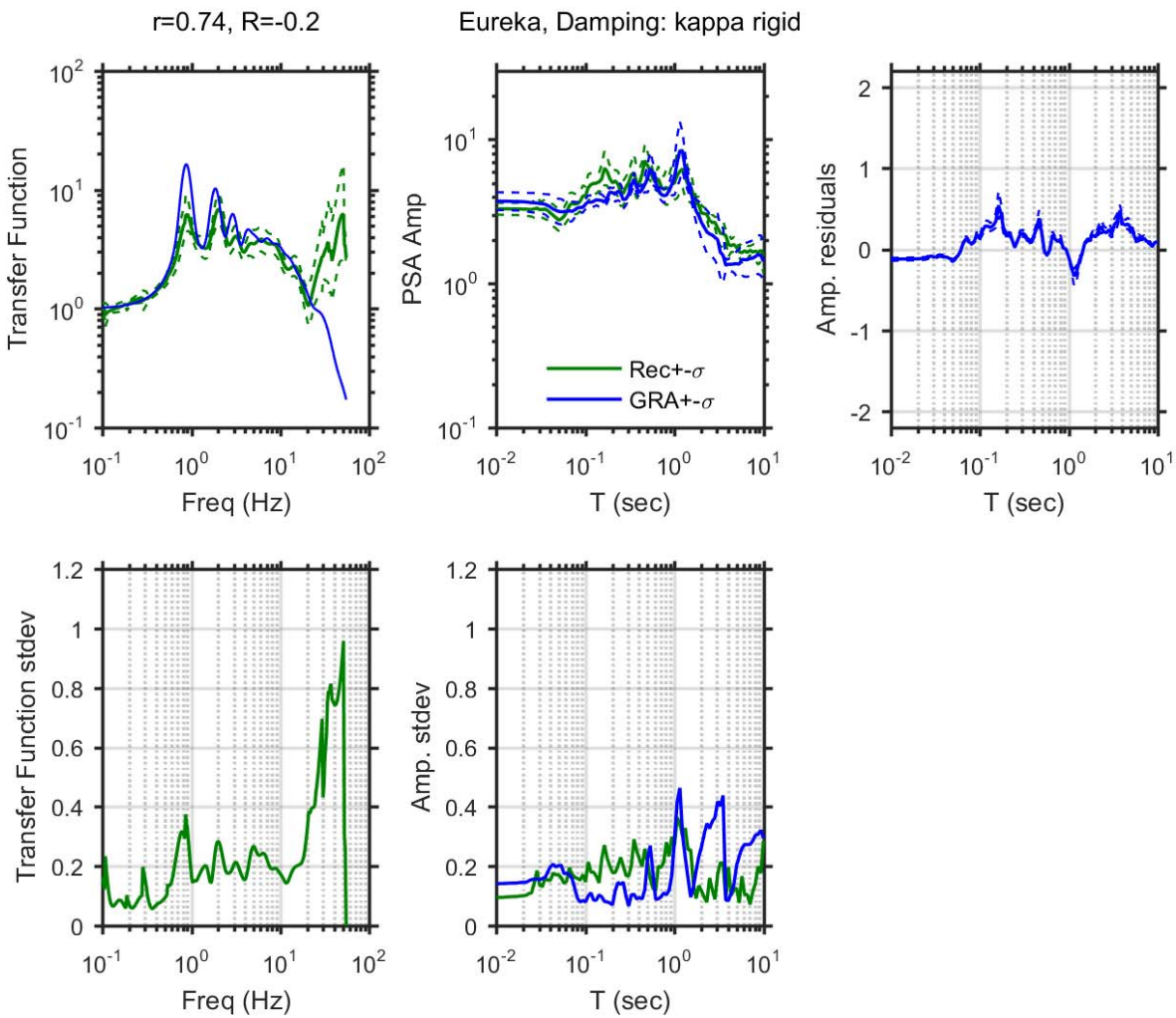

Figure A 32. Observed and simulated site response for Eureka site with κ-informed model for damping; Top left: Theoretical and median ± standard deviation of empirical transfer functions, Top middle: observed and predicted median ± standard deviation of *PS*A amplification, Top right: median ± standard deviation of *PS*A amplification residuals, Bottom left: standard deviation of empirical transfer functions, Bottom middle: standard deviation of observed and predicted *PS*A amplification residuals.

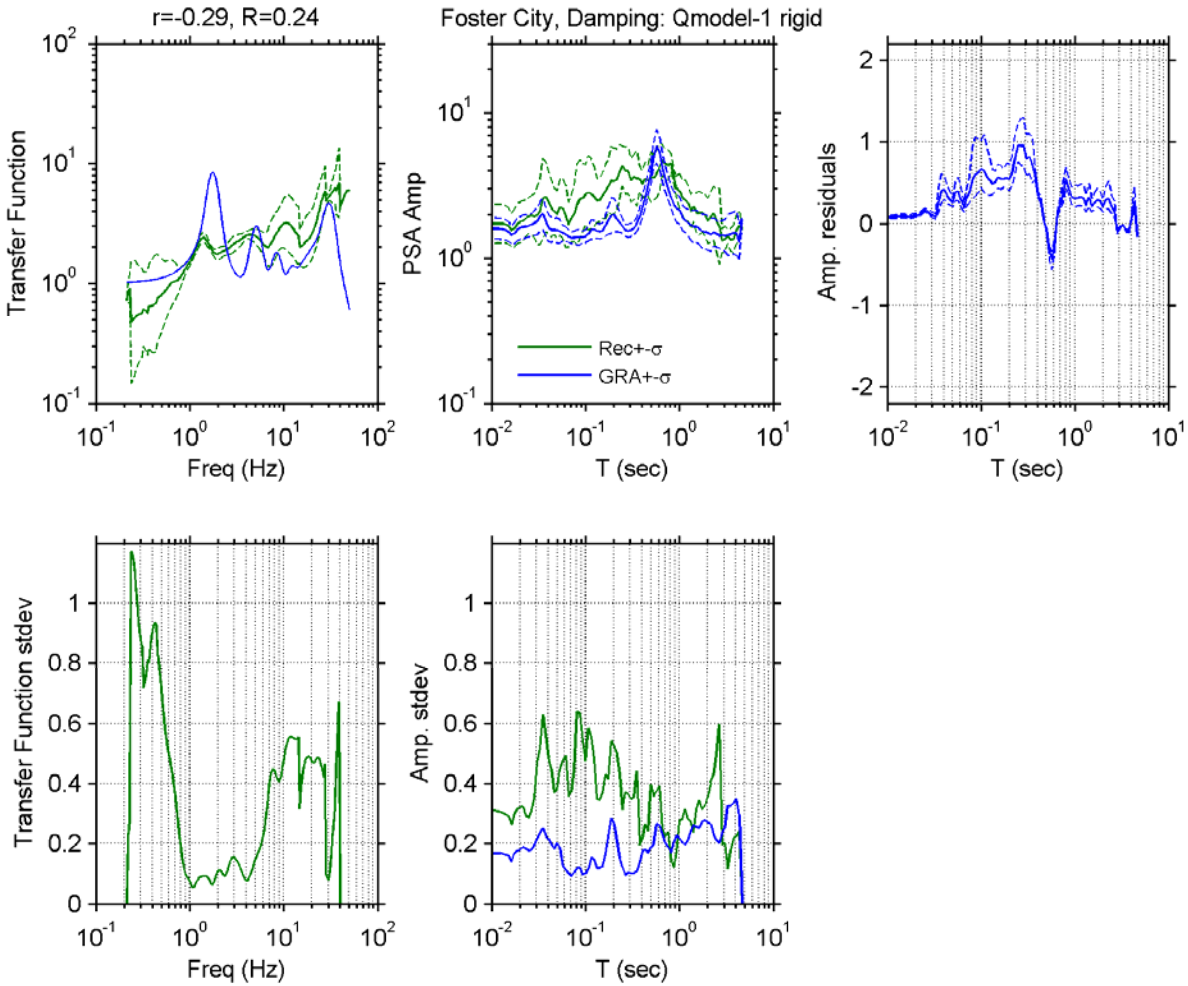

Figure A 33. Observed and simulated site response for Foster City-San Mateo site with V_S-based model for damping; Top left: Theoretical and median ± standard deviation of empirical transfer functions, Top middle: observed and predicted median ± standard deviation of *PS*A amplification, Top right: median ± standard deviation of *PS*A amplification residuals, Bottom left: standard deviation of empirical transfer functions, Bottom middle: standard deviation of observed and predicted *PS*A amplification residuals.

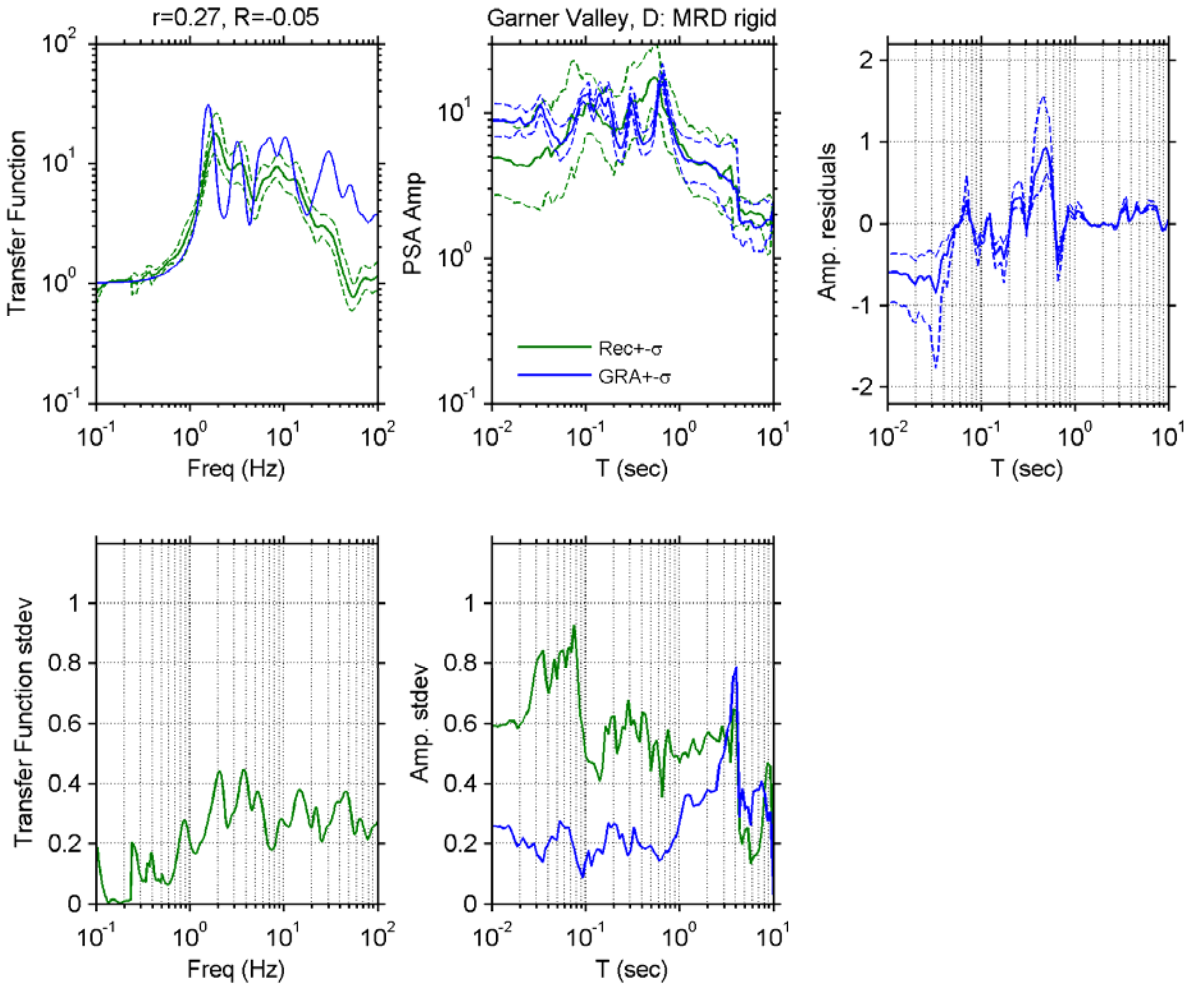

Figure A 34. Observed and simulated site response for Garner Valley site with $D^{L}_{\min}$ model for damping; Top left: Theoretical and median ± standard deviation of empirical transfer functions, Top middle: observed and predicted median ± standard deviation of *PS*A amplification, Top right: median ± standard deviation of *PS*A amplification residuals, Bottom left: standard deviation of empirical transfer functions, Bottom middle: standard deviation of observed and predicted *PS*A amplification residuals.

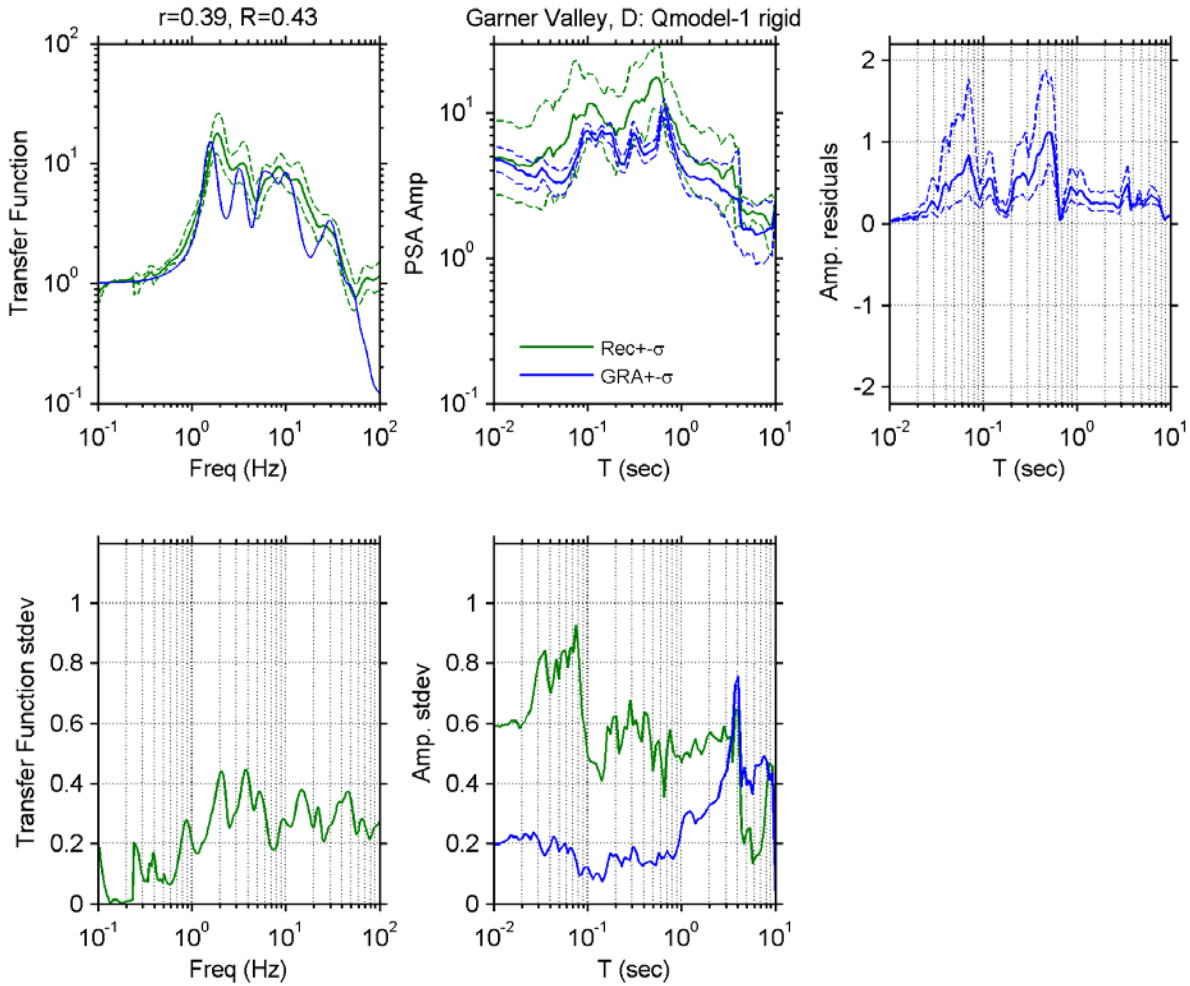

Figure A 35. Observed and simulated site response for Garner Valley site with V_S-based model for damping; Top left: Theoretical and median ± standard deviation of empirical transfer functions, Top middle: observed and predicted median ± standard deviation of *PS*A amplification, Top right: median ± standard deviation of *PS*A amplification residuals, Bottom left: standard deviation of empirical transfer functions, Bottom middle: standard deviation of observed and predicted *PS*A amplification residuals.

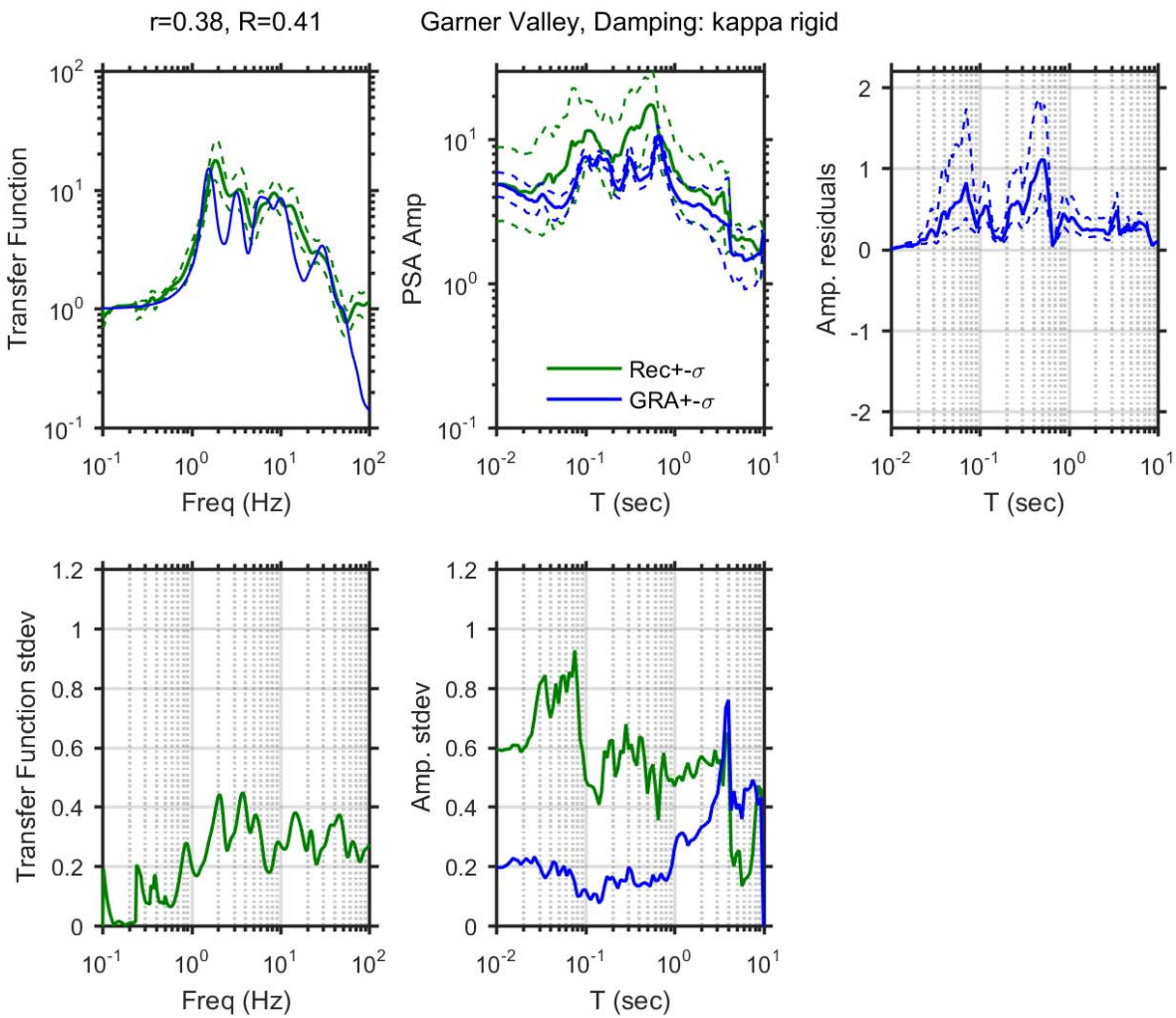

Figure A 36. Observed and simulated site response for Garner Valley site with κ-informed model for damping; Top left: Theoretical and median ± standard deviation of empirical transfer functions, Top middle: observed and predicted median ± standard deviation of *PS*A amplification, Top right: median ± standard deviation of *PS*A amplification residuals, Bottom left: standard deviation of empirical transfer functions, Bottom middle: standard deviation of observed and predicted *PS*A amplification residuals.

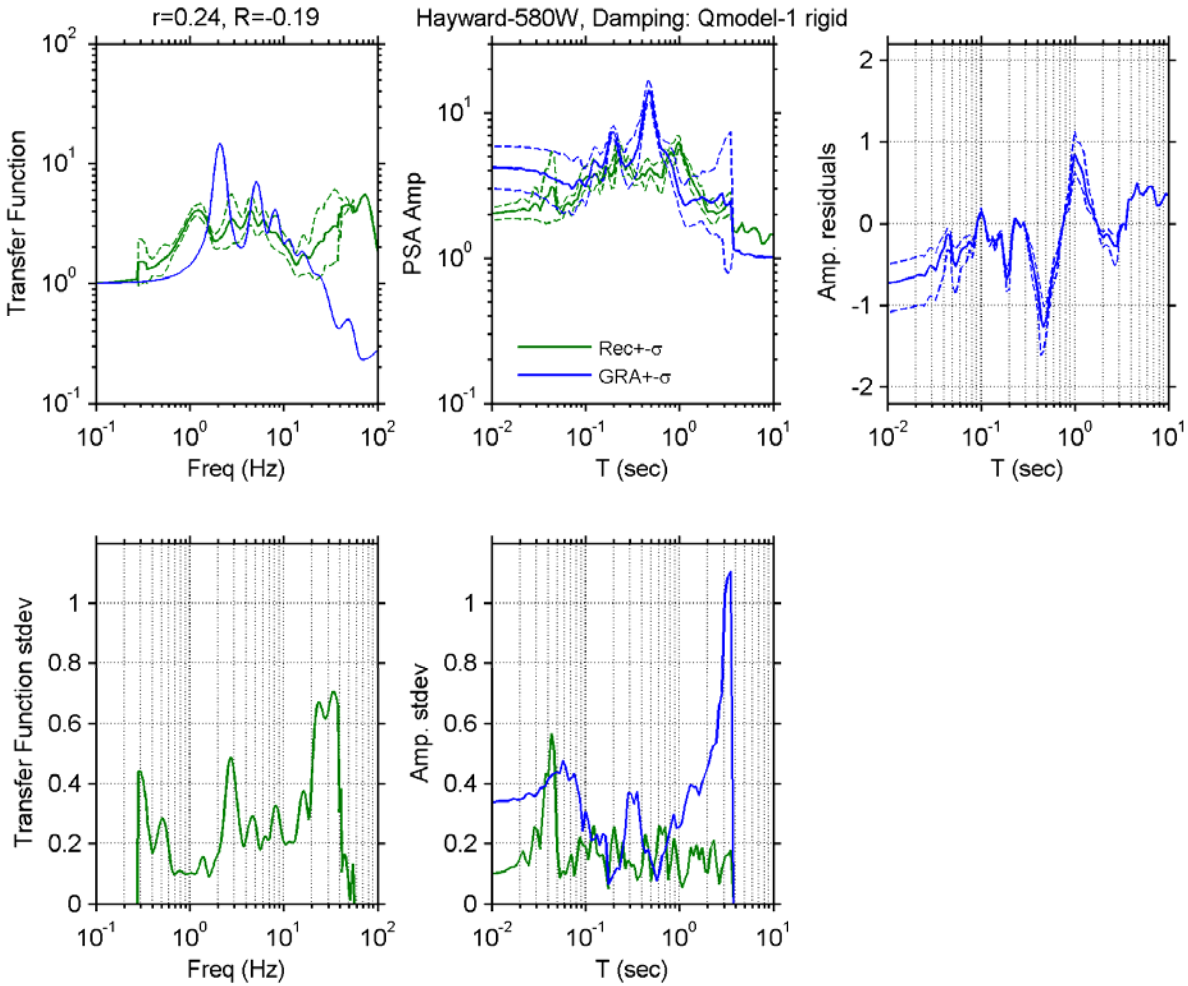

Figure A 37. Observed and simulated site response for Hayward - I580/238 West site with V_S-based model for damping; Top left: Theoretical and median ± standard deviation of empirical transfer functions, Top middle: observed and predicted median ± standard deviation of *PS*A amplification, Top right: median ± standard deviation of *PS*A amplification residuals, Bottom left: standard deviation of empirical transfer functions, Bottom middle: standard deviation of observed and predicted *PS*A amplification residuals.

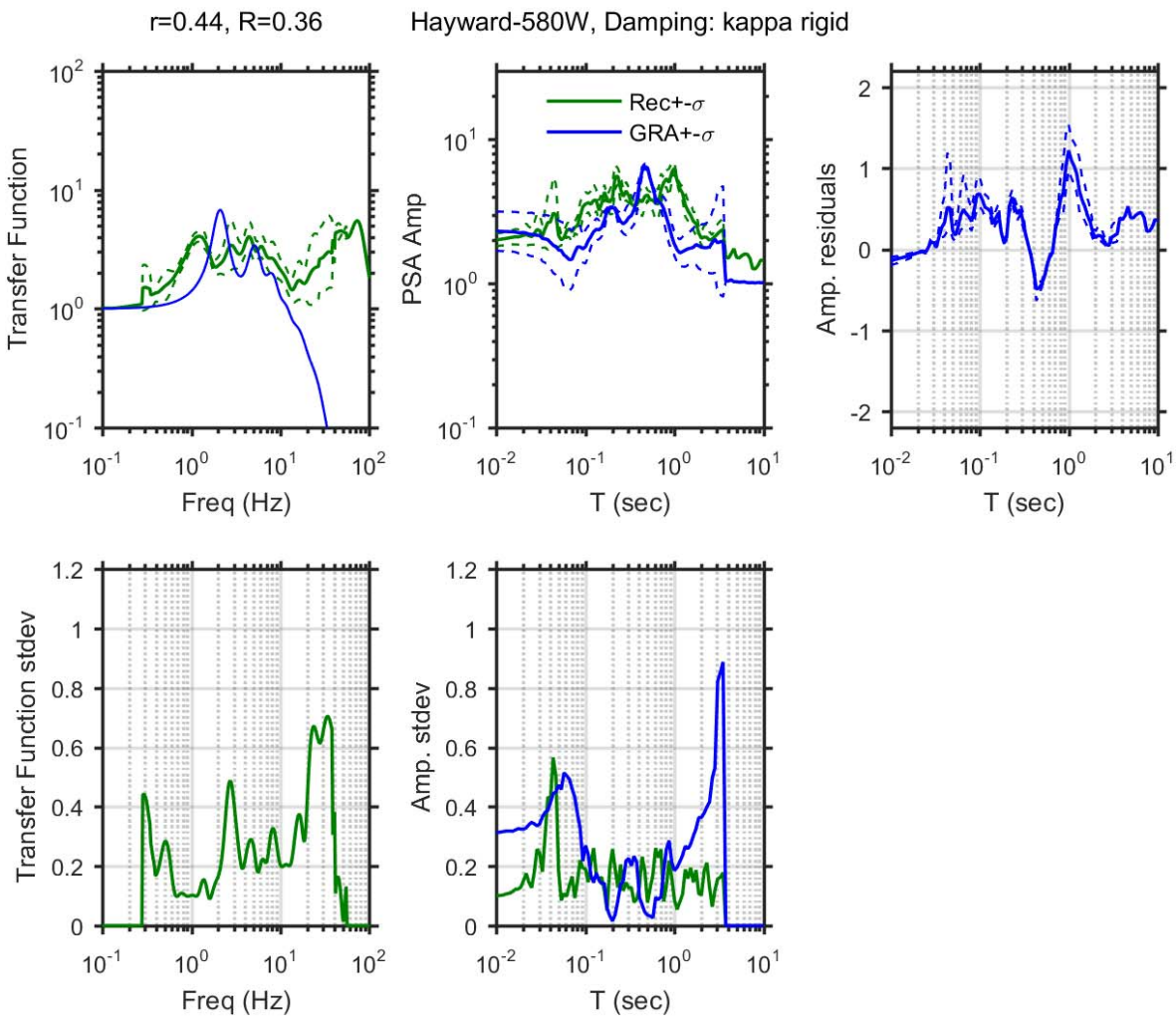

Figure A 38. Observed and simulated site response for Hayward - I580/238 West site with κ-informed model for damping; Top left: Theoretical and median ± standard deviation of empirical transfer functions, Top middle: observed and predicted median ± standard deviation of *PS*A amplification, Top right: median ± standard deviation of *PS*A amplification residuals, Bottom left: standard deviation of empirical transfer functions, Bottom middle: standard deviation of observed and predicted *PS*A amplification residuals.

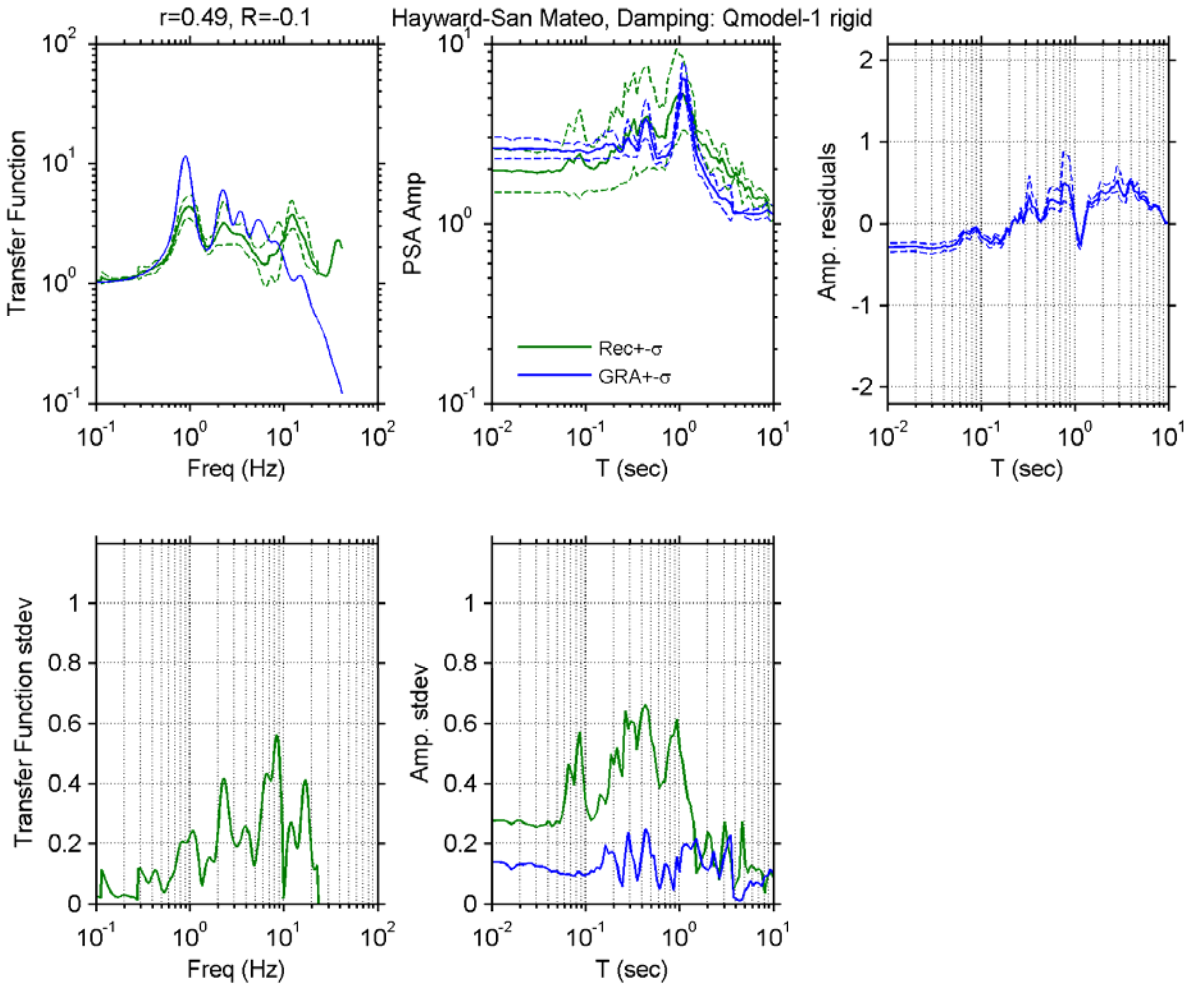

Figure A 39. Observed and simulated site response for Hayward - San Mateo Br site with V_S-based model for damping; Top left: Theoretical and median ± standard deviation of empirical transfer functions, Top middle: observed and predicted median ± standard deviation of *PS*A amplification, Top right: median ± standard deviation of *PS*A amplification residuals, Bottom left: standard deviation of empirical transfer functions, Bottom middle: standard deviation of observed and predicted *PS*A amplification residuals.

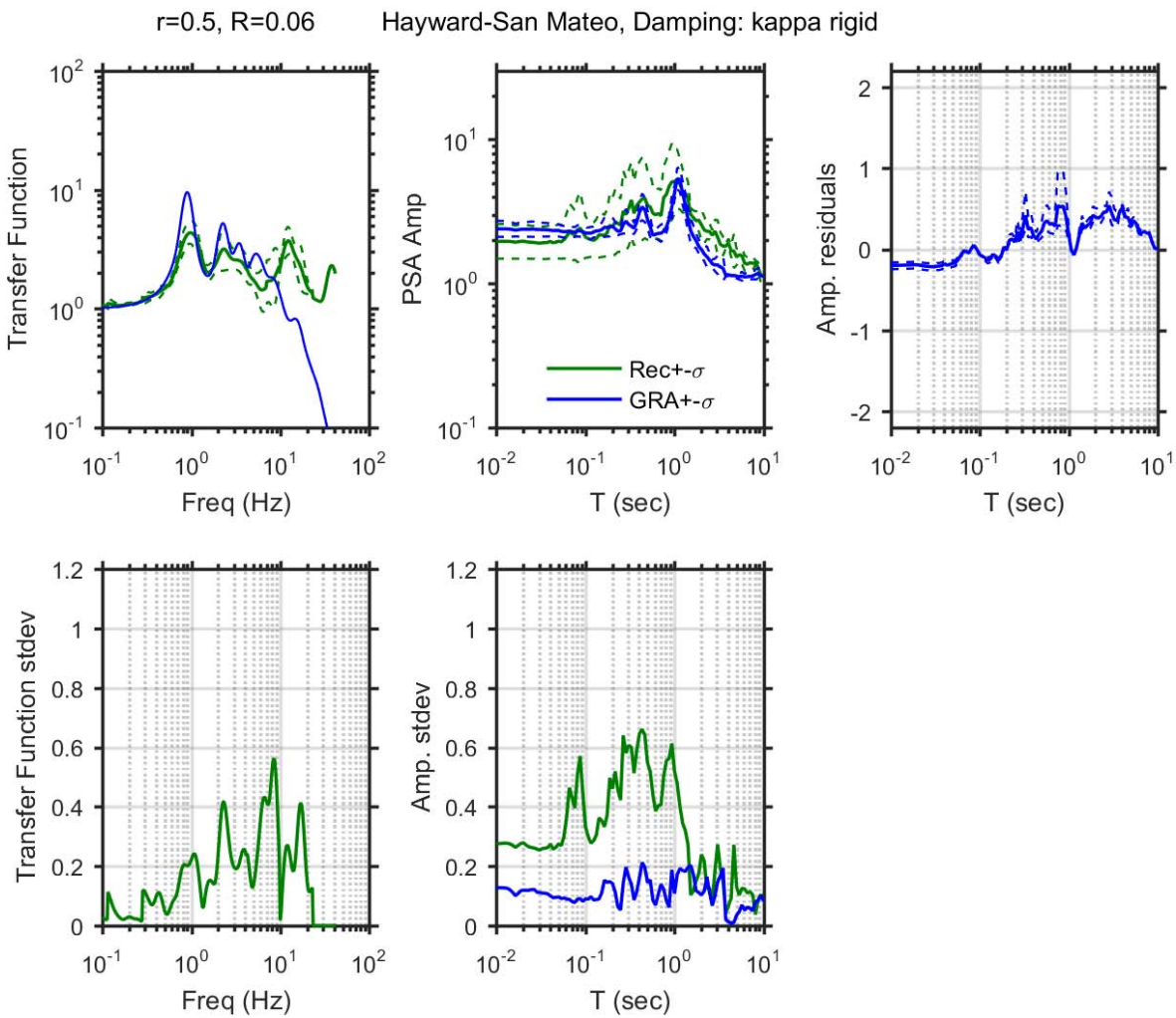

Figure A 40. Observed and simulated site response for Hayward - San Mateo Br site with κ-informed model for damping; Top left: Theoretical and median ± standard deviation of empirical transfer functions, Top middle: observed and predicted median ± standard deviation of *PS*A amplification, Top right: median ± standard deviation of *PS*A amplification residuals, Bottom left: standard deviation of empirical transfer functions, Bottom middle: standard deviation of observed and predicted *PS*A amplification residuals.

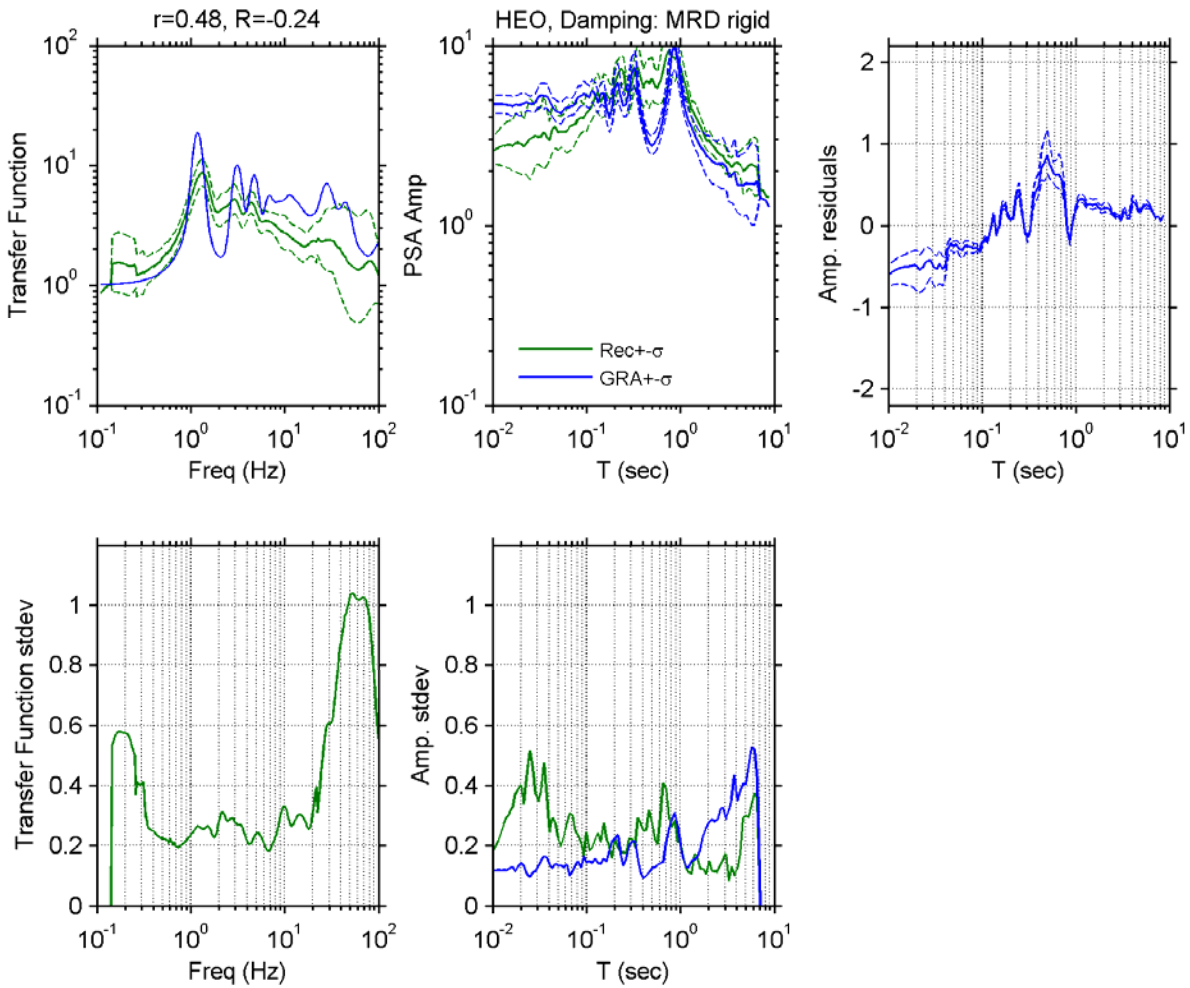

Figure A 41. Observed and simulated site response for Hollister Digital Array (HEO) site with $D^{L}_{\min}$ model for damping; Top left: Theoretical and median ± standard deviation of empirical transfer functions, Top middle: observed and predicted median ± standard deviation of *PS*A amplification, Top right: median ± standard deviation of *PS*A amplification residuals, Bottom left: standard deviation of empirical transfer functions, Bottom middle: standard deviation of observed and predicted *PS*A amplification residuals.

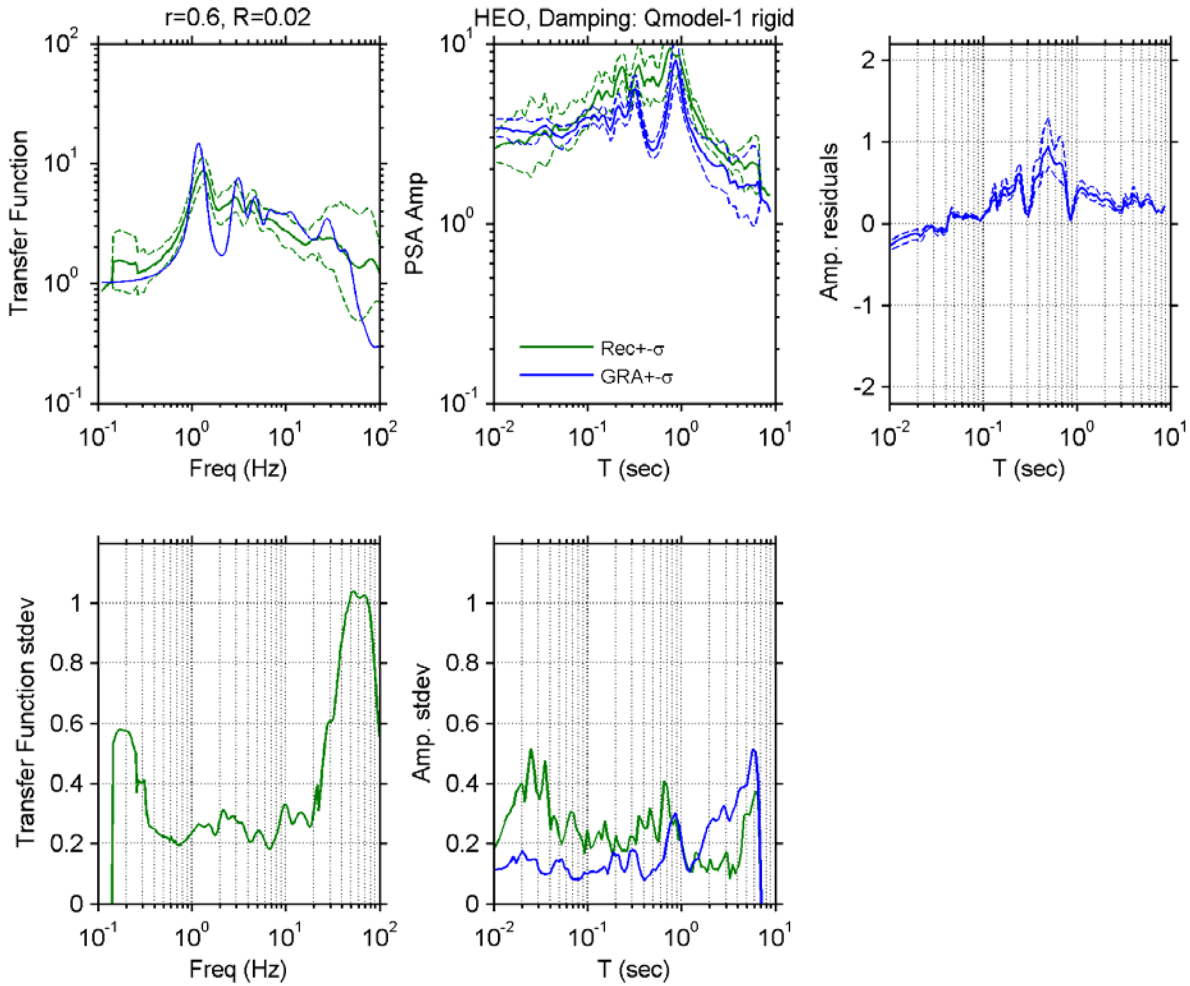

Figure A 42. Observed and simulated site response for Hollister Digital Array (HEO) site with V_S-based model for damping; Top left: Theoretical and median ± standard deviation of empirical transfer functions, Top middle: observed and predicted median ± standard deviation of *PS*A amplification, Top right: median ± standard deviation of *PS*A amplification residuals, Bottom left: standard deviation of empirical transfer functions, Bottom middle: standard deviation of observed and predicted *PS*A amplification residuals.

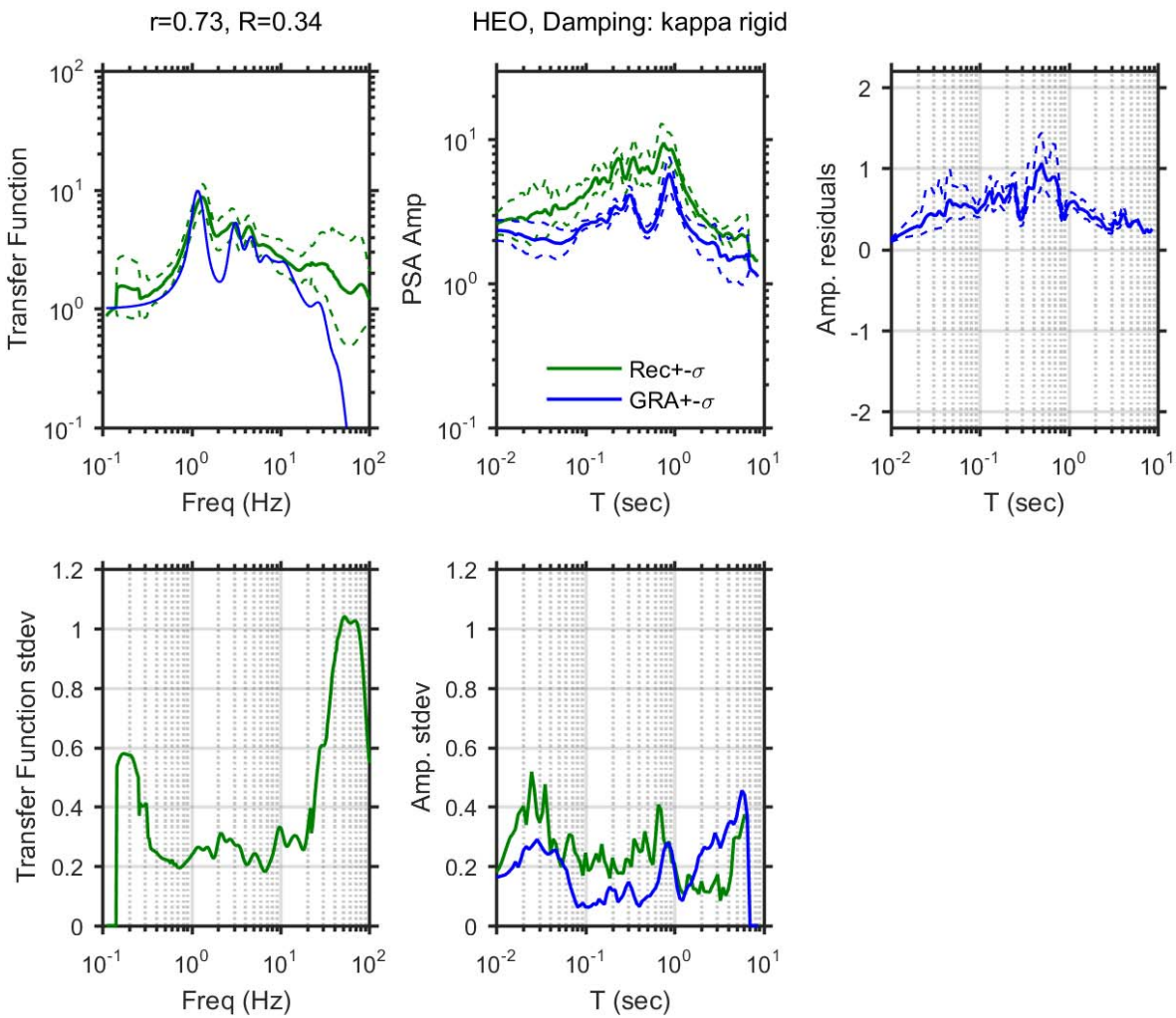

Figure A 43. Observed and simulated site response for Hollister Digital Array (HEO) site with κ-informed model for damping; Top left: Theoretical and median ± standard deviation of empirical transfer functions, Top middle: observed and predicted median ± standard deviation of *PS*A amplification, Top right: median ± standard deviation of *PS*A amplification residuals, Bottom left: standard deviation of empirical transfer functions, Bottom middle: standard deviation of observed and predicted *PS*A amplification residuals.

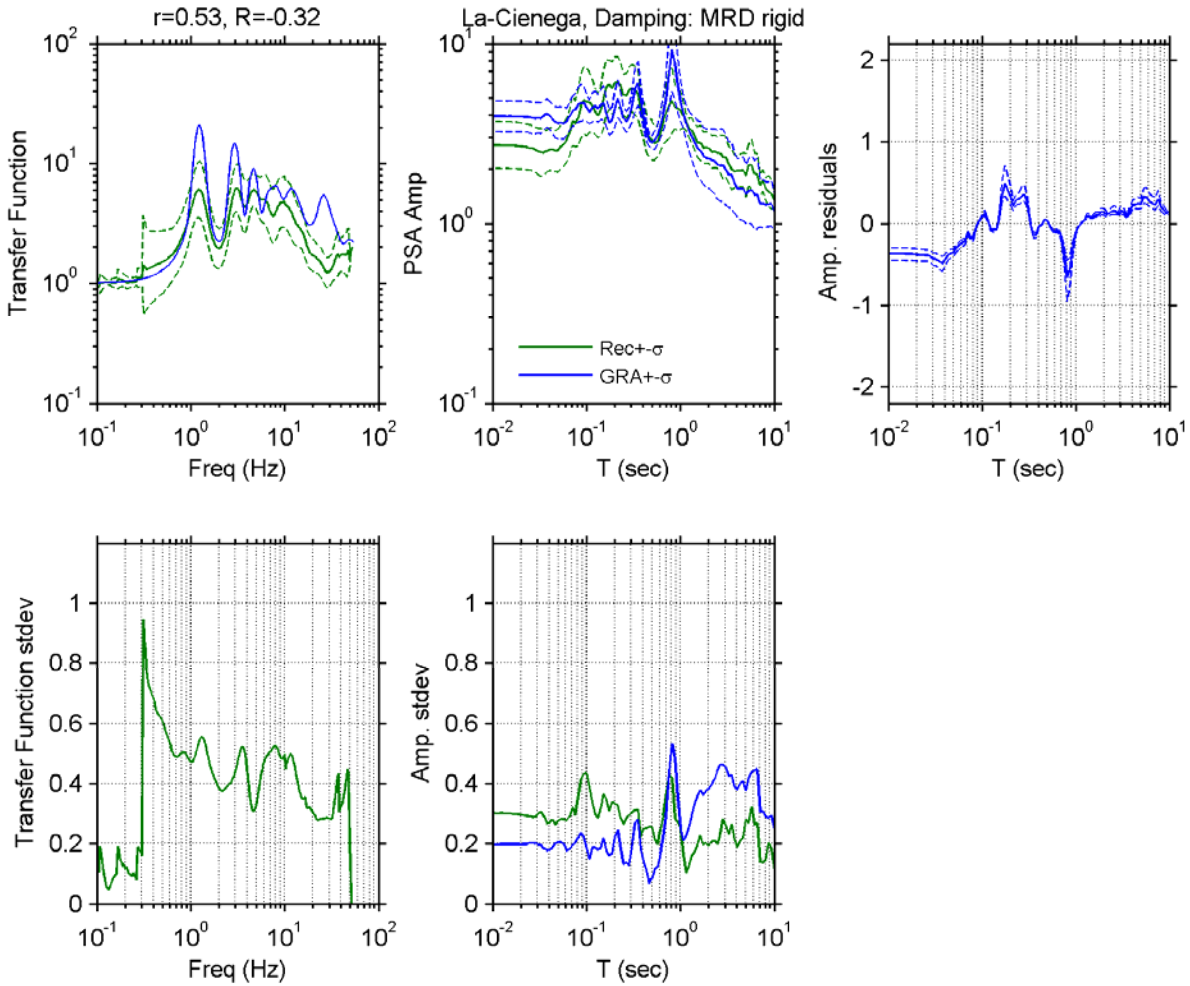

Figure A 44. Observed and simulated site response for La-Cienega site with $D_{\min}^{L}$ model for damping; Top left: Theoretical and median ± standard deviation of empirical transfer functions, Top middle: observed and predicted median ± standard deviation of *PS*A amplification, Top right: median ± standard deviation of *PS*A amplification residuals, Bottom left: standard deviation of empirical transfer functions, Bottom middle: standard deviation of observed and predicted *PS*A amplification residuals.

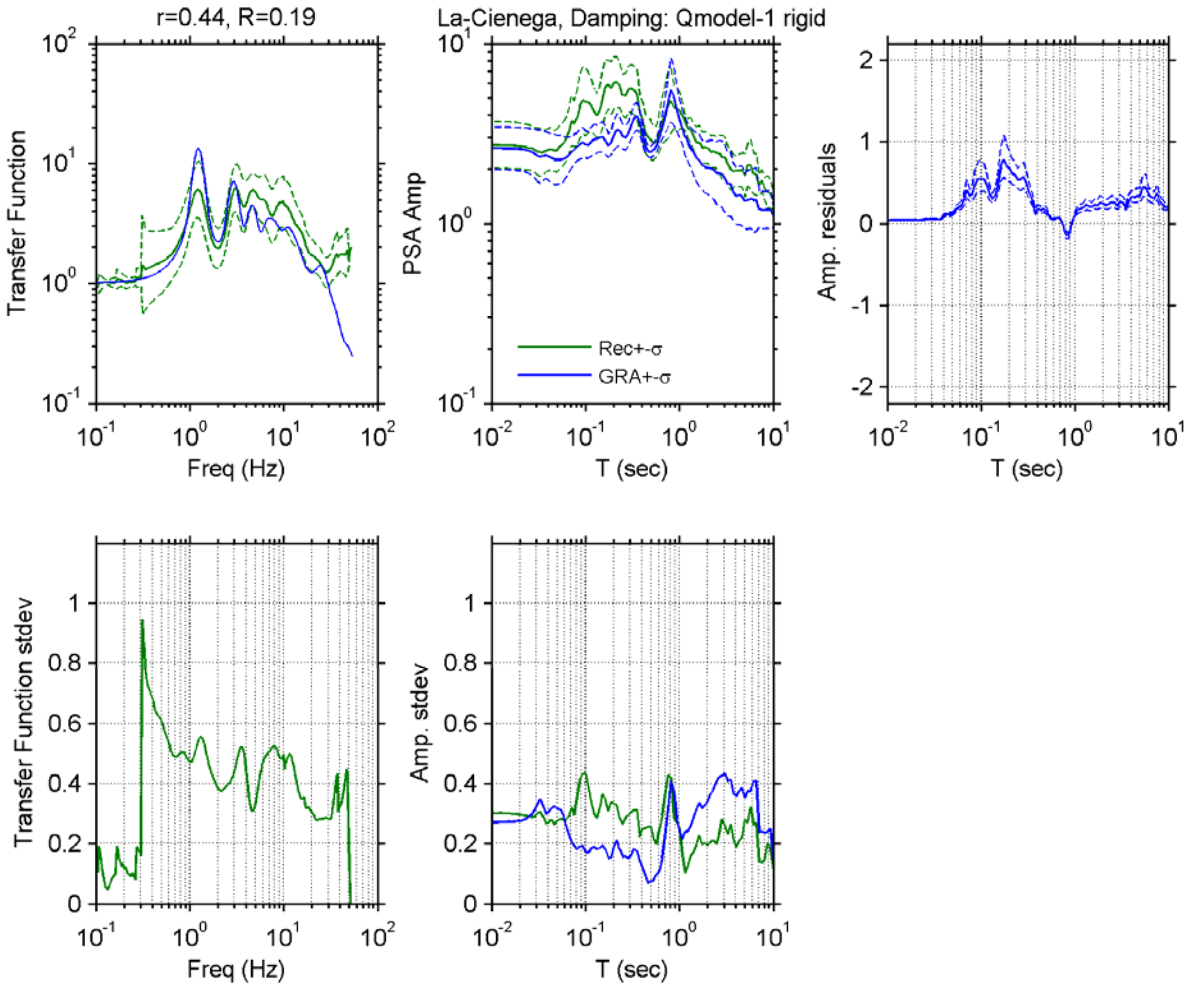

Figure A 45. Observed and simulated site response for La-Cienega site with V_S-based model for damping; Top left: Theoretical and median ± standard deviation of empirical transfer functions, Top middle: observed and predicted median ± standard deviation of *PS*A amplification, Top right: median ± standard deviation of *PS*A amplification residuals, Bottom left: standard deviation of empirical transfer functions, Bottom middle: standard deviation of observed and predicted *PS*A amplification residuals.

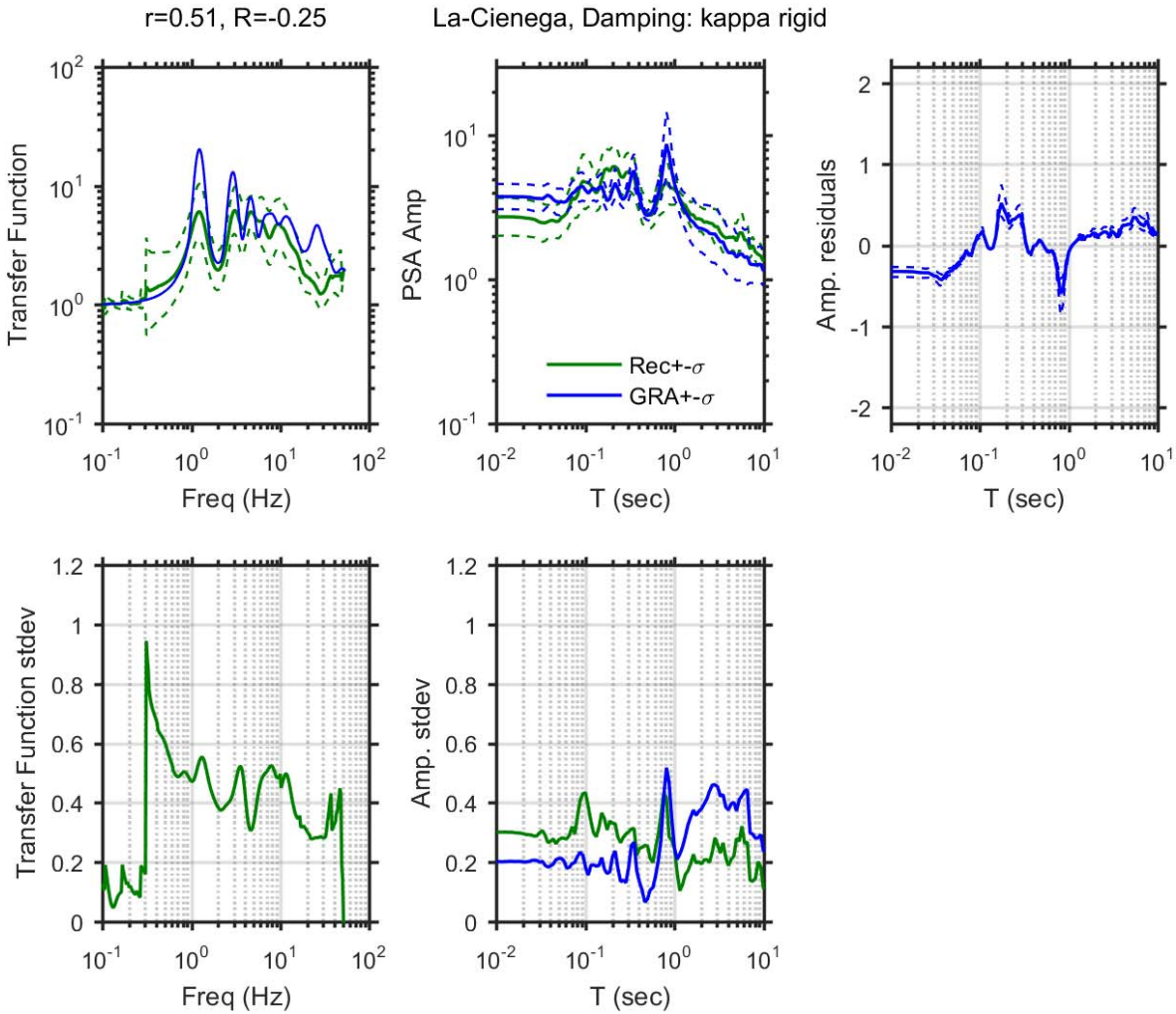

Figure A 46. Observed and simulated site response for La-Cienega site with κ-informed model for damping; Top left: Theoretical and median ± standard deviation of empirical transfer functions, Top middle: observed and predicted median ± standard deviation of *PS*A amplification, Top right: median ± standard deviation of *PS*A amplification residuals, Bottom left: standard deviation of empirical transfer functions, Bottom middle: standard deviation of observed and predicted *PS*A amplification residuals.

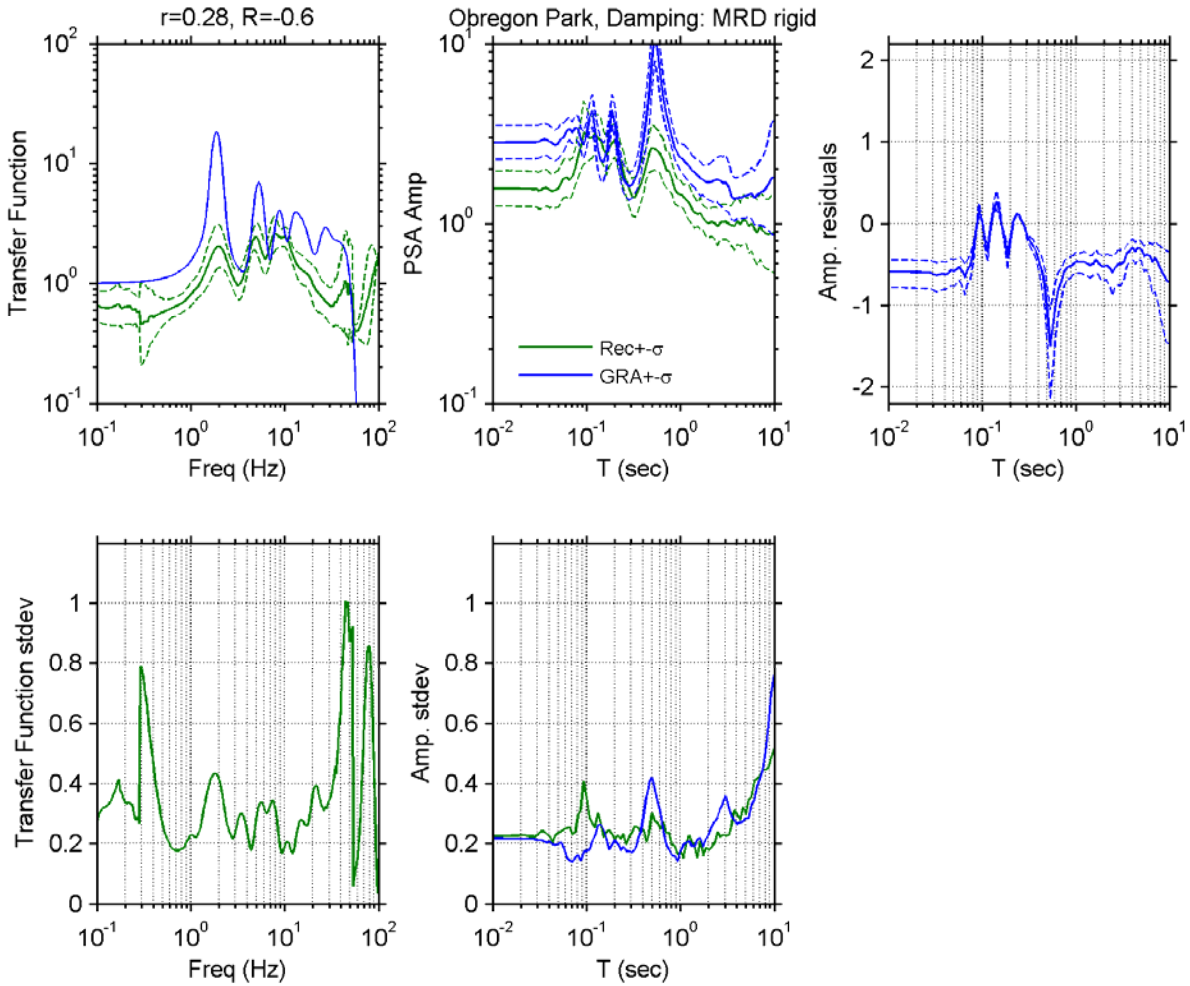

Figure A 47. Observed and simulated site response for Obregon Park site with $D^{L}_{\min}$ model for damping; Top left: Theoretical and median ± standard deviation of empirical transfer functions, Top middle: observed and predicted median ± standard deviation of *PS*A amplification, Top right: median ± standard deviation of *PS*A amplification residuals, Bottom left: standard deviation of empirical transfer functions, Bottom middle: standard deviation of observed and predicted *PS*A amplification residuals.

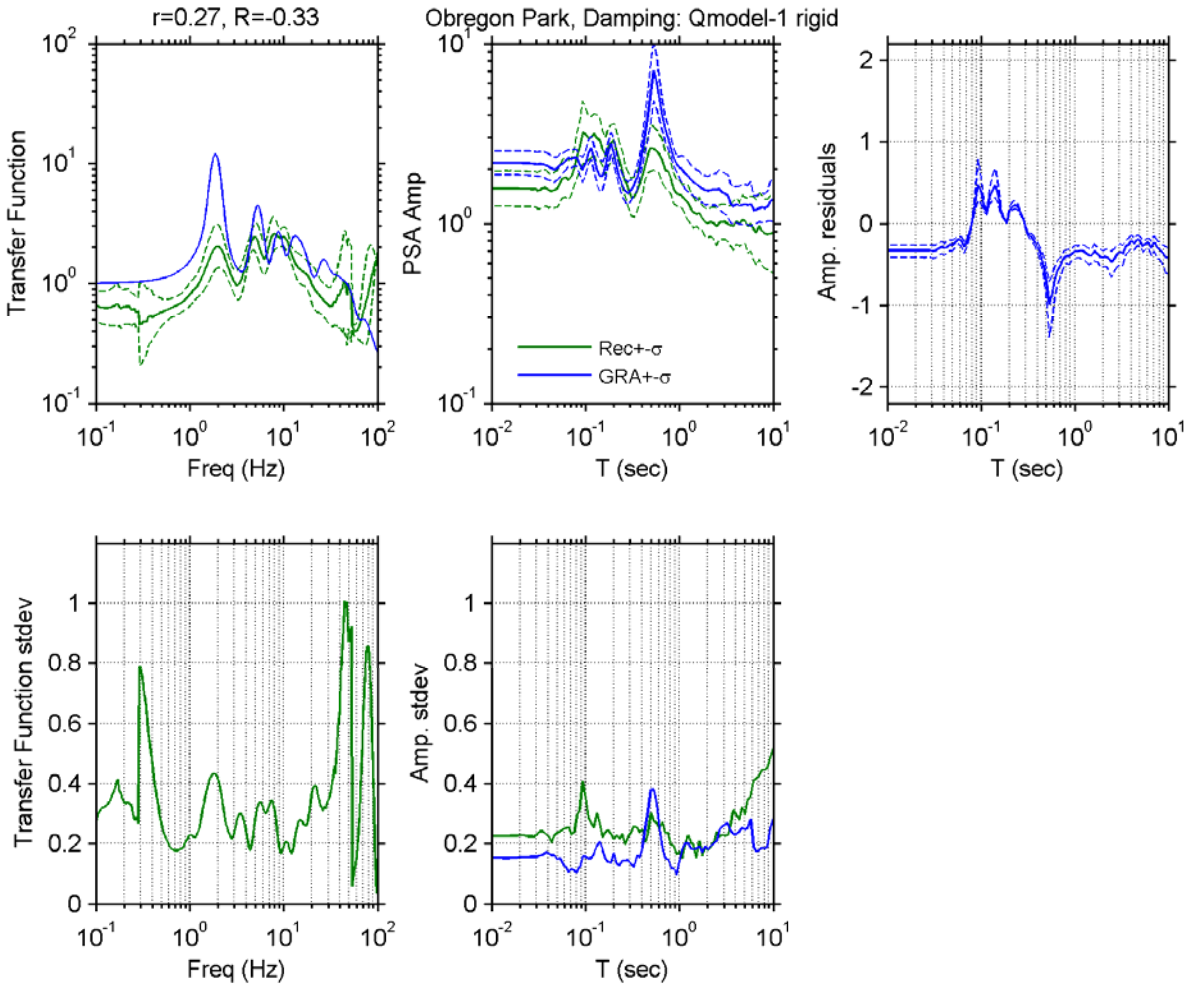

Figure A 48. Observed and simulated site response for Obregon Park site with V_S-based model for damping; Top left: Theoretical and median ± standard deviation of empirical transfer functions, Top middle: observed and predicted median ± standard deviation of *PS*A amplification, Top right: median ± standard deviation of *PS*A amplification residuals, Bottom left: standard deviation of empirical transfer functions, Bottom middle: standard deviation of observed and predicted *PS*A amplification residuals.

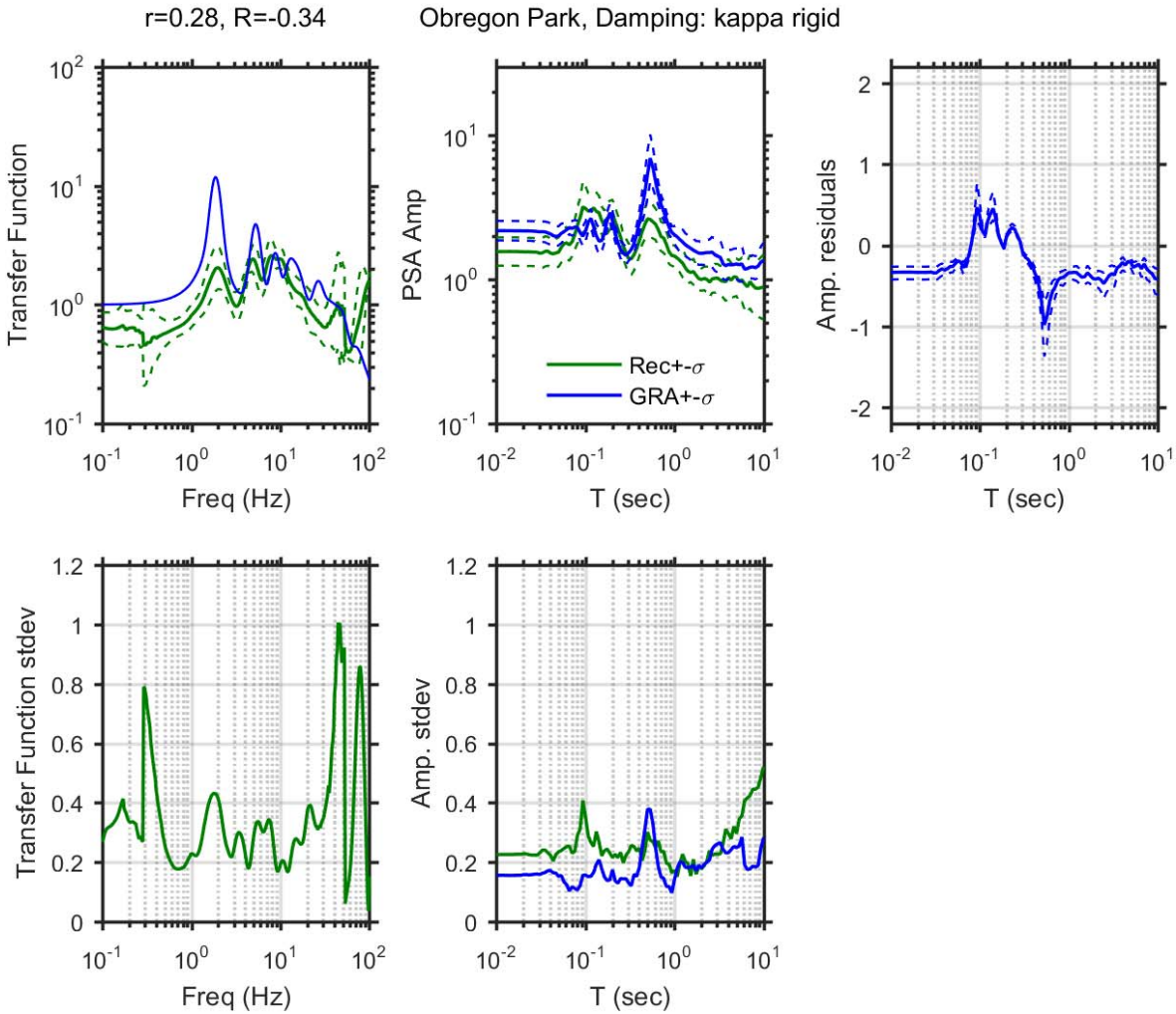

Figure A 49. Observed and simulated site response for Obregon Park site with κ-informed model for damping; Top left: Theoretical and median ± standard deviation of empirical transfer functions, Top middle: observed and predicted median ± standard deviation of *PS*A amplification, Top right: median ± standard deviation of *PS*A amplification residuals, Bottom left: standard deviation of empirical transfer functions, Bottom middle: standard deviation of observed and predicted *PS*A amplification residuals.

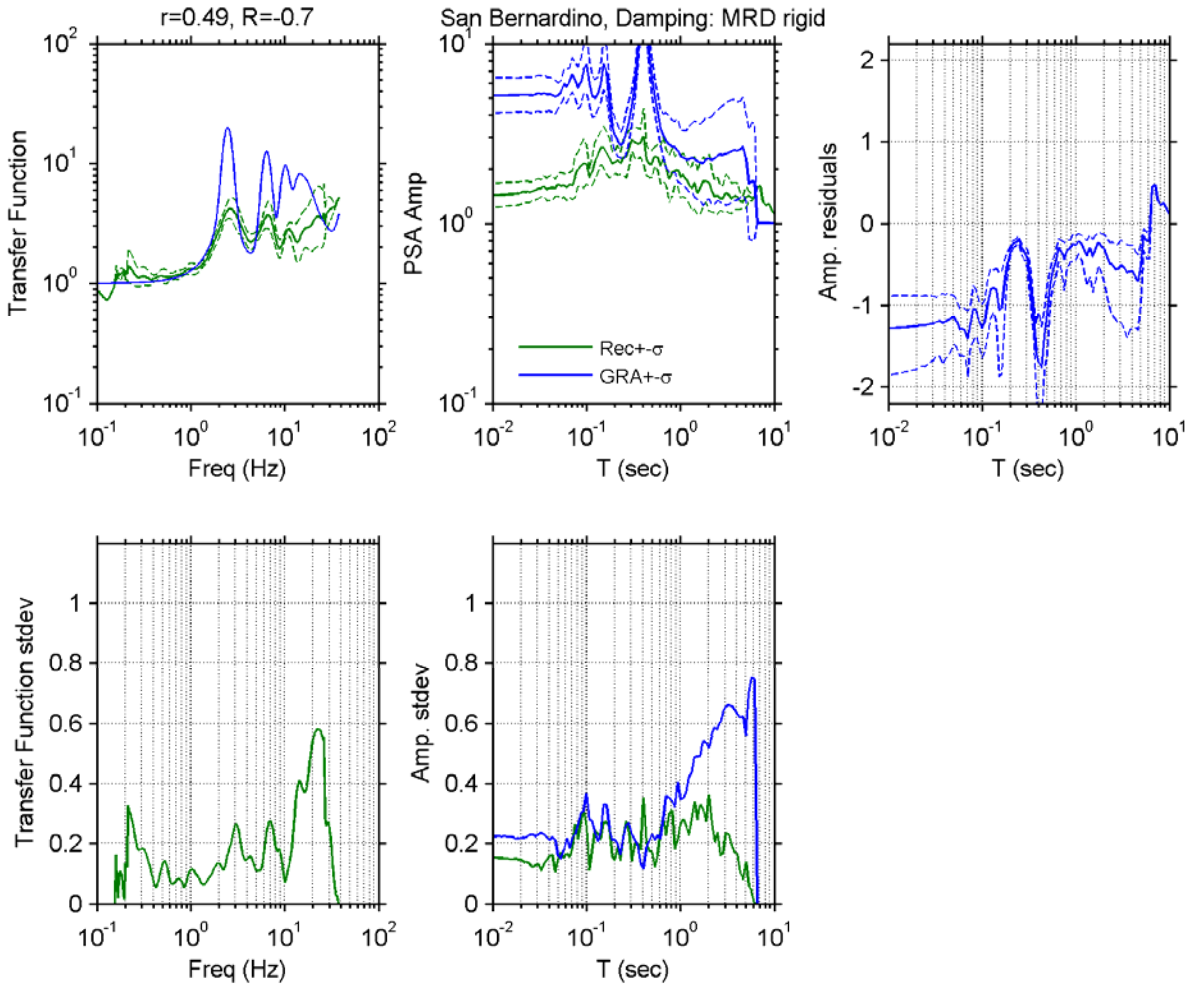

Figure A 50. Observed and simulated site response for San Bernardino site with $D_{\min}^{L}$ model for damping; Top left: Theoretical and median ± standard deviation of empirical transfer functions, Top middle: observed and predicted median ± standard deviation of *PS*A amplification, Top right: median ± standard deviation of *PS*A amplification residuals, Bottom left: standard deviation of empirical transfer functions, Bottom middle: standard deviation of observed and predicted *PS*A amplification residuals.

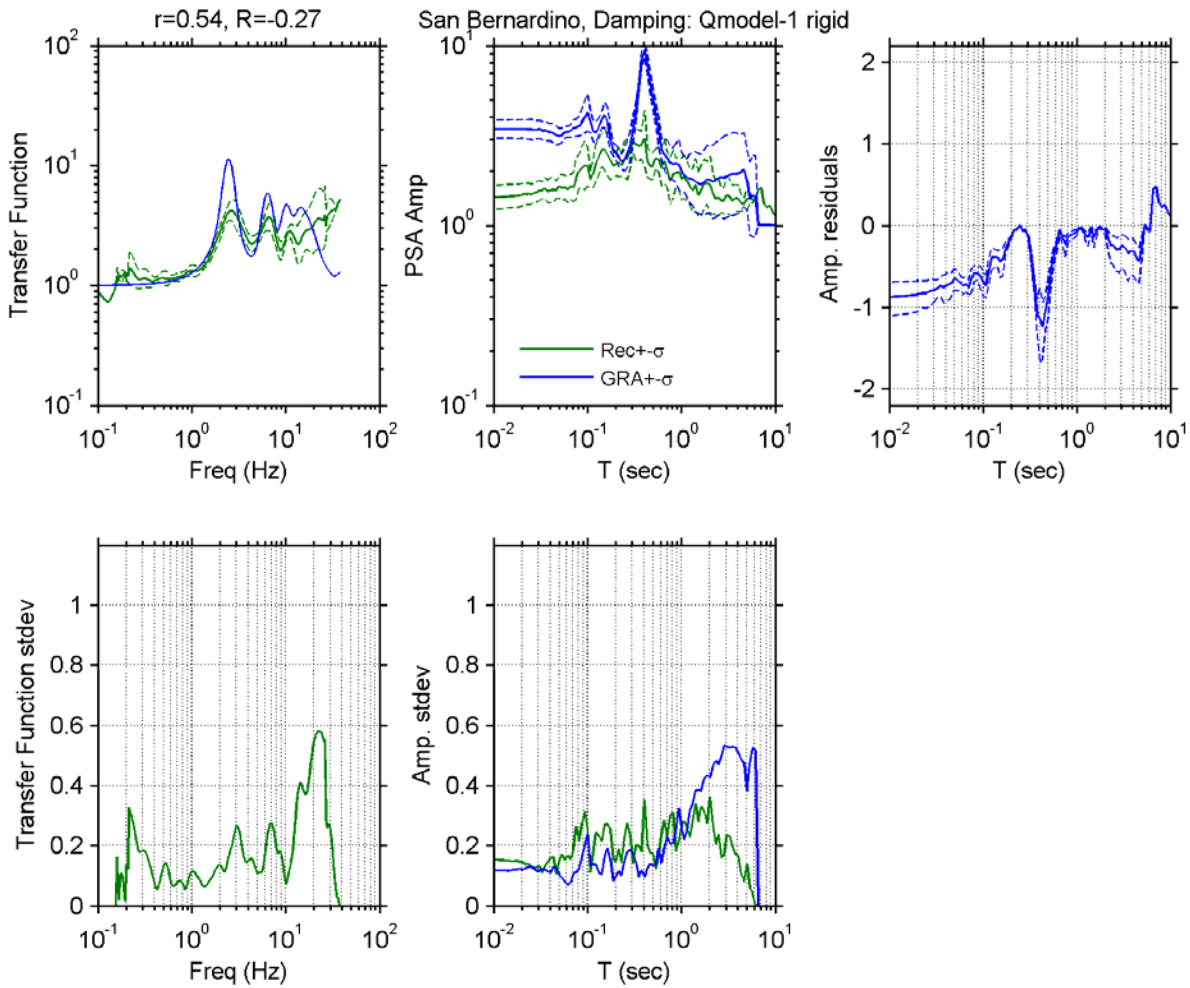

Figure A 51. Observed and simulated site response for San Bernardino site with V_S-based model for damping; Top left: Theoretical and median ± standard deviation of empirical transfer functions, Top middle: observed and predicted median ± standard deviation of *PS*A amplification, Top right: median ± standard deviation of *PS*A amplification residuals, Bottom left: standard deviation of empirical transfer functions, Bottom middle: standard deviation of observed and predicted *PS*A amplification residuals.

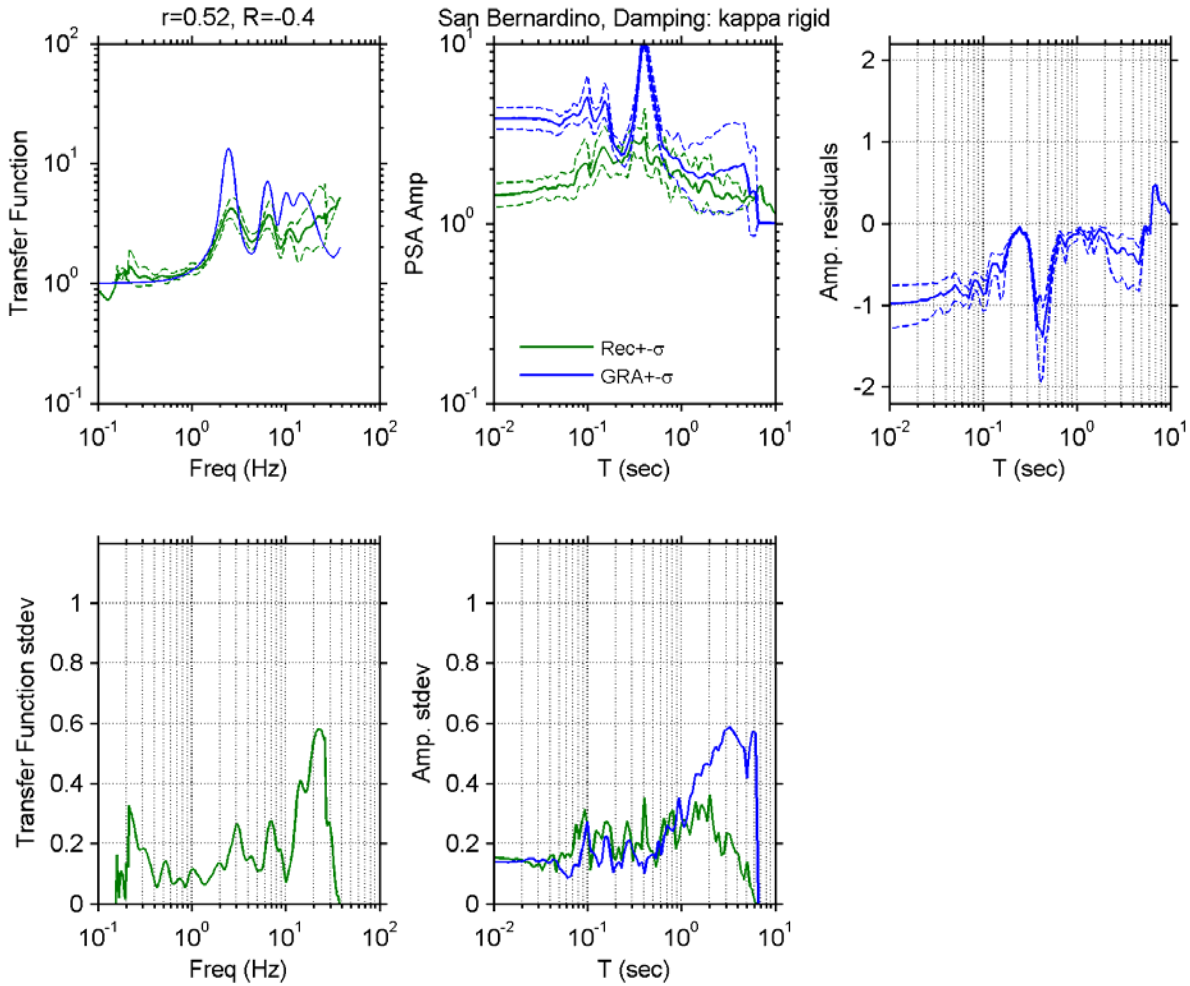

Figure A 52. Observed and simulated site response for San Bernardino site with κ-informed model for damping; Top left: Theoretical and median ± standard deviation of empirical transfer functions, Top middle: observed and predicted median ± standard deviation of *PS*A amplification, Top right: median ± standard deviation of *PS*A amplification residuals, Bottom left: standard deviation of empirical transfer functions, Bottom middle: standard deviation of observed and predicted *PS*A amplification residuals.

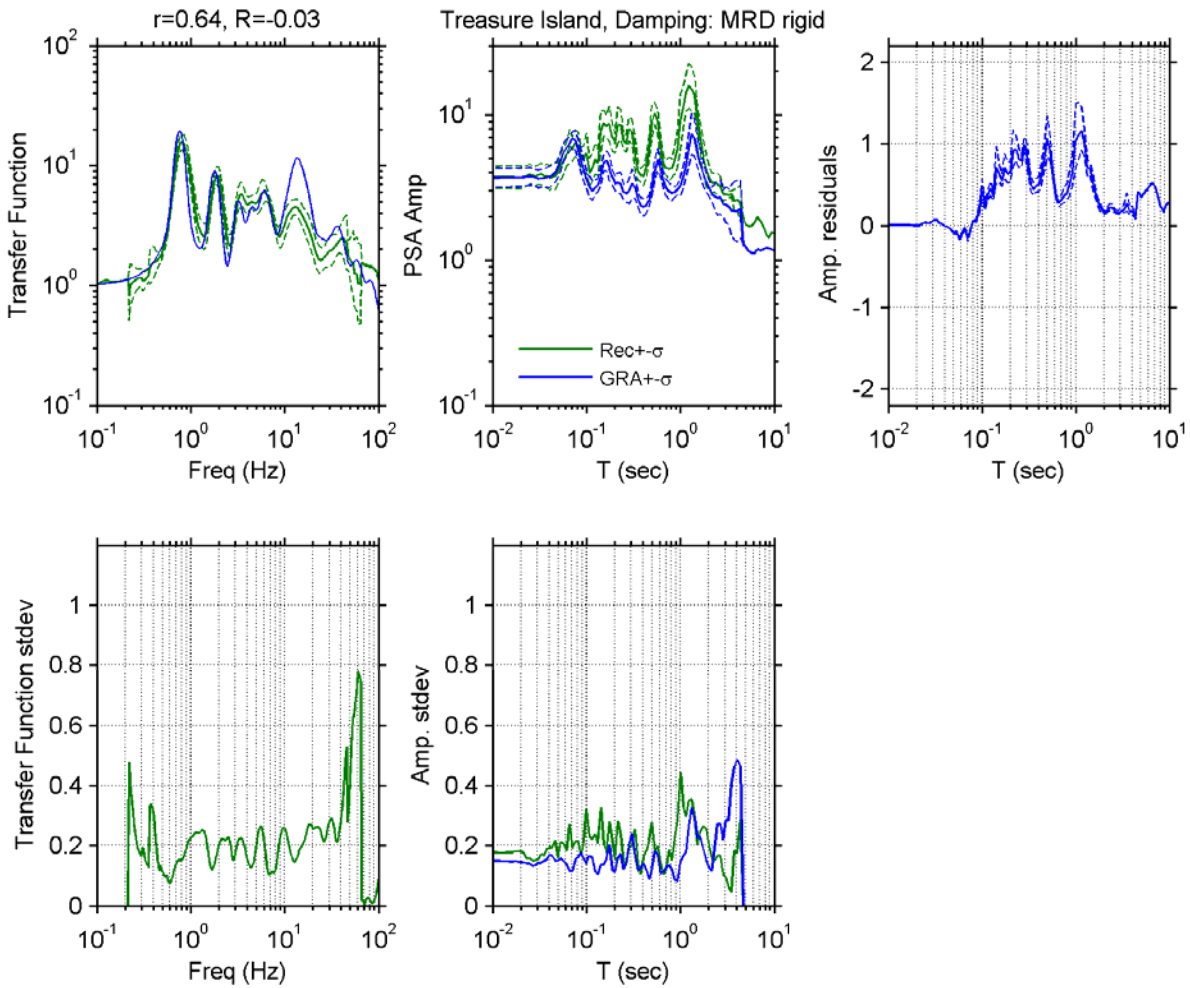

Figure A 53. Observed and simulated site response for Treasure Island site with $D^{L}_{\min}$ model for damping; Top left: Theoretical and median ± standard deviation of empirical transfer functions, Top middle: observed and predicted median ± standard deviation of *PS*A amplification, Top right: median ± standard deviation of *PS*A amplification residuals, Bottom left: standard deviation of empirical transfer functions, Bottom middle: standard deviation of observed and predicted *PS*A amplification residuals.

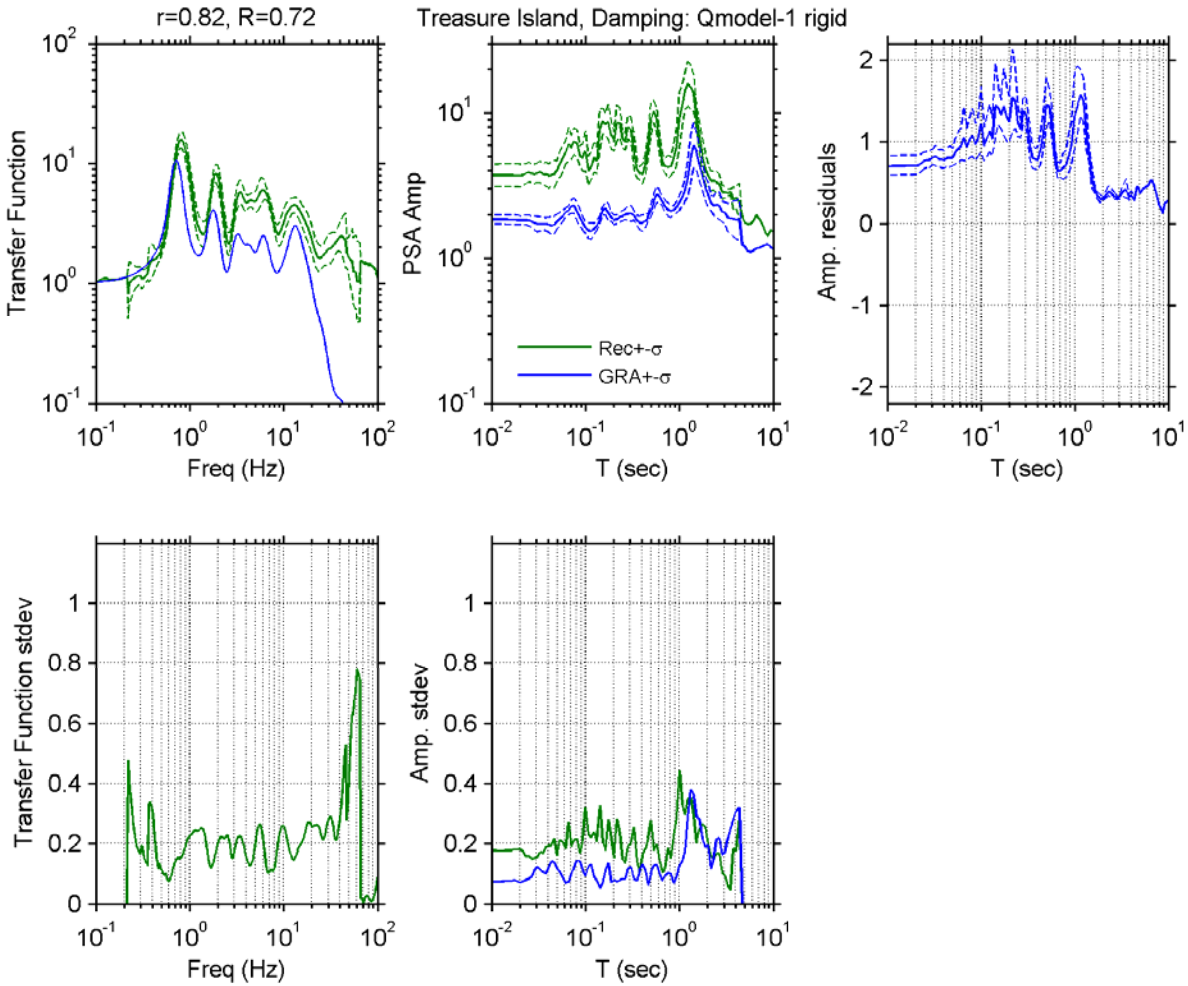

Figure A 54. Observed and simulated site response for Treasure Island site with V_S-based model for damping; Top left: Theoretical and median ± standard deviation of empirical transfer functions, Top middle: observed and predicted median ± standard deviation of *PS*A amplification, Top right: median ± standard deviation of *PS*A amplification residuals, Bottom left: standard deviation of empirical transfer functions, Bottom middle: standard deviation of observed and predicted *PS*A amplification residuals.

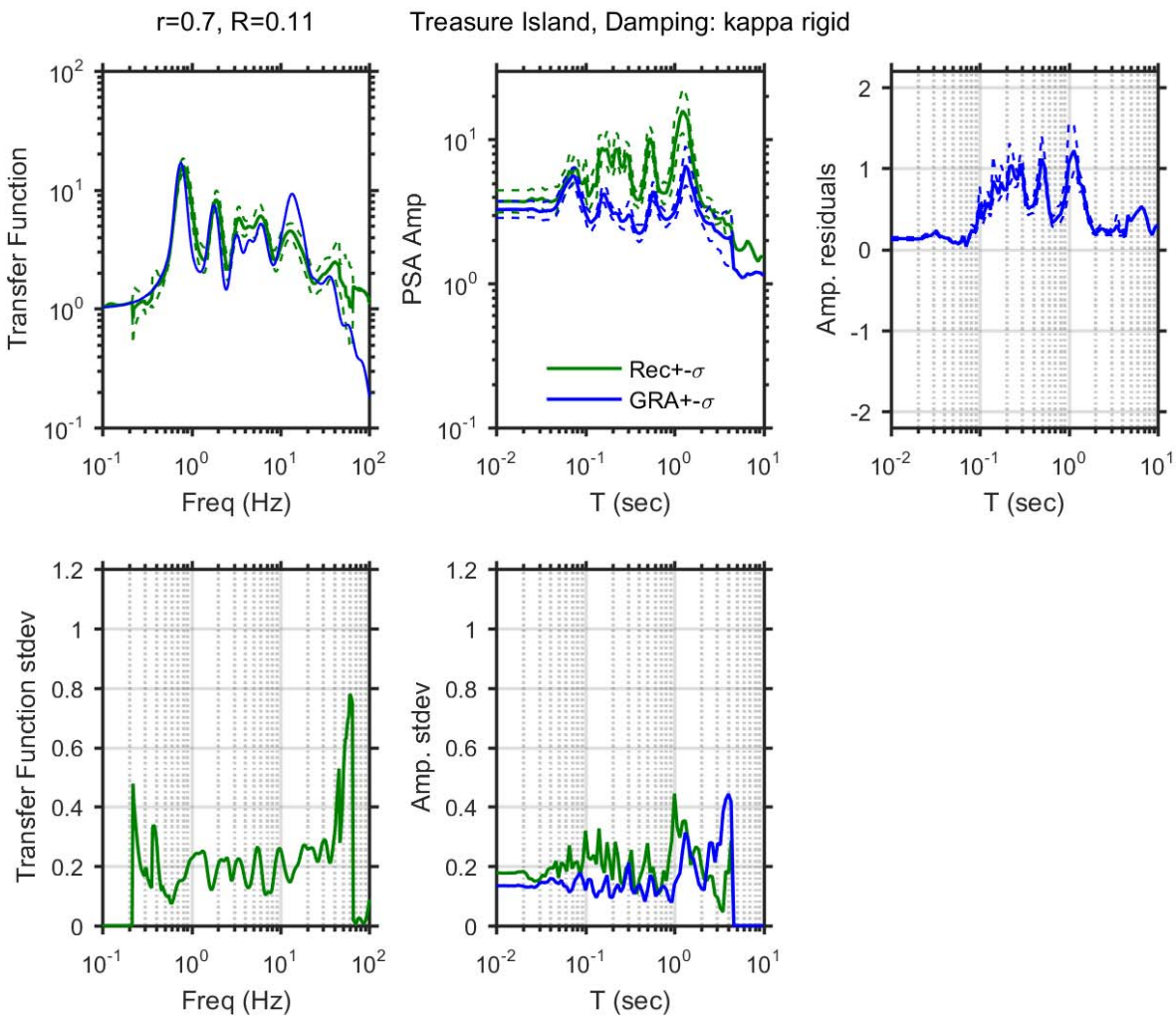

Figure A 55. Observed and simulated site response for Treasure Island site with κ-informed model for damping; Top left: Theoretical and median ± standard deviation of empirical transfer functions, Top middle: observed and predicted median ± standard deviation of *PS*A amplification, Top right: median ± standard deviation of *PS*A amplification residuals, Bottom left: standard deviation of empirical transfer functions, Bottom middle: standard deviation of observed and predicted *PS*A amplification residuals.

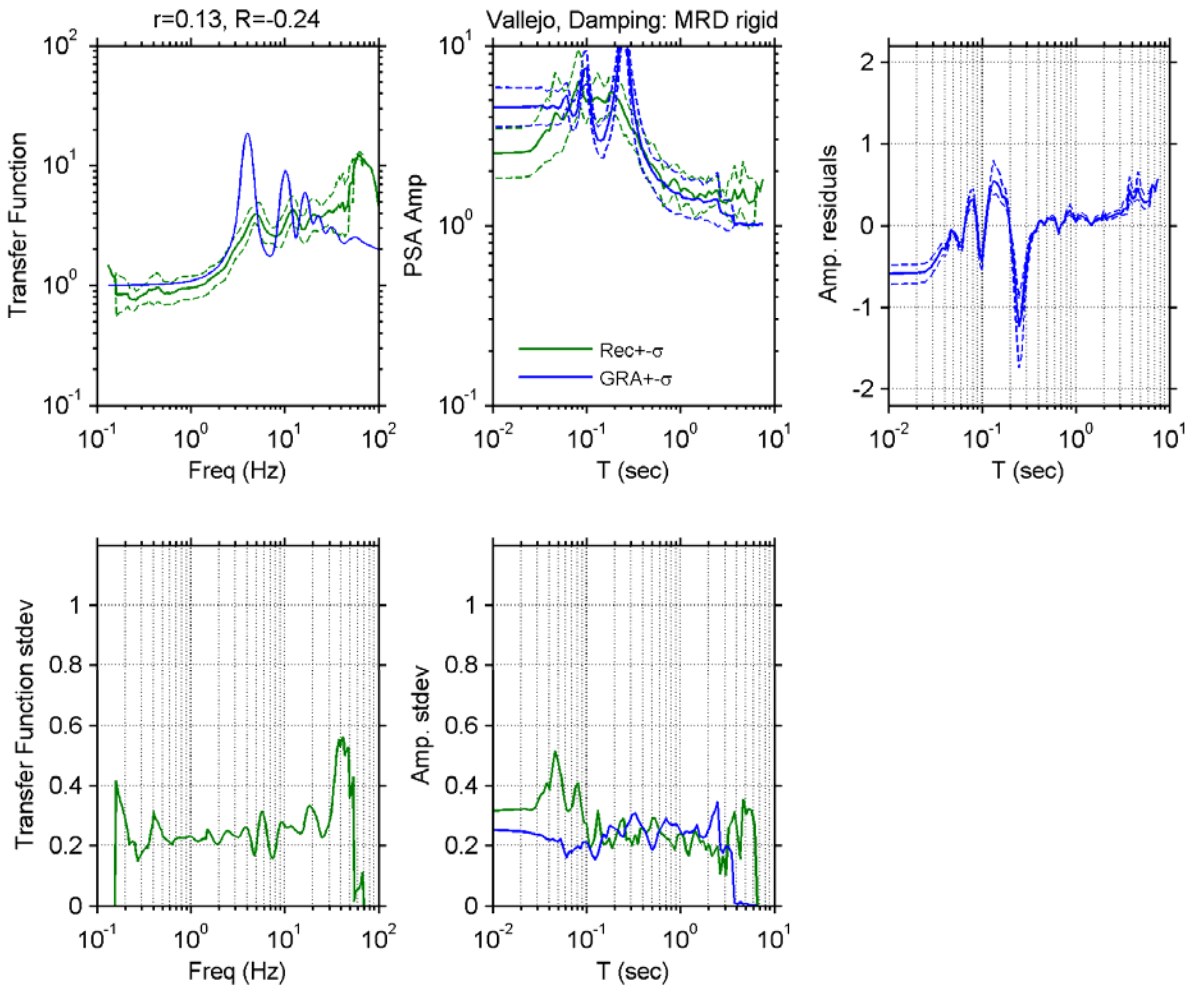

Figure A 56. Observed and simulated site response for Vallejo - Hwy 37/Napa River E site with $D^{L}_{\min}$ model for damping; Top left: Theoretical and median ± standard deviation of empirical transfer functions, Top middle: observed and predicted median ± standard deviation of *PS*A amplification, Top right: median ± standard deviation of *PS*A amplification residuals, Bottom left: standard deviation of empirical transfer functions, Bottom middle: standard deviation of observed and predicted *PS*A amplification residuals.

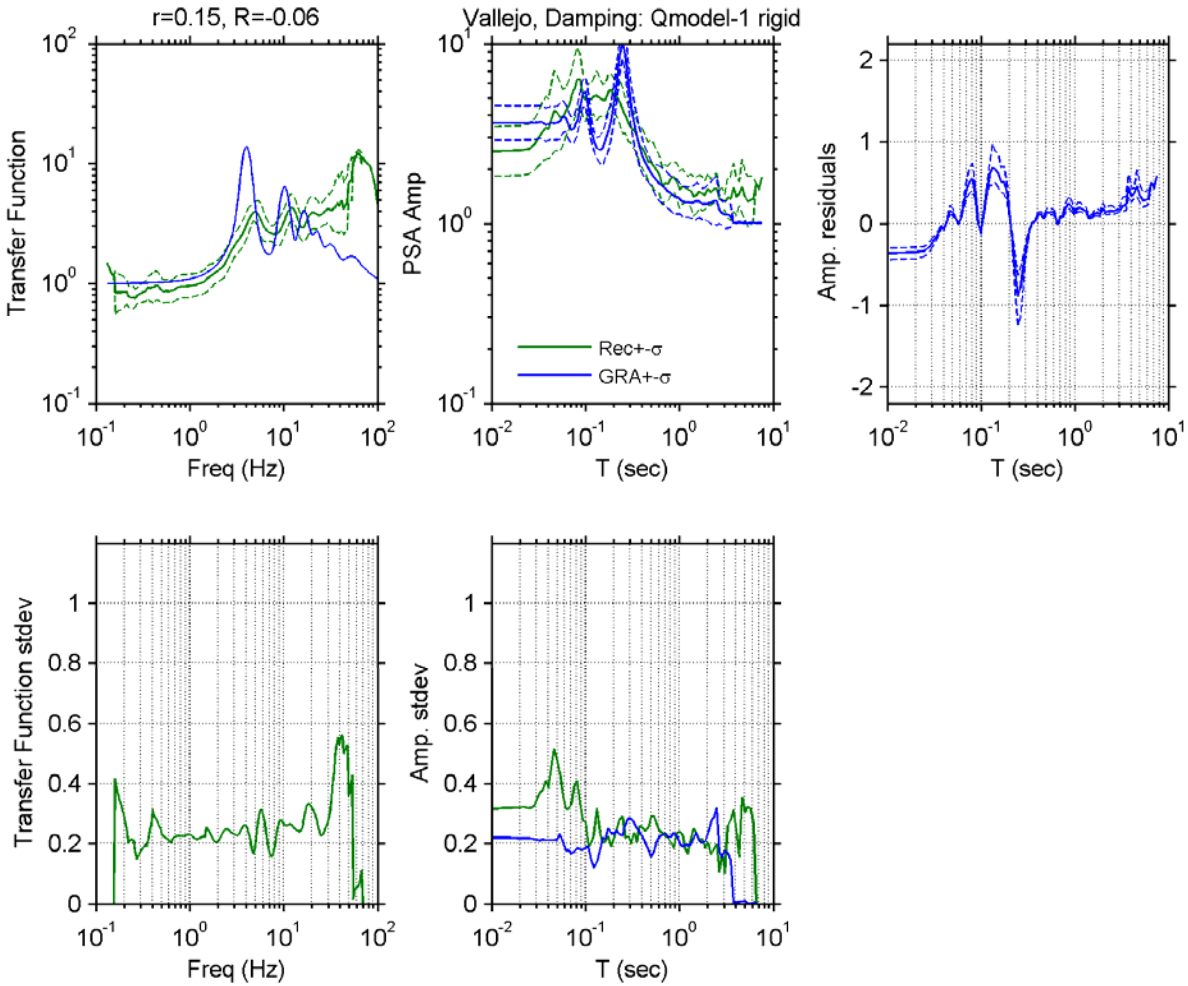

Figure A 57. Observed and simulated site response for Vallejo - Hwy 37/Napa River E site with V_S-based model for damping; Top left: Theoretical and median ± standard deviation of empirical transfer functions, Top middle: observed and predicted median ± standard deviation of *PS*A amplification, Top right: median ± standard deviation of *PS*A amplification residuals, Bottom left: standard deviation of empirical transfer functions, Bottom middle: standard deviation of observed and predicted *PS*A amplification residuals.

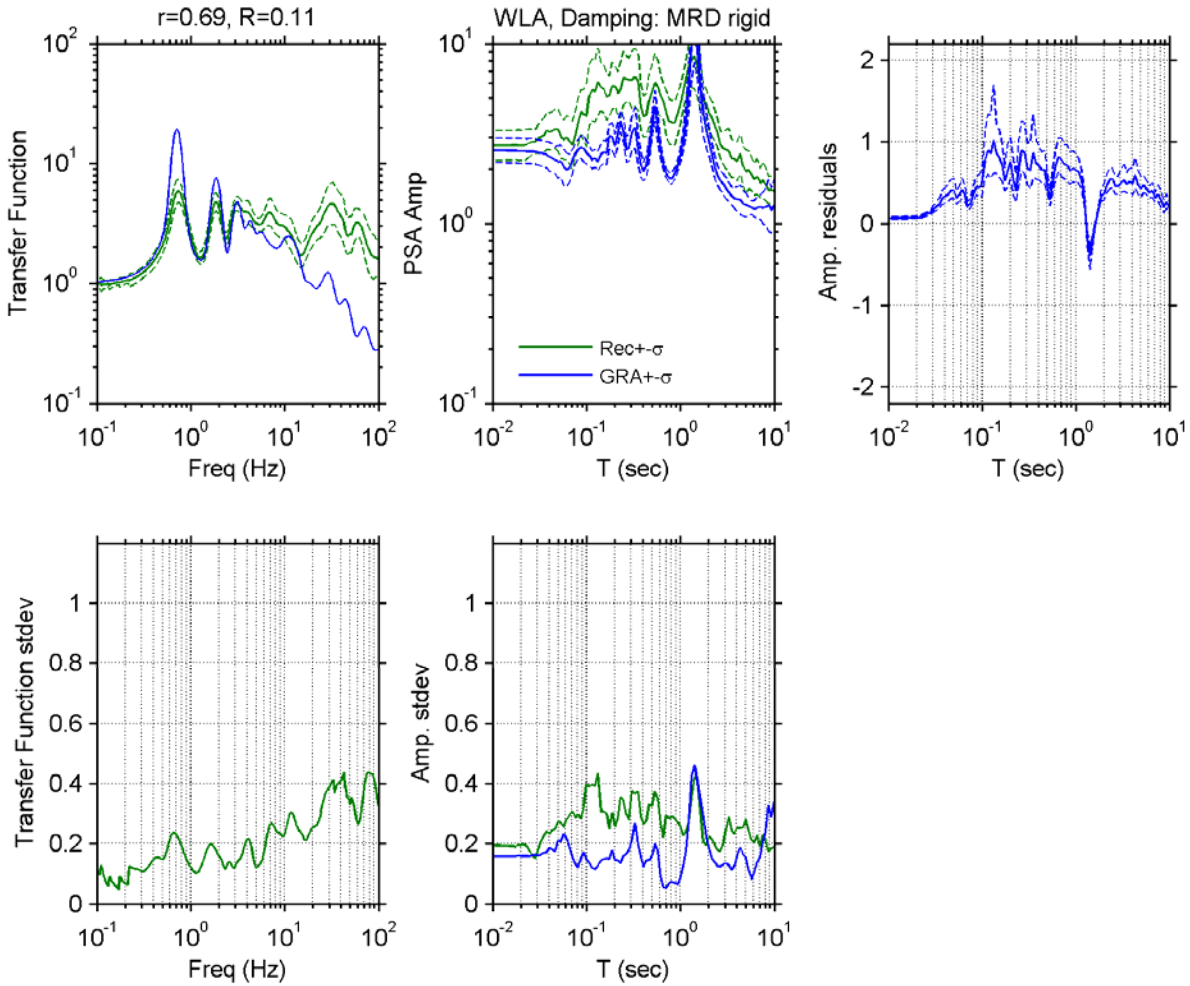

Figure A 58. Observed and simulated site response for Wildlife Liquefaction Array (WLA) site with $D^{L}_{\min}$ model for damping; Top left: Theoretical and median ± standard deviation of empirical transfer functions, Top middle: observed and predicted median ± standard deviation of *PS*A amplification, Top right: median ± standard deviation of *PS*A amplification residuals, Bottom left: standard deviation of empirical transfer functions, Bottom middle: standard deviation of observed and predicted *PS*A amplification residuals.

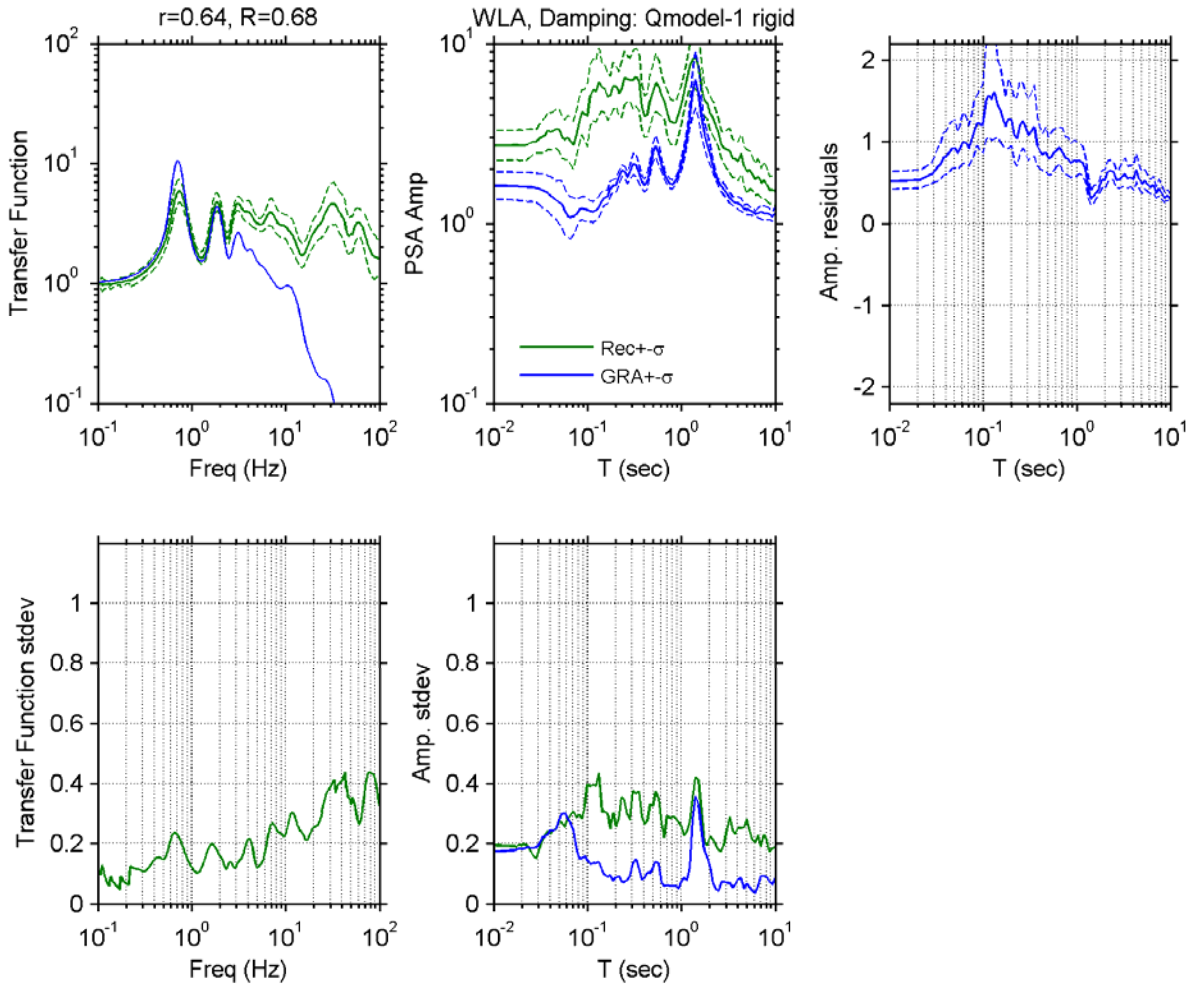

Figure A 59. Observed and simulated site response for Wildlife Liquefaction Array (WLA) site with V_S-based model for damping; Top left: Theoretical and median ± standard deviation of empirical transfer functions, Top middle: observed and predicted median ± standard deviation of *PS*A amplification, Top right: median ± standard deviation of *PS*A amplification residuals, Bottom left: standard deviation of empirical transfer functions, Bottom middle: standard deviation of observed and predicted *PS*A amplification residuals.

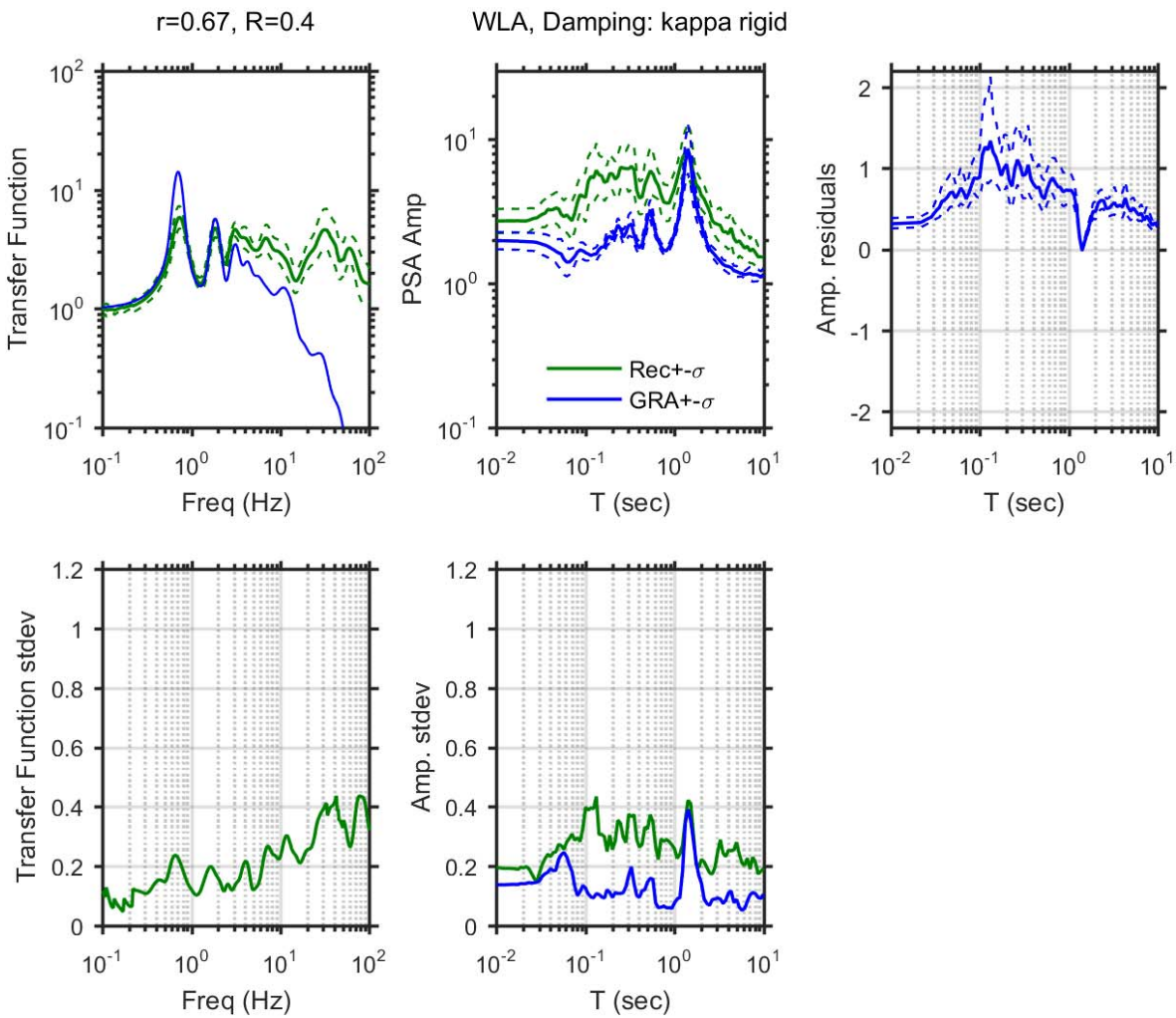

Figure A 60. Observed and simulated site response for Wildlife Liquefaction Array (WLA) site with κ-informed model for damping; Top left: Theoretical and median ± standard deviation of empirical transfer functions, Top middle: observed and predicted median ± standard deviation of *PS*A amplification, Top right: median ± standard deviation of *PS*A amplification residuals, Bottom left: standard deviation of empirical transfer functions, Bottom middle: standard deviation of observed and predicted *PS*A amplification residuals.